New Materials and Processing Routes for Photovoltaics

Benjamin George Freestone

The Department of Physics and Astronomy

University of Sheffield

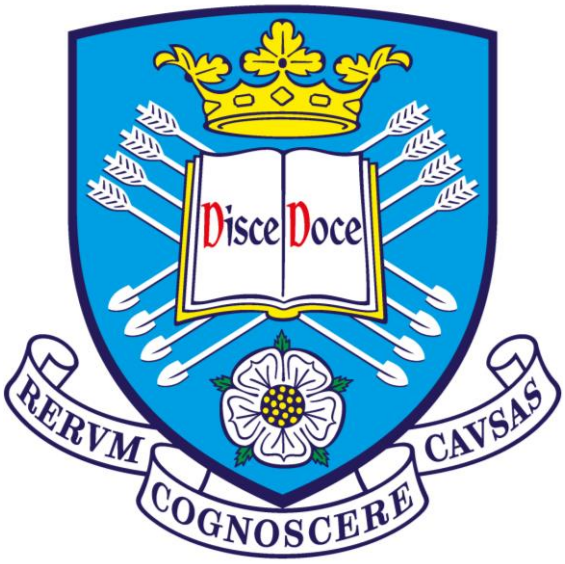

Thesis submitted for the degree of Doctor of Philosophy

November 2018

Acknowledgements

Firstly, I would like to recognise my supervisor Prof. David Lidzey for the chance to work in his research group, Electronic and Photonic Molecular Materials (EPMM). Your direction and encouragement is appreciated and I thank you so much for this opportunity. Many thanks go to my group EPMM, in particular my desk partners Michael Wong-Stringer, Thomas Routledge and Joel Smith. You have made my PhD a fantastic experience with ideas, laughs and a relaxed working atmosphere. Many thanks to Rahul Jayaprakash and my best man, Thomas Kennelly with whom I've spent plenty of wonderful coffee breaks with. To my original office members Richard (Theo) Grant and Christopher Bracher for getting me addicted to tea in my first year.

There are simply not enough words to express the incredible support provided by my beautiful wife; Alexandra Freestone, you are truly my driving force in life. Together with our dog, Brodie, we make such a great team and I cannot wait to see what our future holds. Thank you to my brother, Samuel Freestone and my parents Peter and Deborah Freestone. I am lucky to have such a kind and generous family. To the wonderful support from my in-laws, with special acknowledgement to Janis Kinlin, Alex Conron and Sue August for their continued encouragement and support from all the way across the pond.

A big thank you to my friends back home: Duncan, Thomas, Paul, Roy and George. You are all individually brilliant and funny. Thank you for making my life so full and my childhood so enjoyable. To the friends I made during undergraduate, in particular Steven, Stuart and Luke, thank you for giving me memories I will cherish for a lifetime. To the Sheffield Bears Ice Hockey team, thank you for giving me the opportunity to further my love for ice hockey over the last 3 years. I will never forget beating Hallam University 5-2 in the 2018 Varsity game, each and every moment on the ice was incredible. And lastly to the metal band Arkdown, in particular Alex, Kyle, Ed and Michael. Playing on stage and touring with you four guys was amazing, and I couldn't have asked for a better group to enjoy my passion with.

Abstract

The field of photovoltaics has seen a huge drive towards scalability and efficiency improvements over the last decade, manipulating organic and hybrid semiconducting materials in a number of different ways. In the following thesis, conjugated polymers and perovskite semiconductors are studied for the use in photovoltaic devices, including the photophysical properties and crystallographic analysis on a new low-dimensional perovskite material. A potential scale-up technique that utilises an ultrasonic spray-coating mechanism was also employed with a precursor additive, significantly improving the overall crystalline qualities and optoelectronic properties.

In **Chapter 4**, a series of organic semiconducting polymers are studied, having an electron-donating and an electron-accepting unit along a conjugated polymer backbone. This process allows for improved delocalisation of the π-conjugated electrons along the polymer chain. The optoelectronic properties of such polymers are evaluated, with the impact of the polymer:fullerene weight ratio on photovoltaic performance investigated and compared to a well referenced bulk heterojunction device. In **Chapter 5**, photovoltaic devices are studied that were fabricated using an organic-inorganic hybrid perovskite semiconductor that was deposited from a precursor ink composed of methylammonium iodide (MAI) and lead chloride ($PbCl_2$) in a DMF solution. Here, the effect of the addition of hydroidic iodide (HI) to the precursor ink was explored. The results indicate a significant improvement across all of the device performance metrics after 1 vol% of HI was added to the precursor solution.

In **Chapter 6**, the effect of non-stoichiometric excess of MAI in a MAI:$PbCl_2$ perovskite precursor is shown to facilitate the creation of low-dimensional perovskite crystal structures. This is evidenced using X-ray diffraction analysis, with 2-dimensional (2D) perovskite crystals being shown to co-exist with a bulk 3D perovskite phase. Low-temperature measurements suggest a complex energy-landscape exists within such disordered films. The photovoltaic characteristics of devices fabricated from such materials have low power conversion efficiency, with such reduced efficiency attributed to poor surface coverage and trap states in the film.

Publications

"Improved efficiency in organic solar cells via conjugated polyelectrolyte additive in the hole transporting layer"

J. Mater. Chem. C. 2016, **4**, 10722-10730

"Optimized organometal halide perovskite solar cell fabrication through control of nanoparticle crystal patterning"

J. Mater. Chem. C. 2017, **5**, 2352-2359

"Degradation of inverted architecture $CH_3NH_3PbI_{3-x}Cl_x$ perovskite solar cells due to trapped moisture"

Energy Sci Eng. 2018, **6**, 35-46

"High-performance multilayer encapsulation for perovskite photovoltaics"

Adv. Energy Mater. 2018, **8**, 1801234.

"Low-temperature, high-speed reactive deposition of metal oxides for perovskite solar cells"

J. Mater. Chem. A, 2019, **7**, 2283-2290

"Low-dimensional emissive states in non-stoichiometric methylammonium lead halide perovskites"

Submitted 2019

"Complete solvent extraction of Sn^{4+} enabling high performing tin based perovskite solar cells with high charge carrier mobilities"

Submitted 2019

Conference Presentations

1st International Conference on Perovskite Solar Cells and Optoelectronics (PSCO)

Lausanne, Switzerland (2015) - Poster presentation

2nd International Conference on Perovskite Solar Cells and Optoelectronics (PSCO)

Genoa, Italy (2016) - Poster presentation

13th Photovoltaic Science, Applications & Technology Conference (PVSAT)

Bangor, Wales, U.K. (2017) – Poster presentation

SuperSolar Summer Technical Meeting

Oxford, U.K. (2017) – Poster presentation

U.K. Semiconductors

Sheffield, U.K. (2017) - Oral presentation

European Materials Research Society (E-MRS)

Strasbourg, France. (2018) – Oral presentation

U.K. Semiconductors

Sheffield, U.K. (2018) - Oral presentation

European Optical Society Biennial Meeting (EOSAM)

Delft, Netherlands (2018) – Oral presentation

Contents

Chapter 1

Introduction

The world's population is in constant need of energy. The overwhelming majority of humans on the planet have become accustom to the luxury of powered homes and workspaces, which creates a need for the production and storage of energy. China has used been using coal as an energy source for well over a thousand years [1], whereas until the 13th century, Europe regarded coal as an inferior fuel due to its by-product of smoke and soot [1]. Wood was the fuel source of choice in western Europe before shortages in supply chains forced people to burn coal instead [1,2]. In the 18th century, huge technological and population shifts driven by the steam engine and new methods of smelting and iron refinement depended on coal for mechanical power [3]. However, the excessive use of coal was not without its pitfalls. For instance, a 2015 report on the mortality rate in England and Wales between 1851 and 1900 indicated a reduced life expectancy of 0.57 years combined with a higher mortality rate in urban areas [4]. The health risks associated with the use of coal have been known since at least 1813; black matter on the bronchial glands was routinely found in people who had died prematurely of pulmonary consumption [5]. There clearly needed to be a change in the way electricity was produced, however, coal was absolutely everywhere.

Global energy consumption statistics in the year 2016, show that the total usage of non-renewable fossil fuel sources, such as coal, reached 11,354 million tonnes (oil equivalent), a 1% increase from a 2006 usage study [6]. Burning fossil fuels, such as natural gas and coal, produces greenhouse gases like carbon dioxide (CO_2) and nitrous oxide (N_2O), contributing to a warming effect on the atmosphere of the planet [7]. It is worth noting that current studies suggest the atmosphere contained an amount of CO_2 pre-industrial

revolution at around 280 ppm [8]; estimates in 2016 propose our atmosphere contained over 400 ppm averaged across the year [9]. Greenhouse gases act as a natural blanket by absorbing the re-emitted infrared radiation from the Earth's surface. Without a greenhouse effect, the Earth's effective surface temperature would drop from approximately 14 °C to -18 °C [10]. Alternatively, too much greenhouse gas has a knock-on effect by enlarging the 'atmospheric blanket' and subsequently increasing the average global temperature. As a consequence of global warming, it has been estimated that the global sea level rose by 0.19 meters between 1901 and 2010 and the global sea temperature has risen 0.11 °C per decade between 1971 and 2010 [11]. Strides have been made to combat greenhouse gas emissions and reduce the carbon footprint in the energy sector. The National Grid (UK) announced in April 2018 that they successfully generated electricity lasting 76 hours and 10 minutes without any input from coal-powered sources, which beat the record set in 1880 [12]. The USA-based research group, SEIA also made an announcement indicating that the U.S. installed 2.5 GW_{DC} worth of photovoltaic (PV) systems in the first quarter of 2018; a 13% year-over-year increase which now provides 55% of the U.S. electrical capacity [13]. In addition, the electricity cost for roof-top and utility scale PV systems has dropped by 54% and 64% respectively in the U.S. between 2008 and 2015 [14,15]. Globally there has been a substantial shift towards a renewable technological future in energy production; 2017 reports claim a substantial surge in the world's global on and off-grid PV capacity, which increased by nearly 33% from 2016 [16].

An important sector of renewable energy research is photovoltaics. The photovoltaic effect, (originally discovered by Alexandre Becquerel in 1839), is the process in which electrical current and voltage is produced after illuminating a material with electromagnetic radiation, usually in the form of sunlight [17]. Research progressed and in 1888, Edward Weston filed and received two separate patents, US389124 and US389125, both titled "Solar Cell" [18]. A breakthrough in PV development came from electrochemist and inventor Russell Ohl, who worked for AT&T's Bell Labs in the 1930s. Together with his colleague Jack Scaff, they discovered the P-N junction (discussed further in **Chapter 2**) between two doped slabs of multi-crystalline silicon (multi-Si). They later filed a patent on the discovery entitled "Light-sensitive electric device" [19]. In a paper published

in 1954, Chapin *et.al*. discuss the limitations with their 6% silicon solar cell design, where they discovered a mismatch in material absorption within the incident solar spectrum [20]. The concept of a theoretical maximum efficiency for one-junction PV cells was later mathematically described by Shockley and Queisser in 1961, which states that an efficiency of 33.7% could be obtained for a material with a bandgap of 1.34 eV [21]. In 1989, Blakers *et.al*. reported on a 22.8% monocrystalline silicon (mono-Si) device architecture, known as the PERL cell. It is based on a chemically-passivated top and rear surface, which reduces surface recombination and increases open-circuit voltage (V_{oc}) [22]. Due to recent advancements in mono and multi-Si solar cell technologies, the lab-record efficiencies are now at 26.6% for mono-Si and 22.3% for multi-Si [23–25]. Other inorganic semiconducting materials, such as the gallium arsenide (GaAs) cells, have seen efficiencies reach 27.6 % for a 1 cm^2 thin-film cell [26]. Although efficient, the compound GaAs solar cell is limited fundamentally through its toxicity to living organisms and its composition of the rare earth metal, gallium [27].

Another class of PV cells, whose active layer comprises of organic-only components, have been studied since the photoelectric behaviour in Anthracene was discovered in 1906 [28]. Tang *et al.* made great device improvements when he combined two organic materials in a planar junction (much like the silicon P-N junction) with different ionisation potentials and electron affinities in 1986 [29]. This step improved exciton dissociation at the material boundary, which is required in photovoltaic effect processes to allow the flow of electrical charge throughout the material [30]. The ease at which conjugated electrons can be polarised gives organic semiconductors large absorption coefficients relative to inorganic structures, leading to the use of thinner material layers and thus cheaper material costs [31]. However, severe limitations on the charge transport mechanisms within organic photovoltaic absorber layers lowers the overall power conversion efficiency (PCE) relative to their inorganic photovoltaic counterparts [32,33]. One attractive aspect for using organic semiconductors is the ability to adjust the spectral absorbance by manipulating the delocalised electrons along a polymer chain [34,35]. This can be done by attaching different electron-accepting and electron-donating units at various places along a polymer backbone [36,37]. For instance, poly[N-9'-heptadecanyl-2,7-carbazole-alt-5,5-(4′,7′-di-2-thienyl-2′,1′,3′-benzothiadiazole) (PCDTBT) has been well

studied for its use in a bulk heterojunction organic solar cells [38–40]. The CDTBT monomer contains a benzothiadiazole (BTD) electron-accepting unit and a carbazole electron-donating unit, separated by thiophene units [32], giving PCDTBT an optical bandgap of ≈ 1.9 eV [41].

One particular class of hybrid semiconducting materials, called perovskites are based on a mixture of organic and inorganic components and have been studied for their optoelectronic properties since the 1990s [42]. When mixed with an appropriate solvent in a 1:1 molar ratio, methylammonium iodide (MAI) and lead iodide (PbI_2) produce the $MAPbI_3$ (MAPI) 3-dimensional (3D) perovskite crystal [43–45]. The Pb^{2+} atoms coordinate with iodide atoms to form an octahedral cage, with MA^+ cations positioned at the 8 vertices of a MAPI cubic crystal structure for T > 330 K [46]. The most common type of perovskite solar cell contains organic and inorganic precursors, and since the first introduction of hybrid perovskite solar cells in 2009 [47], PCEs have risen to an astounding 22% for laboratory-scale photovoltaic cells [48]. Organic-inorganic perovskites feature a direct optical bandgap between 1.1 and 1.7 eV, making them ideal materials for use in light-absorbing devices [49]. These hybrid semiconductors also have low effective charge carrier masses and high mobilities [50], which results in long carrier diffusion lengths of up to a micron [51]. It has been shown that by introducing hydrophobic cations in to the precursor solution it is possible to drive crystallisation towards lower-dimensional crystals, such as 0D, 1D and 2D variants of a parent 3D structure [52,53]. Mixed-phase perovskite devices with films containing 2D or quasi-2D and 3D phases have recently been used to fabricate photovoltaic devices with enhanced stability [54].

1.1. Thesis summary and motivation

The aim of this thesis is to investigate the optoelectronic properties of perovskite and new organic semiconductors with a key interest in photovoltaic applications. Initial work has concentrated on bulk heterojunctions fabricated from a polymer:fullerene matrix, which then broadened towards an exploration of organic-inorganic perovskites.

Chapter 2 presents a general background summary regarding the two classes of semiconductors, including a discussion of the current relevant literature. This is followed by a brief introduction to atomic bonding in organics, the P-N junction and techniques used in crystallography to image semiconducting thin-film samples. **Chapter 3** details the various experimental methods and techniques used in this work.

The work presented in **Chapter 4** regards a study done on a series of new donor:acceptor polymers for their use as donor materials in polymer:fullerene bulk heterojunctions. In total, 4 novel donor:acceptor polymers were studied with varying alkyl side chains and donor units. Density functional theory (DFT) calculations indicate a good electron delocalisation along the polymer chain in the ground state, with electron wavefunction overlap across donor and acceptor moieties. Different solution blend weight ratios of polymer:fullerene films were explored, with film topography imaged using an atomic force microscope (AFM). Photovoltaic devices were then fabricated based on the topographical analysis, with the performance of these photovoltaic cells compared to a PCDTBT:PCBM blend reference device. All of the experiments in this chapter were performed at the University of Sheffield. Polymers were synthesised and kindly provided by Ahmed Iraqi and his student, Ary Murad. Supporting DFT calculations were also performed by Natalia Martsinovich (Chemistry Department). PL measurements were undertaken with the help of Rahul Jayaprakash and AFM was conducted by Rachel Kilbride.

In **Chapter 5**, a solution additive known as hydroidic acid (HI) is added to a perovskite precursor to improve the solubility of lead chloride ($PbCl_2$). A study of the solution properties combined with dynamic light scattering (DLS) analysis shows precursor particulates become 3 orders of magnitude smaller after the addition of at least 1 vol% HI. Scanning electron microscopy (SEM) shows an improvement in the thin-film coverage on an ITO/PEDOT:PSS substrate, indicating greater light-absorbing potential when implemented in a photovoltaic device. X-ray diffraction (XRD) measurements on thin-films also indicated a higher order of crystallinity after HI addition. Finally, perovskite solar cells were fabricated using spin and spray-coating techniques, in which both sets of devices showed an improvement in overall performance after the addition

of HI to the precursor. In this chapter, the molar ratio of the precursor blends used to fabricate a $MAPbI_{3-x}Cl_x$ perovskite film contained a small $PbCl_2$-excess (2.9:1 for MAI:$PbCl_2$). In these experiments, SEM was performed by Robert Masters (Materials Science and Engineering) and DLS was performed under the supervision of Sarah Canning (Chemistry department). David Mohamad assisted in experiments and performed spray-coating of perovskite films and Max Reinhardt (Ossila Ltd.) provided technical input in the solution study.

Following this work, studies focused on non-stoichiometric mixtures of precursor materials. In **Chapter 6**, mixed-halide perovskites containing a non-stoichiometric excess of MAI were studied. Grazing incidence X-ray scattering (GIWAXS) is used to evidence the co-existence of low-dimensional perovskite phases with the bulk 3D perovskite, combined with SEM and energy-dispersive X-ray spectroscopy (EDX) analysis. PL spectroscopy performed at cryogenic temperatures indicates multiple excitonic peaks, which are attributed to emission from 2D or quasi-2D low dimensional perovskites (LDPs) at wavelengths between 510 nm and 605 nm together with emission from regions of bulk 3D perovskite $CH_3NH_3PbI_{3-x}Cl_x$ around 770 nm. Photoluminescence excitation spectroscopy of the LDPs reveal energy transfer between LDPs, but not to the surrounding bulk 3D perovskite. Time-resolved photoluminescence measurements demonstrate that LDP excited-state lifetimes decrease as a function of increasing temperature; a process consistent with a thermally-activated charge transfer process. By mapping the distribution of luminescence across the surface with submicron resolution, a close co-localisation of the low-dimensional emitting states and the bulk perovskite material is observed. This chapter involved a collaboration with Joel Smith who helped in the identification of the perovskite crystal structure. Giacomo Piana (University of Southampton) helped perform PL spectroscopy measurements, with other measurements performed by Jonathan Burns (AFM), Andrew Parnell (GIWAXS), Rachel Kilbride (early PL measurements, GIWAXS) and David Coles (photoluminescence excitation [PLE]).

1.2. References

1. Nef, J. U. An Early Energy Crisis and Its Consequences. *Sci. Am.* (1977).

2. Heinburg, R. The Party's Over: Oil, War and the Fate of Industrial Societies. Journal of Economic Literature **3,** *Clairview Books*, 2005).

3. Mumford, L. Technics and Civilization. 156 (1934).

4. Hanlon, W. W. Pollution and Mortality in the 19th Century. *Natl. Bur. Econ. Res.* (2015).

5. Pearson, G. On the Colouring Matter of the Black Bronchial Glands and of the Black Spots of the Lungs. *Philos. Trans. R. Soc. London* **103,** 159–170 (1813).

6. British Petroleum. BP Statistical Review of World Energy 2017. *Br. Pet.* 1–52 (2017).

7. Shafiei, S. & Salim, R. A. Non-renewable and renewable energy consumption and CO_2 emissions in OECD countries: A comparative analysis. *Energy Policy* **66,** 547–556 (2014).

8. Forster, P. & Ramaswamy, V. Changes in Atmospheric Constituents and in Radiative Forcing (IPCC 2007). *Change* **30,** 129–234 (2007).

9. Le Quéré, C. *et al.* Global Carbon Budget 2017. *Earth Syst. Sci. Data* **10,** 405–448 (2018).

10. Hansen, J. Global Trends of Measured Surface Air Temperature. **92,** (1987).

11. Climate Change 2014 Synthesis Report Summary Chapter for Policymakers. **4** (2014).

12. BMRS. Power Generation By Fuel Type. (2018).

13. Perea, A. *et al.* U.S Solar Market Insight: Executive Summary. *GTM Res. SEIA* (2018).

14. Obama, B. The irreversible momentum of clean energy. *Science,* **355,** 126–129 (2017).

15. U.S. DOE. Revolution… Now: The Future Arrives for Five Clean Energy Technologies - 2015 Update. 1–24 (2015).

16. REN21. Renewables 2018 Global Status Report. (2018).

17. Becquerel, M. E. La lumière, ses causes et ses effets. *Firmin Didot frères*, (1868).

18. Weston, E. Apparatus for utilizing solar radiant energy. (1888).

19. Ohl Russell. Light-sensitive electric device. (1941).

20. Chapin, D. M., Fuller, C. S. & Pearson, G. L. A new silicon p-n junction photocell for converting solar radiation into electrical power. *J. Appl. Phys.* **25,** 676–677 (1954).

21. Shockley, W. & Queisser, H. J. Detailed Balance Limit of Efficiency of p-n Junction Solar Cells. *J. Appl. Phys.* **32,** 510–519 (1961).

22. Blakers, A. W., Wang, A., Milne, A. M., Zhao, J. & Green, M. A. 22.8% Efficient

Silicon Solar Cell. *Appl. Phys. Lett.* **55,** 1363–1365 (1989).

23. Green, M. A. *et al.* Solar cell efficiency tables (version 51). *Prog. Photovoltaics Res. Appl.* **26,** 3–12 (2018).

24. Yoshikawa, K. *et al.* Silicon heterojunction solar cell with interdigitated back contacts for a photoconversion efficiency over 26%. *Nat. Energy* **2,** 17032 (2017).

25. Benick, J. *et al.* High-Efficiency n-Type HP mc Silicon Solar Cells. *IEEE J. Photovoltaics* (2017).

26. Kayes, B. M. *et al.* 27.6% Conversion efficiency, a new record for single-junction solar cells under 1 sun illumination, *Conference Record of the IEEE Photovoltaic Specialists Conference* (2011).

27. Webb, D. R., Wilson, S. E. & Carter, D. E. Comparative pulmonary toxicity of gallium arsenide, gallium(III) oxide, or arsenic(III) oxide intratracheally instilled into rats. *Toxicol. Appl. Pharmacol.* **82,** 405–416 (1986).

28. Pochettino, A. On the photo-electric behavior of the Anthracene. *Acad. Lincei Rend.* **15,** 355–363 (1906).

29. Tang, C. W. Two-layer organic photovoltaic cell. *Appl. Phys. Lett.* **48,** 183–185 (1986).

30. Bernede, J. C. Organic Photovoltaic Cells: History, Principle and Techniques. *J. Chil. Chem. Soc.* **53,** 1549–1564 (2008).

31. Hoppe, H. & Sariciftci, N. S. Organic solar cells: An overview. *J. Mater. Res.* **19,** 1924–1945 (2004).

32. Scarongella, M., Laktionov, A., Rothlisberger, U. & Banerji, N. Charge transfer relaxation in donor-acceptor type conjugated materials. *J. Mater. Chem. C* **1,** 2308–2319 (2013).

33. Nelson, J. Organic photovoltaic films. *Curr. Opin. Solid State Mater. Sci.* **6,** 87–95 (2002).

34. Liu, C., Wang, K., Gong, X. & Heeger, A. J. Low bandgap semiconducting polymers for polymeric photovoltaics. *Chem. Soc. Rev.* **45,** 4825–4846 (2016).

35. Leo, K. Elementary Processes in Organic Photovoltaics. **272,** *Springer International Publishing*, (2017).

36. Jao, M.-H., Liao, H.-C. & Su, W.-F. Achieving a high fill factor for organic solar cells. *J. Mater. Chem. A* **4,** 5784–5801 (2016).

37. Yu, J. *et al.* 2,1,3-Benzothiadiazole-5,6-dicarboxylicimide-Based Polymer Semiconductors for Organic Thin-Film Transistors and Polymer Solar Cells. *ACS Appl. Mater. Interfaces* **9,** 42167–42178 (2017).

38. Wang, T. *et al.* Correlating Structure with Function in Thermally Annealed PCDTBT:PC70BM Photovoltaic Blends. *Adv. Funct. Mater.* **22,** 1399–1408 (2012).

39. Zhang, Y. *et al.* PCDTBT based solar cells: one year of operation under real-world conditions. *Sci. Rep.* **6,** 21632 (2016).

40. Liao, H. C. *et al.* Additives for morphology control in high-efficiency organic solar cells. *Mater. Today* **16,** 326–336 (2013).

41. Bae, S. H. *et al.* Printable Solar Cells from Advanced Solution-Processible Materials. *Chem* **1,** 197–219 (2016).

42. Green, M. A. & Ho-Baillie, A. Perovskite Solar Cells: The Birth of a New Era in Photovoltaics. *ACS Energy Lett.* **2,** 822–830 (2017).

43. Leguy, A. M. A. *et al.* Reversible Hydration of $CH_3NH_3PbI_3$ in Films, Single Crystals, and Solar Cells. *Chem. Mater.* **27,** 3397–3407 (2015).

44. D'Innocenzo, V., Srimath Kandada, A. R., De Bastiani, M., Gandini, M. & Petrozza, A. Tuning the light emission properties by band gap engineering in hybrid lead-halide perovskite. *J. Am. Chem. Soc.* **136,** 17730–17733 (2014).

45. Ma, H., Imran, M., Dang, Z. & Hu, Z. Growth of Metal Halide Perovskite, from Nanocrystal to Micron-Scale Crystal: A Review. *Crystals* **8,** 182 (2018).

46. Whitfield, P. S. *et al.* Structures, Phase Transitions and Tricritical Behavior of the Hybrid Perovskite Methyl Ammonium Lead Iodide. *Sci. Rep.* **6,** 35685 (2016).

47. Kojima, A., Teshima, K., Shirai, Y. & Miyasaka, T. Organometal Halide Perovskites as Visible-Light Sensitizers for Photovoltaic Cells. *J. Am. Chem. Soc.* **131,** 6050–6051 (2009).

48. Ahmadi, M., Wu, T. & Hu, B. A Review on Organic-Inorganic Halide Perovskite Photodetectors: Device Engineering and Fundamental Physics. *Adv. Mater.* **29,** 1605242 (2017).

49. Stoumpos, C. C., Malliakas, C. D. & Kanatzidis, M. G. Semiconducting tin and lead iodide perovskites with organic cations: Phase transitions, high mobilities, and near-infrared photoluminescent properties. *Inorg. Chem.* **52,** 9019–9038 (2013).

50. Herz, L. M. Charge-Carrier Mobilities in Metal Halide Perovskites: Fundamental Mechanisms and Limits. *ACS Energy Lett.* **2,** 1539–1548 (2017).

51. Stranks, S. D. *et al.* Electron-hole diffusion lengths exceeding 1 micrometer in an organometal trihalide perovskite absorber. *Science,* **342,** 341–344 (2013).

52. Lin, H., Zhou, C., Tian, Y., Siegrist, T. & Ma, B. Low-Dimensional Organometal Halide Perovskites. *ACS Energy Lett.* 54–62 (2017).

53. Misra, R. K., Cohen, B., Iagher, L. & Etgar, L. Low-Dimensional Organic – Inorganic Halide Perovskite : Structure , Properties , and Applications. 3712–3721 (2017).

54. Grancini, G. *et al.* One-Year stable perovskite solar cells by 2D/3D interface engineering. *Nat. Commun.* **8,** 15684 (2017).

Chapter 2

Background Theory

2.1 Introduction

The following chapter details the various physical and electronic properties within perovskites and organic semiconductors. First, a brief introduction to the photovoltaic effect is given in **Section 2.2**, followed by a discussion on photovoltaic device characterisation in **Section 2.3**. Some background theory on atomic orbitals is covered in **Section 2.4**, with a review on perovskite and organic semiconductors in **Sections 2.5** and **2.6**, respectively. The charge carrier dynamics in organic and hybrid perovskites are described in **Section 2.7**, followed by a brief introduction to the photophysics of organic and hybrid semiconductors in **Section 2.8**.

2.2 The photovoltaic effect

For over 4.6 billion years the Sun has been producing electromagnetic radiation, emitting its energy isotropically across the universe [1]. A certain frequency range of photons emitted by the Sun, known as the visible region, possess a wavelength between 300 nm and 700 nm, which humans (and some animals) observe as blue and red light, respectively [2,3] (**Figure 2.1 (a)**). Incident photons on a semiconductor material that fall within the visible-infrared window are able to excite electrons to higher energy levels or excited states, where they are then able to move freely in a conduction band. If, however,

the excited-state electron is extracted from this conduction band by some built-in asymmetry to an external circuit, a current is produced. This process is called the photovoltaic (PV) effect and was discovered by Alexandre Becquerel in 1839 [4]. The photovoltaic effect is rather similar to that of the photoelectric effect suggested by Einstein in 1905 [5], whereby incident light with enough energy per photon is able to promote an electron from the surface of a metal to a vacuum state, effectively removing it from the solid.

The theoretical maximum power conversion efficiency (PCE) of a single-junction solar cell under Air Mass 1.5 (AM1.5) illumination is known as the Shockley-Queisser limit [6]. With an optimum material bandgap of 1.34 eV (925 nm) under 1000 Wm^{-2} illumination, the theoretical PCE maximum is 33.7%. For silicon (E_g = 1.14 eV, 1130 nm) the theoretical maximum PCE is around 32%. Other photovoltaic systems, such those based on organic semiconductors (OPVs) and hybrid organic-inorganic perovskites (PSCs) have now demonstrated PCEs of 17.3% and 22.7%, respectively [7,8] (**Figure 2.1 (b)**). When photons of energy $E < E_g$ interact with a semiconductor they are not absorbed, and therefore do not induce a photocurrent which results in performance losses. For example, the $CH_3NH_3PbI_3$ perovskite has an optical bandgap of around 1.6 eV (770 nm) and thus does not absorb any photons with E < 1.6 eV [9]. However, for photons with E > 1.6 eV, several other loss mechanisms can occur, such as thermalisation and transmission losses [10], resulting in a further reduction in PCE.

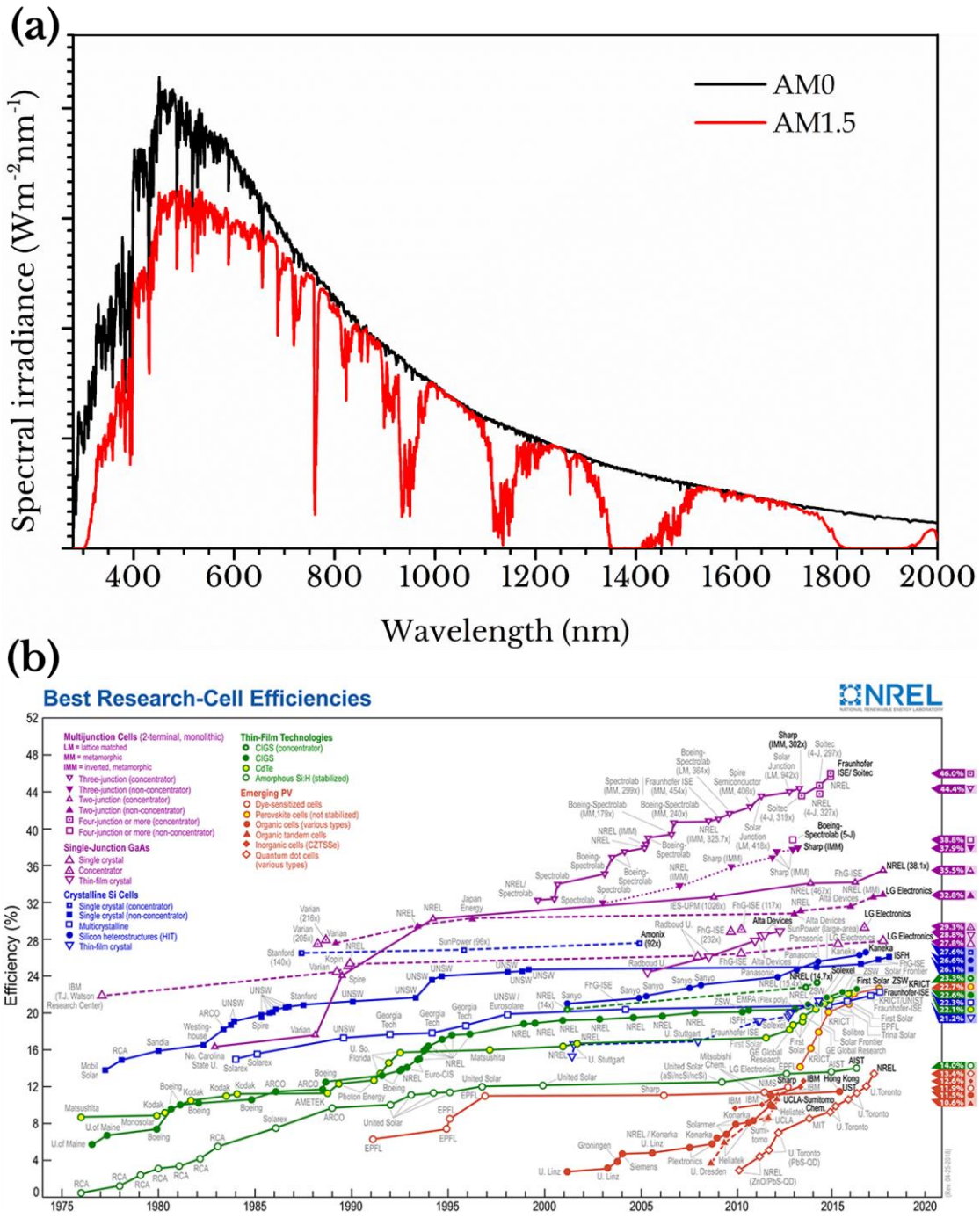

Figure 2.1 - (a) Solar spectrum as recorded outside Earth's atmosphere (AM0 – black curve) and on the Earth's surface at an angle of 41° (AM1.5 – red curve). (b) NREL research cell efficiency records between 1976 and 2018. Perovskite cells are shown as red and yellow circles, organic cells are shown as a solid red circle.

2.3 Characterising photovoltaic devices

A solar cell situated in the dark behaves much like a diode. Minority carriers can drift across the device to become majority carriers, which in turn produce a very small, but measureable current known as the dark saturated current (J_{dark}). A current-voltage (J-V) measurement can be thought of as the superposition of the solar cell diode in the dark and under illumination [11]. Illuminating the solar cell produces charge carriers in the material through the absorption of photons in the active layer. If these charges dissociate through the built-in electric field at a P-N junction, electrons will flow to the cathode and holes will flow toward the anode. This gives rise to a photocurrent in the opposite direction to the dark current, and applying a forward bias (V > 0 V) produces the same current flow as seen for a diode. When the voltage applied to an illuminated solar cell is zero, the current flowing in the device is known as the short-circuit current, J_{sc}, which acts like a reverse bias current, where $J_{sc} >> J_{dark}$. There are a number of factors that determine the value of J_{sc}, such as the incident solar spectrum, the optical properties of the material (reflection and absorption losses), as well as the area of the solar cell. In this thesis, the J_{sc} is described as a current density and is therefore written as the current per unit area (mA cm^{-2}). Another factor that affects the short-circuit current is the power of the incident light, however, this effect is not detailed in this work.

As the forward bias voltage increases, it begins to compensate for the reverse photocurrent produced by the incident light and at an applied voltage the current produced by the cell increases to zero. Note that the photocurrent is given a negative value to distinguish it from the current produced by the cell under forward bias. At this voltage, the device behaves much like it would under open circuit conditions. When the current produced by the illuminated cell is zero, the forward bias fully compensates for the reverse photocurrent, therefore, the applied bias at that value is considered to be the open-circuit voltage, V_{oc}.

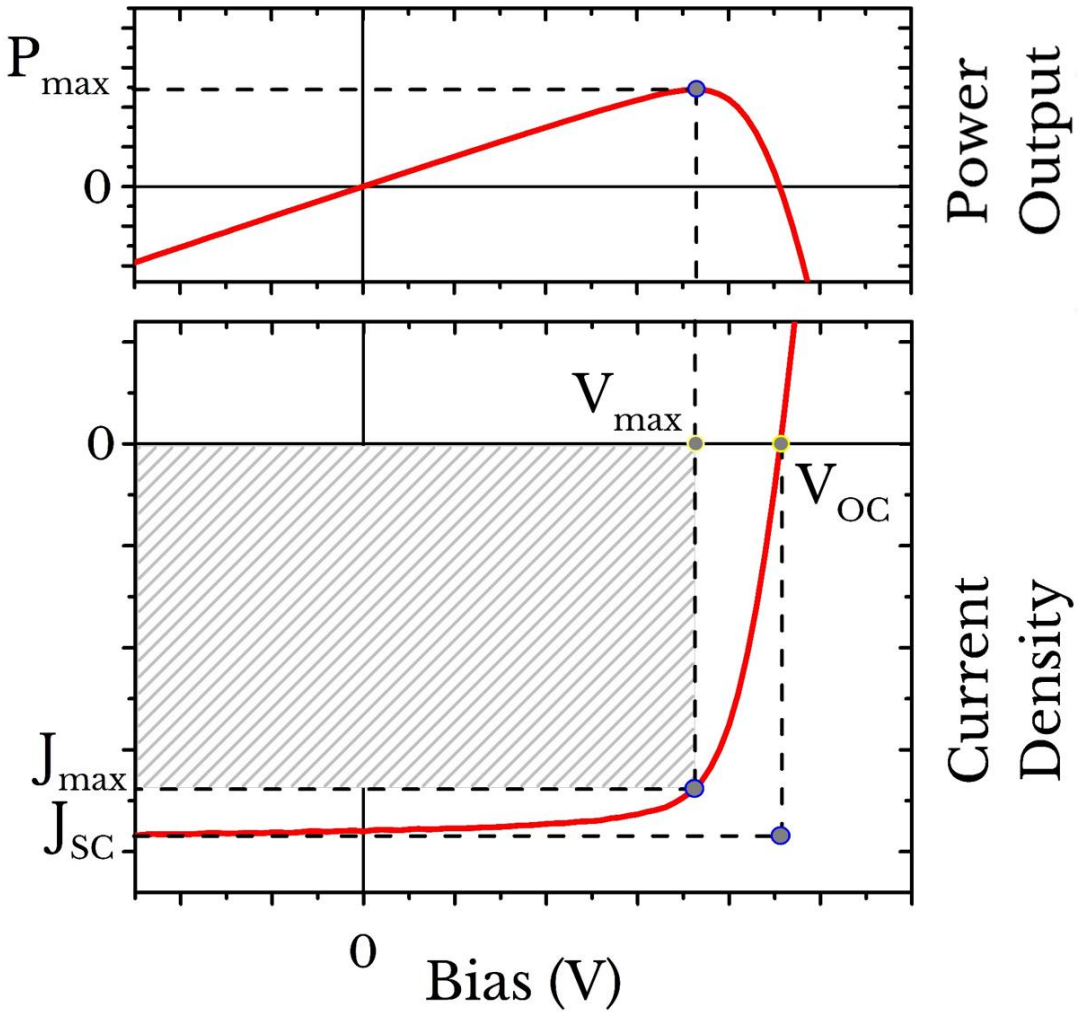

Figure 2.2 - The power output and corresponding current-voltage (J-V) sweep of a typical solar cell. The coloured grey box represents the fill factor of the device, which is clearly reduced compared to the ideal described by the J_{sc} and V_{oc}. The operating parameters for the device shown above under AM1.5 conditions are: PCE = 12.3%, V_{oc} = 0.91 V, J_{sc} = -19.0 mAcm^{-2} and FF = 70.7 %. The maximum power point bias is 0.72 V.

Another useful parameter for characterising photovoltaics is the power output, a product of the voltage and current in the device. The maximum power (P_{max}) available from a cell is calculated through the product of the maximum voltage, V_{max}, and the maximum photocurrent J_{max}. An ideal PV cell would yield a straight line photocurrent up to the V_{oc}, after which it would fall to zero, as shown in **Figure 2.2**. This would suggest that for an ideal solar cell P_{max} is equal to the product of V_{oc} and J_{sc}. In reality, however,

the maximum power available is reduced from the ideal and describes an area shown by the grey box in **Figure 2.2**. The ratio of which the maximum power is reduced is called the fill factor (FF), and is calculated through the following relationship:

$$FF = \frac{J_{max}V_{max}}{J_{sc}V_{oc}} \tag{2.1}$$

where the FF is equal to 100 % (or 1) for an ideal solar cell. The maximum power output for a solar cell can then be described as a function of the FF:

$$P_{max} = J_{max}\,V_{max} = V_{oc}J_{sc}\,FF \tag{2.2}$$

The efficiency (η) can be written as the ratio of the power out to the power in, such that:

$$\eta\,(\%) = \frac{P_{max}}{P_{in}} = \frac{V_{oc}J_{sc}FF}{P_{in}} \tag{2.3}$$

where P_{in} is the power of the incident solar radiation. All of the above parameters can be taken from a simple J-V sweep of a device and therefore it is a useful measurement technique used to characterise solar cells. For the work in this thesis the value of P_{in} was calibrated to 100 mW cm^{-2} at 25°C using a Newport 92251A-1000 solar simulator.

A more quantitative approach is to describe the J-V characteristics using the Shockley diode equation [6], which is first described through the ideal diode equation:

$$J_D(V) = J_{dark}\left[\exp\left(\frac{eV}{k_BT}\right) - 1\right] \tag{2.4}$$

where J_D is the current through the diode, e is the electron charge, V is the diode voltage, k_B is Boltzmann's constant and T is the absolute temperature of the diode. Upon illumination, a photocurrent J_{SC} is produced and the diode equation becomes

$$J(V) = J_D - J_{SC} = J_{dark}\left[\exp\left(\frac{eV}{k_BT}\right) - 1\right] - J_{SC} \tag{2.5}$$

The negative sign for the photocurrent indicates that the J_{SC} flows in an opposite direction to the dark saturation current, as seen in **Figure 2.3 (a)**. However, **Equation 2.5** above does not account for the effect of parasitic resistance present in non-ideal solar cells. Power is lost from the cell through separate resistance pathways, which are named parasitic series and shunt resistances, respectively. **Figure 2.3 (b)** shows an equivalent circuit model for a non-ideal solar cell.

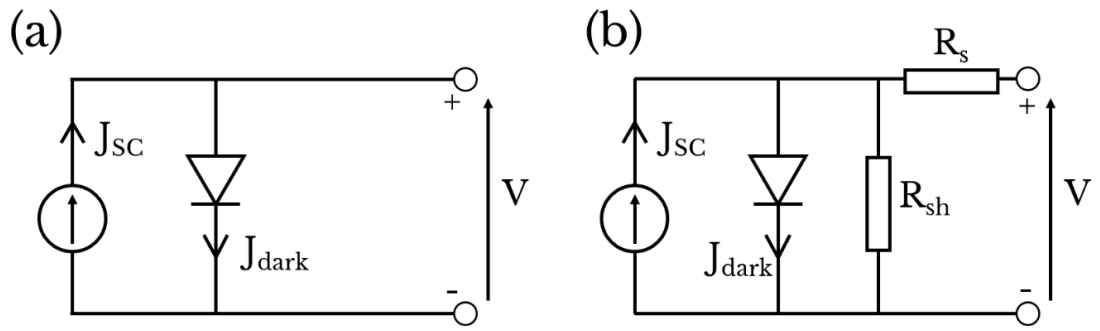

Figure 2.3 - Equivalent solar cell circuits for (a) an ideal cell and (b) a non-ideal cell with the inclusion of series and shunt resistances.

As a PV cell resistance will depend on its geometry and its active area, the series resistance can be derived by substituting for current density in Ohm's law. This yields the units of the series resistance as $\Omega\,cm^2$. The series resistance results from a number of factors, most notably the movement of charge through the p-(i)-n junction, the resistance between semiconductor and metal contact and the resistance of the metal contacts themselves. A large series resistance will lower the FF of the device. It is useful to include the series resistance in the diode equation by substituting in for V and including the ideality factor, n, in **Equation 2.5**:

$$J(V) = J_D - J_{SC} = J_{dark}\left[\exp\left(\frac{e(V + JR_s)}{nk_BT}\right) - 1\right] - J_{SC} \qquad (2.6)$$

Here, the ideality factor, n, is a dimensionless constant, which indicates how close the diode behaves to that of an ideal diode. A value of n = 1 assumes that all recombination occurs via band to band transitions away from the junction and limited only by the minority carriers. Recombination limited by both types of carriers (minority and majority) increases the ideality factor to n = 2 [12].

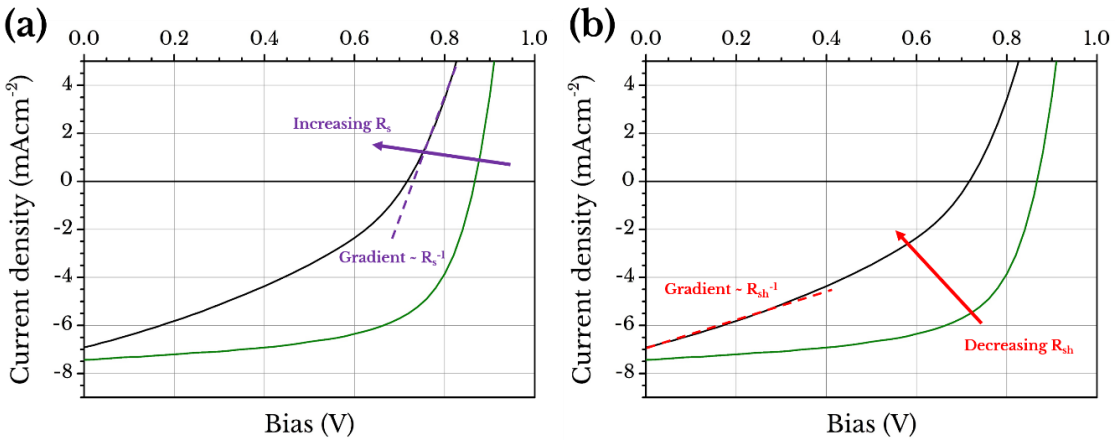

Figure 2.4 – Graphical representation showing the effect of increasing series (R_s) and shunt (R_{sh}) resistances by comparing current-voltage (J-V) measurements on bulk-heterojunction organic solar cells. (a) indicates an increase in R_s (arrow) and the typical gradient measured to obtain a value for R_s (dashed line). (b) shows the effect of decreasing R_{sh} (arrow) on the J-V curve indicated by larger gradient (dashed line).

Another source of resistive losses in a device comes from the shunt resistance, R_{sh}. As shown in **Figure 2.3 (b)**, a low shunt resistance will provide an alternative current pathway for the photocurrent, lowering the current passing through the p-(i)-n junction and thus lowering the output voltage. At lower operating voltages the effect of R_{sh} is substantial because the effective resistance within the solar cell is high due to the parallel nature of the shunt resistance. A shunt resistance component can be included in the diode equation as shown in **Equation 2.6** [13]

$$J(V) = J_D - J_{SC} = J_{dark}\left[\exp\left(\frac{e(V + JR_s)}{nk_BT}\right) - 1\right] + \frac{V + JR_s}{R_{sh}} - J_{SC} \qquad (2.7)$$

The values of R_s and R_{sh} can be estimated from the J-V graph as shown in **Figure 2.4**. The green and black curves are taken from bulk-heterojunction (BHJ) OPVs described in more detail in **Chapter 4**.

Before moving on to discussing the properties of the semiconductors that are used in PV devices, the next session discusses general atomic orbital theory, and demonstrates how this simple framework can be applied to rationalise the structural and electronic properties of a range of PV device applicable materials.

2.4 Atomic orbitals

In the early 20th century, Niels Bohr proposed the idea of a coulumbic interaction between nuclei and orbiting electrons, which challenged J. J. Thompson's original model of circular electron orbits of arbitrary radii around a positively-charged heavy nucleus. In his work published in 1913, Bohr related the spectral lines observed from Hydrogen atoms to a set of discrete energy levels within an atom. Each energy level is associated with an allowed electron orbital, labelled n=1,2,3..., where n increases with the radii of the allowed orbital. This model suggested that electrons can only 'leap' instantaneously between pre-specified orbital energies by absorbing or emitting quanta of fixed energy. Erwin Schrödinger applied his mathematical equations that described an electron as a wavefunction instead of a particle to the confines of the atom. Schrödinger formulated quantum mechanical wavefunctions to describe the probability of finding an electron in a particular location or orbital. These wavefunctions described the 'state' of a single electron within an atom. Plotting the distributions of such orbitals produces electron probability clouds and form the quantum mechanical model of the atom.

The allowed energy levels in an atom can be described using the quantum numbers n (principle quantum number), l (azimuthal quantum number), m_l (magnetic quantum

number) and m_s (spin quantum number), which determine the size (n), shape (l) and orientation (m_l, m_s) of the orbitals. These values are summarised in **Table 2.1** which indicates the formation of 3 atomic orbitals: 1s, 2s and 2p from a total of 10 electrons.

Quantum number				Orbital name		Total number of electrons
n	l	m_l	m_s			
1	0	0	1/2 -1/2	1s		2
2	0	0	1/2 -1/2	2s		8
	1	-1	1/2 -1/2	$2p_x$	2p	
		0	1/2 -1/2	$2p_y$		
		1	1/2 -1/2	$2p_z$		

Table 2.1 – A summary of the allowed quantum numbers n, l, m_l and m_s with corresponding orbital names and total number of electrons per orbital. Only the first two n quantum numbers are listed.

The formation of the atomic orbital is a consequence of the allowed values each quantum number can take. As seen in **Table 2.1**, the 1s orbital is composed of integer quantum numbers n=1, l and m_l = 0, except the spin (m_s), which takes a half integer value of ± ½. The half integer values are a result of the Pauli Exclusion Principle, which states that no two or more identical fermions (particles that possess a spin ½) can occupy the same state within a system simultaneously. An n = 1 energy level has a corresponding azimuthal quantum number (l) of l = 0,1,2..(n-1) = 0. Accordingly, m_l has a range of $-l$ to $+l$ at integer values and m_s = *-s, -s+1, -s+2,..,s-2, s-1, s*. As the electrons in the orbitals are fermions, s = ½, and so m_s = ± ½. The n=2 quantum number is made up of a 2s and a 2p orbital, whereby the 2p orbital has components along the x,y and z axis (p_x, p_y and p_z),

as shown in **Table 2.1**. This is due to the l = 0, 1 quantum numbers, which account for the 2s (l = 0) and 2p (l = 1) shells with corresponding subshells p_x, p_y and p_z. It is these 2p subshells that play an important role in organic chemistry by forming hybridised carbon bonds along polymer chains. For completeness, l = 2 forms 3s, 3p and 3d shells with a maximum of 10 electrons and l = 3 produces 4s, 4p, 4d and 4f with a maximum of 14 electrons. In the following section, the fundamentals of hybridisation in carbon bonds is discussed.

2.4.1 Hybridised carbon bonds

Carbon has an electronic structure of $1s^2\ 2s^2\ 2p^2$ which allows for two covalent bonds to be formed from the two valence electrons. The s-orbitals occupy a spherical region of space with the nucleus at the centre, whereas p-orbitals arrange themselves in symmetric balloon-type regions reflected around the x, y and z planes. $2s^2\ 2p^2$ represents the second energy level in carbon and consists of four orbitals, the 2s and three 2p orbitals: $2p_x$, $2p_y$ and $2p_z$. In order to do this, the carbon atom must promote a lower energy s-orbital electron into an unoccupied p-orbital. This is shown through a simplified electron energy diagram in **Figure 2.5 (a-c)**. Hybridisation occurs when the one remaining electron in the s-orbital (at the same energy level (i.e. 2s, 2p)) mixes with the three other p-orbital electrons, producing four identical electronic orbitals. Overall, the energy lost in forming the four C-H bonds in methane is much larger than the energy it takes to excite an electron from a 2s to a $2p_z$ orbital and is therefore always an exothermic process. The carbon atom can covalently bond with four hydrogens through a sharing of an sp^3 orbital for every 1s orbital in hydrogen. These bonds are formed end-to-end and are called sigma- (σ) bonds. Methane is the simplest example of hybridisation and σ-bonding.

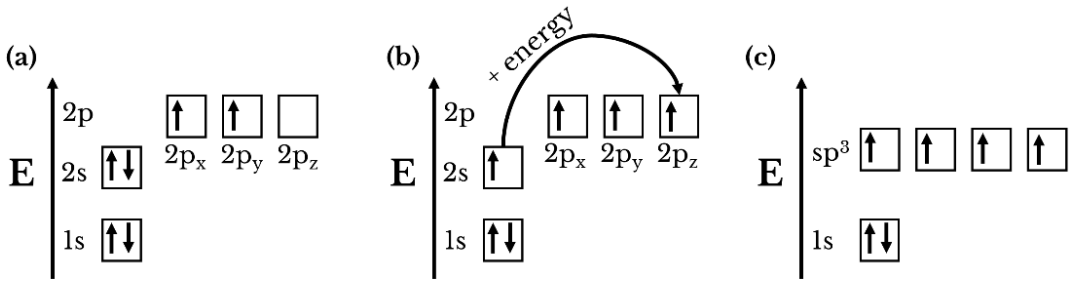

Figure 2.5 - (a) Indicates the ground state of carbon, (b) is the excited state of carbon after promoting an electron from a 2s energy level to the $2p_z$ orbital and (c) shows carbon after hybridisation.

Another example of hybridisation is ethene, which consists of a double carbon bond. The same process occurs; an electron is promoted to the p-orbital from the s-orbital. However, this time only three of the orbitals are hybridised, leaving the $2p_z$ electron unchanged. In doing so, each atom is able to make three bonds; two bonds to hydrogen and one bond to carbon.

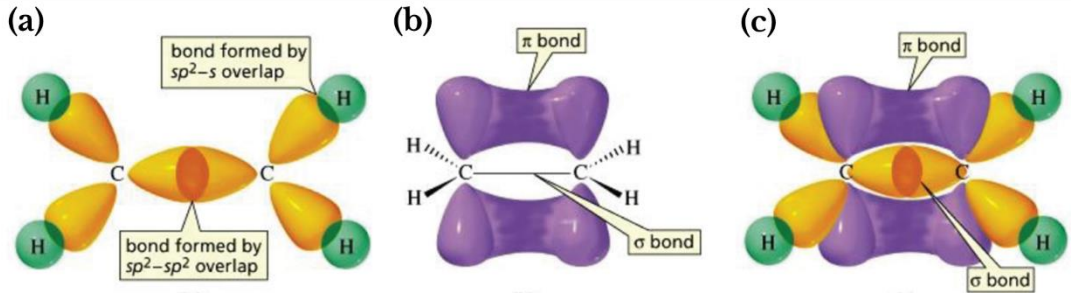

Figure 2.6 – Schematic of the sp^2 hybridisation mechanism in carbon and the formation of π-bonds. (a) displays images of the σ-bonds formed through the in-plane $2p^2$ – $2p^2$ overlap and in-plane sp^2-s (C-H) overlapping bonds, (b) the formation of a π-bond in the perpendicular plane to the σ-bonds and (c) the full electronic picture of ethene (C_2H_4) showing both σ- and π-bonds. Images are taken from reference 15.

These three hybridised sp^2 electrons arrange themselves in the *x*-*y* plane, separated by an angle of 120°, leaving the $2p_z$ electron in a p-orbital perpendicular to the plane of the hybridised electron orbits. As shown in **Figure 2.6 (b)**, the π-bond forms above and below the plane of the σ-bond. Unlike the end-to-end bond formation in a σ-bond, which has highly localised electron densities, π-bonds are formed when overlapping side-on p-orbitals develop a delocalised electronic character [14]. It is these delocalised π-electrons that give many organic molecules their semiconducting properties.

2.4.2 Antibonding and molecular orbitals

As two atoms are brought closer together, their electron wavefunctions begin to overlap with either a constructive or destructive interference. The former provides the atoms with a lower-energy level bonding state (such as σ- and π-bonds). For every σ- and π-bond there exists a corresponding antibonding orbital, denoted as σ^* and π^*, respectively. When a σ- or π-bond is formed, destructive interference of electron wavefunctions creates a region of very low electron density. This results in the creation of an antibonding state, at a higher energy level than the constituent states isolated in an atom. Typically, the antibonding energy state in a molecule is empty in the ground state, however, there are some exceptions such as He_2, which is unstable due to the full 1sσ and antibonding 1sσ* orbitals.

Much like the valence and conductions bands found in metals, organic molecules have energy bands through the bonding and antibonding π-orbitals. sp^2 hybridised organic semiconducting materials have molecular orbitals which are either filled (π-band) or unfilled (π*-band) in the ground state. Further details on organic semiconductors can be found in **Section 2.6** and **Chapter 4**. In a periodic potential, such as in a metal or crystal, the close packing of nuclei produces periodic wavefunctions described by Bloch functions where delocalised electrons are shared across neighbouring atoms.

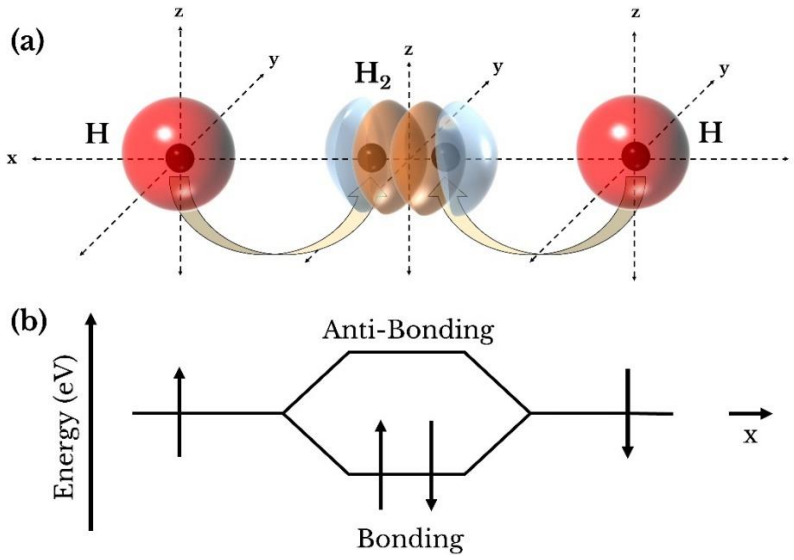

Figure 2.7 – Visual representation of the σ- and σ*- bond formation in H_2. (a) Shows isolated hydrogen atoms (H) with 1s electron probability clouds (red) before forming a covalent bond (H_2). The σ-bond is shown in an orange colour and the σ*- anti-bond is shown in light blue. (b) Equivalent energy diagram for the bonding process in forming an H_2 molecule. The isolated hydrogen atoms each have a lower energy than the σ*-anti-bonding state, however, it is more energetically favourable to form the σ-bonding state.

The overlapping of electron wavefunctions leads to a splitting of the energy levels, consistent with the Pauli Exclusion Principle [15]. In semiconductors, these delocalised electrons are the product of overlapping outer-electron orbitals due to the close-packing nature of the atoms arranged in a lattice. A free atom contains discrete energy levels formed from the electron orbitals as shown in **Table 1**. In a $CH_3NH_3PbI_3$ (MAPI) perovskite, the valence band (VB) is formed from an [6s]-[5p] antibonding orbital, and the conduction band (CB) is a product of [6s]-[5p] antibonding between the lead and iodide atoms. **Section 2.5.3** highlights the semiconducting properties of the perovskites studied in this thesis.

2.5 Perovskite semiconductors

Perovskites are materials whose crystal structure is that of calcium titanium oxide ($CaTiO_3$) with the general formula ABX_3, where A and B correspond to cations of different sizes and where X is an anion. The discovery of $CaTiO_3$ was made by Gustav Rose in Russia in 1839, from which the crystal structure was later named after Count Lev Aleksevich von Perovski, who was a famous Russian mineralogist at that time. The size of the cation 'A' plays a major role in the electronic properties of perovskite crystals [16,17]. One of the most researched perovskite crystal structures used in photovoltaics is methylammonium (MA^+) lead tri-iodide (MAPI), shown in **Figure 2.8**. Here, the crystal structure contains both organic (MA^+) and inorganic (Pb^{2+}) components, of which the inorganic component is covalently bound to iodide ions forming a polyhedral network. At first glance, the ABX_3 formula suggests any charge-neutral combination would form a perovskite crystal. However, as described later extensive research has gone into understanding the crystal structure of perovskites.

In the following section, an overview of the crystal properties of hybrid perovskites is given, including an outline of perovskite photovoltaic device research.

2.5.1 Crystallographic nature of perovskites

An empirical method used to determine the stability and intrinsic distortion of a perovskite crystal structure was developed by V. M. Goldschmidt in 1926 who studied the crystallography of perovskites [18]. Materials that form an ABX_3 structure are arranged in a variety of different crystal space groups depending on the interaction between the small cation 'A' and the BX_6 octahedra. The formulation of what is now known as the Goldschmidt tolerance factor (t) is based on the ionic radii (r) of the A, B and X components and predicts the formability of a perovskite crystal structure using the following relationship:

$$t = \frac{r_A + r_X}{\sqrt{2}\,(r_B + r_X)} \tag{2.8}$$

Here, $r_{A,B,X}$ is the ionic radii for cations A, B and anion X respectively. In general, crystals that have a tolerance factor between 0.9 – 1.0 will form a cubic structure, as shown in **Figure 2.8 (a)** for MAPI. A tolerance factor between 0.71 – 0.90 results in a tilting of the BX_6 octahedra relative to the cubic perovskite structure. Organic-inorganic 3D perovskites typically have a tolerance factor in the range of 0.89 – 1.0 for a cubic structure [19,20]. Slightly lower t values give rise to tetragonal and orthorhombic crystal structures [20]. However, thermal effects and the motion of the MA^+ organic cation greatly affects the resultant crystal structure. For instance, a perovskite crystal can undergo phase-transitions at certain temperatures and is thus categorised by the high temperature α-phase, the intermediate temperature β-phase, and the low temperature γ- phase [21].

In the case of MAPI or the mixed-halide $CH_3NH_3PbI_{3-x}Cl_x$ (MAPIC) perovskites, these phase transitions occur due to the random motion of the organic MA^+ cation within the lead-halide octahedral cage [22]. Previous theoretical models predicted that these MA^+ cations have a total of 24 degrees of freedom [23]. The thermal energy gained by the crystal reduces as the temperature of the sample is lowered with the seemingly random motion of the cation undergoing local ordering by reducing the number of disordered states.

At room temperature, both the MAPI and MAPIC perovskites adopt a tetragonal structure in the β-phase as shown in **Figure 2.8 (b)**. All other tolerance factors that lie outside of this range, i.e. $t < 0.70$ and $t > 1.0$, will not form 3-dimensional (3D) perovskite-like structures [24]. Introducing larger organic cations forces $t > 1$ and thus does not form a stable 3D structure, instead forming 2D perovskite structures [25]. The lattice parameters for the MAPI perovskite in the cubic phase is $a = b = c \approx 6.3$ Å [26,27].

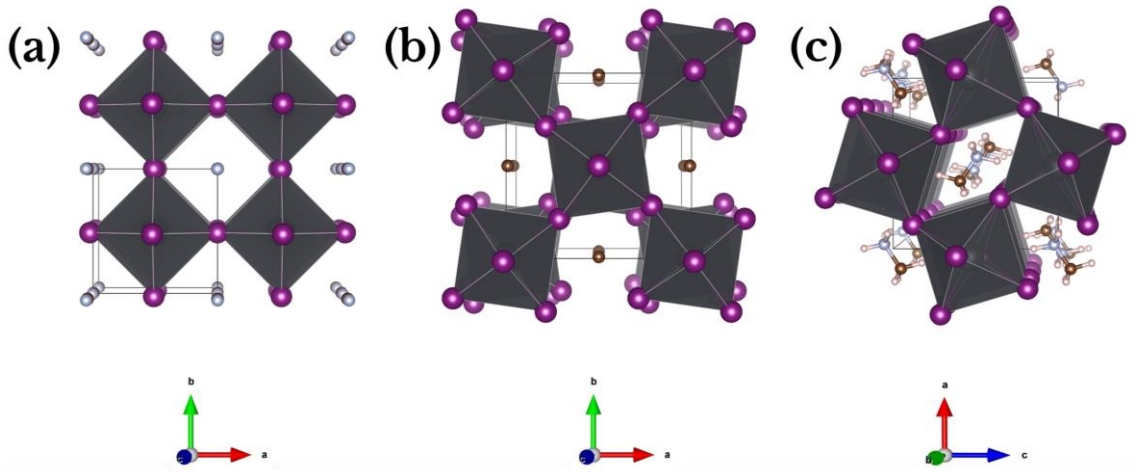

Figure 2.8 - The crystal structure of $CH_3NH_3PbI_3$ (MAPI) in (a) the cubic phase, (b) tetragonal phase and (c) orthorhombic phase. The lead-iodide bonds (grey and purple spheres respectively) exist in a polyhedral arrangement, and form a cage around the methylammonium (MA) molecule (blue and brown spheres indicating carbon and nitrogen, respectively). (a) and (b) are shown along the *c*-axis omitting hydrogen atoms, (c) is shown along the *a*-axis with the inclusion of hydrogen atoms (white) on the MA molecule. Crystallographic information files (CIFs) taken from references (a) [28], (b) [29] and (c) [30].

The 'cubic' nomenclature indicates that the perovskite crystal has *a*, *b* and *c* unit cell parameters that are all equal. It is well understood that the cubic phase is a result of a fully disordered MA^+ cation within the lead-octahedral cage [28]. On lowering the temperature of the crystal to around 300 K, the lattice parameters change due to the ordering of the MA cation [31], consequently tilting the octahedral units shifting the unit cell in to a tetragonal ($a = b \neq c$) space group as shown in **Figure 2.8 (b)**. In this crystal orientation at room temperature, the MAPI and MAPIC perovskites form a unit cell with lattice parameter: $a = b \approx 8.9$ Å and $c \approx 12.7$ Å. In **Chapters 5** and **6**, the MAPIC mixed halide perovskite is subject to crystallographic experiments at room temperature (*c.a.* 20°C) and is thus likely to exist in a tetragonal space group. Further lowering of the temperature to below 140-150 K produces a fully ordered MA^+ cation, stabilising the crystal in to an orthorhombic space group [32,33] as shown in **Figure 2.8 (c)**. Here, the

orthorhombic crystal lattice parameters for the MAPI/MAPIC perovskites have been determined as: a = 8.8 Å, b = 12.6 Å and c = 8.6 Å [22].

2.5.2 2D and quasi-2D perovskites

Non-ideal perovskite structures, (where the Goldschmidt tolerance factor lies outside the range for stable 3D structures) have been studied since the 1950's [34]. Two papers published by Ruddlesden and Popper describe the crystal structures of non-ideal perovskites $Sr_3Ti_2O_7$ [35], Sr_2TiO_4, Ca_2MnO_4 and $SrLaAlO_4$ [36]. Metal-oxide sheets $[MX_6]^{4-}$ of different thicknesses (n = 1 for Sr_2TiO_4 and n = 2 for $Sr_3Ti_2O_7$) placed between two spacer cation interlayers give rise to natural quantum wells [37], in which the metal-oxide slabs act as potential wells between the cation potential barriers. The next metal-oxide layer is shifted in the *ab*-plane through a (½, ½, 0) translation. Replacing the metallic cations (Sr, Ga etc.) with large organic cations, such as aromatic 2-phenylethylammonium (PEA), forms a class of organic-inorganic hybrid Ruddlesden-Popper perovskites (RPPs). 2D RPP based on $[PbI_6]^{4-}$ octahedral slabs and PEA spacer cation, are described by the general formula $(PEA)_2A_{n-1}Pb_nI_{3n+1}$ where A is a monovalent cation such as MA^+. For the pure 2D (n = 1) case, the general formula is PEA_2PbI_4 which is analogous to the Sr_2TiO_4 structure discussed earlier. Increasing the 'n' value enlarges the number of stacked $[PbI_6]^{4-}$ octahedral slabs, with the small monovalent cation MA^+ sitting inside iodide-sharing lead-octahedra in a 3D (n = ∞) structure (**Figure 2.9**). Excitons (a bound state of an electron and a hole) created within these 2D perovskites are confined to the octahedral slabs due to the low dielectric field created by the organic interlayers [38,39]. This natural quantum well effect gives rise to larger exciton binding energies than their 3D counterparts [40,41].

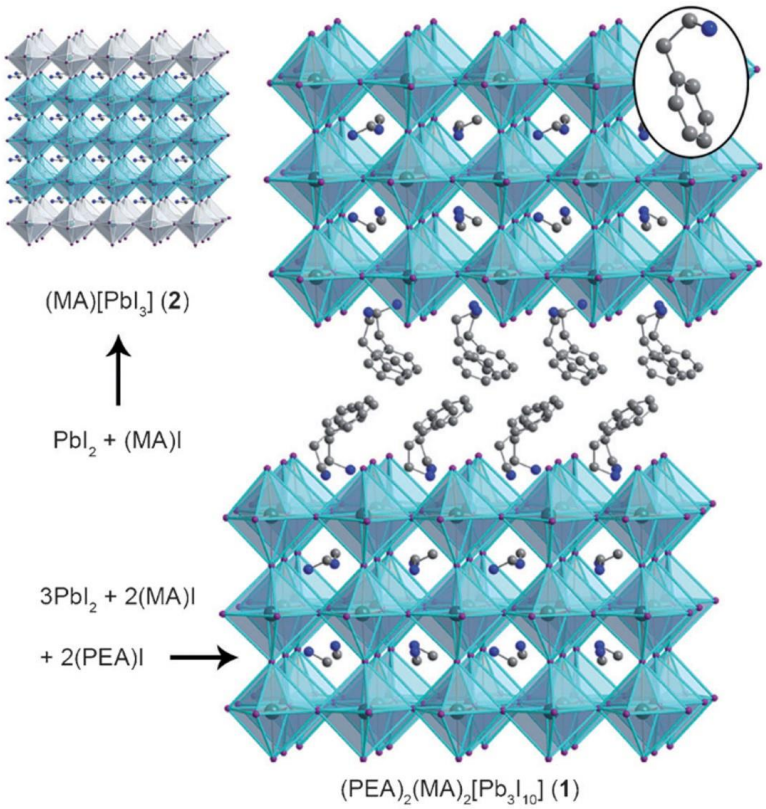

Figure 2.9 – Crystal structures of an n=3 RPP (1) $(PEA)_2(MA)_2(Pb_3I_{10})$ made by intercalating 2-phenylethylammonium (PEA) cations. The 3D (n = ∞) perovskite $MAPbI_3$ (2) is shown in the top left. The repeating octahedral sheets are off-set by a translation of (½, ½, 0). Image taken from reference 41.

Greater n-values give rise to so-called quasi-2D RPPs, such as the n = 3 $(PEA)_2(MA)_2Pb_3I_{10}$ shown in **Figure 2.9**. Quasi-2D perovskites are an interesting class of semiconductors which display the photophysical properties of 2D perovskite materials but with a tuneable quantum-well width formed from the octahedral block thickness. An example of a quasi-2D perovskite quantum-well energy diagram is shown in **Figure 2.10** below. Tuning the well-width (or the octahedral slab thickness) is achieved by the incorporation of large hydrophobic cations in the precursor solution at different concentrations. For instance, Smith *et al*. studied a perovskite solution containing a (PEA)I:(MA)I : PbI_2 precursor ratio of 2 : 2 : 3 which formed the $(PEA)_2(MA)_2Pb_3I_{10}$ (n = 3) RPP [42]. Considering these form the class of $(PEA)_2(MA)_{n-1}[Pb_nI_{3n+1}]$ RPPs, creating a fully 2D $(PEA)_2[PbI_4]$ (n =

1) perovskite would require the precursor ratio of (PEA)I : (MA)I : PbI_2 to be 2 : 0 : 1. Upon increasing the octahedral layer thickness (n) and thus approaching the bulk 3D crystal (n → ∞), the molar ratio of the organic-cations shift towards increased MAI, whereby a (PEA)I : (MA)I : PbI_2 of 0 : 1 : 1 would create a 3D MAPI perovskite.

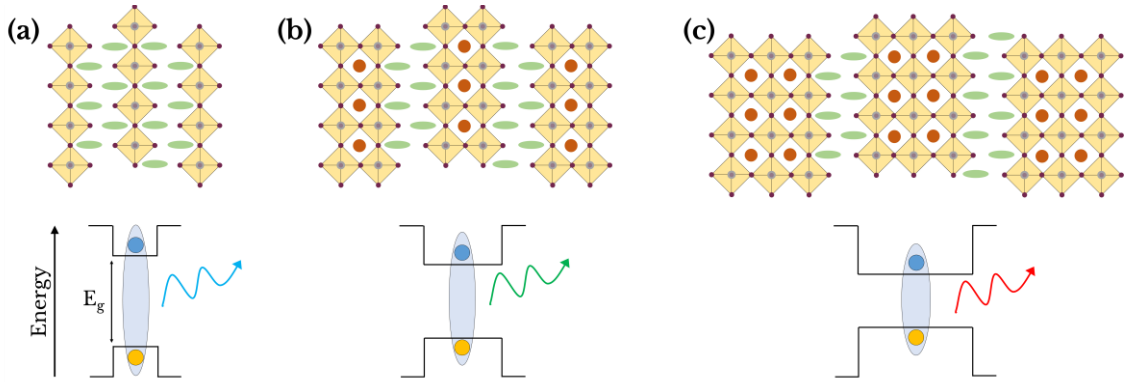

Figure 2.10 – Crystal structures and resulting quantum-well energy diagrams for (a) n = 1, (b) n = 2 and (c) n = 3 low-dimensional perovskites. The green ovals represent organic cations within the spacer layer. Note as 'n' increases the well width also increases and the bandgap decreases, resulting in a red-shift in emission wavelength.

Another type of 2D and quasi-2D perovskite, where the adjacent octahedral slabs are shifted along the *ab*-plane by (½,0) or (0,0), are termed Dion-Jacobson perovskites (DJPs) [43,44]. In contrast to RPP phases, DJPs contain only one cation in the spacer layer, and are described by the general formula $(R\text{-}NH_3)(MA)_{n-1}Pb_nI_{3n+1}$. Until recently, studies on DJPs have mainly focused on inorganic-only constituents (such as $KCa_2Nb_3O_{10}$) [45]. Most notably, work published by Mao *et al.* indicated the formation of a DJP phase using MA^+ and 3-(aminomethyl)piperidinium (3AMP) as the small and large organic cations, respectively [46]. Interestingly, these hybrid DJPs exhibit wider electronic bandgaps compared to their RPP relatives for a given 'n' octahedral thickness [47]. Soe *et al.* published work on the first alternating-cation interlayer DJP/RPP hybrid material (ACI) in 2017, in which lead-iodide octahedral slabs were intercalated with alternating cations of

guanidinium (GA^+) and MA^+ [48]. This new hybrid perovskite structure has a general formula of $(GA)(MA)_nPb_nI_{3n+1}$; similar to that of the DJP class of 2D perovskites with an additional small cation (MA) within the spacer layer. Likewise, for a given 'n' sized perovskite structure, the authors found a red-shift in the bandgap absorption and emission wavelengths relative to the RPP comparable materials. In **Chapter 6**, the crystallographic and optoelectronic properties of a new type of perovskite using only MA^+ as a spacer cation is presented, suggesting a similar behaviour to the ACI class of hybrid structures.

Imaging thin-film perovskites using XRD and GIWAXS is described in **Section 3.8.5**. One way to describe the periodicity of a crystal plane is through the use of Miller indices. A unit crystal cell can be described in terms of a coordinate system defined by an *a*, *b* and *c* axis as shown in **Figure 2.8** and **Figure 2.11**. From this, the miller indices of a given plane can be calculated through several steps; the first is to determine the plane-intercepts along the *a*, *b* and *c* axis and finally taking the reciprocal of these values (to the smallest integer) produces the Miller indices. For example, the well characterised (110) plane is shown in **Figure 2.11** drawn on to the tetragonal-phase MAPI perovskite.

As indicated in **Figure 2.11**, the planes shown in red intersect both the *a*- and *b*-axis of the unit cell at exactly 1 unit in length. Thus, the plane is said to intersect the unit cell at (a, b, ∞). Here, infinity indicates that this plane does not cross the *c*-axis. Dividing the intersecting coordinates by the respective cell-dimensions, i.e. (a/a, b/b, ∞/c) and then finding the reciprocal produces a plane with the miller indices of (110). This technique can also be used for fractional axis-intercepts such as the (002) plane. The (110) plane of the MAPI/MAPIC perovskite is a useful measure for XRD experiments as it defines the lead-to-lead distance within a perovskite unit cell.

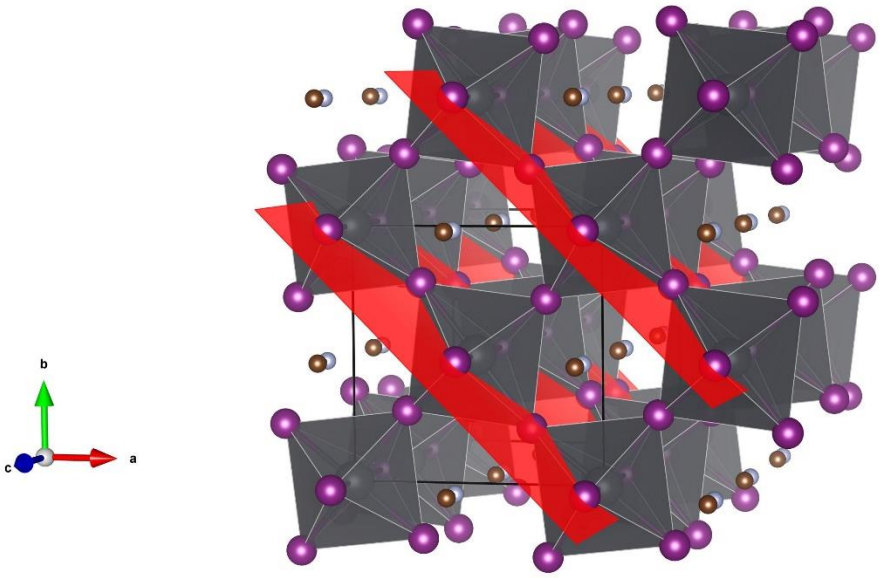

Figure 2.11 - Representation of the (110) planes (red) within the tetragonal-MAPI perovskite unit cell with a characteristic d-spacing of ≈ 6.3 Å. The MA^+ cations (blue-brown) are shown without hydrogen atoms for clarity, lead atoms (centre of octahedra) are shown in grey and the iodide ions are shown in purple. The unit cell for the *I4/mcm* tetragonal space group has been draw in black.

Typical XRD scans of crystalline MAPI/MAPIC thin films produce a reflection signal around 14.2° (2θ) [22,49,50], indicating a interplanar distance (d-spacing) of ≈ 6.3 Å using Bragg's law:

$$n\lambda = 2dsin(\theta) \tag{2.9}$$

Here, n is the plane order, λ is the X-ray wavelength, d is the interplanar distance and θ is the incident angle.

Lead iodide (PbI_2) (which is both a perovskite precursor compound and a degradation product), crystallises in such a way that its (001) plane has a d-spacing of ≈ 6.8 Å for the 2H-polytype and can therefore be identified in X-ray diffraction patterns [51]. In **Chapter 5**, XRD is used to show improved crystallisation upon a solution additive in the perovskite precursor through an increase in reflection intensity and a reduction in impurities. In **Chapter 6**, more complex multi-dimensional (2D/3D) perovskite films are

studied and are shown to be characterised by larger d-spacing values relative to the 3D perovskites studied in **Chapter 5**.

2.5.3 Semiconducting properties of organic-inorganic perovskites

Perovskites are crystals with a corresponding valence and conduction band (CB) much like conventional inorganic semiconductors. For convenience, $MAPbI_3$ will be used as an example in this section. The electronic structure of $MAPbI_3$ is determined primarily through the large metal cation (Pb^{2+}) and the halide ion (I^-) with corresponding atomic orbitals of [Xe] $4f^{14}$ $5d^{10}$ $6s^2$ $6p^0$ and [Kr] $4d^{10}$ $5s^2$ $5p^6$, respectively. The valence band (VB) is formed from a σ*-antibonding orbital from a hybridised bond between the Pb [6s] - I [5p] orbitals (which forms a $[PbI^6]^{4-}$ unit). Similarly, the CB is determined by the Pb [6p] - I [5p] π*-antibonding and Pb [6p] - I [5s] σ*-antibonding orbitals. Although dynamic in motion, the MA^+ cation does not contribute significantly to the overall density of states, well below the valence band maximum (VBM) energy within an $MAPbI_3$ crystal. The semiconducting properties of $MAPbI_3$ arise from the occupied 6p shell which lies below the VBM. As a result, the band structure forms a direct-gap semiconductor although its electronic properties are different to that of the direct-gap semiconductor Gallium Arsenide (GaAs). The orientation of the MA^+ cation can shift the band alignment forming an indirect bandgap, which is positioned slightly below the direct bandgap energy by ≈ 25 meV [52]. The transition between VB and CB is formed of contributions from Pb [s] and I [p] to Pb [p] orbitals, with a relatively high transition probability compared to GaAs giving the $MAPbI_3$ greater optical absorption qualities.

The band formation in lead-halide perovskites following the $APbX_3$ formula has a profound impact on the positioning of defect-sites within the energy bands. A comparison of possible defect or trap sites formed in direct bandgap semiconductors is shown in **Figure 2.12**. As the bandgap is formed between bonding and antibonding states in GaAs (or CdSe), ionic vacancies will lead to a weak bonding orbital within the bandgap

[53]. In contrast, $APbX_3$ perovskites possess a bandgap which is formed from two antibonding orbitals, and thus any vacancy will result in a trap state residing in or close to the surface of the VB or CB [54].

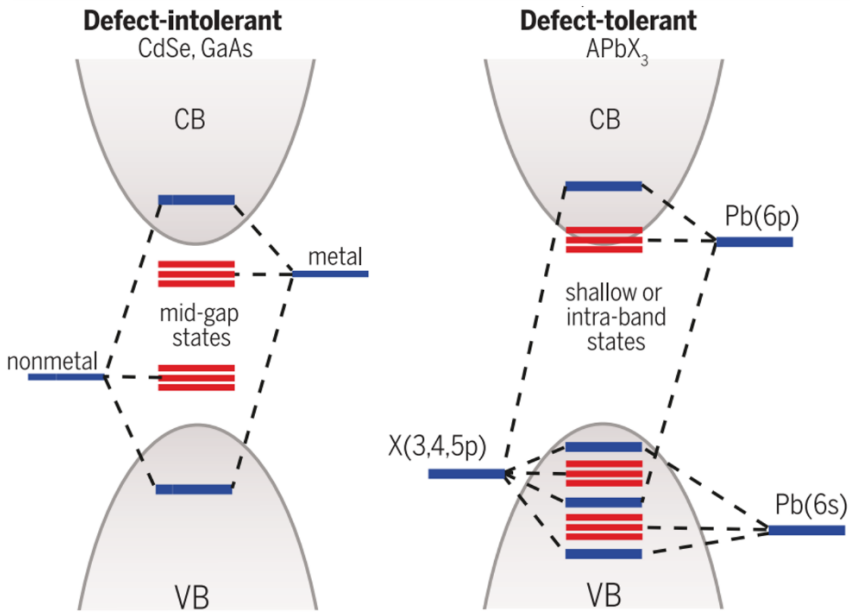

Figure 2.12 – A schematic representation of the formation of defect trap states within direct bandgap semiconductors CdSe, GaAs (left) and hybrid organic-inorganic perovskites (right). The blue lines represent molecular orbitals and the red lines signify trap states. VB and CB indicate the valence and conduction bands, respectively. For the $APbX_3$ diagram, A is the A-site cation and X is a halide (such as iodine or chlorine). Image taken from reference 54.

2.5.4 Perovskite photovoltaics

The first use of a perovskite in a photovoltaic device came in 2006, when a molecular dye sensitizer layer in a dye-sensitized solar cell was replaced by a methylammonium lead bromide ($MAPbBr_3$) perovskite, achieving a power conversion efficiency (PCE) of 2.2% [55,56]. A few years later Kojima *et al.* improved the efficiency of this type of device by including the iodide perovskite $MAPbI_3$ as the sensitizer layer, which increased the PCE

to 3.8% [57]. This efficiency was further improved with work published by Im *et al.* in 2011, implementing $MAPbI_3$ quantum-dots in a dye-sensitized cell with an efficiency of 6.6% demonstrated under Air Mass 1.5 (AM1.5) sun intensity [58]. One major drawback for such dye-sensitized cells was the poor stability due to the polar iodide electrolyte solution that was used, which attacked and dissolved the perovskite layer [59]. Pioneering work by the research groups of Murikami and Snaith demonstrated a solid-state perovskite solar cell based on a non-conducting alumina (Al_2O_3) mesoporous scaffold layer that was coated with a mixed halide $MAPbI_2Cl$ perovskite film [60]. Here, the electrolyte contact was replaced using an organic hole-conducting layer called spiro-MeOTAD (2,2, 7,7-tetrakis (N,N-di-p-methoxyphenamine)-9,9-spirobiflourene) (see **Figure 2.13 (a)**). This film structure proved to be a much more stable architecture and was able to withstand irradiation for over 1000 hours and achieved a champion PCE of 10.9%. Not only did this remove the need for a liquid electrolyte, it was shown that perovskites possess ambipolar transporting qualities; a conclusion reached by replacing the mesoporous scaffold from n-type TiO_2 to insulating Al_2O_3. In mid 2013, Snaith *et al*. submitted two papers reporting planar n-i-p architecture devices without the need for a mesoporous architecture [61,62], achieving 15% and 11% PCEs for vapour and solution processed devices, respectively. The planar n-i-p device architecture is shown in **Figure 2.13 (b)**. Recent advancements, including the introduction of mixed-cation mixed-halide perovskites such as $Cs_{0.10}FA_{0.90}Pb(I_{0.83}Br_{0.17})_3$ (Cs = caesium, FA = formamidinium), have seen efficiencies increase to above 20% PCE [63].

The majority of the research to this point was done on architectures based on an n-i-p junction, whereby the light first enters a glass substrate that is coated in an n-type semiconductor and the perovskite layer, with the perovskite then coated by a p-type semiconductor. For convenience, the n-i-p device structure is generally referred to as a 'normal' architecture device. Work published in 2013 by Jeng *et al.* showed that it was possible to form a planar architecture device whilst also reversing the polarity to p-i-n (or inverted architecture), by coating the substrate with a thin layer of the p-type organic semiconductor poly(3,4-ethylenedioxythiophene) polystyrene sulfonate (PEDOT:PSS) (**Figure 2.13 (c)**) [64]. PEDOT:PSS has been widely used in organic photovoltaics due to its optical transmittance in the visible range combined with a tuneable conductivity and

high work function (5.2 eV). An energy diagram for a p-i-n inverted architecture perovskite device using a MAPI active layer is shown in **Figure 2.13 (d).** In **Chapter 4**, the effect of solution additives on a $MAPbI_{3-x}Cl_x$ precursor and its effect on device performance is characterised using current-voltage (J-V) measurements. By incorporating a mixed-perovskite system such as $(FA_{0.95}PbI_{2.95})_{0.85}(MAPbBr_3)_{0.15}$, devices have now reached 20+% PCE in p-i-n based solar cells [65] using 10 nm of poly[bis(4-phenyl)(2,4,6-trimethylphenyl) amine] (PTAA) as a hole-conducting layer.

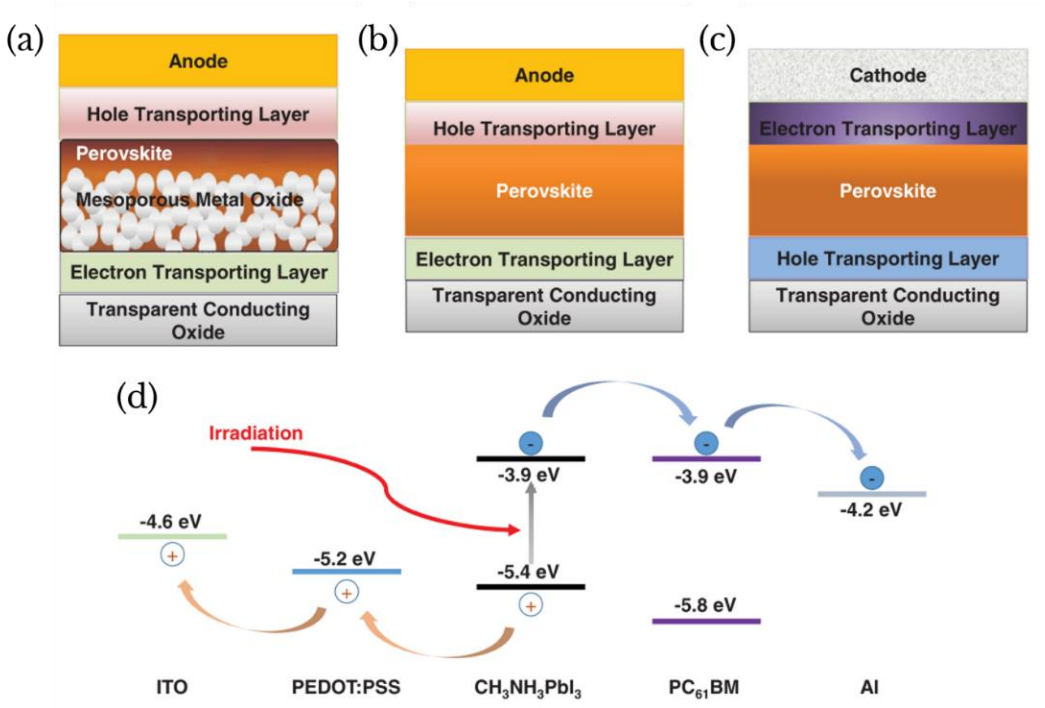

Figure 2.13 - Schematic of the various architectures used in lead halide perovskite solar cells. (a) mesoporous n-i-p, (b) planar n-i-p and (c) planar p-i-n. Part (d) indicates the energy band alignment for a common p-i-n device with the $MAPbI_3$ perovskite in the absorber layer. The photovoltaic devices presented in Chapters 5 and 6 of this thesis follow the architecture shown in part (c). Image taken from reference 65.

There has been a recent surge in the potential perovskite PV scale-up due to the low temperature processing routes used to process such materials. One such advancement is utilising spray-coating to fabricate perovskite solar cells. This processing technique has been used for OPV solar cells since 2007 [66]. This large-area processing method has recently been used to fabricate fully-sprayed inverted-architecture perovskite solar cells reaching efficiencies of 9.9% [67]. PEDOT:PSS was used for the p-type layer in every device fabricated in this thesis due to its ease of fabrication, low-temperature annealing and its potential for scale-up.

2.6 Organic semiconductors

2.6.1 Semiconducting properties of organic semiconductors

Organic semiconductors are widely used in this thesis. They are both included in perovskite devices as charge extraction layers, and are used in fully organic devices discussed in **Chapter 4.**

The outer-most energetic electrons in an organic semiconductor can be found in the highest occupied molecular orbital (HOMO) where the top of the HOMO level is also referred to as the ionisation potential of the molecule [68,69]. The next allowed electron energy state above the HOMO level is the lowest unoccupied molecular orbital (LUMO), which is analogous to the CB in an inorganic semiconductor. The LUMO level corresponds to the antibonding π^* orbital energy and is also referred to as the excited state of the molecule. The difference between the HOMO and LUMO levels for a given system is termed the material bandgap (E_g). A commonly used polymer, named polyethylene $(C_2H_4)_n$, contains only C-C single bonds with a spare p_z electron on each carbon atom. As the C-C bonds appear identical in this case, the π-electrons can theoretically delocalise along an entire polymer chain. This leads to an apparent indistinguishability between the π and π^* orbitals and therefore the absence of a

bandgap. If this scenario was indeed true, polymers with a similar backbone to polyethylene would behave like metals due to the partially filled LUMO level [70]. Peierls' instability law suggests that identical single C-C bonds along a 1D polymer chain will undergo bond length alterations caused by the coupling of phonons and electrons [71,72]. Phonons are periodic vibrations from a collection of atoms in a crystal lattice and can exchange energy with the electrons, forming the basis of Peierls instability [73]. The commonly studied polymers polyethylene and polystyrene are shown in **Figure 2.14 (a)** and **(b)**, respectively. It can be seen that these polymers are formed from a single carbon-carbon σ-bond backbone, producing highly localised electrons with such polymers acting as insulators [76]. The properties of non-conjugated (saturated) polymers, such as polyethylene (bottles, plastic bags) and polystyrene (food packaging, surfboards) [77] make them useful for purposes that require insulating qualities. However, in the field of optoelectronics it is a requirement that a polymer can transport electrical charge along its backbone, and it thus requires alternating C-C and C=C bonds permitting the delocalisation of charge through π-electron orbitals.

Conjugated polymers are molecules that exhibit alternating single and double (or triple) carbon bonds. Alternating single-double bonds between carbon atoms result in the formation of a rigid molecular. As shown earlier, a double carbon bond is formed from a σ-bond and a π-bond. As the bonds in conjugated polymers are not symmetric (1.36 Å and 1.44 Å for single and double bonds in polyacetylene, respectively) [74], regions of lower electron density lead to the formation of an energy gap across sections of a polymer chain. This then separates the π and π* orbitals, with preferential filling of the lower energy π-bonding orbital resulting in HOMO and LUMO levels. Delocalised π-electrons are confined to a few units along a polymer chain, rather than the entire chain itself. It is this feature in polyacetylene (**Figure 2.14 (c)**) that gives rise to its semiconducting behaviour with a bandgap of around 1.4 eV [73,75].

A benzene ring is another example of conjugation and is composed of six carbons that alternate between single and double bonds. The benzene (C_6H_6) aromatic structure consists of six sp^2 hybridised carbons, each contributing a single valence electron to the π−orbital whilst C-C and C-H are bonded through σ-bonds. It is these π−orbitals that are

delocalised and exist above and below the molecular plane. As with carbons sp^2 hybridisation, the reason for benzenes hexagonal structure is due to the sp^2 orbitals, forming a 6-carbon ring with a bond angle of 120°.

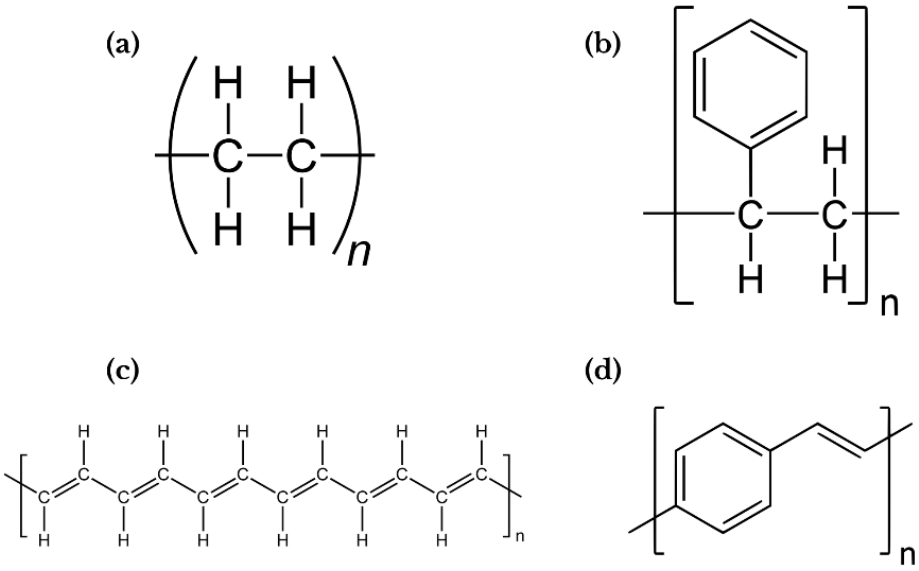

Figure 2.14 - Representative diagrams of non-conjugative polymers (a) polyethylene and (b) polystyrene alongside conjugated polymers (c) polyacetylene and (d) polyphenylene vinylene (PPV).

Conjugated polymers behave like a semiconductor with a narrow HOMO-LUMO energy bandgap; however, the overall band structure can be modified by doping the polymer chains with p-type (electron donors) or n-type (electron acceptors). The effect of conjugation on the energy gap in organic semiconductors is substantial. Some examples of this are saturated polymers polyethylene and polystyrene (**Figure 2.14 (a)** and **(b)**) with an E_g = 7 eV and 4.4 eV, respectively [76], whereas, conjugated polymers polyacetylene and PPV (**Figure 2.14 (c)** and **(d)**) have bandgaps of 1.4 - 1.9 eV [78] and 2.4 eV [79], respectively. By adding electron-donor or electron-accepting units along a monomer structure, for example thiophene (C_4H_4S) (donor) and 2,1,3-benzothiadiazole

($C_6H_4N_2S$) (acceptor) subunits, the push-pull behaviour towards delocalised π-electrons can be exploited which is discussed in more detail in **Chapter 4**.

2.6.2 Organic photovoltaics

Whilst perovskite photovoltaics have seen remarkable gains in both efficiency and stability over the last decade, it is worth noting the most efficient mixed inorganic-organic systems utilise a lead-halide precursor material. One major disadvantage to these devices is the intrinsic toxicity of water soluble lead-based compounds, which in principle creates a problem for scalable technologies [80,81]. Photovoltaics based around inorganic compounds, such as monolithic cadmium telluride (CdTe) have now reached a PCE of 19% for cells with an active area of 7040 cm^2 and similarly 24% for crystalline Silicon (c-Si) with an active area of 13177 cm^2 [8]. However, despite the excellent photovoltaic performance of CdTe based cells, current research suggests a major limiting factor for large-scale CdTe production is the relative abundance of the rare-earth element tellurium [82].

An alternative PV technology is that of organic-semiconductor photovoltaics (OPVs). OPVs have been studied for a number of years; for example photoconductivity measurements were first performed on anthracene crystals in 1906 [83] and later the photovoltaic effect was first reported in 1959 in anthracene crystals placed between two sodium-chloride (NaCl) solutions [84]. Several other organic-based photovoltaic systems were studied during the 1960s [85,86], however, a major breakthrough was the development of the OPV solar cell architecture. Initially, OPVs were designed using a single-layer architecture, also called a Schottky diode, whereby photo absorption occurred in an organic film (or crystal) placed between two electrodes [68,87] (see **Figure 2.15 (a)**).

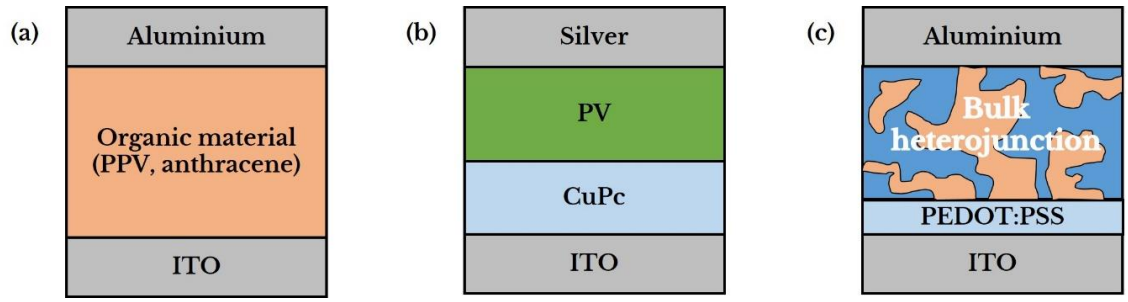

Figure 2.15 - The progression in organic photovoltaic (OPV) device architecture from (a) single-junction, (b) bilayer architecture and (c) bulk heterojunction, where the acceptor material (blue) is phase separated from the donor material (pink). The device stack shown in (b) is modelled on the influential bilayer architecture reported by Tang *et al.* [88], where CuPc stands for copper phthalocyanine and PV is a perylene tetracarboxylic derivative.

The built-in electric field caused by the difference in electrode work functions is typically not high enough to successfully dissociate the photo-generated exciton in conjugated polymers. As both charge carriers diffuse through the same material, charge-carrier recombination becomes a dominant loss mechanism. Therefore, this type of device does not yield many free charge-carriers and generates very little photocurrent.

Tang *et al.* reported the first bilayer photovoltaic cell made by depositing a 50 nm layer of a perylene tetracarboxylic derivative (PV) on top of 30 nm of copper phthalocyanine (CuPc), using a vacuum evaporation technique with this bi-layer sandwiched between ITO and silver electrodes [88] (see **Figure 2.15 (b)**). This system allowed exciton dissociation to occur at the interface between the layers, with holes being transported in the CuPc layer towards the ITO interface and electrons through the PV layer to the silver electrode. In this early device, a PCE of 0.95 % was recorded under AM2 conditions. Such devices were hindered by exciton diffusion lengths, which are typically around 10 nm in conjugated polymers [89–91]. Therefore, in a bilayer OPV only excitons photo-generated within a diffusion-limited distance of the heterojunction are likely to dissociate into free carriers, a process that ultimately lowers the PCE of the device

For photovoltaic applications, such excitons need to be broken apart in order to produce mobile free charge carriers and thus create an electrical current. Due to the large binding energy of organic semiconductors (300 – 500 meV) excitons are not able to thermally dissociate. Excitons are intrinsically short lived quasiparticles that typically exist on the order of nanoseconds [92,93]. **Figure 2.16 (a-c)** indicates the charge transfer mechanism at a donor (D)-acceptor (A) interface. The energetic requirement for such a dissociation of charges is that both the HOMO and LUMO levels of the acceptor molecule must be lower-lying than the donor molecule. If the LUMO level of the acceptor exists at a higher energy than the donor, there is no thermodynamic process to drive electron-transfer. Issues in photovoltaic cell performance can arise when the electron and hole recombine, which happens either in the donor polymer or at the donor-acceptor interface.

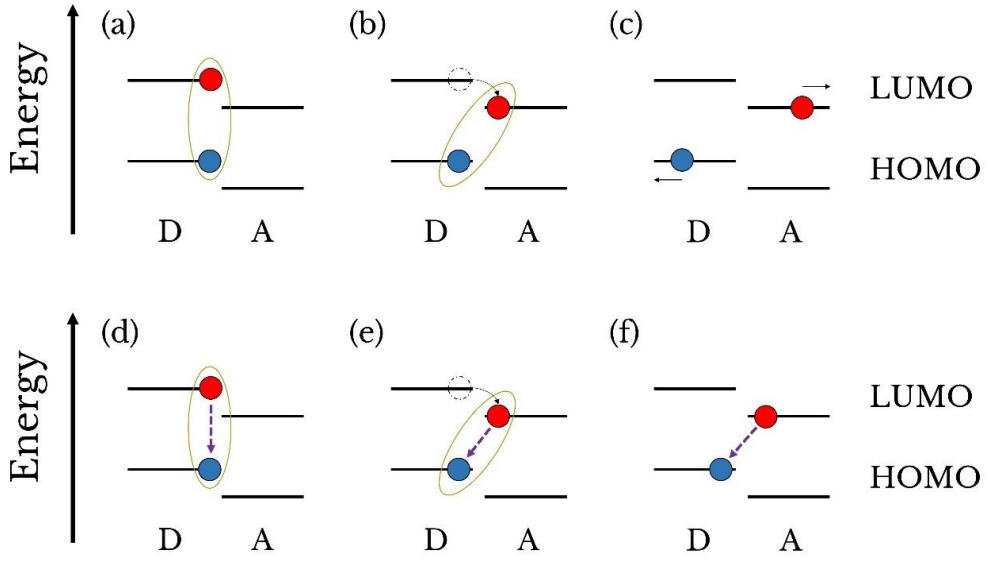

Figure 2.16 - (a) The electron (red) and hole (blue) coulombically-bound pair (exciton) at the interface between a donor (D) material and an acceptor (A) material. (b) The exciton is still bound, however, the electron has transitioned across the interface to the LUMO level of the acceptor unit. (c) Both the electron and hole have sufficient energy to exceed the Coulomb potential and are considered free carriers. The various recombination pathways shown for an electron and hole across a LUMO-HOMO D-A interface are: (d) Geminate recombination, (e) geminate recombination in the charge transfer state and (f) non-geminate recombination.

Figure 2.16 (b) illustrates the concept of a charge-transfer (CT) state whereby the exciton is still coulombically bound, however, the electron has transferred to an acceptor molecule. This CT state has been measured in a poly(3-hexylthiophene) (P3HT):PCBM (1:2) BHJ system with a lifetime of 500 ps [94]. Providing the exciton does not recombine, the condition for successful CT exciton dissociation into free charge carriers is given by the following relationship:

$$\Delta E_{HOMO} \; or \; \Delta E_{LUMO} \; \geq \; E_B \tag{2.10}$$

where the difference in HOMO and LUMO energies of the two materials are given by ΔE_{HOMO} and ΔE_{LUMO}, respectively. The various ways in which an exciton can recombine across a donor-acceptor system is shown in **Figure 2.16 (d-f)**. Exciton recombination is the most likely cause of a reduction in photo-generated charge carriers and thus the most prominent process that contributes to a loss of photocurrent [95]. If electron-hole recombination happens in the same material shortly after the exciton was dissociated, it is called geminate recombination (**Figure 2.16 (d)**).

Another major breakthrough was the use of Buckminsterfullerene (C_{60}) and its more soluble derivative [6,6]-phenyl-C_{61}-butyric acid methyl ester ($PC_{61}BM$) as the p-type semiconducting layer [96]. PCBM has a low-lying LUMO level [97,98] and thus possesses a high electron affinity making it an excellent electron-accepting material for photovoltaic applications. Another important discovery was that fast (picosecond [ps]) intermolecular electron charge transfer (ICT) occurred between PCBM and a conjugated polymer in a bilayer configuration [99]. PCBM has better solubility in common organic solvents than C_{60} (45 mg/ml and 6.5 mg/ml in chlorobenzene, respectively [100]), making it ideal for solution-processable photovoltaics [101]. The idea of introducing organic molecules in a heterojunction with different ionisation potentials and electron affinities inspired the development of a BHJ architecture (**Figure 2.15 (c)**) [96]. A major efficiency improvement for BHJ organic cells was shown by Yu *et al*. in 1995, who engineered a blend of poly(2-methoxy-5-(2'-ethyl-hexyloxy)-1,4-phenylene vinylene) (MEH-PPV) and PCBM at a 1:4 weight ratio, achieving a PCE of 2.9% [102]. Since this discovery, work has been focused on morphological studies using processing additives in BHJ blends that

incorporate donor:acceptor polymers [103], reaching efficiencies above 11% for a 1 cm^2 cell [8]. Non-fullerene acceptors within a BHJ have also shown promise as hole-selective materials in the absorber layer of a solar cell [104]. A more detailed discussion on the BHJ in organic photovoltaics can be found in the introduction to **Chapter 4**.

2.7 Charge transport in organic and hybrid semiconductors

Organic molecules can be excited through the resonant absorption of photons of energy E, greater than or equal to the material bandgap, E_g. Conjugated organic semiconductors typically have HOMO to LUMO (excitation) energies in the visible range and can therefore be considered as optically active. In the case of $E > E_g$ or $E = E_g$, where E_g is the material bandgap, an electron is able to absorb the incident photon's energy and become promoted to an excited state. This leaves a positively charged vacancy (a hole) in the HOMO level that exerts an attractive Coulomb force on the photo excited electron. The promoted electron and its hole counterpart are thus coulombically bound (as an exciton) and in a PV device, must be separated to produce a current flow in an external circuit (as shown in **Figure 2.16**). All types of semiconductors and insulators are able to support excitons, which in condensed matter theory are considered an elementary particle [105,106]. The extent to which the two charges are bound is called the exciton binding energy; its strength is governed by the dielectric constant, ε_r, within the material itself. The dielectric constant, also known as the relative permittivity, is the measure of the charge-screening properties of a material relative to vacuum [107]. For example, the dielectric field strength in the vacuum has a value of 1, whereas in water ε_r is equal to 88 at 0°C [108]. It is known that the dielectric constant has a great effect on the behaviour of excitons in organic and inorganic semiconductors.

Organic semiconductors, which have relatively small ε_r values, produce tightly bound excitons with length scales around 10 Å and binding energies in the range of 0.1-1 eV [109]. Such short-range excitons are termed Frenkel excitons, and are usually the size of a

crystal's unit cell [110]. In contrast, inorganic semiconductors, such as GaAs, possess relatively large ε_r values, allowing a larger separation of excitons through electric field screening coupled with small exciton binding energies [111]. Relatively long range excited states are termed Wannier-Mott excitons and typically have binding energies on the order of a few meV, which means that at room temperature (kT ≈ 25.7 meV) most excitons undergo spontaneous dissociation. The Bohr radius is defined as the distance between an electron-hole pair. Perovskite semiconductors, such as $CH_3NH_3PbI_3$, have been shown to have exciton binding energies between 50 meV [112] and 37 meV [113], with respective Bohr radii of 22 Å and 28 Å. A quantum-dot is a semiconductor which occupies such a small space that the Bohr radius of the exciton generated is on the same order as the quantum dot unit cell.

The movement of a free electron along a polymer or lattice will attract positive ions and repel negative ions. In doing so, it causes local distortions, and the local distortions that follow the excited charges give rise to an elementary excitation called a polaron. Polarons can be described as either lattice distortions in the HOMO level with a hole, or lattice distortions in the LUMO level accompanied by an electron. These distortions and consequential band energy decrease, causing new states to be formed within the band gap of the material. The population of polarons can be increased by doping a polymer system [114]. In organic materials, mobile carriers are usually classified as a hole in the HOMO level or an electron occupying the LUMO level. When an electron is promoted into the LUMO level, it occupies space within a π*-bond. Along with an electronic excitation, the monomer skeleton often undergoes a structural relaxation around a charge, causing a shift in bond lengths or bond angles. An "aromatic" or "benzoid" structure is formed from confined π-electrons in the polymer's ground state and is a more energetically favoured system to its counterpart, namely a "quinoid" structure. Quinoidal structures are formed from π* antibonding when the polymer is in the excited state [115,116]. An example of a transition between a benzoidal to a quinoidal structure is illustrated in **Figure 2.17** for a PEDOT monomer. The quinoidal structure of PEDOT demonstrates the movement of the C=C bonds, aligning preferentially along the polymer backbone. By doing so, bond length variations are reduced and a narrowing of the bandgap, E_g, is expected [117].

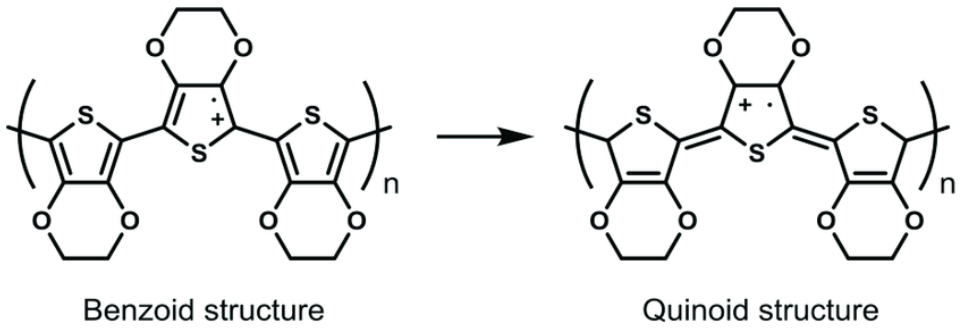

Figure 2.17 – The benzoid and quinoidal structure of poly(3,4-ethylenedioxythiophene) (PEDOT). Note the re-ordering of the C=C bonds in the quinoidal system. Image taken from reference 118.

Charge transport within a $MAPbI_3$ crystal begins with a photogenerated charge. Unlike in organic polymers, whereby the charge must transport itself by hopping between and along a polymer chain, charge carriers in perovskites can transport through delocalised energy bands. This ultimately leads to better charge carrier mobilities in the $MAPbI_3$ perovskite (10 – 150 $cm^2V^{-1}s^{-1}$) [118,119] compared to typical conjugated polymers (10^{-4}-10^{-2} $cm^2V^{-1}s^{-1}$) [120]. As a consequence, long carrier diffusion lengths are possible in perovskite films with low monomolecular recombination rates. The diffusion length of a charge carrier can be calculated using the following relationship [121]:

$$L_D = \sqrt{D_n \tau_n} \tag{2.11}$$

where L_D is the diffusion length, D_n and τ_n are the diffusion constant and charge carrier lifetime, respectively. Measuring the charge carrier lifetimes is discussed in more detail in **Section 2.8**, **Chapter 5** and **Chapter 6**. The diffusion lengths of charge carriers in perovskites have been measured at over 1000 nm for electrons and holes in thin films [122] and up to 100 microns in single crystals [123], distances that are much longer than the exciton diffusion lengths that are found in a typical organic semiconductor (1-10 nm) [124,125].

2.7.1 The P-N junction

For an exciton to successfully dissociate into separate positive and negative charges, it must first diffuse to a point of energetic asymmetry within a material system. One example of such a material asymmetry is that of the P-N junction, discovered in 1940 by Russell Ohl. Undoped Silicon (Si) is an intrinsic semiconductor, and thus the holes already present in the material are caused by thermally excited electrons promoted to the CB. Doping this material with a group III element, such as Boron, increases the hole concentration and therefore the material is deemed to be a p-type (positive) semiconductor. If the same intrinsic semiconductor is instead doped with a group V element, such as phosphorous, the electron concentration is increased, and thus the material is considered to be an n-type (negative) semiconductor. When n- and p-type semiconductors are brought into contact they form a so-called P-N junction. Here, an imbalance in work functions between the p-type and n-type materials cause a built-in electric field to occur at the P-N junction, which forms a favourable path for electrons to flow from the p-type to the n-type and vice-versa for holes, as seen in **Figure 2.18**. This flow of charge creates a charge depletion zone around the P-N junction, causing a high resistance barrier for majority carriers and a low resistance path for minority carriers. When an electron (or hole) finds itself within a p-type (or n-type) material it becomes a minority charge carrier. These minority carriers are meta-stable and so will recombine with an opposite charge in a timescale known as the minority carrier lifetime.

Figure 2.18 (a) and **(b)** indicates the cross-sectional device architecture of post-fabricated OPV and perovskite solar cell devices, respectively, with parts **(c)** and **(d)** representing the energetic landscape of such devices. The band energy bending has been enhanced (relative to the size of the layer) for easier viewing. Applying a forward bias to these devices reduces the depletion region (indicated as sloped energy levels in **Figure 2.18 (c)** and **(d)**), increasing the diffusion current acting in the opposite direction to the drift current.

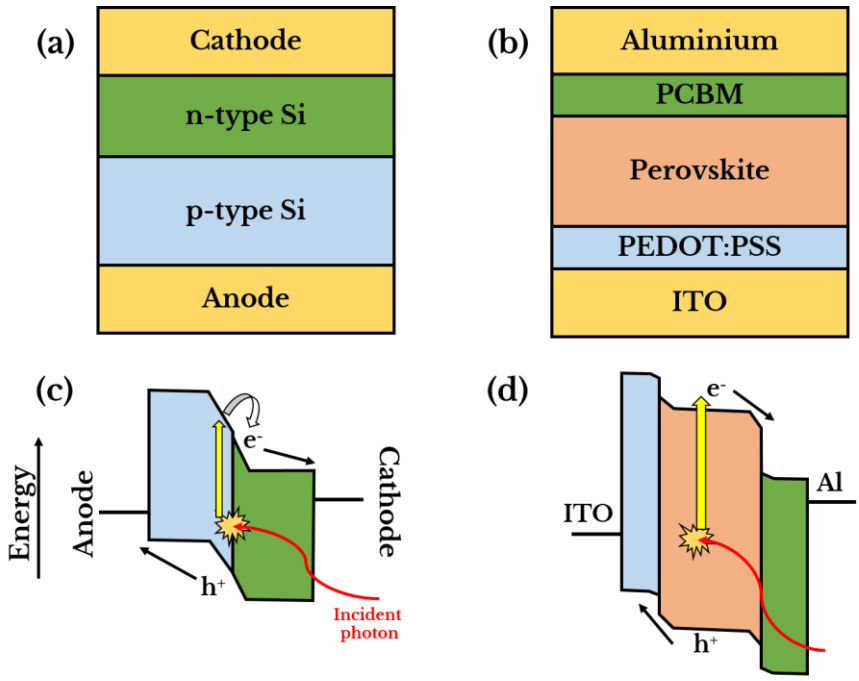

Figure 2.18 – Representative device architectures for (a) typical planar P-N Silicon solar cell and (b) n-i-p perovskite planar solar cell. (c-d) Schematics of the charge separation process within a solar cells shown in (a-b). The degree of band-bending has been enhanced to indicate the built-in electric field promoting charge separation.

In reverse bias, where the polarity across the device is switched, the depletion region increases in size restricting the flow of the diffusion current. Within the depletion region, mobile ions exist in Debye layers (≈ 10 nm), where the decrease in electric potential by a factor of '1/e' is known as the Debye length. The perovskite device heterojunctions that are explored in this thesis are based on a p-i-n structure, whereby the intrinsic semiconductor is a perovskite absorber layer sandwiched between p- and n-type charge-selective semiconductors. Charge separation in hybrid perovskite crystals occurs rapidly following illumination under typical device operating conditions [126], with photogenerated carriers having long carrier diffusion lengths [127]. The role of the p- and n-type semiconductors in a perovskite solar cell device are to selectively transport mobile carriers out of the perovskite layer. Unlike organic semiconductors, the low-trap densities and large carrier diffusion lengths allow charges to be extracted at a planar interface in a perovskite solar cell [128].

2.8 Photophysics of organic and hybrid semiconductors

In **Chapters 4**, *5* and **6** of this thesis, the absorption and photoluminescence spectra of organic and perovskite semiconductors is studied. In the following section, the absorption and emission processes involved in organic and hybrid semiconductors is discussed.

2.8.1 Absorption of electromagnetic radiation

The absorption of electromagnetic radiation can be defined as the process of transferring the energy of a photon to an electron, promoting it to a higher energy state. The lower-energy states which are filled in the ground state of a semiconductor at 0 K form the VB, whilst the vacant higher-energy states form the CB. From the parabolic approximation of the quantised electronic energy around the centre of the Brillouin zone, there exists an energy range in which electronic states are forbidden. The parabolic approximation holds well for wide bandgap semiconductors (such as those studied in this thesis), however, this approximation fails to account for any interaction between the VB and CB, and thus fails for narrower bandgap semiconductors. The energy required to excite the electron from the top of the VB to the bottom of the CB in a direct-gap semiconductor is called the bandgap energy (E_g) (see **Figure 2.19 (a)**). For direct-gap semiconductors all excitation mechanisms exist as perpendicular transitions in wavevector (k)-space. In organic semiconductors, the bandgap energy is defined as the energy difference between the HOMO and LUMO levels ($\pi \rightarrow \pi^*$ transition, for example), which are analogous to the VB and CB, respectively. Some materials such as crystalline silicon (c-Si) have indirect bandgaps, whereby the top of the VB and the bottom of the CB are displaced in k-space, and require a phonon to supply the additional momentum for a complete transition (**Figure 2.19 (b)**).

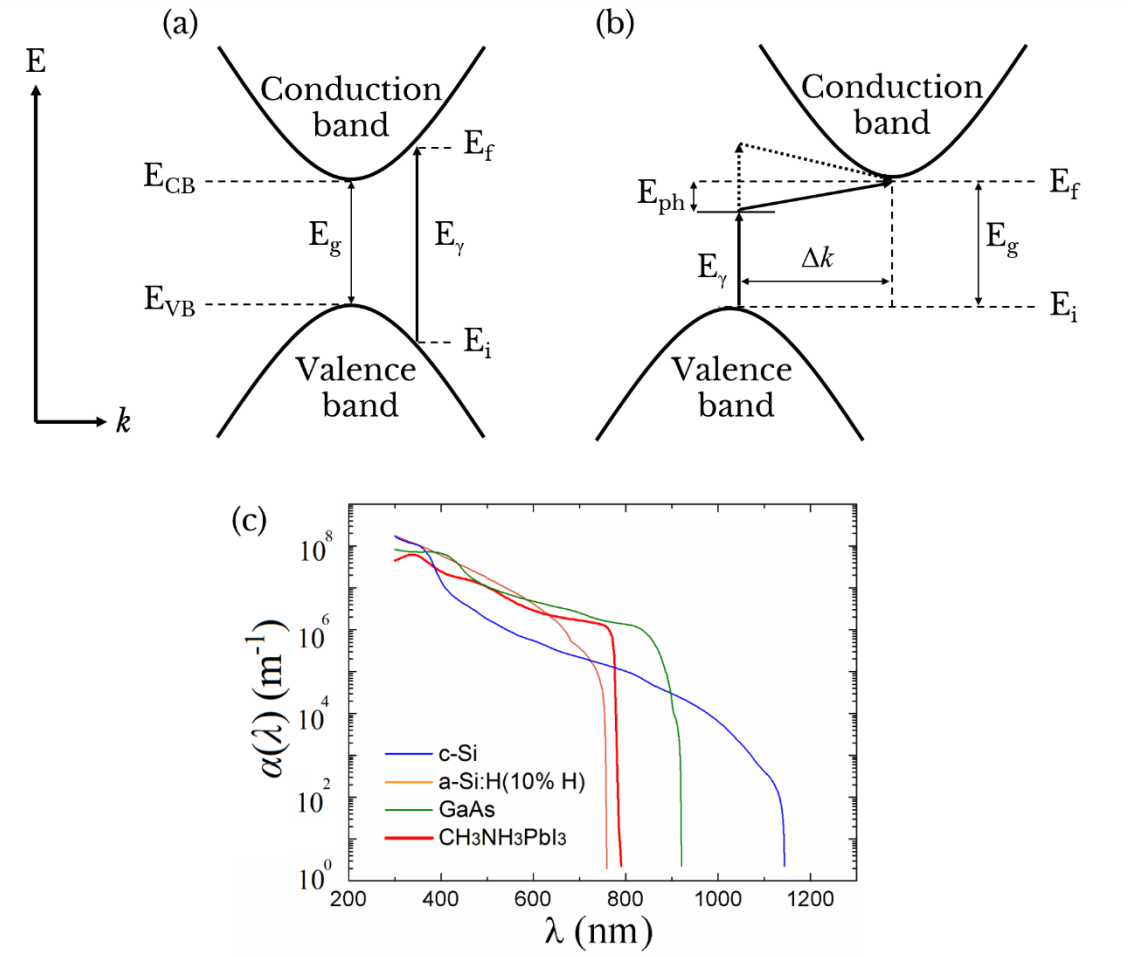

Figure 2.19 – The energy (E) vs wavevector (k) schematics shown as a parabolic approximation for (a) a direct-gap semiconductor and (b) an indirect-gap semiconductor. (c) Indicates the absorption coefficients at room temperature for crystalline-silicon (blue), amorphous-silicon (orange), gallium-arsenide (green) and methylammonium lead-iodide (red) as a function of wavelength. Part (c) was taken from reference 131.

As light enters a material, the intensity of the light as a function of the distance travelled (x) can be described by Beer's law:

$$\mathrm{I(x)} = I_0 e^{-\alpha x} \qquad (2.12)$$

where I_0 is the light intensity at $x = 0$ and α is the absorption coefficient with units of inverse length (x^{-1}).

The absorption coefficient of a material is strongly dependant on the frequency (or wavelength) of the light that enters the medium. The ratio of the light intensity at a depth of x to the intensity at x = 0 is known as the transmittance, T(λ). In some experiments the absorbance A(λ) of a material is measured which is related to the transmittance through the relationship:

$$\frac{I(x)}{I_0} = e^{-\alpha x} = T(\lambda) \tag{2.13}$$

$$A(\lambda) = -\log_{10} T(\lambda) \tag{2.14}$$

Figure 2.19 (c) plots the absorption coefficients of direct-gap semiconductors $MAPbI_3$, GaAs and amorphous silicon (a-Si) together with the indirect-gap c-Si. The sharp increase in absorption coefficient at the absorption edge in direct-gap semiconductors make them excellent thin-film solar cell materials. For most visible wavelengths, the absorption coefficient of the $MAPbI_3$ (MAPI) perovskite is almost 10 times that of c-Si. For example, at 600 nm the absorption coefficient for MAPI and c-Si are 4 x 10^4 cm^{-1} and 6 x 10^3 cm^{-1}, respectively [129]. A direct consequence of using materials with large absorption coefficients in a device is the ability to use thinner absorber layers, thereby permitting cheaper fabrication processes to be implemented.

The electronic spectra of organic molecules are arranged in order of increasing energy on a similar basis to that of atomic energy levels. As mentioned earlier, in a conjugated molecule the π-electrons first arrange themselves in orbitals with the higher-energy electrons occupying the HOMO level. The next available energy state is the LUMO level, and the energy required to jump between the top of the HOMO and the bottom of the LUMO levels is the molecular bandgap. As a conjugated molecule gains energy in this transition, the LUMO state is therefore referred to as being an excited state of the molecule and any electrons occupying the LUMO band are termed π*- electrons. The lowest energy process then involves promoting an electron from the HOMO to the LUMO, which is written as the $\pi \rightarrow \pi^*$ transition. Due to the highly localised nature of σ-bonds, the $\sigma \rightarrow \sigma^*$ transition requires a much higher energy to break the initial σ-bond. As discussed in **Section 2.5.2**, the VBM in organic lead tri-halide perovskites such as

MAPI is mainly formed from the [5p] orbitals of iodine, and the CBM is mainly from the [6p] orbitals of the lead cation.

The accepted direct gap transition energy for the MAPI perovskite is ≈ 1.6 eV [130,131], which blue-shifts as the halide anions become more electronegative (such as Br^- and Cl^-). A 3 : 1 molar solution of MAI:$PbCl_2$ produces a perovskite with small amounts of Cl^- (most of the chloride escapes during the anneal stage as MACl), which is denoted by $MAPbI_{3-x}Cl_x$ (MAPIC). Small doping levels of chloride in a MAPIC perovskite have been shown to have no measurable impact on the bandgap [132]. At room temperature in the tetragonal space group, MAPI (MAPIC) has an emission peak at ≈ 1.61 eV, as well as a higher-energy peak (≈ 1.55 eV) at room temperature which disappears at higher excitation power densities [133]. In the orthorhombic phase at 4 K (or above 400 GPa [133]), the MAPIC bandgap widens to ≈ 1.68 eV.

Atoms arranged within a molecule vibrate around their bonds, which alongside the electronic energy, adds to the overall energy in the system. Once in an excited state, the periodic arrangement of atoms can also change its vibrational state through various vibrational modes. It is important to note that the frequency at which atoms vibrate in a molecule is in the range of 10^{13} - 10^{14} Hz, with electronic transitions occurring in the 10^{15} Hz range [134,135]. This indicates that a molecule is likely to be found in its ground state before absorption, as the vibrational modes have energies in the range of 0.04 – 0.4 eV, whilst the energy provided via thermal background, k_BT, is ≈ 0.025 eV at room temperature. The Born-Oppenheimer approximation states that the atomic and electronic transitions in a crystal or molecule act independently to one another as the atoms in molecules are much heavier than the electrons involved in electronic transitions. To first promote an electron from the ground state to an excited state, a molecule must first absorb some additional energy. In the ground state, the additional vibrational energy is denoted as $(n_1 + ½)\hbar\Omega_1$, where n is the number of quanta excited (with selection rules only allowing $\Delta n \pm 1$), and Ω is the angular frequency. This gives quantised energy levels above the immediate ground state energy level, S_0 with corresponding energy E_1. When n_1 quanta of states of frequency Ω_1 are excited, the energy of a molecule in the ground state can be written as $E = E_1 + (n_1 + ½)\hbar\Omega_1$. In the case

of a ground state to excited state transition, the singlet excited state (with energy E_2) will also couple to vibrational modes of a molecule with the energy of such levels given by $(n_2 + ½)\hbar\Omega_2$. Assuming the electron is in the lowest energy level in the ground state (and $n_1 = n_2 = 0$), the minimum energy for successful absorption of a photon is [134]:

$$E_{ph} = (E_2 + \frac{1}{2}\hbar\Omega_2) - (E_1 + \frac{1}{2}\hbar\Omega_1) \qquad (2.15)$$

where E_{ph} is the minimum incident photon energy required to instigate the $S_0 \rightarrow S_1$ transition. There is a high probability that a photon will carry more energy than is required for this transition, leaving the system in an excited state with excess vibrational energy. Before the system relaxes to the bottom of the CB (LUMO), where the electron can then reduce back into the VB (HOMO), the excess vibrational energy is lost in a radiationless process as heat energy is transferred into the solid.

The filled bands in a molecular ground state configuration are formed of paired electrons with anti-parallel spins and a quantum number, S, which represents the overall spin of that state is equal to zero (S = 0). The letter 'S' used here is for the total spin quantum number, and is to be distinguished from the ground and multiple excited singlet states ($S_{0,1,2...}$). In exciting the molecule by promoting an electron from the HOMO to the LUMO (or VB to CB), one unpaired electron is left in the LUMO (CB) and one unpaired electron is left in the HOMO (VB). The addition rules for angular momentum quantum numbers states that the excited state can have an overall spin quantum number S = 0 or 1, due to the multiplicity rule that suggests there are (2S + 1) degenerate levels [134]. This gives rise to a triplet state, where S = 1 is produced from a state where the electrons have parallel spin vectors (see **Figure 2.20 (a)**). The triplet states in general have a lower energy value than their equivalent singlet states. Incident photons carry a spin of zero; therefore, only spin-allowed transitions between states of the same spin value can occur. For example, the singlet to triplet $S_0 \rightarrow T_1$ transition is forbidden as it violates quantum number conservation ($S = 0 \rightarrow 1$); however in the transition between singlet-singlet $S_0 \rightarrow S_1$ ($S = 0 \rightarrow 0$), the first singlet excited state (also called the absorption edge) is allowed and tends to dominate the absorption spectrum.

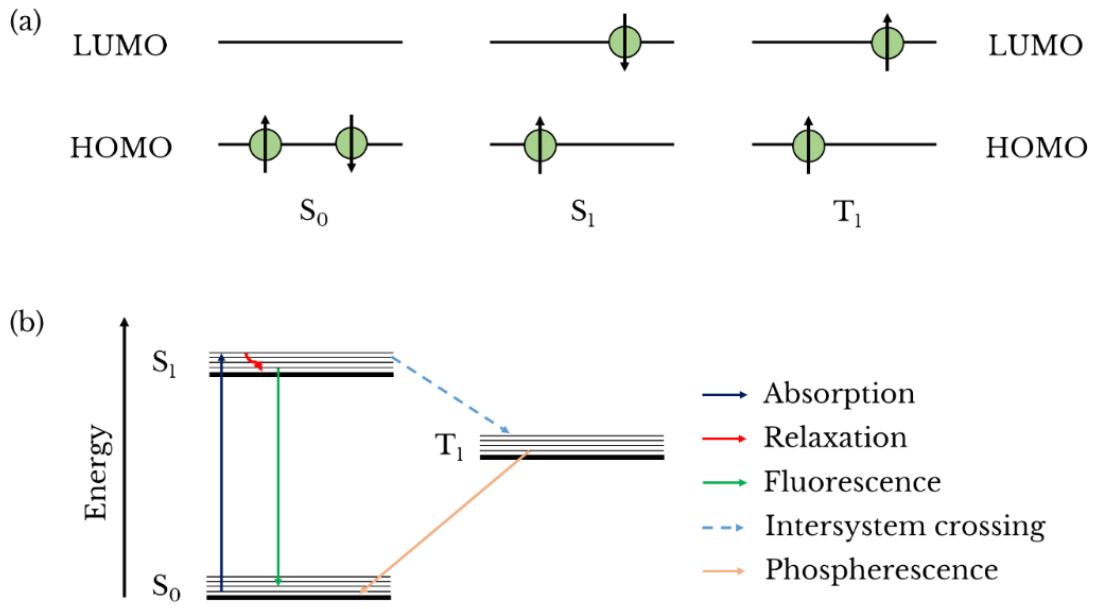

Figure 2.20 - (a) Visual representation of the ground state (S_0), first excited singlet state (S_1) and first excited triplet state (T_1). Singlet states can be recognised through electrons (green) with anti-parallel spins (shown by arrows). (b) Jablonski diagram for a given singlet-triplet system. The absorption of a photon (dark blue) promotes an electron into the first excited state (S_1), producing an excited singlet state. Thermal relaxation (red) occurs before the electron reaches the bottom of the LUMO (CB), then relaxing to the ground state via an $S_1 \rightarrow S_0$ transition with an emission of a photon (green). A small proportion of the electrons in the excited S_1 state can transfer to the triplet (T_1) state nonradiatively (dashed blue). Electrons in the T_1 triplet state can transition to the S_0 ground state producing phosphorescence (pink).

These same rules apply to the relaxation of electrons and the emission of photons. The relative lifetimes of singlet and triplet states are substantially different and lead to both fluorescence and phosphorescence (**Figure 2.20 (b)**) emission processes. As the transition between singlet states is dipole-allowed, it creates a favoured relaxation pathway with a decay lifetime of the order of a few nanoseconds [136]. On the other hand, with a triplet-singlet transition, the lower probability (due to the spin-forbidden mechanism) is indicative of a process with a much longer lifetime. These dipole-forbidden pathways typically have lifetimes on the order of milliseconds (ms), with experimental values for the anthracene ($C_{14}H_{10}$) at upwards of 20 ms [137,138]. The process

of photoluminescence is the emission of electromagnetic radiation following the absorption of a higher energy photon, shown as a green arrow in **Figure 2.20 (b)** ($S_1 \rightarrow S_0$ transition). Experiments performed in **Chapters 4**, **5** and **6** detected the photoluminescence produced from semiconductor samples.

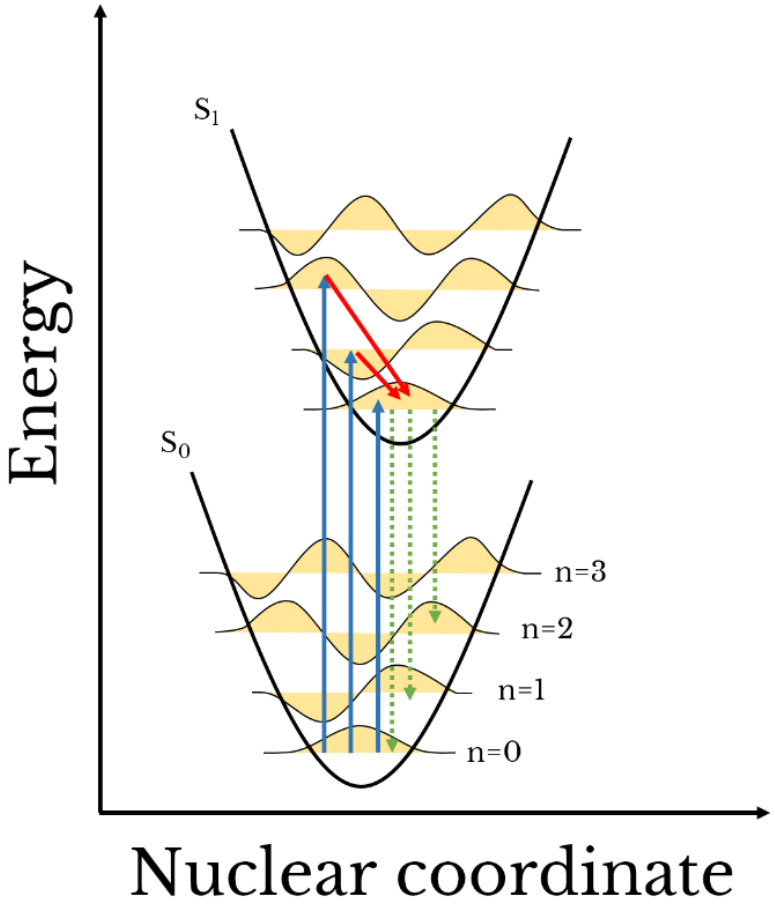

Figure 2.21 - The Franck-Condon principle applied to a two-level system including the ground state (S_0) and the first excited singlet state (S_1), including vibrational energy levels (n=0,1,2,3..) shown for each of the two energy states. The blue arrows indicate absorption and subsequent promotion of an electron to the S_1 excited state, the red arrows indicate non-radiative relaxation and the dotted green arrows show fluorescence from the lowest vibrational state in the S_1 to the ground state.

The difference in energy between the peak absorption feature and emission energy ($S_0 \rightarrow S_1$ and $S_1 \rightarrow S_0$ respectively), is called the Stokes shift [139]. The probability that a transition from a vibrational –electronic energy level to another within a crystal or molecule is proportional to the degree of overlap for the vibronic wavefunctions, as shown in **Figure 2.21**. This is known as the Franck-Condon principle which describes the intensity of each possible transition for both absorption and emission of light. Such transitions are more likely to occur if the electronic wavefunctions overlap. Mathematically it can be described by the Franck-Condon factor using the square of the vibrational overlap integral, whereby the largest numerical values expressed are also the more likely transitions and thus produce the most intense features in a measured absorption/emission spectrum.

2.8.2 Charge carrier lifetimes

After optical excitation, a singlet energy state can be excited through the $S_0 \rightarrow S_1$ transition and relax again following the $S_1 \rightarrow S_0$ transition as shown in **Figure 2.20,** emitting a photon. Assuming a non-interacting environment, the fluorescence decay rate can be written as

$$\frac{dN}{dt} = -CN \tag{2.16}$$

where N is the total number of electrons excited following excitation and C is the decay constant. Solving the above equation yields the solution

$$N(t) = N(0)e^{-kt} \tag{2.17}$$

where N(t) describes the decrease in excited electrons, N(0) is the number of excited electrons at t=0, k is the rate constant and t is the measured time. Assuming N(t) is proportional to the fluorescence intensity at time t, the emission intensity (I) can be expressed using

$$I(t) = I(0)e^{-kt} \tag{2.18}$$

This allows the decay constant to be directly measured from fluorescence lifetime measurements [140,141]. The characteristic lifetime of a sample, τ, is equal to k^{-1} when the number of excited electrons in the sample is equal to 1/e (or 36.8%) of N(0). However, not all processes can be fitted with a singular exponential term, and require instead a multi-exponential series to describe the decay process. The decay constant, k, is a total sum over all of the possible radiative and non-radiative pathways. An example of a non-radiative process is the transfer of energy to another system or a reaction that takes place in the excited state. This allows **Equation 2.18** to be written as

$$I(t) = I(0) \sum_i A_i \, e^{-\frac{t}{\tau_i}} \tag{2.19}$$

where A_i is the amplitude of the exponential term. It is common to find a multi-exponential fitting on organic-inorganic perovskites fluorescence lifetime measurements [142,143]. Multiple exponential fits are used to describe a system that has independent emitters which decay by different decay processes.

2.9 References

1. Bonanno, A., Schlattl, H. & Paternò, L. The age of the Sun and the relativistic corrections in the EOS. *Astron. Astrophys.* **390,** 1115–1118 (2002).
2. Bowmaker, J. K. & Dartnall, H. J. Visual pigments of rods and cones in a human retina. *J. Physiol.* **298,** 501–511 (1980).
3. Douglas, R. H. & Jeffery, G. The spectral transmission of ocular media suggests ultraviolet sensitivity is widespread among mammals. *Proc. R. Soc. B Biol. Sci.* **281,** (2014).
4. Becquerel, M. E. La lumière, ses causes et ses effets. (1868).
5. Einstein, A. Über einen die Erzeugung und Verwandlung des Lichtes betreffenden heuristischen Gesichtspunkt. *Ann. Phys.* **322,** 132–148 (1905).
6. Shockley, W. & Queisser, H. J. Detailed balance limit of efficiency of p-n junction solar cells. *J. Appl. Phys.* **32,** 510–519 (1961).
7. Meng, L. *et al.* Organic and solution-processed tandem solar cells with 17.3%

efficiency. *Science.* **361,** 1094–1098 (2018).

8. Green, M. A. *et al.* Solar cell efficiency tables (version 51). *Prog. Photovoltaics Res. Appl.* **26,** 3–12 (2018).

9. Colella, S. *et al.* $MAPbI_{3-x}Cl_x$ Mixed Halide Perovskite for Hybrid Solar Cells: The Role of Chloride as Dopant on the Transport and Structural Properties. *Chem. Mater.* **25,** 4613–4618 (2013).

10. Solanki, C. S. & Beaucarne, G. Advanced solar cell concepts. *Energy Sustain. Dev.* **11,** 17–23 (2007).

11. Lindholm, F. A., Fossum, J. G. & Burgess, E. L. Application of the Superposition Principle to Solar-Cell Analysis. *IEEE Trans. Electron Devices* **26,** 165–171 (1979).

12. Ahmadi, M., Wu, T. & Hu, B. A Review on Organic-Inorganic Halide Perovskite Photodetectors: Device Engineering and Fundamental Physics. *Adv. Mater.* **29,** 1605242 (2017).

13. Green, M. Solar Cells- Operating Principles, Technology and System Applications. *Englewood Cliffs, NJ, Prentice-Hall, Inc., 288* (1982).

14. Moiz, S. A., Khan, I. A., Younis, W. A. & Karimov, K. S. Space Charge–Limited Current Model for Polymers. *InTech,* 92-94 (2016).

15. Pauli, W. Über den Zusammenhang des Abschlusses der Elektronengruppen im Atom mit der Komplexstruktur der Spektren. *Zeitschrift für Phys.* (1925).

16. Xie, L. *et al.* Understanding the Cubic Phase Stabilization and Crystallization Kinetics in Mixed Cations and Halides Perovskite Single Crystals. *J. Am. Chem. Soc.* **139,** 3320–3323 (2017).

17. Gebhardt, J., Kim, Y. & Rappe, A. M. Influence of the Dimensionality and Organic Cation on Crystal and Electronic Structure of Organometallic Halide Perovskites. *J. Phys. Chem. C* **121,** 6569–6574 (2017).

18. Goldschmidt, V. M. Die Gesetze der Krystallochemie. *Naturwissenschaften* **14,** 477–485 (1926).

19. Li, C. *et al.* Formability of ABX_3 (X = F, Cl, Br, I) halide perovskites. *Acta Crystallogr. Sect. B Struct. Sci.* **64,** 702–707 (2008).

20. Green, M. A., Ho-Baillie, A. & Snaith, H. J. The emergence of perovskite solar cells. *Nat. Photonics* **8,** 506–514 (2014).

21. Stoumpos, C. C., Malliakas, C. D. & Kanatzidis, M. G. Semiconducting tin and lead iodide perovskites with organic cations: Phase transitions, high mobilities, and near-infrared photoluminescent properties. *Inorg. Chem.* **52,** 9019–9038 (2013).

22. Baikie, T. *et al.* Synthesis and crystal chemistry of the hybrid perovskite $(CH_3NH_3)PbI_3$ for solid-state sensitised solar cell applications. *J. Mater. Chem. A* **1,** 5628 (2013).

23. Kawamura, Y., Mashiyama, H. & Hasebe, K. Structural Study on Cubic – Tetragonal Transition of $CH_3NH_3PbI_3$. *J. Phys. Soc. Japan* **71,** 1694–1697 (2002).

24. Li, Z. *et al.* Stabilizing Perovskite Structures by Tuning Tolerance Factor: Formation of Formamidinium and Cesium Lead Iodide Solid-State Alloys. *Chem. Mater.* **28,** 284–292 (2016).

25. Cohen, B.-E., Wierzbowska, M. & Etgar, L. High efficiency quasi 2D lead bromide

perovskite solar cells using various barrier molecules. *Sustain. Energy Fuels* **1,** 1935–1943 (2017).

26. Brivio, F. *et al.* Lattice dynamics and vibrational spectra of the orthorhombic, tetragonal, and cubic phases of methylammonium lead iodide. *Phys. Rev. B* **92,** 144308 (2015).

27. Pistor, P., Borchert, J., Fränzel, W., Csuk, R. & Scheer, R. Monitoring the Phase Formation of Coevaporated Lead Halide Perovskite Thin Films by in Situ X-ray Diffraction. *J. Phys. Chem. Lett.* **5,** 3308–3312 (2014).

28. Whitfield, P. S. *et al.* Structures, Phase Transitions and Tricritical Behavior of the Hybrid Perovskite Methyl Ammonium Lead Iodide. *Sci. Rep.* **6,** 35685 (2016).

29. Yamada, Y. *et al.* Dynamic Optical Properties of $CH_3NH_3PbI_3$ Single Crystals As Revealed by One- and Two-Photon Excited Photoluminescence Measurements. *J. Am. Chem. Soc.* **137,** 10456–10459 (2015).

30. Lee, J.-H., Bristowe, N. C., Bristowe, P. D. & Cheetham, A. K. Role of hydrogen-bonding and its interplay with octahedral tilting in $CH_3NH_3PbI_3$. *Chem. Commun.* **51,** 6434–6437 (2015).

31. Ong, K. P., Goh, T. W., Xu, Q. & Huan, A. Structural Evolution in Methylammonium Lead Iodide $CH_3NH_3PbI_3$. *J. Phys. Chem. A* **119,** 11033–11038 (2015).

32. Beecher, A. N. *et al.* Direct Observation of Dynamic Symmetry Breaking above Room Temperature in Methylammonium Lead Iodide Perovskite. (2016).

33. Poglitsch, A. & Weber, D. Dynamic disorder in methylammoniumtrihalogenoplumbates (II) observed by millimeter-wave spectroscopy. *J. Chem. Phys.* **87,** 6373 (1987).

34. Chen, Y. *et al.* 2D Ruddlesden–Popper Perovskites for Optoelectronics. *Adv. Mater.* **30,** 1–15 (2018).

35. Ruddlesden, S. N. & Popper, P. The compound $Sr_3Ti_2O_7$ and its structure. *Acta Crystallogr.* **11,** 54–55 (1958).

36. Ruddlesden, S. N. & Popper, P. New compounds of the K_2NIF_4 type. *Acta Crystallogr.* **10,** 538–539 (1957).

37. Kamminga, M. E. *et al.* Confinement Effects in Low-Dimensional Lead Iodide Perovskite Hybrids. *Chem. Mater.* **28,** 4554–4562 (2016).

38. Koutselas, I. B., Ducasse, L. & Papavassiliou, G. C. Electronic properties of three- and low-dimensional semiconducting materials with Pb halide and Sn halide units. *J. Phys. Condens. Matter* **8,** 1217–1227 (1996).

39. Hong, X., Ishihara, T. & Nurmikko, A. V. Dielectric confinement effect on excitons in PbI_4-based layered semiconductors. *Phys. Rev. B* **45,** 6961–6964 (1992).

40. Milot, R. L. *et al.* Charge-Carrier Dynamics in 2D Hybrid Metal–Halide Perovskites. *Nano Lett.* **16,** 7001–7007 (2016).

41. Mitzi, D. B. Synthesis, Crystal Structure, and Optical and Thermal Properties of $(C_4H_9NH_3)_2MI_4$ (M = Ge, Sn, Pb). *Chem. Mater.* **8,** 791–800 (1996).

42. Smith, I. C., Hoke, E. T., Solis-Ibarra, D., McGehee, M. D. & Karunadasa, H. I. A Layered Hybrid Perovskite Solar-Cell Absorber with Enhanced Moisture Stability. *Angew. Chemie Int. Ed.* **53,** 11232–11235 (2014).

43. Hojamberdiev, M. *et al.* New Dion–Jacobson Phase Three-Layer Perovskite $CsBa_2Ta_3O_{10}$ and Its Conversion to Nitrided $Ba_2Ta_3O_{10}$ Nanosheets via a Nitridation–Protonation–Intercalation–Exfoliation Route for Water Splitting. *Cryst. Growth Des.* **16,** 2302–2308 (2016).

44. Dion, M., Ganne, M. & Tournoux, M. Nouvelles familles de phases $MIMII_2Nb_3O_{10}$ a feuillets "perovskites". *Mater. Res. Bull.* **16,** 1429–1435 (1981).

45. Jacobson, A. J., Johnson, J. W. & Lewandowski, J. T. Interlayer chemistry between thick transition-metal oxide layers: synthesis and intercalation reactions of $K[Ca_2Na_{n-3}Nb_nO_{3n+1}]$ ($3 < n < 7$). *Inorg. Chem.* **24,** 3727–3729 (1985).

46. Mao, L. *et al.* Hybrid Dion–Jacobson 2D Lead Iodide Perovskites. *J. Am. Chem. Soc.* **140,** 3775–3783 (2018).

47. Stoumpos, C. C. *et al.* Ruddlesden–Popper Hybrid Lead Iodide Perovskite 2D Homologous Semiconductors. *Chem. Mater.* **28,** 2852–2867 (2016).

48. Soe, C. M. M. *et al.* New Type of 2D Perovskites with Alternating Cations in the Interlayer Space, $(C(NH_2)_3)(CH_3NH_3)_nPb_nI_{3n+1}$: Structure, Properties, and Photovoltaic Performance. *J. Am. Chem. Soc.* **139,** 16297–16309 (2017).

49. Lee, M. V. *et al.* Transamidation of dimethylformamide during alkylammonium lead triiodide film formation for perovskite solar cells. *J. Mater. Res.* **32,** 45–55 (2017).

50. Senanayak, S. P. *et al.* Understanding charge transport in lead iodide perovskite thin-film field-effect transistors. *Sci. Adv.* **3,** e1601935 (2017).

51. Palosz, B. The structure of PbI_2 polytypes 2H and 4H: a study of the 2H-4H transition. *J. Phys. Condens. Matter* **2,** 5285–5295 (1990).

52. Motta, C. *et al.* Revealing the role of organic cations in hybrid halide perovskite $CH_3NH_3PbI_3$. *Nat. Commun.* **6,** 7026 (2015).

53. Zhao, Y. & Zhu, K. Organic–inorganic hybrid lead halide perovskites for optoelectronic and electronic applications. *Chem. Soc. Rev. Chem. Soc. Rev* **45,** 655–689 (2016).

54. Kovalenko, M. V, Protesescu, L. & Bodnarchuk, M. I. Properties and potential optoelectronic applications of lead halide perovskite nanocrystals. *Science.* **358,** 745–750 (2017).

55. Kojima, A., Teshima, K., Shirai, Y. & Miyasaka, T. Novel Photoelectrochemical Cell with Mesoscopic Electrodes Sensitized by Lead-halide Compounds. *210th ECS Meet.* 1 (2006).

56. Green, M. A. & Ho-Baillie, A. Perovskite Solar Cells: The Birth of a New Era in Photovoltaics. *ACS Energy Lett.* **2,** 822–830 (2017).

57. Kojima, A., Teshima, K., Shirai, Y. & Miyasaka, T. Organometal Halide Perovskites as Visible-Light Sensitizers for Photovoltaic Cells. *J. Am. Chem. Soc.* **131,** 6050–6051 (2009).

58. Im, J.-H., Lee, C.-R., Lee, J.-W., Park, S.-W. & Park, N.-G. 6.5% Efficient Perovskite Quantum-Dot-Sensitized Solar Cell. *Nanoscale* **3,** 4088 (2011).

59. Park, N. G. Perovskite solar cells: An emerging photovoltaic technology. *Mater. Today* **18,** 65–72 (2015).

60. Lee, M. M., Teuscher, J., Miyasaka, T., Murakami, T. N. & Snaith, H. J. Efficient

hybrid solar cells based on meso-superstructured organometal halide perovskites. *Science* **338,** 643–7 (2012).

61. Liu, M., Johnston, M. B. & Snaith, H. J. Efficient planar heterojunction perovskite solar cells by vapour deposition. *Nature* **501,** 395–8 (2013).

62. Eperon, G. E., Burlakov, V. M., Docampo, P., Goriely, A. & Snaith, H. J. Morphological control for high performance, solution-processed planar heterojunction perovskite solar cells. *Adv. Funct. Mater.* **24,** 151–157 (2014).

63. Saliba, M. *et al.* Cesium-containing triple cation perovskite solar cells: improved stability, reproducibility and high efficiency. *Energy Environ. Sci.* **9,** 1989–1997 (2016).

64. Liu, T., Chen, K., Hu, Q., Zhu, R. & Gong, Q. Inverted Perovskite Solar Cells: Progresses and Perspectives. *Adv. Energy Mater.* **6,** 1600457 (2016).

65. Luo, D. *et al.* Enhanced photovoltage for inverted planar heterojunction perovskite solar cells. *Science.* **360,** 1442–1446 (2018).

66. Bishop, J. E., Routledge, T. J. & Lidzey, D. G. Advances in Spray-Cast Perovskite Solar Cells. *J. Phys. Chem. Lett.* **9,** 1977–1984 (2018).

67. Mohamad, D. K., Griffin, J., Bracher, C., Barrows, A. T. & Lidzey, D. G. Spray-Cast Multilayer Organometal Perovskite Solar Cells Fabricated in Air. *Adv. Energy Mater.* **6,** 1600994 (2016).

68. Bernède, J. C. Organic photovoltaic cells: History, principle and technique. *J. Chil. Chem. Soc.* **53,** 1549–1564 (2008).

69. Spanggaard, H. & Krebs, F. C. A brief history of the development of organic and polymeric photovoltaics. *Sol. Energy Mater. Sol. Cells* **83,** 125–146 (2004).

70. Brazovskii, S. & Kirova, N. Physical theory of excitons in conducting polymers. *Chem. Soc. Rev.* **39,** 2453–2465 (2010).

71. Peierls, R. More Surprises in Theoretical Physics. *Am. J. Phys.* (1992).

72. O'Reilly, E. P. Quantum Theory of solids. *CRC Press* **53,** (2013).

73. Patil, A. O., Heeger, A. J. & Wudl, F. Optical properties of conducting polymers. *Chem. Rev.* **88,** 183–200 (1988).

74. Yannoni, C. S. & Clarke, T. C. Molecular Geometry of cis- and trans-Polyacetylene by Nutation NMR Spectroscopy. *Phys. Rev. Lett.* **51,** 1191–1193 (1983).

75. Awuzie, C. I. Conducting Polymers. *Mater. Today Proc.* **4,** 5721–5726 (2017).

76. Ohki, Y., Fuse, N. & Arai, T. Band gap energies and localized states in several insulating polymers estimated by optical measurements. in *2010 Annual Report Conference on Electrical Insulation and Dielectic Phenomena* 1–4 (IEEE, 2010).

77. Andrady, A. L. & Neal, M. A. Applications and societal benefits of plastics. *Philos. Trans. R. Soc. B Biol. Sci.* **364,** 1977–1984 (2009).

78. Kasowski, R. V., Hsu, W. Y. & Caruthers, E. B. Electronic properties of polyacetylene, polyethylene, and polytetrafluoroethylene. *J. Chem. Phys.* **72,** 4896–4900 (1980).

79. Giro, R., Caldas, M. J. & Galvão, D. S. Band gap engineering for poly(p-phenylene) and poly(p-phenylene vinylene) copolymers using the tight-binding approach. *Int. J. Quantum Chem.* **103,** 588–596 (2005).

80. Lyu, M., Yun, J.-H., Chen, P., Hao, M. & Wang, L. Addressing Toxicity of Lead: Progress and Applications of Low-Toxic Metal Halide Perovskites and Their Derivatives. *Adv. Energy Mater.* **7,** 1602512 (2017).

81. Qiu, L., Ono, L. K. & Qi, Y. Advances and challenges to the commercialization of organic–inorganic halide perovskite solar cell technology. *Mater. Today Energy* **7,** 169–189 (2018).

82. Zweibel, K. The Impact of Tellurium Supply on Cadmium Telluride Photovoltaics. *Science.* **328,** 699–701 (2010).

83. Pochettino, A. On the photo-electric behavior of the Anthracene. *Acad. Lincei Rend.* **15,** 355–363 (1906).

84. Kallmann, H. & Pope, M. Photovoltaic effect in organic crystals. *J. Chem. Phys.* **30,** 585–586 (1959).

85. Mark, P. & Helfrich, W. Space-charge-limited currents in organic crystals. *J. Appl. Phys.* **33,** 205–215 (1962).

86. Geacintov, N., Pope, M. & Kallmann, H. Photogeneration of charge carriers in tetracene. *J. Chem. Phys.* **45,** 2639–2649 (1966).

87. Nelson, J. Organic photovoltaic films. *Curr. Opin. Solid State Mater. Sci.* **6,** 87–95 (2002).

88. Tang, C. W. Two-layer organic photovoltaic cell. *Appl. Phys. Lett.* **48,** 183–185 (1986).

89. Halls, J. J. M., Pichler, K., Friend, R. H., Moratti, S. C. & Holmes, A. B. Exciton diffusion and dissociation in a poly(p-phenylenevinylene)/C60 heterojunction photovoltaic cell. *Appl. Phys. Lett.* **68,** 3120–3122 (1996).

90. Markov, D. E., Amsterdam, E., Blom, P. W. M., Sieval, A. B. & Hummelen, J. C. Accurate measurement of the exciton diffusion length in a conjugated polymer using a heterostructure with a side-chain cross-linked fullerene layer. *J. Phys. Chem. A* **109,** 5266–5274 (2005).

91. Tamai, Y., Ohkita, H., Benten, H. & Ito, S. Exciton Diffusion in Conjugated Polymers: From Fundamental Understanding to Improvement in Photovoltaic Conversion Efficiency. *J. Phys. Chem. Lett.* **6,** 3417–3428 (2015).

92. Ohkita, H. *et al.* Charge carrier formation in polythiophene/fullerene blend films studied by transient absorption spectroscopy. *J. Am. Chem. Soc.* **130,** 3030–3042 (2008).

93. Kippelen, B. & Brédas, J.-L. Organic photovoltaics. *Energy Environ. Sci.* **2,** 251 (2009).

94. Arndt, A. P. *et al.* Time-resolved charge-transfer state emission in organic solar cells: Temperature and blend composition dependences of interfacial traps. *J. Phys. Chem. C* **119,** 13516–13523 (2015).

95. Pal, S. K. *et al.* Geminate Charge Recombination in Polymer/Fullerene Bulk Heterojunction Films and Implications for Solar Cell Function. *J. Am. Chem. Soc.* **132,** 12440–12451 (2010).

96. Shaheen, S. E. *et al.* 2.5% Efficient Organic Plastic Solar Cells. *Appl. Phys. Lett.* **78,** 841–843 (2001).

97. Larson, B. W. *et al.* Electron affinity of Phenyl-C61-butyric acid methyl ester

(PCBM). *J. Phys. Chem. C* **117**, 14958–14964 (2013).

98. Yoo, S. H., Kum, J. M. & Cho, S. O. Tuning the electronic band structure of pcbm by electron irradiation. *Nanoscale Res. Lett.* **6**, 1–7 (2011).

99. Sariciftci, N. S., Smilowitz, L., Heeger, A. J. & Wudl, F. Photoinduced Electron Transfer from a Conducting Polymer to Buckminsterfullerene. *Science.* **258**, 1474–1476 (1992).

100. Wang, C. I. & Hua, C. C. Solubility of C_{60} and PCBM in Organic Solvents. *J. Phys. Chem. B* **119**, 14496–14504 (2015).

101. Li, G. *et al.* High-efficiency solution processable polymer photovoltaic cells by self-organization of polymer blends. *Nat. Mater.* **4**, 864–868 (2005).

102. Yu, G., Gao, J., Hummelen, J. C., Wudl, F. & Heeger, A. J. Polymer Photovoltaic Cells: Enhanced Efficiencies via a Network of Internal Donor-Acceptor Heterojunctions. *Science.* **270**, 1789–1791 (1995).

103. Peet, J. *et al.* Efficiency enhancement in low-bandgap polymer solar cells by processing with alkane dithiols. *Nat. Mater.* **6**, 497–500 (2007).

104. Laquai, F., Andrienko, D., Deibel, C. and Neher, D. Charge Carrier Generation, Recombination, and Extraction in Polymer–Fullerene Bulk Heterojunction Organic Solar Cells. *Adv. Polym. Sci.* **272**, 267–291 (2008).

105. Tanaka, K. *et al.* One-dimensional excitons in inorganic-organic self-organized quantum-wire crystals $[NH_2C(I) = NH_2]_3PbI_5$ and $[CH_3SC(=NH_2)NH_2]_3PbI_5$. *Phys. E Low-Dimensional Syst. Nanostructures* **25**, 378–383 (2005).

106. Tongay, S. *et al.* Defects activated photoluminescence in two-dimensional semiconductors: Interplay between bound, charged, and free excitons. *Sci. Rep.* **3**, 1–5 (2013).

107. Giorgi, G., Yoshihara, T. & Yamashita, K. Structural and electronic features of small hybrid organic–inorganic halide perovskite clusters: a theoretical analysis. *Phys. Chem. Chem. Phys.* **18**, 27124–27132 (2016).

108. Malmberg, C. G. & Maryott, A. A. Dielectric constant of water from 0 to 100 C. *J. Res. Natl. Bur. Stand. (1934).* **56**, 1 (1956).

109. Knupfer, M. Exciton binding energies in organic semiconductors. *Appl. Phys. A* **77**, 623–626 (2003).

110. Frenkel, J. On the transformation of light into heat in solids. *Phys. Rev.* **37**, 17–44 (1931).

111. Nam, S. B. *et al.* Free-exciton energy spectrum in GaAs. *Phys. Rev. B* **13**, 761–767 (1976).

112. Tanaka, K. *et al.* Comparative study on the excitons in lead-halide-based perovskite-type crystals $CH_3NH_3PbBr_3$ $CH_3NH_3PbI_3$. *Solid State Commun.* **127**, 619–623 (2003).

113. Hirasawa, M., Ishihara, T., Goto, T., Uchida, K. & Miura, N. Magnetoabsorption of the lowest exciton in perovskite-type compound $(CH_3NH_3)PbI_3$. *Phys. B Condens. Matter* **201**, 427–430 (1994).

114. Dai, L. Chapter 2: Conducting Polymers. *Intell. Macromol. Smart Devices* **1980**, 1–41 (1975).

115. Liu, C., Wang, K., Gong, X. & Heeger, A. J. Low bandgap semiconducting polymers for polymeric photovoltaics. *Chem. Soc. Rev.* **45,** 4825–4846 (2016).

116. Piro, B. *et al.* Fabrication and Use of Organic Electrochemical Transistors for Sensing of Metabolites in Aqueous Media. *Appl. Sci.* **8,** 928 (2018).

117. Brédas, J. L. Relationship between band gap and bond length alternation in organic conjugated polymers. *J. Chem. Phys.* **82,** 3808–3811 (1985).

118. Zhang, M., Zhang, X., Huang, L.-Y., Lin, H.-Q. & Lu, G. Charge transport in hybrid halide perovskites. *Phys. Rev. B* **96,** 195203 (2017).

119. Karakus, M. *et al.* Phonon-Electron Scattering Limits Free Charge Mobility in Methylammonium Lead Iodide Perovskites. *J. Phys. Chem. Lett.* **6,** 4991–4996 (2015).

120. Bartelt, J. A., Lam, D., Burke, T. M., Sweetnam, S. M. & McGehee, M. D. Charge-Carrier Mobility Requirements for Bulk Heterojunction Solar Cells with High Fill Factor and External Quantum Efficiency > 90%. *Adv. Energy Mater.* (2015).

121. Bisquert, J. The physics of solar cells: Perovskites, Organics, and Photovoltaic Fundamentals. *CRC Press* (2018).

122. Stranks, S. D. *et al.* Electron-hole diffusion lengths exceeding 1 micrometer in an organometal trihalide perovskite absorber. *Science.* **342,** 341–344 (2013).

123. Long, M. *et al.* Nonstoichiometric acid–base reaction as reliable synthetic route to highly stable $CH_3NH_3PbI_3$ perovskite film. *Nat. Commun.* **7,** 13503 (2016).

124. Nelson, J. Organic photovoltaic films. *Curr. Opin. Solid State Mater. Sci.* **6,** 87–95 (2002).

125. Gao, Y. *et al.* Recent development on narrow bandgap conjugated polymers for polymer solar cells. *Polymers (Basel).* **9,** (2017).

126. Guzelturk, B. *et al.* Terahertz Emission from Hybrid Perovskites Driven by Ultrafast Charge Separation and Strong Electron-Phonon Coupling. *Adv. Mater.* **30,** 1704737 (2018).

127. Shi, D. *et al.* Low trap-state density and long carrier diffusion in organolead trihalide perovskite single crystals. *Science.* **347,** 519–522 (2015).

128. Bai, S. *et al.* High-performance planar heterojunction perovskite solar cells: Preserving long charge carrier diffusion lengths and interfacial engineering. *Nano Res.* **7,** 1749–1758 (2014).

129. Ziang, X. *et al.* Refractive index and extinction coefficient of $CH_3NH_3PbI_3$ studied by spectroscopic ellipsometry. *Opt. Mater. Express* **5,** 29 (2015).

130. Mao, P., Zhou, Q., Jin, Z., Li, H. & Wang, J. Efficiency-Enhanced Planar Perovskite Solar Cells via an Isopropanol/Ethanol Mixed Solvent Process. *ACS Appl. Mater. Interfaces* **8,** 23837–23843 (2016).

131. Ishihara, T. Optical properties of PbI-based perovskite structures. *J. Lumin.* **60–61,** 269–274 (1994).

132. Li, Y. *et al.* Fabrication of Planar Heterojunction Perovskite Solar Cells by Controlled Low-Pressure Vapor Annealing. *J. Phys. Chem. Lett.* **6,** 493–499 (2015).

133. Wang, T. *et al.* Indirect to direct bandgap transition in methylammonium lead halide perovskite. *Energy Environ. Sci.* **10,** 509–515 (2017).

134. Fox, M. Optical Properties of Solids. *Oxford University Press* (2010).

135. Landau, L. D. & Lifshitz, E. M. Mechanics. *Vol 1: Course of Theoretical Physics*. (1982).

136. Klingshirn, C. F. Semiconductor Optics. *Springer Berlin Heidelberg* (2012).

137. Melhuish, W. H. & Hardwick, R. Lifetime of the triplet state of anthracene in lucite. *Trans. Faraday Soc.* **58,** 1908–1911 (1962).

138. Jackson, G. & Livingston, R. Unimolecular decay of the triplet state of anthracene in fluid and viscous media. *J. Chem. Phys.* **35,** 2182–2186 (1961).

139. Zhu, X., Su, Q., Feng, W. & Li, F. Anti-Stokes shift luminescent materials for bio-applications. *Chem. Soc. Rev.* **46,** 1025–1039 (2017).

140. Li, C. *et al.* Efficient perovskite/fullerene planar heterojunction solar cells with enhanced charge extraction and suppressed charge recombination. *Nanoscale* **7,** 9771–9778 (2015).

141. Guo, Y., Lei, H., Xiong, L., Li, B. & Fang, G. An integrated organic–inorganic hole transport layer for efficient and stable perovskite solar cells. *J. Mater. Chem. A* **6,** 2157–2165 (2018).

142. Zhao, Q. *et al.* Improving the photovoltaic performance of perovskite solar cells with acetate. *Sci. Rep.* **6,** 38670 (2016).

143. Dai, J., Zheng, H., Zhu, C., Lu, J. & Xu, C. Comparative investigation on temperature-dependent photoluminescence of $CH_3NH_3PbBr_3$ and $CH(NH_2)_2PbBr_3$ microstructures. *J. Mater. Chem. C* **4,** 4408–4413 (2016).

Chapter 3

Experimental methods

This chapter details the experimental procedures and apparatus used throughout this thesis, with specific interest paid to photoluminescence (PL) spectroscopy, x-ray diffraction and photovoltaic characterisation. The first section details the materials, solutions and sample preparation commonly used. The second section describes a brief background to the physics behind the apparatus used in the characterisation of the samples. The general idea behind the following chapter is to give the reader a working knowledge of the environment used throughout the experiments presented in this thesis. Unless stated otherwise, all experimental work was performed at the Department of Physics & Astronomy or the Department of Chemistry, University of Sheffield, U.K.

3.1 Materials

All solvents, solutes and general materials were used as obtained and additional information such as product codes are shown in parenthesises. Dry components methylammonium iodide (MAI) (99.9% - M271), lead-chloride ($PbCl_2$) (99.999% - M281) and [6,6]-phenyl-C60(or C70)-butyric acid methyl ester ($PC_{60}BM$ or $PC_{70}BM$) (95% - M113) were purchased from Ossila Ltd. Solution additive hydriodic acid (HI) was purchased from Sigma Aldrich. The widely used p-type semiconductor poly(3,4-ethylenedioxythiophene) (PEDOT) doped with poly(styrene sulfonate) (PSS) anions (PEDOT:PSS) (1:6) (Heraeus Clevios™, Al 4083) was purchased from Ossila Ltd. Polymer donor systems for the use in OPV devices were provided by Dr. Ahmed Iraqi, University

of Sheffield, Chemistry Department, U.K. Solvents other than de-ionised (DI) water used throughout this thesis include N,N-dimethylformamide (DMF) (99.8%, anhydrous), chlorobenzene (CB) (99.8%, anhydrous), 1,2-dichlorobenzene (1,2-DCB) (99%, anhydrous), toluene (99.8%, anhydrous), isopropanol (IPA), chloroform (CF) and Hellmenex concentrate were all purchased from Sigma Aldrich. Indium tin-oxide (ITO) patterned quartz and quartz coated float glass substrates were also purchased from Ossila Ltd. All substrates throughout this thesis were cleaned in an identical manner unless stated otherwise, as per **Section 3.2**. Poly(methyl methacrylate) (PMMA) was purchased from Sigma-Aldrich and used to encapsulate moisture-unstable films in **Chapter 6**.

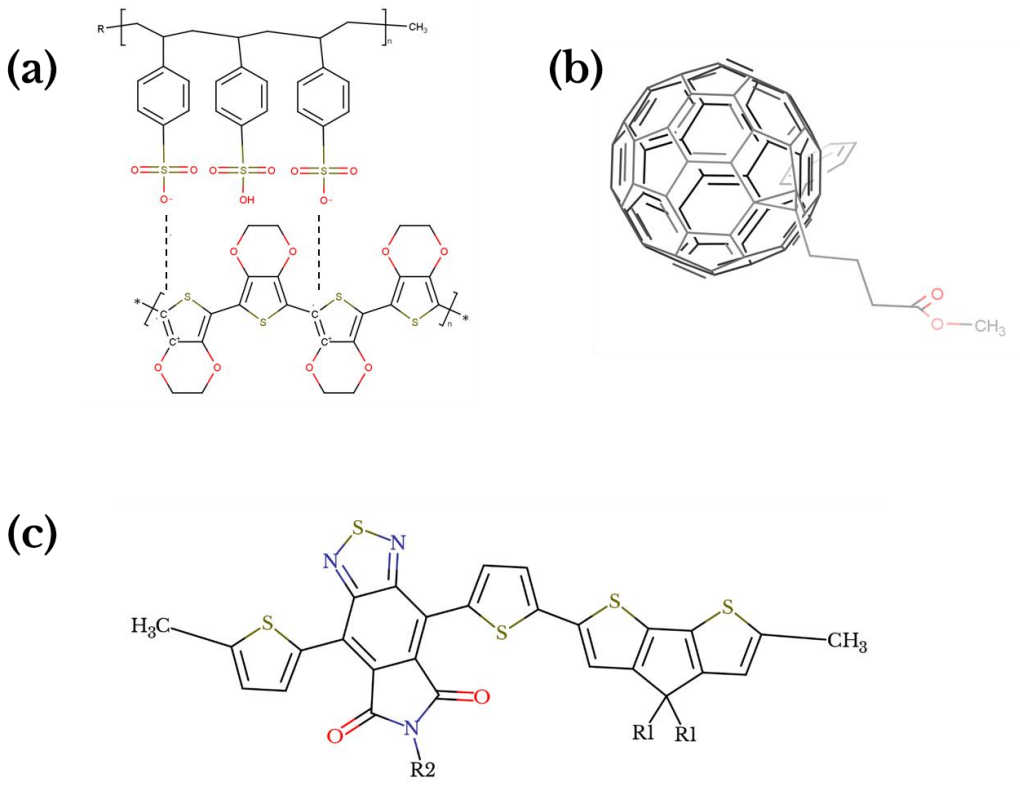

Figure 3.1 - Representative structures of (a) PEDOT:PSS (dashed lines indicate coulomb interaction), (b) $PC_{60}BM$ and (c) PCPDTDTBTDI where R1,2 represent separate functional groups discussed in **Chapter 4**.

3.2 Substrate cleaning procedure

Substrates were cleaned in boiling DI water that was added to a Pyrex dish containing Hellmanex (Z805939, 5 vol %) solution. The substrates contained within a substrate rack were then immersed in to the boiling DI - Hellmanex solution and sonicated for 10 minutes. After this step, substrates were transferred to a new Pyrex dish containing boiling DI water to remove any excess Hellmanex from the substrates and sonicated again for 10 minutes. Once finished, the substrates were placed in to a third Pyrex dish containing IPA at room temperature and sonicated for a further 10 minutes. Then, substrates were dried using a nitrogen gun followed by solution deposition. UV-Ozone treatment of the quartz/ITO substrate was used for PV experiments only. This fabrication step has been previously shown to improve the contact between interfaces by removing excess carbon from the surface and increasing the ITO work function [1,2]. UV-Ozone was not used in some circumstances because the solution cleaning procedure was sufficient to allow a thin-film to be deposited for non-PV experiments. When used, clean ITO substrates were treated with UV-Ozone for 20 minutes before solution deposition.

3.3 Solution preparation and deposition

To prepare solutions, dry precursor materials were first weighed in air and added to amber vials before the addition of a solvent system. Studies involving solutions where the solvents DMF, CB and DCB are used were mixed decanted inside a glovebox from larger storage bottles to form the solution. In all circumstances other than PEDOT:PSS, solutions were heated to 70°C for one hour to allow the solute to completely dissolve. In some cases, magnetic stir bars were used to further promote solubility by stirring the heated solution.

3.3.1 Perovskite solution preparation

For perovskite solutions, MAI and $PbCl_2$ were first weighed sequentially in to an amber vial. The molar ratio in which these compounds were mixed varies throughout this work, however a reference molar ratio of 3:1 (MAI:$PbCl_2$) was used and described in more detail in **Chapters *5*** and **6**. The final solution concentration for all perovskite mixtures was held at a value of 500 mg/ml unless otherwise stated. After weighing both compounds, the amber vial was transferred to a N_2 glovebox together with a HI solution. DMF and HI were then sequentially decanted in to the vial at (100-X) vol% and X vol%, respectively. The 'X' value here represents a known concentration of HI in solution discussed in more detail in **Chapter *5***. The solution was then vortex mixed for approximately 30 seconds and transferred to a hot plate at 70°C. This heating step was performed either in a N_2 glovebox or in the air depending on casting and annealing conditions chosen for that experiment. Typically, perovskite solutions were left for no longer than one hour on a hotplate before deposition.

This time-limited heating step was implemented to reduce any DMF degradation effects whereby DMF can degrade to formic acid and dimethylamine over time [3]. For perovskite PV devices, solutions were first cooled to room temperature before filtering through a 0.45 µm polytetrafluoroethylene (PTFE) filter. This was only performed in PV experiments to further reduce the chances of aggregates forming in the film after deposition. Solutions were then vortex mixed once more after approximately 15 minutes on the hot plate (at 70°C) to fully dissolve any remnant particles in the solution. After this second vortex mixing step, solutions were left for another 45 minutes before deposition of the perovskite active layer.

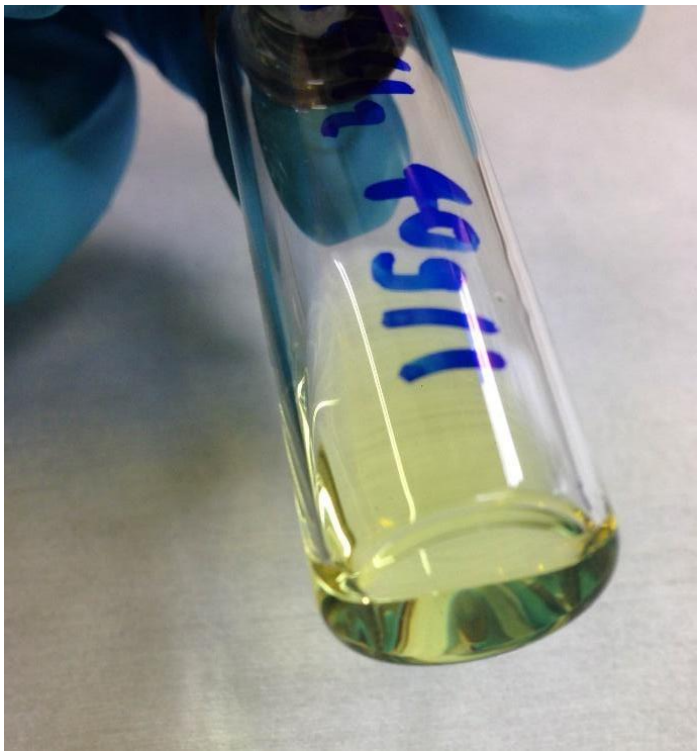

Figure 3.2 - Photograph of a 500 mg/ml solution of 3:1 (MAI:$PbCl_2$) containing 99 vol% DMF and 1 vol% HI. The vial used here was transparent so show the reader the colour of the solution. Note the solution is free of aggregates due to the addition of HI and further vortex mixing. During the experimental section of this thesis, amber vials were used to remove any potential light-degradation effects [4].

3.3.2 Organic solution preparation

Preparing solutions for use in OPV cells followed the same procedure as described with the perovskite solutions in **Section 3.3.1**. First, a dry donor polymer was weighed followed by $PC_{60}BM$ or $PC_{70}BM$ in an appropriate weight ratio with the donor polymer (typically 1:3 for donor:acceptor blends) and is described in more detail in **Chapter 4**. Once weighed, the vial was transferred to the glovebox and a chosen solvent, typically CB or CB:DCB blend was decanted to make up a final solution concentration of 20 mg/ml. After adding the solvent, the vial was vortex mixed and a magnetic stir bar was added before heating at 60°C overnight. Stirring the OPV solutions overnight helped the

mixture dissolve into solution as some solutions contained aggregates that could be dispersed on the thin-film surface post-spin coating. Once dissolved, solutions were first cooled before using a 0.45 μm PTFE filter system to remove any large aggregates. Unless stated, all OPV device active layers were deposited at room temperature on to room temperature substrates and deposited via spin coating. Active layer thicknesses varied depending on the polymer chosen due to a variation in polymer molecular weights.

3.3.3 Spin-coating

Before solution deposition, ITO substrates were cleaned as described in **Section 3.2**. Unless stated otherwise, solutions were deposited using a 'one-step' dynamic-casting method whereby a solution was deposited from a pipette in one smooth motion on to a spinning substrate. The final film thickness can be calculated by the following relationship,

$$T \propto \frac{c\,\eta}{\sqrt{\omega}} \tag{3.1}$$

where T is the thickness of the final film, c is the solution concentration, η is the solution viscosity and ω is the spin speed. As the solution is deposited on to a fast (> 1000 rpm) spinning substrate there is substantial expulsion of material due to the rotational forces exerted on the top surface of the fluid. Eventually, the thickness of the fluid layer becomes thin enough to co-rotate with the spinning substrate. At this point, when the substrate has reached its final rpm, the rotational acceleration balances the viscous sheer drag of the fluid layer [5]. From here, the film is thin enough such that the viscous forces of the fluid control the film thinning rate and any remaining thickness variations is controlled via the post-spin annealing step. For most thin-film applications it is useful to fine tune the film thickness, T, by simply adjusting the spin speed which follows the following relationship

$$\omega = \omega_R \left(\frac{T_R}{T}\right)^2 \tag{3.2}$$

where ω_R and T_R are the spin speed and sample thickness of the reference sample, respectively. Although spin-coating has been shown to achieve highly uniform films with good thickness control [6,7], it comes with some drawbacks. Firstly, there is a large percentage of waste material through this deposition technique, estimated to be between 95-98% of initial solution [5,8]. Secondly as the substrate area increases, the forces on the edge of the substrate also increases, leading to the possible fracture of large-area substrates.

3.3.4 Spray-coating

Spin-coating was the preferred choice for solution deposition as the substrates and final pixel areas were relatively small. However, even though spin-coating produced highly uniform films there is currently no potential scale-up technique which utilises this deposition method. Spray-coating was then explored using a USI prism 300. Here, the ultra-sonic tip was held at 40 mm above the substrate surface and vibrated at 35 kHz while fluid from a coating reservoir above was fed to the tip. The ink droplets created were directed to the surface using a carrier gas whose pressure was set to 10 psi giving a wide spray pattern (*c.a.* 50 mm). At the same time, the spray head was scanned a distance of 150 mm over ITO device substrates in a single pass. It was found that multiple pass spray-routines created poor quality films as they tend to re-dissolve the underlying films. Unlike airbrush techniques in which droplets contain very little solvent when they reach the surface, ultrasonic spray-cast films consist of droplets that coalesce to form a fully wet film before drying [31]. Note that the width of the spray-pattern is significantly larger than that of the individual device pixels (each having a size (2 x 2) mm^2), and thus significant heterogeneity across the spray-mist pattern at the sample surface is not anticipated. Substrates were mounted on a hotplate to ensure stable elevated temperatures in order to control the wet film drying rate.

3.4 Sample architecture

All devices described in this thesis were based on a planar architecture [9]. Both organic and perovskite devices were fabricated using an "inverted" (or p-i-n junction) architecture, where the incident light enters through the transparent anode side first. Processing temperatures did not exceed 120 °C which is favourable for potential scale-up applications and large-scale production by minimising the energy used.

3.5 Sample preparation

All photovoltaic devices were fabricated on to 20 mm x 15 mm float glass coated with a 100 nm pre patterned fully oxidized ITO layer, as shown in **Figure 3.3**. The ITO surface roughness was measured at approximately 1 nm RMS with a resistance of 20 Ω per square [10]. Before solution deposition, substrates were cleaned as described in **Section 3.2**. When used, a sample of PEDOT:PSS solution was decanted from the storage container situated in the fridge and warmed slowly to room temperature. If the solution was not first warmed before deposition a visible reduction in surface coverage was noticed, as well as the appearance of small comets of material. PEDOT:PSS was chosen for its ease of use and low processing temperatures [11,12] and was filtered through a 0.45 μm polyvinylidene fluoride (PVDF) filter before deposition. While still at room temperature, PEDOT:PSS was then spin coated forming a typical layer thickness in the range of 30 – 35 nm and subsequently annealed for 15 minutes at 120 °C. PEDOT:PSS was first spin coated and annealed in air (30 RH%) with some experiments utilising an identical secondary annealing step inside the glovebox to ensure a moisture-free film [13].

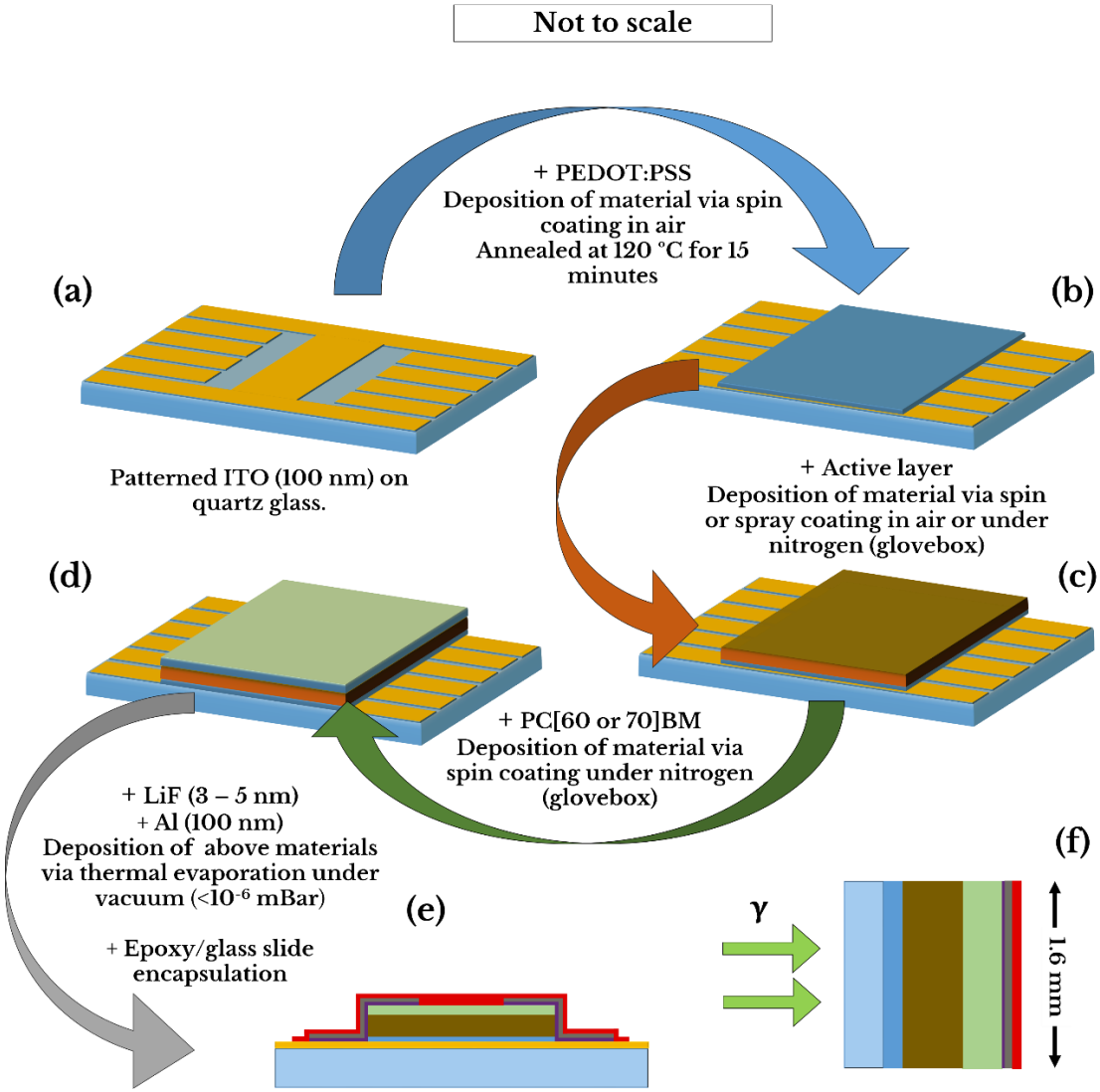

Figure 3.3 - Schematic representation of a typical PV device fabrication routine used with both perovskites and OPVs. The individual arrows are a guide to the 5 stages of fabrication and images (a-e) have been shown after solvent swabbing of excess material to expose the ITO contact. (a) The quartz/ITO substrate after cleaning. (b) After spin-coating of PEDOT:PSS layer in air (c.a. 30 nm). (c) Deposition of active layer via spin or spray coating in air or under nitrogen (70 – 500 nm). (d) Spin-coated layer of PCBM under nitrogen (70 – 150 nm). (e) Post-thermal evaporation of top contacts using LiF (3-5 nm) or BCP (5 nm) and Al or Ag (100 nm) under high vacuum (<10^{-7} mBar) and encapsulated with an epoxy resin/glass slide combination for increased moisture stability. (f) Active area slice from the device shown in (e) indicating one side of the pixel area (≈ 0.025 cm^2). Green arrows have been added to indicate the direction of incident simulated AM1.5 light. During OPV fabrication parts (c) and (d) are combined with the active layer deposited from a bulk heterojunction precursor solution.

Variations in the film thickness could be caused by several factors, including insufficient filtering and solution warming as well as temperature and humidity fluctuations. Once annealed, the active area was deposited either in air or in a N_2 glovebox. PCBM was then solution processed via spin coating completing the n-i-p junction. Electrical contact between the p-type semiconductor and ITO was done by thermal evaporation under high vacuum (see **Figure 3.3 (e)**). To deposit cathode contacts, substrates were first transferred to the glovebox and loaded on to an evaporation mask. The evaporation mask used to fabricate photovoltaic devices was designed to deposit 6 or 8 contacts depending on the ITO substrate, each creating a pixel having an active area of 2.5 mm^2. The loaded mask was then inserted in to a thermal evaporation chamber and evacuated to a pressure of approximately 10^{-7} mbar. Evaporated films of Lithium fluoride (LiF), bathocuproine (BCP), Silver (Ag) and Aluminium (Al) were used throughout this thesis. LiF and BCP were deposited at a rate of 0.1 Å/s to form a layer of approximately 3 nm and Al or Ag at a rate of 1 Å/s forming a 100 nm thick layer.

3.5.1 Perovskite and organic photovoltaic device fabrication

To deposit the perovskite active layer, ITO / PEDOT:PSS substrates were typically spun at 3000 rpm for 30 seconds whilst dynamically depositing 60 µL of perovskite solution. For most experiments, the solution was maintained at 70°C with substrates heated to 90°C before deposition. This process is known as "hot-casting" and has been shown to cause preferential orientation of perovskite crystal structures. Immediately following spin coating, 'wet' perovskite films were annealed at a temperature of 90°C for a typical time of 90 minutes, either in air or inside a N_2 glovebox. Film thicknesses and surface roughness were determined post-annealing using a Dektak surface profiler. In cases where the perovskite active layer was annealed inside a N_2 glovebox, degradation could occur between first air-exposure and final profilometry measurement. However, no visible film degradation was observed before or after determining the thickness and roughness properties, thus the values quoted throughout this thesis are representative of the final films used within photovoltaic devices. Once annealed, perovskite samples

were then cooled to room temperature before a final film of $PC_{70}BM$ was dynamically deposited on top of the active layer creating a film thickness of approximately 100-150 nm. After spin coating $PC_{70}BM$ samples were then placed inside a thermal evaporation chamber ready for cathode deposition, as described in **Section 3.5**. For OPVs, the preparation of the ITO / PEDOT:PSS substrate, polymer:PCBM and cathode layers is identical to that of the perovskite devices mentioned above and shown in **Figure 3.3**. Once cooled to a normal N_2 glovebox operating temperature (23°C), ITO/PEDOT:PSS substrates were typically spun at 1000 rpm during solution deposition. After spin coating, films were annealed at 60°C for 5 minutes to remove any excess solvent left in the films forming an approximate 70 nm active layer film.

3.6 Processing Conditions

When processing solutions and thin-films in air the temperature of the laboratory was fixed at 22°C, with humidity controlled over a range of 30±5 RH%. This humidity control was especially crucial when depositing perovskite solutions and hot-plate annealing the resultant 'wet' films. Processing under nitrogen was done using a glovebox system. The average H_2O and O_2 sensor readings were in the range of 0.1 – 0.9 ppm. To thermally evaporate a top contact onto a device, substrates were placed inside an evaporation chamber situated within the glovebox. This greatly improved the ease of fabrication and reduced processing times. By eliminating the exposure of samples to the ambient atmosphere, it ensured samples were more phase-pure and stable before the evaporation process.

3.7 Thin-film characterisation

The work presented in this thesis was carried out on thin-film semiconductors. In **Chapters 4**, *5* and **6**, characterisation of specific thin-films was undertaken to understand the crystal structures and photoluminescence properties of organic and perovskite thin-films. In this section, a brief overview of the characterisation techniques used is discussed.

3.7.1 Surface profilometry

Atomic force microscopy (AFM) is a topographical mapping technique that relies on a small tip (several nm in size) at the end of a cantilever that moves across the surface of a sample. A technique known as tapping mode, oscillates the cantilever close to its resonant frequency and records the tip making contact with the sample surface at maximum displacement. Variations in the frequency of the cantilever are recorded by a reflected laser beam focused on to a 4 quadrant photodiode (see **Figure 3.4**). A feedback loop established between the photodiode and the cantilever housing maintains a constant amplitude by changing the height of the tip. These changes in position are recorded at each predetermined interval and then used to build a topographical profile of the sample surface. In **Chapters 4** and **6** an AFM was used to map the surface of a sample in 3D by taking multiple line-profiles of the surface within a designated area using a raster-scan system.

A Veeco Dektak surface profiler which measures the vertical displacement of a stylus in contact with a surface was used for all film thickness and surface roughness measurements. The line profiles are then used to accurately determine the depth and surface contour to enable effective planarization in a device stack. Before Dektak measurements, samples were first scored in straight lines across the film. After scratching, the films were then blown using a nitrogen gun to remove any excess material from the surface.

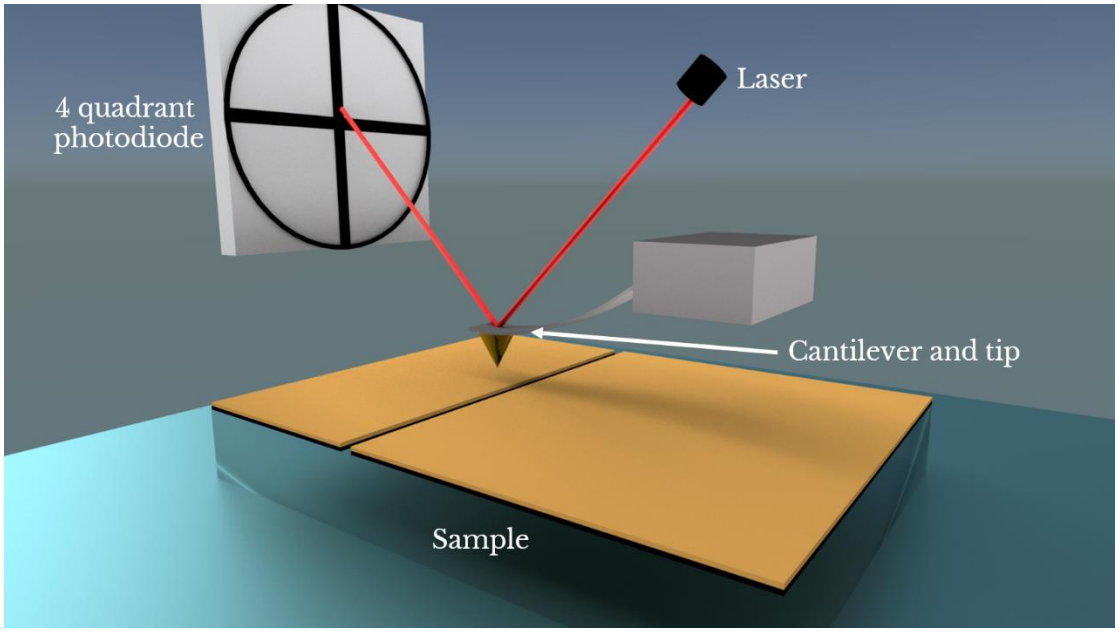

Figure 3.4 - Schematic representation of the atomic force microscope (AFM). The cantilever is attached to a rigid body on the machine housing and scanned in straight lines across a film. Small variations in the amplitude of the cantilever-tip is detected through a displacement of the laser spot on a photodiode.

A minimum of 3 profiles was taken per sample and the values quoted throughout this thesis are the mean scratch depth and standard deviations from those line profiles. For surface roughness measurements, the same line profiles were used except a root-mean-square (RMS) value was determined between scratched regions of the film. Again, the RMS values quoted in this thesis have been calculated from a minimum of 3 line profiles. The importance of determining film thickness and roughness was critical in optimising solar cell performance. Planarising films could only be done once a pre-layer roughness was determined. If a thin-film had an RMS roughness of, say, 40 nm, the next layers (typically electron-blocking) would have to be thicker than 40 nm to effectively planarise it and reduce the chances of forming a Schottky junction [14].

Scanning electron microscopy (SEM) is an imaging technique in which high-energy electrons are focused on to a small area of a target sample. Electrons are first produced

inside an electron gun, usually from a tungsten wire or lanthanum hexaboride (LaB_6) crystal source [15] and are then allowed to exit through a small slit in the housing. Below this slit is positioned an anode which attracts the electrons away from the filament. This is combined with a lens that allows the electron beam to be focused down on to the sample. The electron beam energy used throughout this thesis was between 1 and 5 keV and the gun chamber was held at a pressure of around $<10^{-9}$ mBar. The sample chamber was pumped down to at least 10^{-6} mBar before imaging. High vacuum is required because gas particles within the chamber are able to scatter the incident electron beam. SEM images and energy-dispersive X-ray spectroscopy (EDX) analysis were collected using an FEI Nova NanoSEM 450, FEI Inspect F50 or a JEOL SEM.

Once focused, the electrons interact with the sample surface in a multitude of ways, creating products such as backscattered electrons (BSE), secondary electrons (SE) and characteristic X-rays used for EDX. SEs are produced as an ionisation product after the primary electron beam interacts with the sample and are used mainly for topographical information. BSEs are produced when electrons are scattered off atoms in the material, allowing for a deeper penetration depth and increased sensitivity to the atomic mass of the scattered nuclei. For EDX, the primary electron beam ionises the target atom leaving a vacancy or 'hole' on the core shell. An electron from the outer shell of the target atom then fills in the vacancy, releasing excess energy by emitting a characteristic photon of known energy. In **Chapter 6**, EDX is used to determine the chloride content within perovskite thin-films containing a non-stoichiometric excess of MAI.

3.8 Spectroscopy

This thesis reports on two specific semiconductor systems; conjugated-polymers and perovskites. A variety of spectroscopic techniques are employed such as optical absorption and photoluminescence in both steady-state and time-resolved configurations (SSPL and TRPL, respectively). All UV-Visible absorption measurements presented in this thesis were taken in The Department of Physics & Astronomy, The

University of Sheffield. Photoluminescence experiments were also performed in Sheffield with the exception of data presented in **Chapters *5* & 6**, whereby low-dimensional perovskite thin-films required a more sophisticated setup with fluence and temperature controls provided by the Department of Physics & Astronomy, The University of Southampton.

3.8.1 UV-Visible Absorbance

The light absorption mechanism of perovskite and polymer:fullerene thin-films is covered in **Section 2.8.1**. UV to visible (UV-Vis) spectra were determined through the change in transmission of light from a deuterium/tungsten-halogen lamp (Ocean Optics – DH-2000-BAL), using collection fibre-optic cables (Ocean Optics) in series with a spectrometer (Ocean Optics – HR2000+ES). For all measurements, samples were placed in an Oxford Instruments Drystat, with temperature being controlled between room temperature and 4 K in typical intervals of 10 K. All measurements were performed under low-vacuum ($<10^{-3}$ mBar). A reference was obtained for the sample by first measuring a UV-Vis spectrum of the substrate (and appropriate base layers), as well as a reference spectrum obtained from the light source represented as I_0 in **Equations 2.12** and **2.13**. In **Figure 3.5**, the UV-Vis light source is shown as a bright white column, focused towards the sample using an array of lenses. The transmitted beam (blue) is first collimated and then focused onto a collection fibre-optic cable that is connected to a spectrometer.

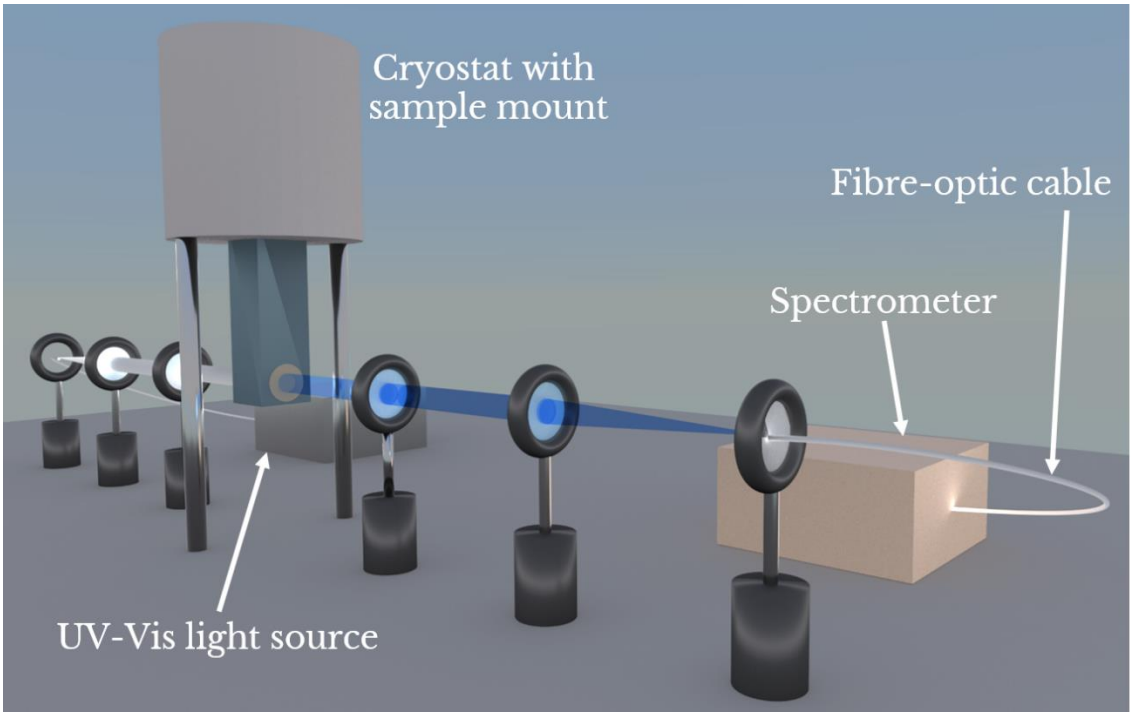

Figure 3.5 - Schematic of the temperature-dependant absorption setup. The transmission from the sample is marked in blue. The reference spectrum is produced from a deuterium/tungsten-halogen lamp that can be seen at the rear to the left. Light produced from this lamp is then sent down a fibre-optic cable (seen to the left of the figure).

3.8.2 Steady-state and time-resolved photoluminescence

Both SSPL and TPRL are processes that involve illuminating a sample with a laser having an energy greater than the material bandgap. The luminescence produced from the sample is then collected and directed to a detector. SSPL and TRPL are routine tools in the characterisation of semiconducting films, giving insights in to quenching effects and charge carrier lifetimes, respectively [16,17].

In **Chapters 4**, *5* and **6**, where SSPL was performed at The University of Sheffield, the emission of perovskite films were characterised as a function of temperature using a 405 nm laser-diode (power ≈ 1 mW). The experimental setup is detailed in **Figure 3.6**, which shows a similar experimental geometry to the UV-Vis apparatus. This was designed to

be able to collect information regarding the transmission and emission properties of the sample at a given temperature on the same sample. In practice, absorption and SSPL measurements are performed independently at the same temperature using the same focusing lenses and spectrometer. Luminescence was collected using a fibre-optic cable and transmitted to an Ocean Optics CCD spectrometer. As with absorption measurements, samples were placed in an Oxford Instruments Drystat with temperature controlled between 300 K and 4 K. In **Chapter 6**, SSPL measurements of mixed-phase low dimensional perovskite films were taken at the Department of Physics and Astronomy, University of Southampton using the experimental setup shown in **Figure 3.7**. The excitation repetition rate was set to 800 kHz using a power between 0.4 and 200 μW.

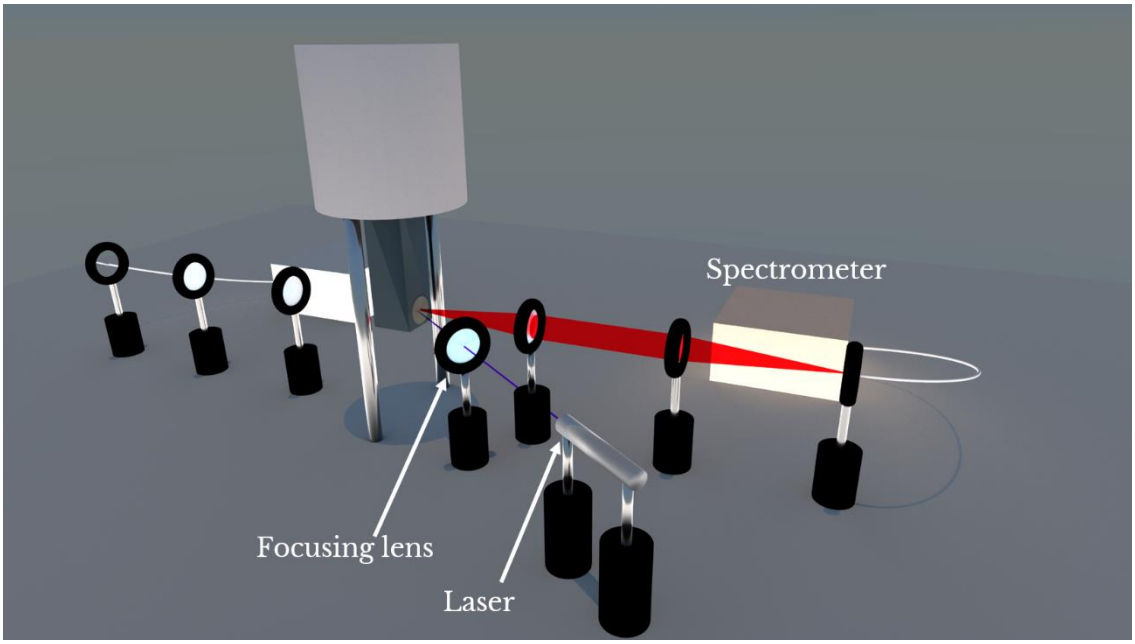

Figure 3.6 – The apparatus used for temperature-dependant steady-state photoluminescence (SSPL) measurements. Typically, SSPL data was taken in parallel with the absorption data from the same sample. As shown above, the UV-Vis light source is off (using a shutter) to allow the PL emission (shown in red) to be sent to the spectrometer on a different collection channel.

In TRPL, a sample is excited with a short laser light pulse, with the resultant emission spectrum recorded as a function of time. TRPL was performed at the Department of Physics and Astronomy, University of Southampton, U.K., using a time-correlated single photon counting (TCSPC) technique on a home-made setup shown in **Figure 3.7**. Here, samples were placed in an APD Cryogenics DMX helium cryostat, with 405 nm laser pulses (having width of 140 fs at a repetition rate of 4 MHz and fluences from 0.75 nJ cm^{-2} to 377 nJ cm^{-2}) provided by a Coherent Chameleon Ultra Ti-Sapphire laser system used to excite the film. The emitted PL was first monochromated using a Bentham M300 single monochromator and then detected using a single photon counter APD detector. The estimated temporal resolution of the TCSPC system is ≈ 300 ps. For both SSPL and TRPL performed at the University of Southampton the diameter of the laser spot on the surface of the sample was approximately 130 µm.

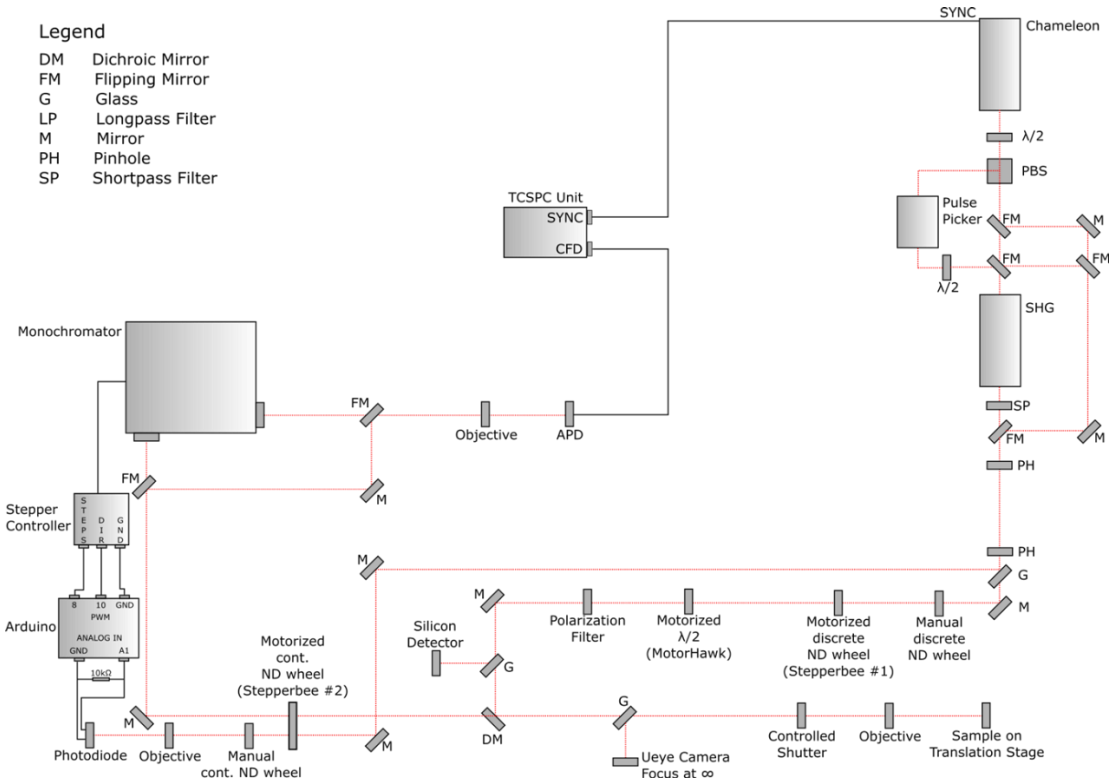

Figure 3.7 - Schematic of the apparatus used at the Department of Physics & Astronomy, University of Southampton. Image courtesy of Giacomo Piana.

3.8.3 Photoluminescence excitation

To investigate energy-transfer processes within the perovskite thin-films in **Chapter 6**, PL emission intensity over the spectral-range 520-800 nm was recorded while the excitation wavelength was scanned between 455 and 705 nm in 2 nm increments. Here, the excitation was provided by light from a Fiannium supercontinuum laser that was filtered using a SPEX monochromator (FWHM = 1.5 nm). Emission was then recorded using an Andor 303i CCD spectrometer, with samples being mounted in a cold-finger nitrogen cryostat. The sample chamber was evacuated to a pressure of at least 10^{-3} mBar before measurements began. A spectrum was then obtained at 77 K and room temperature.

3.8.4 Dynamic light scattering

In **Chapter 5**, the particulate size in a perovskite precursor was measured as a function of the concentration of hydroidic acid (HI) as a solution additive. By performing dynamic light scattering (DLS), the average diameter of the particles in solution could be examined with varying HI concentration, shedding light on the solubility issues for the perovskite precursor material $PbCl_2$. In DLS, a sample solution was exposed to a continuous laser beam where the fluctuations of the laser signal are measured at a known angle (θ) by a photon detector behind the sample. For the experiments performed in **Chapter 5**, a fixed angle θ was used to determine the mean particle size. This technique measures the diffusion of particles moving under Brownian motion, and converts this a size distribution using the Stokes-Einstein relationship:

$$D_h = \frac{k_B T}{6\pi\mu D_t} \tag{3.3}$$

where D_h is the hydrodynamic diameter, k_B is Boltmann's constant, T is the sample temperature, μ is the dynamic viscosity and D_t is the translational diffusion coefficient. **Equation 3.3** above assumes a liquid with a low Reynolds number. The velocity at which

particles move in solution due to Brownian motion is defined by the translational diffusion coefficient (m^2s^{-1}). Comparing the light intensity between small time intervals, a solution of larger particles will result in the correlation of the signal taking longer to decay than that of a solution of smaller particles [18], as smaller particles move more rapidly in the same solvent. This is known as the photon auto-correlation function and describes the velocity of Brownian motion for particles in solution (D_t), the measured parameter in DLS. Perovskite precursor ink solutions were prepared under representative conditions discussed in **Section 3.3.1** above and analysed using a Malvern Zetasizer NanoZS instrument. The collected data was averaged over three consecutive measurements of ten runs each at a temperature of 25°C.

3.8.5 X-ray diffraction

X-ray diffraction (XRD) experiments have been widely used to characterise the crystal properties of a range of semiconducting thin-films and solution blends including those used in photovoltaics [19–24]. The elastic scattering of X-rays from periodic crystal planes allows measurements to be made with length-scale resolutions of Angstroms to several nanometers. As shown in **Figure 3.8**, incident X-rays of energy E_0 interact with a sample in a given volume of material. Several interactions can occur between the X-rays and the crystal lattice of atoms. The first and most crucial is that of coherent scattering, also known as Thompson scattering [25]. Here, incident photons of energy E_0, which is relatively small compared to the ionisation energy of the target atom, elastically scatter with atomic electrons with no phase change or energy loss. This causes a simple scattering of the photons direction that remain at an energy E_0 and in phase. Another mechanism, in which the electron absorbs some of the energy E_0 but still scatter the incident photons is called incoherent or Compton scattering [26]. In this case, the photon is able to partially transfer energy to the electron, however in doing so reduces its final energy, E_1, such that $E_1 < E_0$ and also induces a phase change. Fluorescence from the sample can occur when incident energy E_0 is able to eject a K-shell electron, leaving a 'hole' that is then filled by a cascading electron from an outer shell. In doing so, the

excess energy is released as a characteristic photon. Energy transfer can also arise between inner and outer shell electrons, after which the outer shell electron is promoted to a vacuum level and ejected as an Auger electron.

In **Chapters *5*** and **6**, perovskite thin-films were subject to experiments designed to probe the crystallographic properties of post-annealed films. Two main experiments were used, that of 1D X-ray diffraction (XRD) and glancing-incidence wide-angle X-ray scattering (GIWAXS). The former, which involves a 1D detector to measure the scattered X-ray counts as a function of angle subtended from the sample, is used to detect small changes in the unit cell parameters of the perovskite crystal.

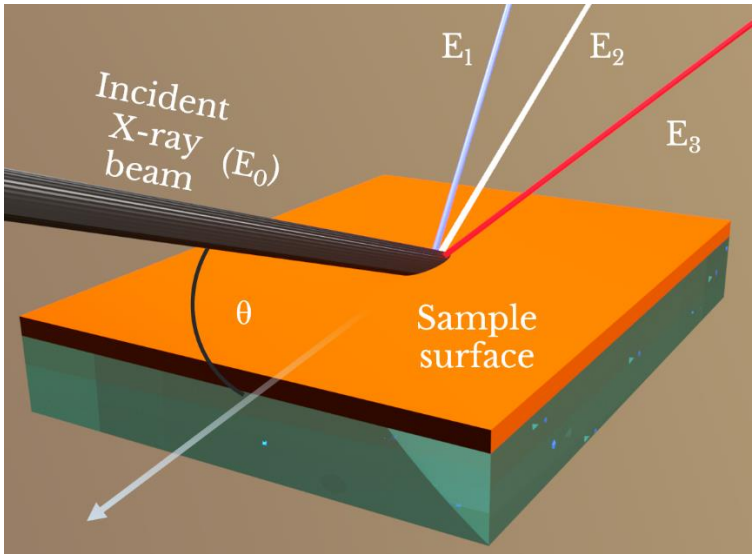

Figure 3.8 – Representation of the different scattering products obtained from X-ray diffraction experiments. The incident beam with energy E_0 scatters off the material within a characteristic penetration depth, producing non-elastic products (Compton scattering (E_1) and fluorescence (E_3)) and coherent Thompson scattering ($E_2 = E_0$).

For XRD measurements performed in **Chapter *5***, the θ-2θ geometry was used whereby a sample is positioned such that the surface is facing perpendicular to the direction of

the incoming X-ray beam. The incident X-rays scatter off periodic crystal planes according to the Bragg diffraction law as follows [27]:

$$2dsin(\theta) = n\lambda \tag{3.4}$$

where d is the distance between repeating crystal planes, θ is the scattering angle, n is a positive integer and λ is the wavelength of the incident light.

The sample is then rotated slowly, changing the angle (θ) to the direction of the beam, where θ = 90° corresponds to the sample surface being perpendicular to the beam as shown in **Figure 3.9 (b)**.

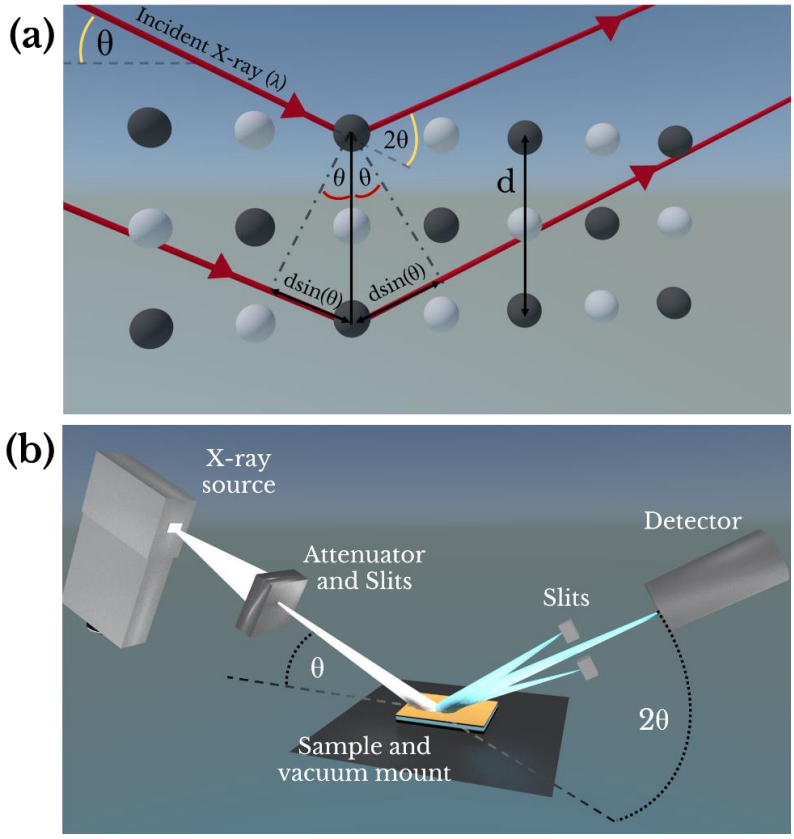

Figure 3.9 – (a) An illustration of Bragg's law displaying parallel X-rays scattering off a crystal lattice. (b) Visual representation of the XRD apparatus used in **Chapter 5**. The sample on the vacuum mount changes the angle of incidence (θ) and the detector maintains the angle 2θ. The X-ray source with attenuator and slits is fixed in place during the experiment. The scattered X-ray intensity is measured as a function of the angle 2θ.

The coherent X-rays are then collected in a detector as it scans across the angle 2θ. The detector runs moves around angle 2θ in typical steps of 0.02° with an integration time of 0.2 s per step. The scan range for the XRD measurements were usually made between 5 and 40° (2θ) with the exception of the LDP perovskites (**Chapter 6**), which require smaller angle detection due to the large d-space values.

GIWAXS uses the same diffraction mechanism as 1D XRD but instead measures the scattered X-rays across a 2D detector. By using a 2D detector, the scattering vector of the coherent X-rays, Q_i, can be determined in the x,y and z directions. GIWAXS was performed in a similar geometry to that of XRD with the addition of a secondary dimension for detecting the angular dependence of the scattered X-rays. This additional dimension, allows information to be gathered about the orientation of the repeating crystals relative to the plane of the substrate. **Figure 3.10 (a-c)** demonstrates the scattering of X-rays with initial wavevector k_i incident on a sample such that $k = 2\pi/\lambda$. The X-ray scatters off the sample at a certain angle (2θ) with a resulting wavevector k_0. The momentum transfer $\vec{Q}$, is defined as the change in k, such that

$$\vec{Q} = \vec{k_0} - \vec{k_i} \tag{3.5}$$

where $\vec{Q}$ is a vector in reciprocal-space and both $\vec{Q}$ and $\vec{k}$ have units of inverse distance. The maximum $\vec{Q}$ is the elastic condition where $k_i = k_0 = 2\pi/\lambda$, and hence the locus of possible scattering vectors in 3 dimensions is defined as the surface of a sphere (termed the Ewald sphere) with a diameter $\vec{Q} = 4\pi/\lambda$. The detector records all signals where the reciprocal-space and the Ewald sphere intercept such that

$$\vec{Q} = Q = \frac{4\pi}{\lambda}\sin\theta \tag{3.6}$$

The reciprocal-space is the Fourier transform of a real-space structure, and the peaks observed in reciprocal-space correspond to a repeat spacing in real-space. Q is related to the real-space spacing (d) such that $Q = 2\pi/d$. This is shown in **Figure 3.10 (d)**, where $\vec{Q}$ is displayed on a detector in Q-space which is directly related to the interplanar-spacing, d.

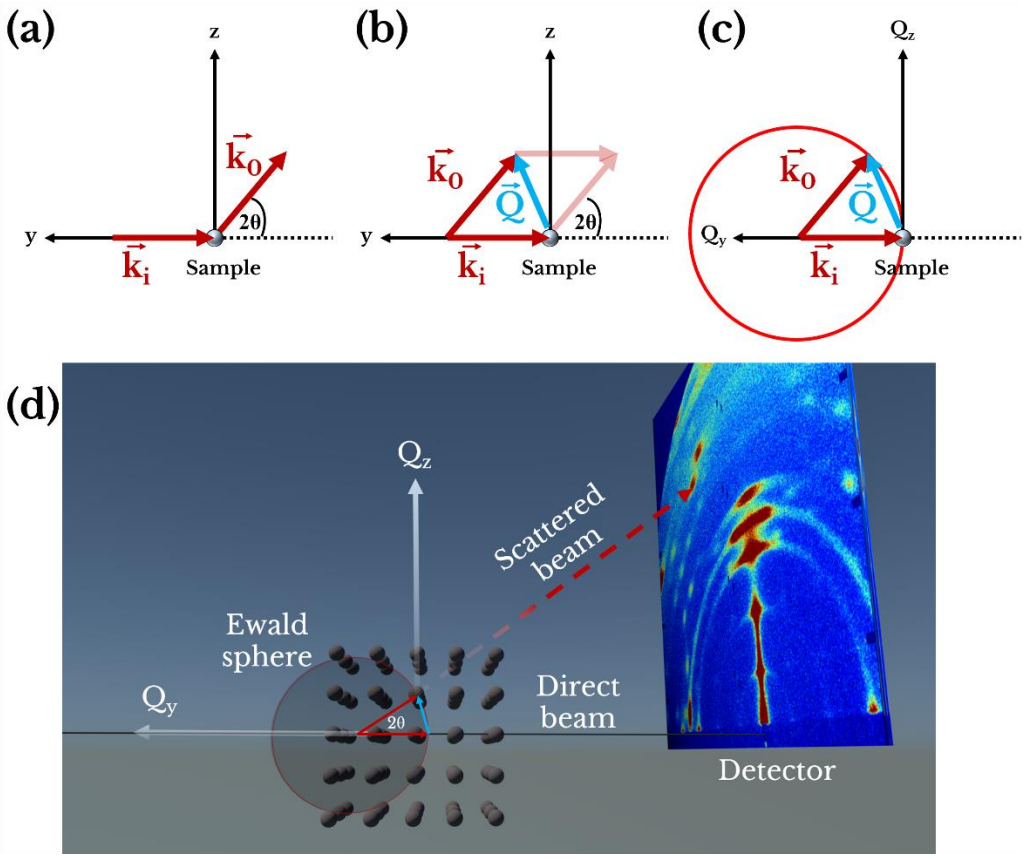

Figure 3.10 - (a-c) Schematic showing the formulation of a Ewald sphere (seen in 2D) which demonstrates the relationship between the diffraction angle (2θ), the wavevector for the incident (k_i) and diffracted (k_0) X-rays and the reciprocal lattice of the crystal vector (Q). In reality, Q has components in all x-, y-and z- axis. (d) 3-dimensional (3D) representation of the Ewald sphere applied to a crystalline sample with a representative detector image. The Q_x axis is directed in to the page. The red and blue arrows in part (d) represent the initial and final wavevectors and Q, respectively.

Scattering features on the detector which lie in the Q_z plane only indicate repeated-planes growing preferentially out of the plane of the substrate. Likewise, scattering detected in the Q_{xy} planes are a result of crystal planes grown perpendicular to the substrate. A summation of identical crystal planes grown with no preferred orientation will appear as a semi-circle on a 2-dimensional (2D) detector, as shown in **Figure 3.10 (d)**. For GIWAXS measurements presented in this thesis, a sample was placed inside a

Kapton-sealed chamber that was pumped down to a pressure < 10^{-3} mBar. Here, scattered X-rays with a wavelength λ = 1.34114 Å were imaged on to a 2D detector (Pilatus 1M) in both Q_{xy} and Q_z. For perovskite measurements, the sample was angled at 0.3° below the horizon, creating an X-ray penetration depth of approximately 150 nm [28]. In **Chapter 4**, polymer samples were subject to the same experimental conditions at an incident angle of 0.16° below the horizon to ensure a good penetration depth. Measurement integration times were set to 5 minutes and no visible beam damage was present after collecting data. Unless stated otherwise, samples imaged under GIWAXS have been encapsulated using PMMA from a solution in toluene (50 mg/ml).

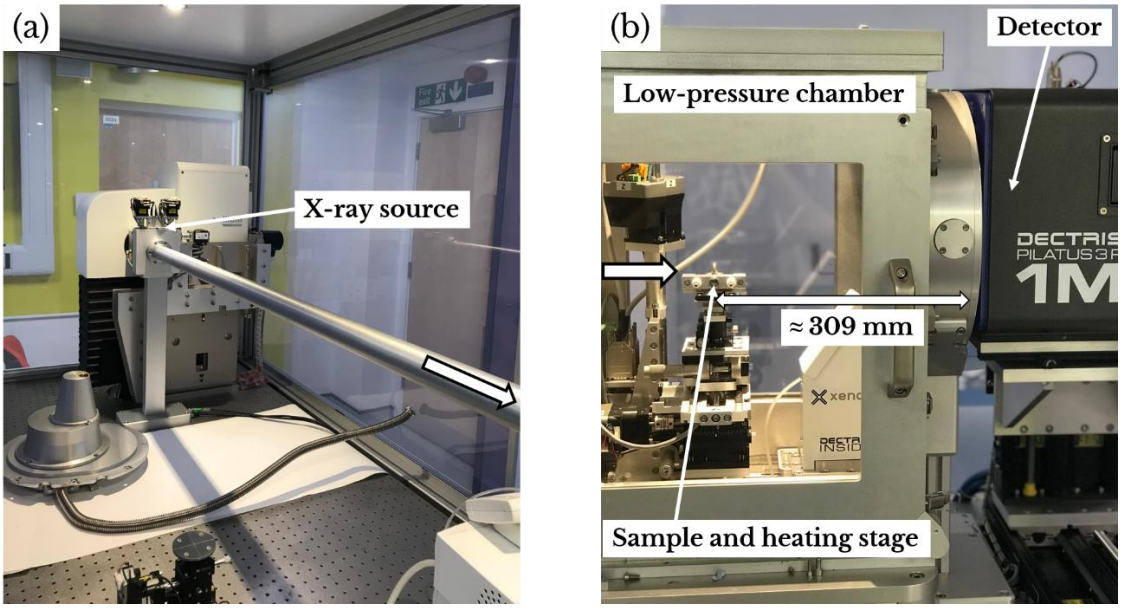

Figure 3.11 – Photographs of the experimental apparatus used for glancing-incidence wide-angle X-ray scattering (GIWAXS) in the Department of Chemistry, University of Sheffield. (a) X-rays are produced and sent down a collimation tube towards the sample chamber (white arrow indicates X-ray direction of travel). (b) The narrow X-ray beam enters the low-pressure chamber incident on a sample that is mounted on a heated tilt stage at a pre-determined angle below the horizon. The scattered X-rays are collected on a 2-dimensional (2D) detector at a sample-to-detector distance of approximately 309 mm.

The sample-to-detector distance was chosen to be 309 mm and gives a corresponding 'Q-space' detection range of approximately 0.1 – 2.5 $Å^{-1}$ (63 Å – 2.5 Å in d-space).

3.9 Photovoltaic device characterisation

The method for characterising encapsulated PV devices was the same for both perovskites and OPVs. Following the fabrication routine described in **Sections 3.3** and **3.5**, devices were removed from the glovebox into the ambient atmosphere of the cleanroom. Devices were then placed in to a push-fit test board that was designed to operate with the pre-patterned 8-pixel ITO substrates. Before any J-V measurement, a shadow mask was placed on top of the glass-facing side of the device to effectively create 8 – 0.025 cm^2 pixels. A Newport 92251A-1000 solar simulator was used to produce a simulated AM1.5 solar spectrum which was calibrated using an NREL certified silicon reference cell (100 $mWcm^{-2}$ at 25 °C). PCEs were determined for a cell initially held at -0.2 V, swept to +1.2 V and back to – 0.2 V a rate of 0.2 V s^{-1}.

3.10 References

1. Hu, T. *et al.* Effect of UV–ozone treatment on ITO and post-annealing on the performance of organic solar cells. *Synth. Met.* **159**, 754–756 (2009).
2. Lee, K. H., Jang, H. W., Kim, K.-B., Tak, Y.-H. & Lee, J.-L. Mechanism for the increase of indium-tin-oxide work function by O2 inductively coupled plasma treatment. *J. Appl. Phys.* **95**, 586–590 (2004).
3. Noel, N. K. *et al.* Unveiling the Influence of pH on the Crystallization of Hybrid Perovskites, Delivering Low Voltage Loss Photovoltaics. *Joule* **1**, 328–343 (2017).
4. Lee, S.-W. *et al.* UV Degradation and Recovery of Perovskite Solar Cells. *Sci. Rep.* **6**, 38150 (2016).
5. Sahu, N., Parija, B. & Panigrahi, S. Fundamental understanding and modeling of spin coating process: A review. *Indian J. Phys.* **83**, 493–502 (2009).
6. Marinova, N. *et al.* Light Harvesting and Charge Recombination in $CH_3NH_3PbI_3$ Perovskite Solar Cells Studied by Hole Transport Layer Thickness Variation. *ACS Nano* **9**, 4200–4209 (2015).

7. Liu, D., Gangishetty, M. K. & Kelly, T. L. Effect of $CH_3NH_3PbI_3$ thickness on device efficiency in planar heterojunction perovskite solar cells. *J. Mater. Chem. A* **2,** 19873–19881 (2014).

8. Tay, F. E. H. Self-Assembled Monolayers (SAM) for Tunneling Sensors *Materials & Process Integration for MEMS.* **9,** 113-132 (2002).

9. You, J., Meng, L., Hong, Z., Li, G. & Yang, Y. in *Organic-Inorganic Halide Perovskite Photovoltaics* 307–324 (Springer International Publishing, 2016).

10. Mohamad, D. K., Griffin, J., Bracher, C., Barrows, A. T. & Lidzey, D. G. Spray-Cast Multilayer Organometal Perovskite Solar Cells Fabricated in Air. *Adv. Energy Mater.* **6,** 1600994 (2016).

11. Li, Y. *et al.* High-efficiency robust perovskite solar cells on ultrathin flexible substrates. *Nat. Commun.* **7,** 1–10 (2016).

12. Chae, J., Dong, Q., Huang, J. & Centrone, A. Chloride Incorporation Process in $CH_3NH_3PbI_{3-x}Cl_x$ Perovskites via Nanoscale Bandgap Maps. *Nano Lett.* **15,** 8114–8121 (2015).

13. Bracher, C., Freestone, B. G., Mohamad, D. K., Smith, J. A. & Lidzey, D. G. Degradation of inverted architecture $CH_3NH_3PbI_{3-x}Cl_x$ perovskite solar cells due to trapped moisture. *Energy Sci. Eng.* **6,** 35–46 (2018).

14. Berhe, T. A. *et al.* Organometal halide perovskite solar cells: degradation and stability. *Energy Environ. Sci.* **9,** 323–356 (2016).

15. Kowalczyk, J. M. D., Hadmack, M. R., Szarmes, E. B. & Madey, J. M. J. Emissivity of lanthanum hexaboride thermionic electron gun cathode. *Int. J. Thermophys.* **35,** 1538–1544 (2014).

16. Chen, L. *et al.* Effect of Different $CH_3NH_3PbI_3$ Morphologies on Photovoltaic Properties of Perovskite Solar Cells. *Nanoscale Res. Lett.* **13,** 140 (2018).

17. Yang, W. S. *et al.* Iodide management in formamidinium-lead-halide–based perovskite layers for efficient solar cells. *Science.* **356,** 1376–1379 (2017).

18. Stetefeld, J., McKenna, S. A. & Patel, T. R. Dynamic light scattering: a practical guide and applications in biomedical sciences. *Biophys. Rev.* **8,** 409–427 (2016).

19. Zhao, J. *et al.* Efficient organic solar cells processed from hydrocarbon solvents. *Nat. Energy* **1,** 15027 (2016).

20. Barrows, A. T. *et al.* Monitoring the Formation of a $CH_3NH_3PbI_{3-x}Cl_x$ Perovskite during Thermal Annealing Using X-Ray Scattering. *Adv. Funct. Mater.* **26,** 4934–4942 (2016).

21. Pattanasattayavong, P. *et al.* Electric field-induced hole transport in copper(i) thiocyanate (CuSCN) thin-films processed from solution at room temperature. *Chem. Commun.* **49,** 4154–4156 (2013).

22. Juraić, K. *et al.* GISAXS and GIWAXS analysis of amorphous-nanocrystalline silicon thin films. *Nucl. Instruments Methods Phys. Res. Sect. B Beam Interact. with Mater. Atoms* **268,** 259–262 (2010).

23. Parnell, A. J. *et al.* Nanoscale phase separation of P3HT PCBM thick films as measured by small-angle X-ray scattering. *Macromolecules* **44,** 6503–6508 (2011).

24. Chen, B.-A. *et al.* In Situ Identification of Photo- and Moisture-Dependent Phase Evolution of Perovskite Solar Cells. *ACS Energy Lett.* **2,** 342–348 (2017).

25. Van Der Veen, F. & Pfeiffer, F. Coherent X-ray scattering. *J. Phys. Condens. Matter* **16**, 5003–5030 (2004).

26. Christillin, P. Nuclear Compton scattering. *J. Phys. G Nucl. Phys.* **12**, 837–851 (1986).

27. Bragg, W. L. The diffraction of short electromagnetic waves by a crystal. *Proc. Camb. Philol. Soc.* (1913).

28. Alsari, M. *et al.* In situ simultaneous photovoltaic and structural evolution of perovskite solar cells during film formation. *Energy Environ. Sci.* **11**, 383–393 (2018).

Chapter 4

CPDT/DBS-based donor:acceptor copolymers for photovoltaic applications

In this chapter, the optoelectronic properties of a number of new conjugated organic polymers are studied for their use in photovoltaic (PV) devices. These donor:acceptor (D-A) materials are based on the electron-donating cyclopentadithiophene (CPDT) and dibenzosilol (DBS) moieties together with a 2,1,3-benzothiadiazole-5,6-dicarboxylic imide (BTDI) electron-accepting unit. Devices were developed using conjugated polymers in a polymer:PCBM bulk heterojunction (BHJ) system. These BH devices were compared with those based on the well documented poly[N-9'-heptadecanyl-2,7-carbazole-alt-5,5-(4',7'-di-2-thienyl-2',1',3'-enzothiadiazole)] (PCDTBT) system. Two sets of polymers were studied, CPDT/BTDI polymers which have a narrower bandgap than that of PCDTBT, and DBS/BTDI polymers which have a wider bandgap relative to PCDTBT. Theoretical modelling of the CPDT/BTDI polymers indicate a degree of delocalisation of the HOMO level along the donor units. Both CPDT and DBS-containing polymers showed a reduced absorption coefficient compared with films of PCDTBT having similar thickness. X-ray scattering studies on polymer:PCBM (1:3 by weight) blends indicate the presence of an amorphous mixture of polymer:PCBM with no preferred in- or out-of-plane molecular orientation.

4.1. Introduction

Organic semiconductors have been a hot-topic in photovoltaic research since the discovery of the BHJ made by Yu et al in 1995. Here, the authors fabricated a photo-

active layer comprised of a p-phenylene-vinylene (PPV) derivative mixed with the fullerene PCBM, that were spin-cast from the same solution [1]. The incorporation of an electron-accepting molecule within the polymer solution resulted in efficient exciton dissociation. This proved an important step due to the short exciton diffusion lengths in polymers and relatively high exciton binding energies [2]. Previous approaches, such as bilayer organic junction solar cells [3,4], utilised an electron-donating/electron-accepting polymer bilayer structure positioned between an ITO anode and a metal cathode, and initially achieved a PCE of around 1% under AM2 conditions [5]. The use of a BH requires some form of charge-selection to reduce the chances of recombination of separated holes and electrons at the interfaces. An efficient way to create a hole-selective contact is to coat a thin-layer of hole-conducting polymer poly(3,4-ethylenedioxythiophene)-polystyrenesulfonate (PEDOT:PSS) onto an ITO electrode; this simultaneously acts as an electron-blocking layer and reduces the roughness of the ITO conducting surface [6,7]. In a standard architecture device, the BH active layer is coated on top of the ITO/PEDOT:PSS bilayer, followed by sequential thermal evaporation of a hole-blocking layer and a low work-function cathode.

A widely explored organic polymer for PV applications is poly(3-hexylthiophene-2,5-diyl) (P3HT). This material is comprised of repeating thiophene units (see **Figure 4.1 (a)**) having hexyl (C_6H_{13}) side chains, and when blended with PCBM can reach a PCE in excess of 4% [8,9]. However, P3HT has an absorption onset of ≈1.9 eV (≈650 nm) [10] and consequently is not well matched to the visible solar spectrum. Significant steps have been made to optimise the HOMO and LUMO levels in polymers in order to better match the solar spectrum; one common approach is the development of donor-acceptor (D-A) copolymers [11,12]. Such molecular architectures permit greater electron delocalisation along the conjugated polymer backbone through a push-pull mechanism between D and A moieties. Such D-A copolymers also allow for systematic tuning of the energetic-bandgap through a difference in electron densities between the donor and acceptor units along the polymer backbone. By combining high-lying HOMO levels and low-lying LUMO levels, a narrowing of the bandgap can be achieved. The tuneable

nature of D-A polymers make them an attractive system for research in photovoltaic and light-emitting applications.

Another well explored D-A polymer is the material PCDTBT [13–16]. This has an absorption onset at around 1.9 eV [17] (see **Table 4.1**), with PCDTBT:PCBM BH solar cells having efficiencies reported in excess of 7% PCE [18]. The structure of PCDTBT is shown in **Figure 4.1 (g)** and comprises a 2,1,3-benzothiadiazole (BTD) electron-donor and carbazole electron-acceptor units, separated by thiophene monomers. The carbazole moiety has additional aliphatic side chains, which have been shown to improve solubility [19]. The BTD unit possesses excellent aromaticity through the 5 pairs of π-electrons [20] which act to planarise the molecular structure [21].

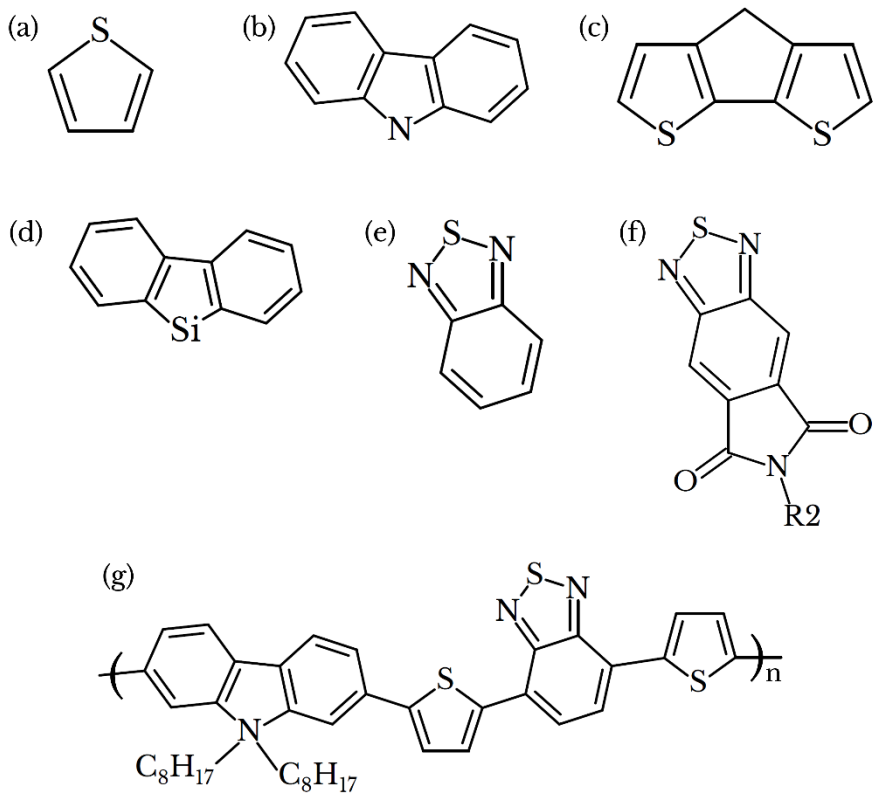

Figure 4.1 - Structures of donor and acceptor units used throughout this chapter. Here, part (a) is a thiophene unit, with (b), (c) and (d) being carbazole, cyclopentadithiophene (CDPT) and dibenzosilole (DBS), respectively. Parts (e) and (f) show 2,1,3-benzothiadiazole (BTD) and 2,1,3-benzothiadiazole-5,6-dicarboxylic imide (BTDI), respectively. Part (g) shows the donor-acceptor (D-A) repeating structure of PCDTBT.

In this chapter, four new D-A polymers are studied with the molecular structures shown in **Figure 4.2**. Polymers PCPDTDTBTDI-8,DMO and PCPDTDTBTDI-8,8 (named P1 and P2, respectively) are shown in **Figure 4.2 (a)** and **(b)**, where both P1 and P2 share the same octyl side chain attached to the CDPT electron-donor unit. The CDPT unit has been well documented in literature [22–26], with its derivatives resulting in reduced HOMO-LUMO energies and stronger intermolecular interactions [27,28]. The polymers PDBSDTBTDI-DMO and PDBSDTBTDI-8 (P3 and P4, respectively) are shown in **Figure 4.2 (c)** and **(d)**. These materials were synthesised to incorporate the DBS electron-donating moiety - another well studied donor unit [29–31]. The DBS unit has previously demonstrated improved thermal stability compared to their polyfluorene analogues [31,32]. The electron-accepting unit in all novel D-A polymers explored was chosen to be BTDI; a strong acceptor moiety [33–35]. Here, the additional side chains were modified, with polymers P1 and P3 incorporating a 3,7-dimethyloctyl (DMO) branched alkyl chain, whereas P2 and P4 contained an octyl side chain attached to the acceptor unit.

The donor polymers used in the following study were synthesised by Ary Murad (Chemistry Department, University of Sheffield). 4,4-dioctyl-2,6-dibromocyclopenta[2,1-b:3,4-b']dithiophene was copolymerised using direct arylation with 4,7-di(thien-2-yl)-2,1,3-benzothiadiazole-5,6-*N*-(3,7-dimethyloctyl)dicarboxylic and 4,7-di(thien-2-yl)-2,1,3-benzothiadiazole-5,6-dicarboxylic anhydride to produce the D-A polymers P1 and P2, respectively. This was performed using a tris(dibenzylideneacetone)dipalladium(0)-chloroform-adduct/tris(2-methoxyphenyl) ($Pd_2(dba)_3.CHCl_3$/P(*o*-MeOPh)$_3$) catalyst, caesium carbonate (Cs_2CO_3) base and pivalic acid ($C_5H_{10}O_2$) in anhydrous toluene with n,n-dimethylformamide (DMF) as a co-solvent. The P3 and P4 copolymers were synthesised *via* Suzuki polymerisation between bis-boronate esters and dibromides. The polymerisations were performed using a diacetatobis(tri-*o*-tolylphosphine)palladium(II) (Pd{P(*o*-tol)$_3$}2(OAc)$_2$) catalyst and a sodium bicarbonate ($NaHCO_3$) base in anhydrous tetrahydrofuran (THF).

HOMO and LUMO electron density calculations on PCDTBT, P1 and P2 were undertaken using density functional theory (DFT) using the B3LYP hybrid functional

on monomers and dimers. To simplify the calculations, alkyl side chains were replaced by methyl groups. The calculations were performed by Natalia Martsinovich (Chemistry Department, University of Sheffield).

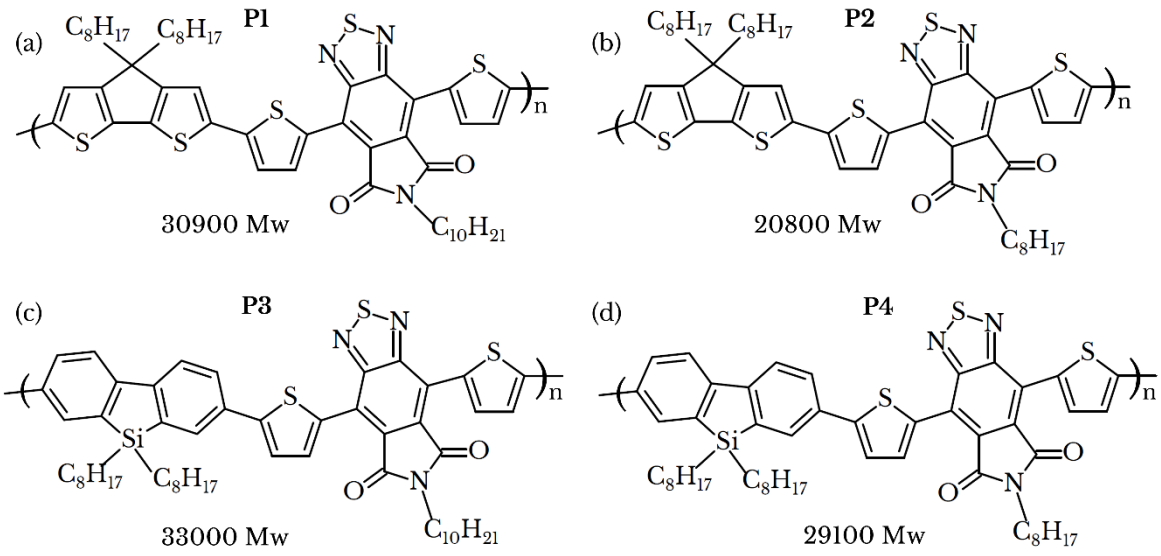

Figure 4.2 - Chemical structures of the D-A polymers used in this chapter. The letter R represents a side chain. The chemical structures for the copolymers are shown for (a) P1, (b) P2, (c) P3 and (d) P4. The average molecular weight (g mol^{-1}) of each polymer is indicated in each diagram. Note the Mw for PCDTBT used in this chapter was 34,900.

4.2. Electronic, optical and topographic properties

Before introducing experimental data, the results of theoretical modelling of the electronic properties of the materials will first be discussed. Here, quantum mechanical calculations were performed using DFT on PCDTBT, P1 and P2 only. The alkyl side chains used in both PCDTBT, P1 and P2 were substituted for methyl groups before running simulations. The resulting molecular orbitals determined are shown in

Figure 4.3. In both the monomer and dimer models for polymers PCDTBT, P1 and P2, the distribution of the HOMO and LUMO levels overlap with the BTD (PCDTBT) or the BTDI (P1, P2) acceptor unit, signifying a photo-induced electron-transfer pathway between electron donor and acceptor subunits [36]. It is worth noting that the calculations suggest that the HOMO is distributed along the polymer backbone, with partial localisation on the donor unit; a result more apparent in the calculations performed on the dimers (**Figure 4.3 (c)** and **(d)**). This result provides some evidence for the efficient push-pull characteristics of the D-A polymers and their application as a donor material [37].

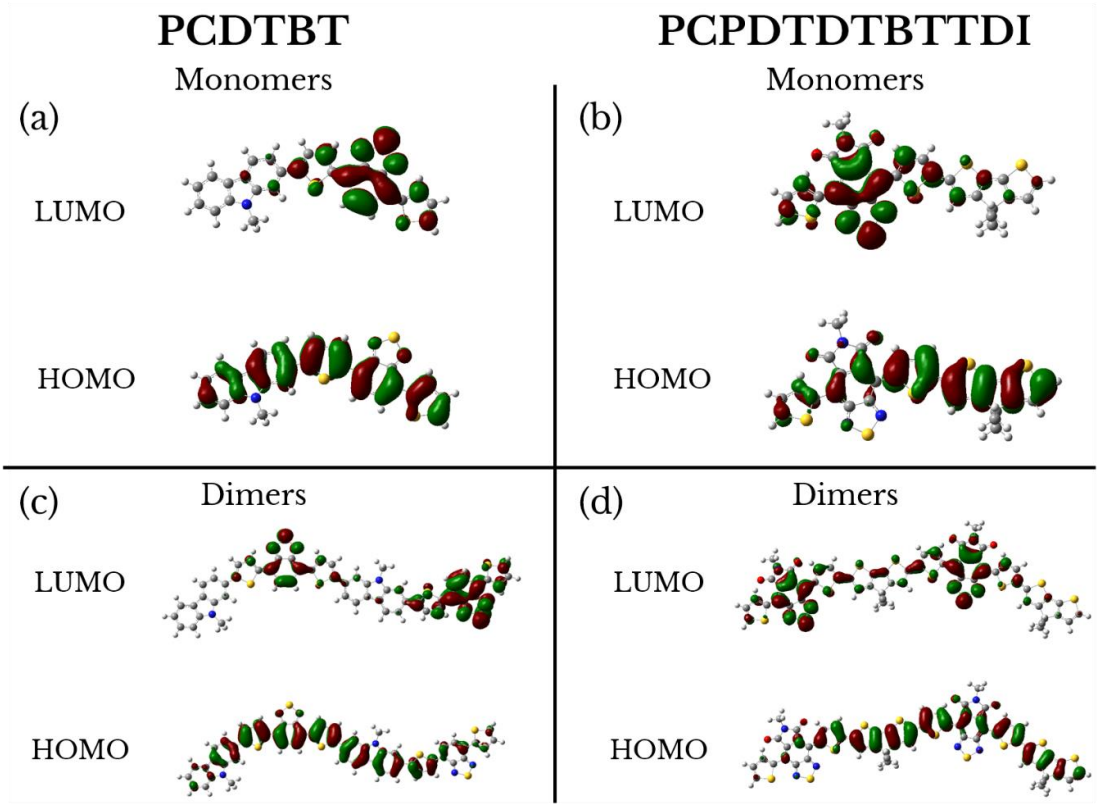

Figure 4.3 – HOMO and LUMO electron density calculations on (a), (c) PCDTBT and (b), (d) P1 and P2 provided by Natalia Martsinovich, Chemistry Department, University of Sheffield. Calculations were made using density functional theory (DFT) using the B3LYP hybrid functional on (a), (b) monomers and (c), (d) dimers. To simplify the calculations, alkyl side chains were replaced by methyl groups.

The DFT calculations suggest a LUMO density mostly confined on to the acceptor moiety for P1 and P2, which is similar to the PCDTBT orbital densities shown in **Figure 4.3 (a)**. Calculations were not performed on polymers P3 and P4, however these polymers are expected to be similar to P1 and P2 as the electron-donating unit (DBS) used in P3 and P4 results in similar electron orbital densities to those shown in **Figure 4.3 (b)** and **(d)** [29,38]**.** However, as P3 and P4 include a weaker donating moiety relative to P1 and P2, the HOMO and LUMO levels are likely to be more localised on the corresponding acceptor and donor units (due to the reduced push-pull ability), thereby increasing the electronic bandgap of the polymer [39].

To characterise D-A polymers, thin-film samples were spin-coated from a 20 mg/ml 1:1 solution of 1,2-dichlorobenzene:chlorobenzene (DCB:CB) [40] onto quartz glass to create films having a thickness of approximately 80 nm. Such films were then characterised using cyclic voltammetry, UV-Visible transmission, DekTak surface profilometry and steady-state photoluminescence (SSPL). The measured HOMO and LUMO levels are presented in **Table 4.1** were measured by Ary Murad, Chemistry Department, University of Sheffield, where the onsets of oxidation were determined from cyclic voltammograms on drop cast polymer films on platinum (Pt) as the working electrode in Bu_4NClO_4/CH_3CN (0.1 M) *vs* Ag/Ag^+ reference electrode. For more details please see reference 41.

The absorbance of all polymers when cast into thin-film, including PCDTBT and the fullerene-acceptor $PC_{60}BM$, are shown in **Figure 4.4**. Each sample was spin-coated from a room-temperature solution onto quartz substrates. After coating, films were then annealed for 5 minutes at 60˚C to remove any residual solvent. The absorbance was calculated from transmission data using the following relationship:

$$A = 2 - \log_{10}(\%T) \tag{4.1}$$

where A is the absorbance of the film and T is the transmission measured as a percentage (%). The optical properties, including relative HOMO and LUMO levels are summarised in **Table 4.1.** All polymers are characterised by two absorption peaks at both short and longer wavelengths, and cover the majority of the visible spectrum. The higher-energy peak observed in all polymers is attributed to a π-π^* transition [33,43], with the lower-energy peak associated with intramolecular charge transfer (ICT) between donor and acceptor units [33,44].

	Name	λ_{max} (nm)	λ_{onset} (nm)	E_g^{op} (eV)	E_{peak}^{Abs} (eV)	E_{peak}^{PL} (eV)	HOMO (eV)	LUMO (eV)	E_g^{elec} (eV)
	PCDTBT	393	654	1.89	2.23	1.81	-5.50	-3.60	1.90
P1	PCPDTDTBTDI-8,DMO	737	942	1.32	1.69	1.32	-5.20	-3.47	1.73
P2	PCPDTDTBTDI-8,8	725	930	1.33	1.70	1.32	-5.10	-3.44	1.66
P3	PBDSDTBTDI-DMO	387	713	1.74	2.13	1.54	-5.58	-3.46	2.12
P4	PBDSDTBTDI-8	388	705	1.76	2.13	1.81	-5.58	-3.42	2.16

Table 4.1 - Complete list of D-A polymers including thin film absorbance data. λ_{max} and λ_{onset} refer to the optical absorbance maximum intensity and absorption onset at longer wavelengths, respectively. E_g^{op} is the optical bandgap calculated from the low-energy absorption onset. E_{peak}^{Abs} and E_{peak}^{PL} are the peak absorption and peak photoluminescence (PL) energies, respectively. E_g^{elec} is the energy difference between the HOMO and LUMO levels. The HOMO and LUMO values for PCDTBT are taken from reference 48 [42].

It is immediately clear the absorption peaks corresponding to π-π* transitions occur at higher energies in polymers P3, P4 and PCDTBT than P1 and P2. The peaks associated with π-π* transitions have energies of 2.69 eV (P1 and P2) and 3.19 eV (P3 and P4). A noticeable broadening of the π-π* transition peak can also be seen in **Figure 4.4** when the DBS donor unit is used (P1 and P2). A broad absorption spectrum is important in photovoltaic applications as it will create a larger absorbing window for the incoming solar radiation. The overall absorption spectra for the polymers P1, P2, P3 and P4 shown in **Figure 4.4** are very similar with the exception of an overall red-shift seen for P1 and P2. This red-shift is likely explained by an increase in π-electron delocalisation caused by the stronger electron-donating qualities of the CPDT moiety used in polymers P1 and P2 [45]. A greater π-electron delocalisation will also improve the electron-wavefunction overlap between the CPDT (donor) and BTDI (acceptor) monomers, which has previously been observed to induce a red-shift in the steady-state absorption between 4,7-di(thien-2-yl)-2,1,3-benzothiadiazole (DTBT) and CDTBT (PCDTBT oligomers) [46,47].

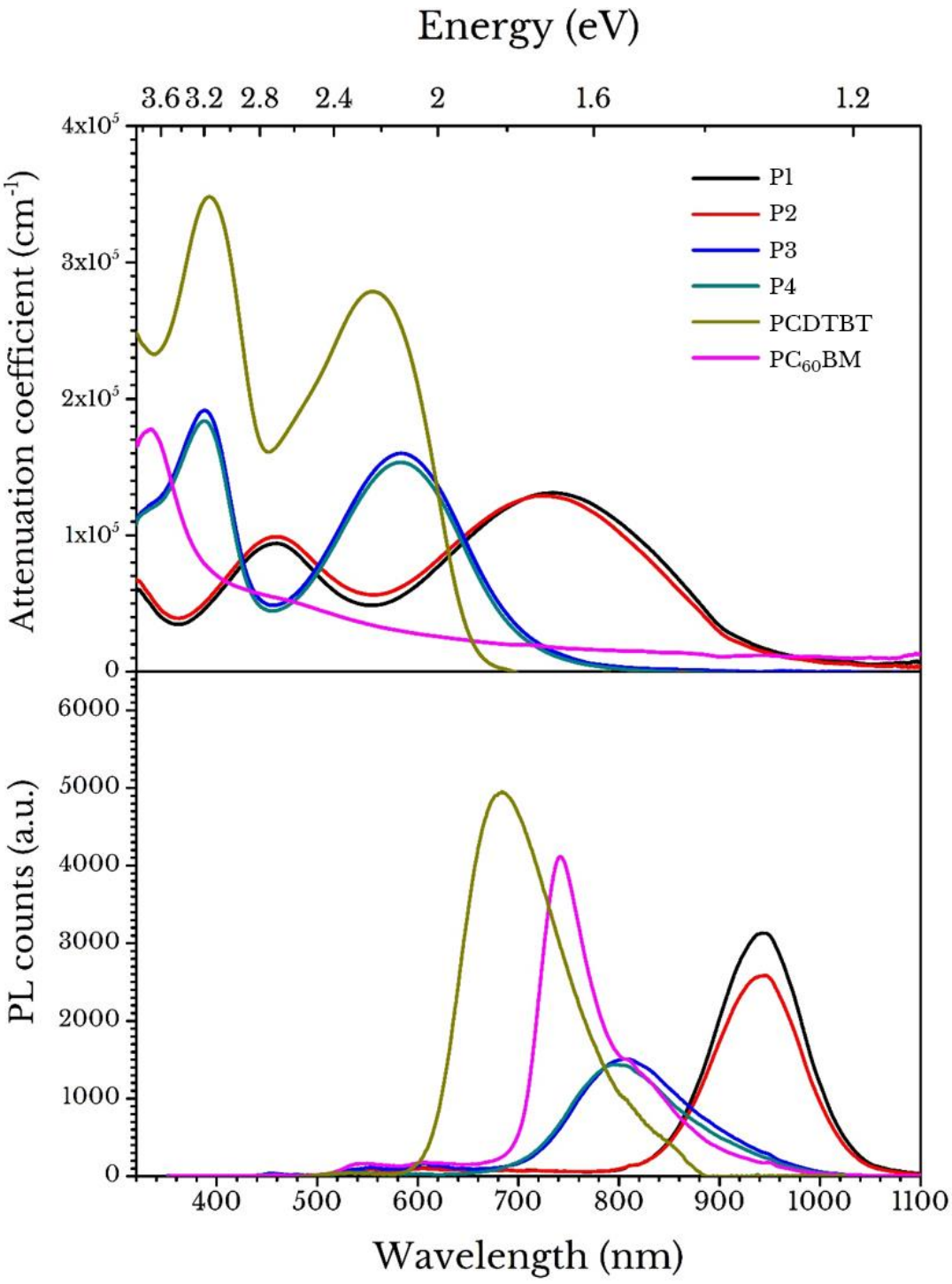

Figure 4.4 – Attenuation coefficient from polymer films (≈ 70 nm) cast from a 1:1 (CB:DCB) solvent (top) and steady-state photoluminescence (SSPL) (bottom) spectra of P1 (black), P2 (red), P3 (blue), P4 (cyan), PCDTBT (gold) and $PC_{60}BM$ (magenta). All samples shown here were spin-cast onto quartz glass. The excitation wavelength used to generate PL was 475 nm.

The absorption coefficient observed for the PCDTBT film is much higher than those of the new polymer films, perhaps due to a reduction in optical density for the new polymers studied here. One possible explanation could be due to molecular distortions occurring along the polymer chains for copolymers P1 – 4. It has previously been shown that the oscillator strength, and thus absorption coefficient, can be negatively affected due to oligomer curvature [48]. Thus, it can be speculated that the observed reduction in absorption coefficient may be due to PCDTBT presenting a more rigid, planar conformation than the polymers studied in this chapter.

The steady-state photoluminescence (SSPL) spectra for all polymers and $PC_{60}BM$ thin-film samples were recorded as shown in **Figure 4.4 (b)**. Samples were measured under ambient conditions with an excitation wavelength of 475 nm. Again, all precursor solutions were made from the same 1:1 DCB:CB solvent system (at 20 mg/ml), spin-cast at 1000 rpm and annealed under nitrogen for 5 minutes at 60°C (70-80 nm thickness).
For all polymers, a single broad peak was observed at the following wavelengths: 943 nm (P1), 942 nm (P2), 806 nm (P3) and 799 nm (P4). The $PC_{60}BM$ film was also characterised by an emission at a peak at 743 nm, with a broad shoulder at around 825 nm; a result similar to previous reports [49,50]. Much like the ICT peak observed in absorption, polymers P3 and P4 have a blue-shifted peak emission wavelength relative to emission from P1 and P2. Indeed, a bathochromic shift in PL emission of 0.23 eV is observed between polymers P1/P2 and P3/P4. This energy-shift is around 50% of that seen for the ICT peak energy observed in absorption (0.43 eV).
It has previously been reported that bathochromic effects are induced through a simultaneous destabilisation of the HOMO level (via σ-π conjugation) and stabilisation of the LUMO level (via σ*-π* conjugation) [25].

Interestingly, there is a difference in energy between the peak in absorption associated with ICT and PL peak emission for the D-A polymers. P1 and P2 show a Stokes shift of ≈ 0.38 eV, whereas P3 and P4 have a Stokes shift of ≈ 0.58 eV. For reference, the PCDTBT thin-film had a Stokes shift of 0.42 eV between ICT maxima and PL peak intensities. The enhanced Stokes shift for the DBS-containing polymers P3 and P4 is indicative of

an ICT-type electronic reorganisation following excitation [51]. The total reorganisation energy immediately following excitation can be thought of as a sum of the change in equilibrium geometries on the donor unit and acceptor unit, following the oxidation of the donor and reduction of the acceptor units, respectively [52]. The reduction in Stokes shift for polymers P1 and P2 relative to P3 and P4 can likely be explained by geometry relaxation. Here, the polymer geometry difference between the energy-minimised S_0 ground state and energy-minimised S_1 state is greater for DBS-containing polymers P3 and P4 than it is for CDPT-containing polymers P1 and P2. The consequence of a higher reorganization energy due to polymer geometry distortion is an enlarged Stokes shift [53]. Along with reorganizational energies, other factors such as the solubility and aggregation properties of each polymer will also affect the Stokes shift [53–55].

To probe the PL quenching ability and thus charge-transfer capabilities of the polymer:PCBM blends, SSPL was used on films of representative thickness to those used in PV devices. Here, each sample was exposed to a continuous-wave (CW) laser at 405 nm with an incident power of 1 mW. As shown in **Figure 4.5**, the emission from samples utilising a 1:1 polymer:PCBM weight ratio exhibit increased PL emission relative to samples made from a 1:3 blend. This result suggests a more efficient exciton quenching mechanism for the higher PCBM concentration films, a result consistent with previous reports based on similar polymer:PCBM films [56,57]. Interestingly, polymer:PCBM blends containing P3 and P4 produced a peak PL emission count much larger than those observed in P1 and P2-containg blends. For example, the 1:1 blend of P3 produced a peak PL count 250x brighter than a 1:1 blend containing P1.

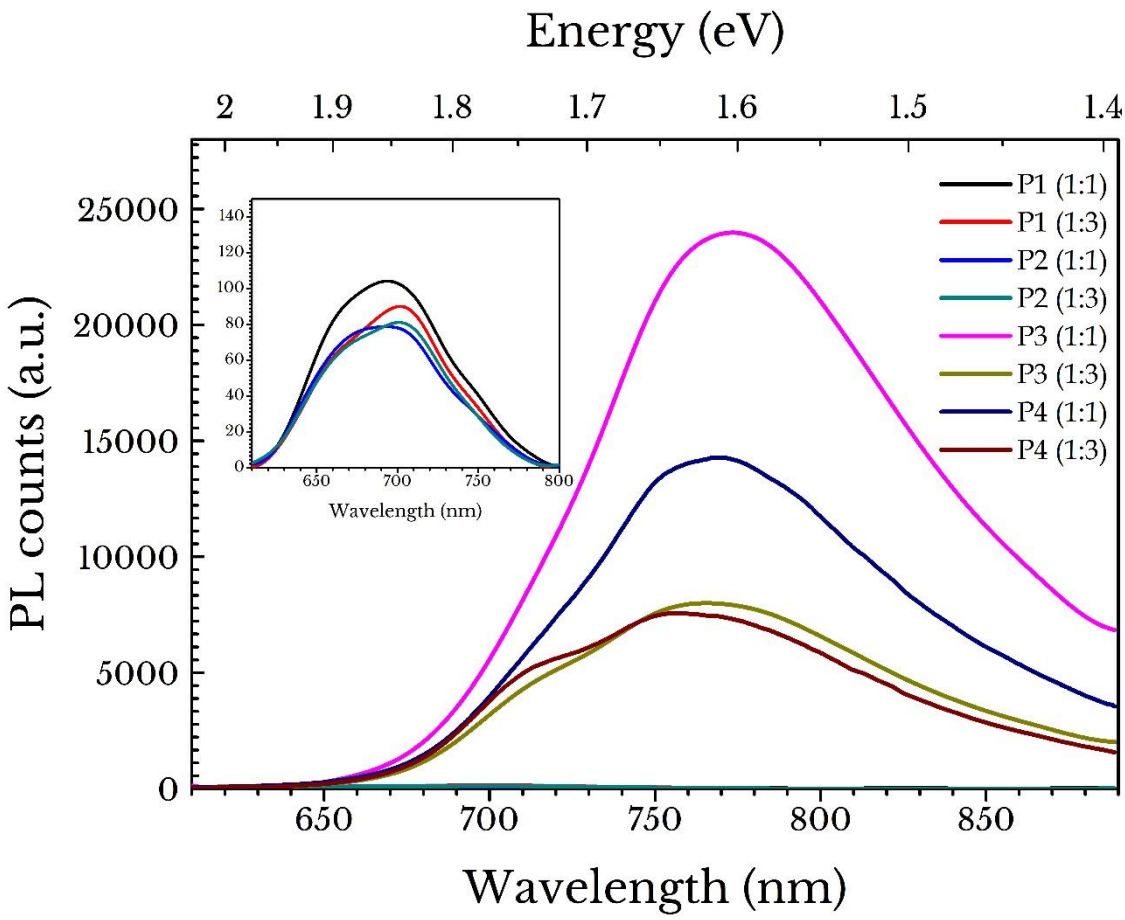

Figure 4.5 - The PL quenching abilities of the polymer:PCBM blends using weight ratios of (1:1) and (1:3) (polymer:PCBM). Inset: PL emission spectra of P1 and P2 blends with PCBM. Note that all spectra were accumulated over a 5 second integration period.

One possible explanation for this behaviour is poor mixing of polymer chains with domains of PCBM, thus resulting in poor exciton-quenching due to a reduced interfacial area between polymer and PCBM. This would directly impact the performance of the solar cells by reducing the short-circuit current, as the photogenerated excitons are not able to dissociate before recombining and therefore do not contribute to the photocurrent of the solar cell.

Figure 4.6 and **Figure 4.7** show 3-dimensional (3D) and 2D data files taken using a DekTak surface profilometer (500 x 500 nm area) for blends of the different polymers

with PCBM. Here, blends were prepared at 1:1 and 1:3 by weight with PCBM. All films were cast in the same way using a solution made from a 1:1 mixture of CB:DCB and annealed at 60°C for 5 minutes, replicating the device fabrication protocol discussed later. Topographic images of polymer:fullerene blends incorporating polymers P1 and P2 are shown in **Figure 4.6**. It can be seen that the film for polymer P1 appears to be structured at a length-scale of ≈ 8 nm, with the features observed most likely corresponding to fullerene domains. Indeed, it is found that increasing the fullerene concentration from 1:1 (a,b) to 1:3 (c,d) appears to increase the size of such surface features from approximately 8 nm to 19 nm. This increase in PCBM concentration is also accompanied by a reduction in film root-mean square (RMS) roughness. P1 (1:1) has an RMS roughness of 1.1 nm, whilst the 1:3 films had an average RMS roughness of 0.8 nm.

Polymer	Blend ratio (polymer:PCBM)	RMS roughness (nm)	Average domain size (nm)
P1	(1:1)	1.1 ± 0.2	7.7 ± 1.6
	(1:3)	0.8 ± 0.1	19 ± 4.2
P2	(1:1)	2.2 ± 0.1	7.7 ± 1.1
	(1:3)	1.2 ± 0.2	12.5 ± 3.9
P3	(1:1)	2.3 ± 0.1	9.6 ± 3.0
	(1:3)	1.5 ± 0.1	11.5 ± 2.6
P4	(1:1)	2.0 ± 0.2	26.3 ± 7.1
	(1:3)	2.2 ± 0.2	10.6 ± 2.2

Table 4.2 – Root mean square (RMS) surface roughness and the average domain size for polymer:PCBM blends made from (1:1) and (1:3) (w/w) solutions. The RMS values were obtained from a minimum of 5 line profiles and the average domain size was evaluated from a minimum of 12 domains per sample.

There is a clear difference in overall film quality shown between 1:1 and 1:3 weight ratios using polymer P2, as shown in **Figure 4.6 (e-h)**.

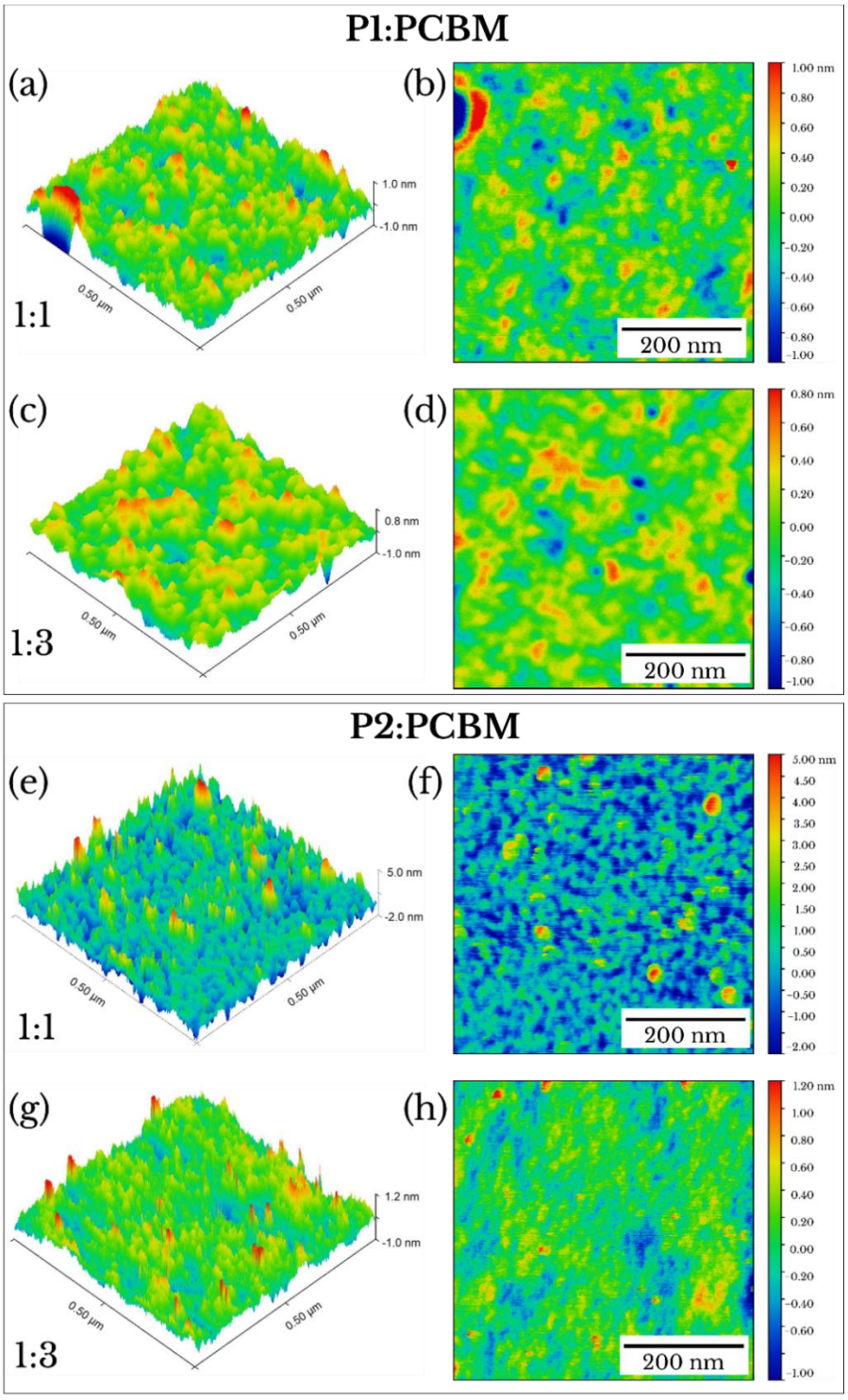

Figure 4.6 - Atomic force microscopy (AFM) images of polymer:PCBM samples P1 (a-d) and P2 (e-h) using polymer:PCBM ratios of 1:1 (a,b,e,f) and 1:3 (c,d,g,h) across a 0.5 µm² area. 3-dimensional (3D) renders are shown in the left-hand column and 2D plots are shown on the right hand side. Each image has been individually normalised to highlight topographical features. Each film was cast from a solution containing a 1:1 mixture of CB:DCB.

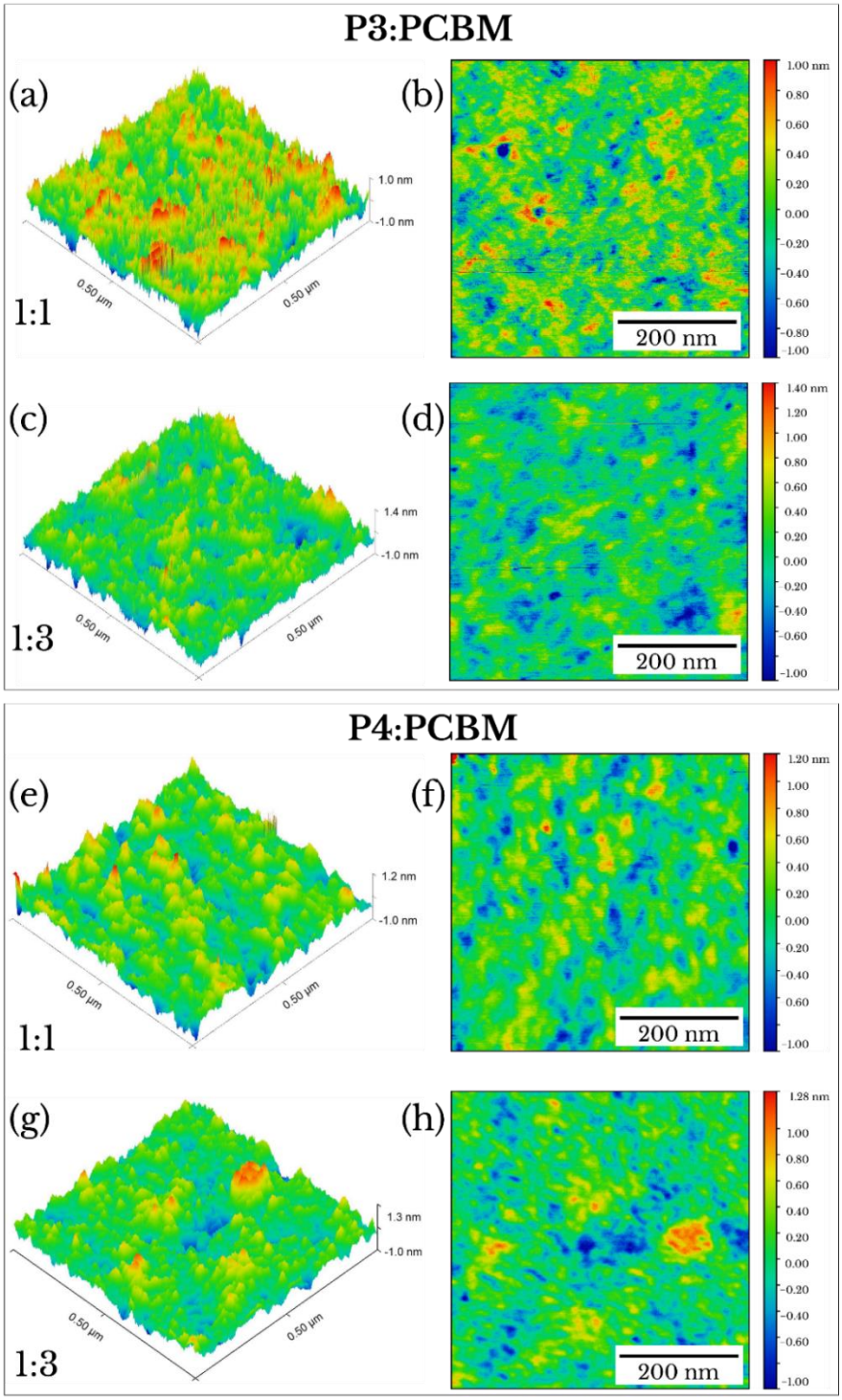

Figure 4.7 - Atomic force microscopy (AFM) images of polymer:PCBM samples P3 (a-d) and P4 (e-h) using polymer:PCBM ratios of 1:1 (a,b,e,f) and 1:3 (c,d,g,h). 3-dimensional (3D) renders are shown in the left-hand column and 2D plots are shown on the right. Each image has been individually normalised to highlight topographical features. Each film was cast from a solution containing a 1:1 mixture of CB:DCB.

It is found that increasing the weight ratio to 1:3 reduces the density of domains whilst simultaneously lowering the overall surface roughness from 2.2 nm (1:1) to 1.2 nm (1:3). P3 and P4 blend films had an RMS surface roughness of approximately 2 nm. There seems to be no immediate impact on the topography by varying the donor unit from CDPT (P1 and P2) to DBS (P3 and P4). Replacing the octyl side chain (P1, P3) with a DMO alkyl chain (P2, P4) on the acceptor moiety also does not seem to affect the overall film surface post annealing. The dark blue areas observed in **Figures 4.6** and **4.7** indicate low height levels and are likely linked to poor substrate surface coverage post-annealing. Further work on such copolymer:fullerene thin-film topographies in photovoltaic applications should focus on improving surface coverage to develop the absorbing potential and short-circuit current of the BHJ absorber layer.

4.3. X-ray diffraction

To study the structural properties of the polymers, glancing-incidence wide-angle X-ray scattering (GIWAXS) was used to characterise polymer films and polymer:PCBM blends cast from a 1:1 (CB:DCB) solvent mixture. **Figure 4.8 (a)** and **(b)** displays GIWAXS detector images of polymers P1 and P3 cast onto quartz glass. Due to limitations on available material, only neat films of polymers P1 and P3 were studied using GIWAXS. For measurement, each sample was positioned above the critical angle (0.16°) to ensure a full penetration of the X-rays into the sample. In both images, a clear ring can be seen at Q ≈ 0.4 $Å^{-1}$ with diffuse diffraction rings at Q ≈ 1.7 $Å^{-1}$ and 2.2 $Å^{-1}$. Similar GIWAXS spectra have been obtained from a pure-PCDTBT film with diffraction scattering features observed at Q ≈ 0.35 $Å^{-1}$ and 1.42 $Å^{-1}$ (d-spacing of 18 Å and 4.42 Å). These reflections have been assigned to the polymer layer spacing (or lamella packing distance) and (010) π-π stacking distance, respectively [58,59].

For polymer P1, the bright diffraction rings seen at Q ≈ 0.34 $Å^{-1}$ and 1.76 $Å^{-1}$ have a corresponding d-spacing of 18.5 Å and 3.6 Å, respectively. Here, the 18.5 Å reflection is assigned to the lamella packing distance, which is the distance between stacked polymer chains grown perpendicular to the substrate surface. Similarly, polymer P3 has strong

reflections observed at Q ≈ 0.30 Å^{-1} and 1.71 Å^{-1} (20.9 Å and 3.7 Å, respectively). The larger spacing value determined (20.9 Å) is again attributed to lamella packing, suggesting that polymer P1 undergoes a more compact stacking in the Q_z direction.

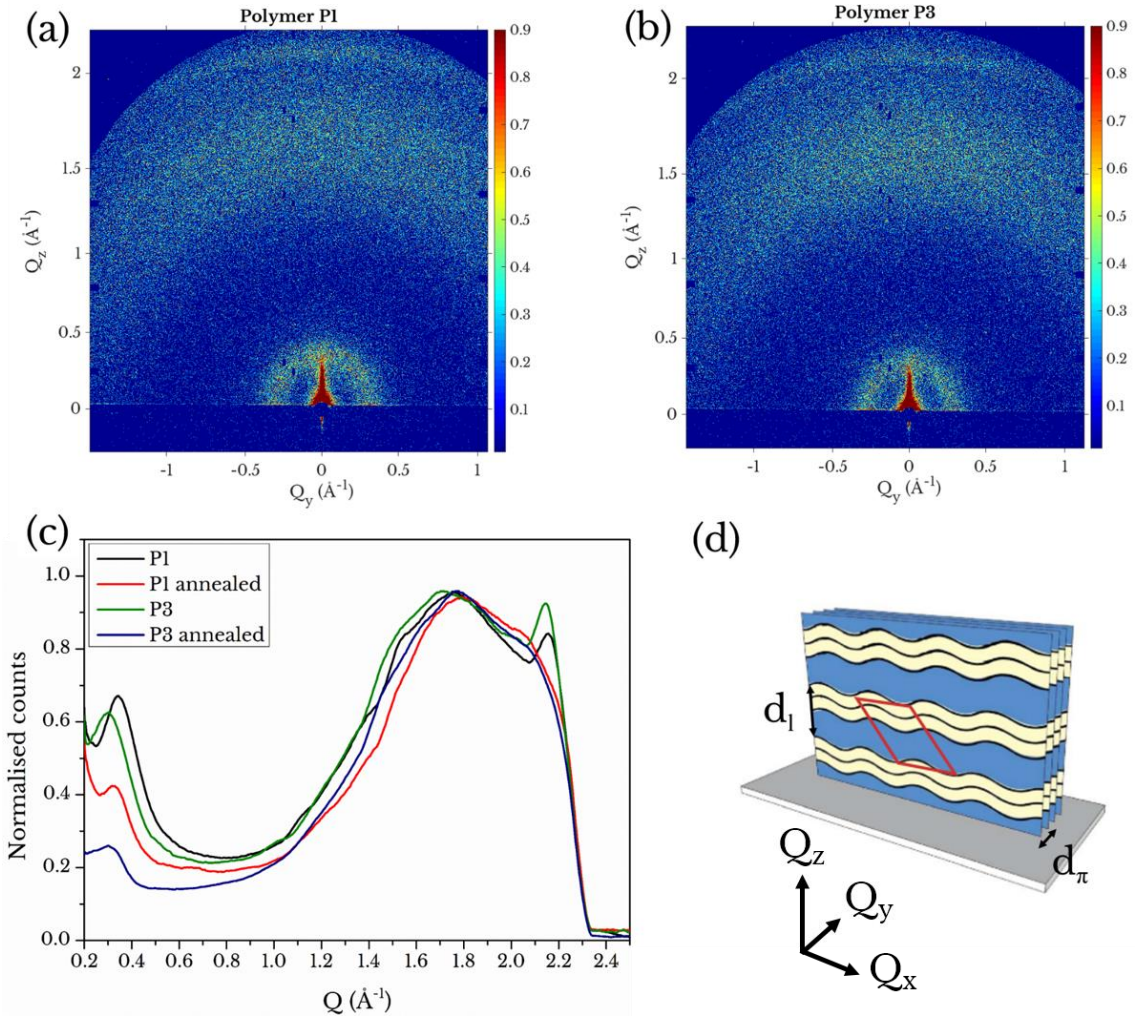

Figure 4.8 – Glancing-incidence wide-angle X-ray scattering (GIWAXS) detector images of (a) raw polymer P1 without high-temperature annealing and (b) raw polymer P3 without high-temperature annealing. (c) Normalised radial integration plots of raw polymers P1 and P3 before and after anneal. Each sample was exposed to 5 minutes of X-ray beam without any sign of beam damage. (d) A representation of the perpendicular stacking and repeating unit cell (red polygon). dl and dπ represent the lamella packing and π-π stacking distance, respectively. Image (d) was taken from reference 53.

As P1 and P3 possess the same alkyl side chains, the overall reduction in lamella packing distance for P1 relative to P3 could be due to the DBS moiety on P3 causing a reduction in interdigitated side chains, an effect that has been observed in P3HT polymorphs [60]. The azimuthally integrated radial profile plots of neat P1 and P3 are observed in **Figure 4.8 (c)** indicate a shoulder at Q ≈ 1.53 $Å^{-1}$ (4.1 Å), which is ≈ 0.4 Å larger (in d-space) than the peak reflection detected at Q ≈ 1.7 $Å^{-1}$. The lateral offset between the parallel polymer layers (shown in red in **Figure 4.8 (d)**) could be displaced by ≈ 3.6 Å (P1) and 3.7 Å (P3), leading to a similar π-π stacking distance of 4.1 Å for both P1 and P3. It is currently unclear which reflection corresponds to the π-π stacking distance, however, reports on the PCDTBT unit cell have shown a parallelogram-like structure shown **Figure 4.8 (d)** in red [58].

To attempt to identify the glass transition properties of P1 and P3, each sample was exposed to a high-temperature anneal (180°C) for 90 minutes, which is slightly above the glass transition temperature (T_g) of PCDTBT [13]. **Figure 4.8 (c)** displays radial integration plots of polymers P1 and P3 before and after high-temperature annealing. For polymer P1, the observed diffraction peak at low Q shifts from ≈ 0.34 $Å^{-1}$ to 0.33 $Å^{-1}$ with a corresponding shift in the peak diffraction ring from ≈ 1.76 $Å^{-1}$ to 1.79 $Å^{-1}$. The latter could be explained from a reduction in the π-π stacking distance when the polymer film is annealed above T_g, an effect observed in neat PCDTBT films [61]. The change in lamella packing for P1 after the high-temperature annealing cycle is small (18.5 Å to 19 Å), and is most likely caused by a lattice expansion through a straightening of the polymer backbone in the crystalline phase. Similar effects are also observed for P3 with the reflection at Q ≈ 1.71 $Å^{-1}$ shifting to 1.78 $Å^{-1}$, however, the Q ≈ 0.30 $Å^{-1}$ peak appears to remain stable after high-temperature annealing. This suggests the unit cell formed from the lamella packing of P3 is identical in both the amorphous and crystalline phase, with the π-π stacking distance narrowing by 0.14 Å to 3.53 Å. Polymer:fullerene blends were also studied using GIWAXS. Such blends were prepared as detailed in **Section 3.3.2**, and were spin-cast from a 1:1 (CB:DCB) solvent under identical conditions. For all polymers, the weight ratio was maintained at 1:3 (polymer:PCBM).

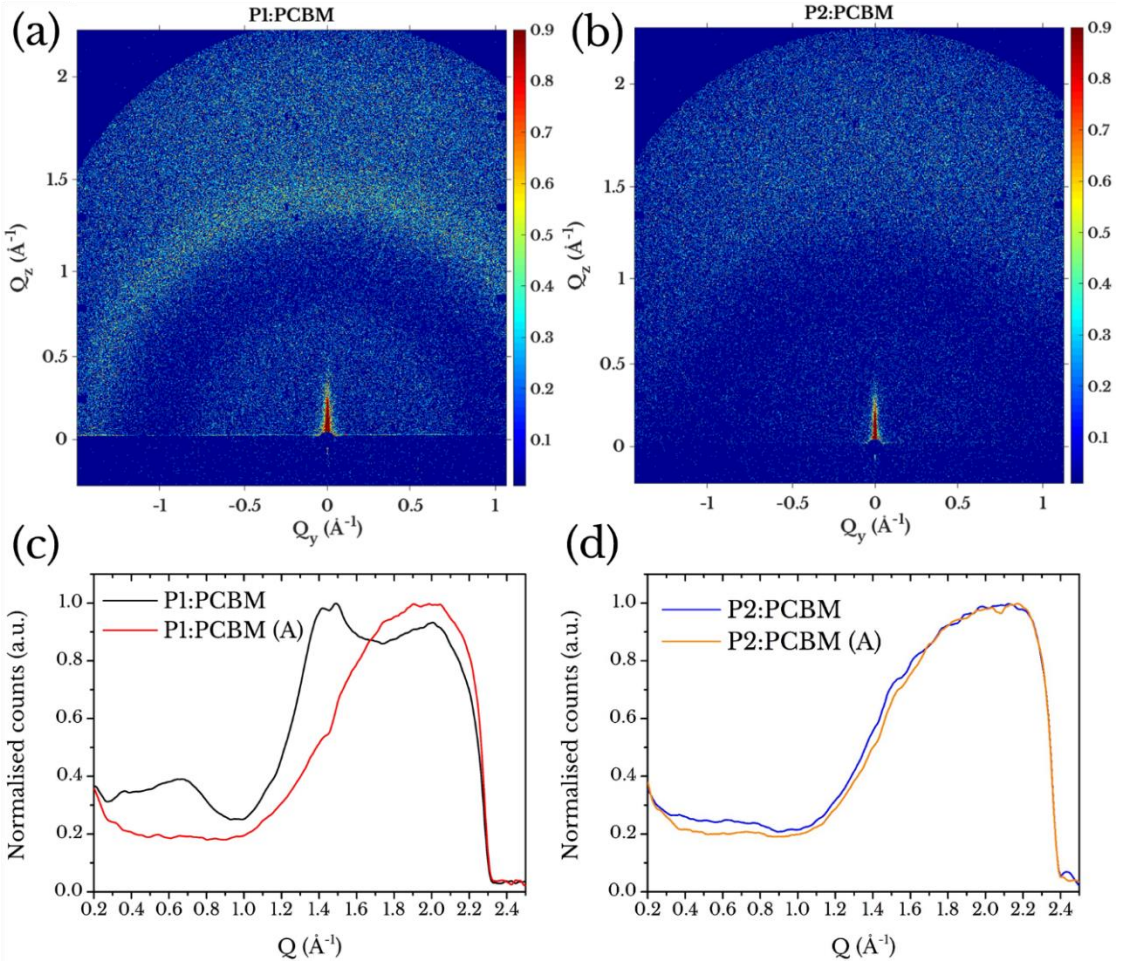

Figure 4.9 – GIWAXS detector images of 1:3 (polymer:PCBM) blends for (a) P1 and (b) P2. Parts (c) and (d) indicate radially integrated spectra across Q of blends without and with high-temperature annealing (A) for P1:PCBM and P2:PCBM, respectively.

Figure 4.9 (a) and **(b)** present GIWAXS images for polymer blends of P1 and P2 with PCBM before thermal annealing. Here, diffraction rings can be seen for the P1:PCBM blend around Q ≈ 0.70 Å^{-1}, 1.42 Å^{-1} and 1.50 Å^{-1} along with additional peaks seen at Q ≈ 0.36 Å^{-1} and 2.00 Å^{-1} shown more clearly in the radial integration spectra presented in **Figure 4.9 (c).** In the pre-annealed P1:PCBM film, scattering features observed at Q ≈ 0.36 Å^{-1} and 1.50 Å^{-1} can be assigned to the polymer layer spacing and π-π stacking distance as they are similar to those shown in **Figure 4.9 (c)**. The additional peaks at Q ≈ 0.70 Å^{-1} and 2.00 Å^{-1} have previously been ascribed to amorphous domains of PCBM [13]. It is worth noting that broad peaks have also been observed centred around Q ≈ 1.38 Å^{-1}

for spin-cast and doctor-bladed PCBM [62,63]. One possible explanation for the double peak around Q ≈ 1.50 Å^{-1} is the intercalation of PCBM within the polymer π-π stacking direction, enlarging the average π-π stacking distance by 0.6 Å (3.7 Å to 4.3 Å).

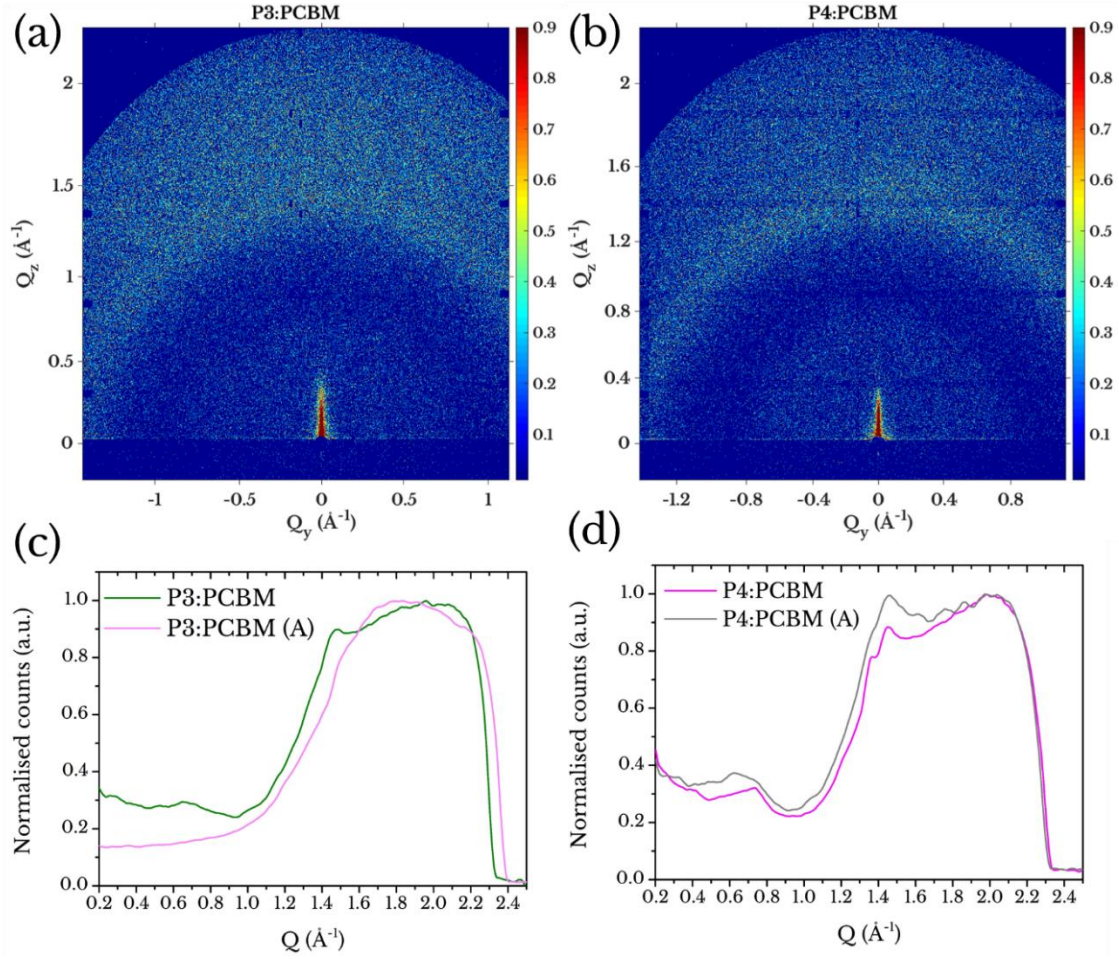

Figure 4.10 - GIWAXS detector images of 1:3 (polymer:PCBM) blends for (a) P3 and (b) P4. Parts (c) and (d) indicate radially integrated spectra across Q of blends with and without high-temperature annealing for P3:PCBM and P4:PCBM, respectively.

Upon annealing beyond T_g, the P1:PCBM film loses all scattering features at low-Q whilst maintaining a shoulder at Q ≈ 1.50 Å^{-1} and a broad peak centred at Q ≈ 2.00 Å^{-1}. This broadening of the Q ≈ 2.00 Å^{-1} (PCBM) peak is likely caused by increased disorder in the film and a clear reduction in long-range order as compared to the as-cast (60°C, 5 mins)

film. When comparing GIWAXS spectra obtained from a radial integration for P2:PCBM (**Figure 4.9 (b)**), a seemingly unchanged amorphous spectrum persists regardless of a high-temperature annealing stage. Returning to the AFM images shown in **Figure 4.6**, it suggests P2:PCBM blends are characterised by small, well dispersed amorphous domains. Previous studies of low molecular weight polymers have indicated finer, nanoscale domains from spin-cast (D-A) polymer:PCBM films, ascribed to a combination of polymer chain conformation and inter-chain interactions [64].

Polymers P3 and P4, which contain a DBS and BTDI (D-A) backbone-structure, have similar GIWAXS patterns to as-prepared films blended with PCBM. In both blends, the reflections seen at Q ≈ 0.70 $Å^{-1}$ and 2.00 $Å^{-1}$ can be assigned to PCBM. One interesting feature is the reflection around Q ≈ 1.46 $Å^{-1}$, which is seen for P3:PCBM before high-temperature annealing and P4:PCBM before and after annealing. After annealing at high-temperature, the Q ≈ 1.46 $Å^{-1}$ diffraction peak disappears in the P3:PCBM blend, most likely caused by a lack of crystallised domains in the amorphous film.
After studying the electronic, topographical and crystallographic properties of the new polymers, photovoltaic devices were fabricated to test the operating performance of polymer:PCBM blends. A relatively short π-π stacking distance was shown for neat films of polymers P1 and P3, suggesting that efficient charge transport should occur between adjacent polymer chains.

4.4. Photovoltaic performance

An energy level diagram depicting the measured HOMO and LUMO levels for the polymers used in this study is shown in **Figure 4.11**. A dotted box is drawn around the D-A polymers used within the bulk heterojunction, along with the electron-accepting molecule $PC_{60}BM$. The LUMO level of all D-A polymers is significantly lower than that of PEDOT:PSS, making it a suitable electron-blocking transport layer. A series of devices were fabricated in an inverted p-i-n architecture, in which light enters the device through the ITO anode. Devices were fabricated as outlined in **Chapter 3 Section 3.5.1**.

In all cases, the PEDOT:PSS and active layer thicknesses were measured at approximately 35 nm and 70-80 nm, respectively. Following active layer deposition, wet films were dried at 60 °C for 5 minutes to remove any residual solvent. The top cathode contact was fabricated through a sequential thermal deposition of bathocuproine (BCP) and aluminium, with layer thicknesses of 3 nm and 100 nm, respectively.

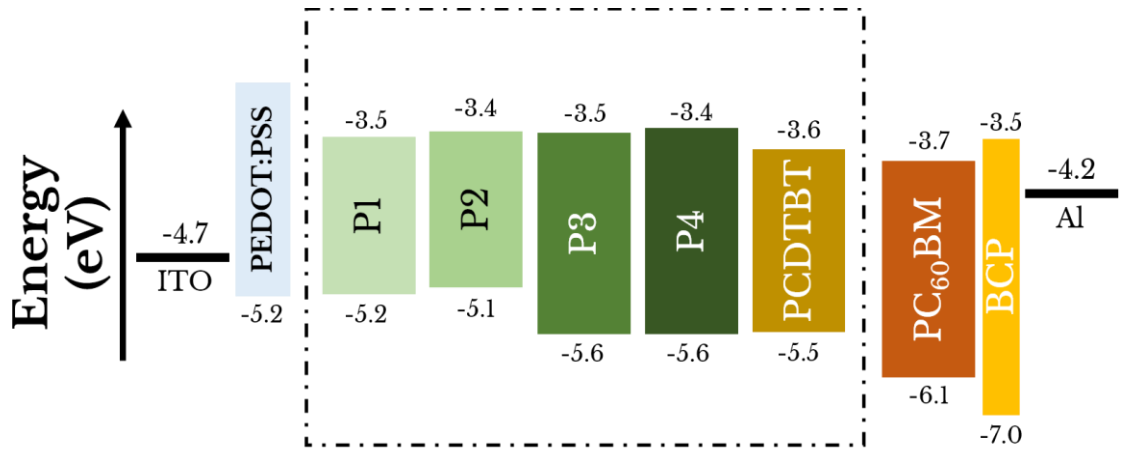

Figure 4.11 - Energy band diagram indicating the relative HOMO and LUMO levels of the donor-acceptor (D-A) polymers (P1-P4) used in this chapter, along with PCDTBT [42], electron-blocking PEDOT:PSS [65], fullerene-acceptor $PC_{60}BM$ (measured by Ossila Ltd.), including the ITO [65] and LiF/Al [66] electrodes. HOMO and LUMO levels for the different D-A polymers were measured by Ary Murad, Chemistry Department, University of Sheffield. Data correct to one decimal point.

Due to the limited amount of each polymer available, only weight ratios of 1:1 and 1:3 (polymer:PCBM) were studied in photovoltaic devices using the solvent system DCB:CB (1:1) for all blends. Blends based on P1 and P2 were also cast using a CB solvent-only precursor.

Polymer	Solvent [a]	Blend ratio [b]	Active layer thickness (nm)	Voc (V)	FF (%)	Jsc ($mAcm^{-2}$)	PCE (%)
P1	CB:DCB	1:1	75 ± 5	0.43 ± 0.17	29 ± 6	-3.51 ± 0.83	0.43 ± 0.18
		1:3	74 ± 4	0.63 ± 0.15	36 ± 5	-4.87 ± 0.70	1.27 ± 0.44
Champion [c]				**0.72**	**36**	**6.9**	**1.77**
		1:3	120 ± 8	0.57 ± 0.12	31 ± 4	-3.02 ± 1.11	0.39 ± 0.18
	CB	1:3	73 ± 3	0.31 ± 0.16	30 ± 2	-3.41 ± 0.96	0.78 ± 0.39
P2	CB:DCB	1:1	72 ± 4	0.48 ± 0.16	30 ± 3	-2.06 ± 0.66	0.46 ± 0.28
		1:3	75 ± 4	0.53 ± 0.16	34 ± 5	-2.84 ± 0.96	0.58 ± 0.10
Champion				**0.64**	**31**	**-4.64**	**0.92**
		1:3	123 ± 6	0.49 ± 0.24	32 ± 5	-1.40 ± 0.53	0.23 ± 0.13
	CB	1:3	70 ± 4	0.36 ± 0.22	32 ± 4	-2.22 ± 0.51	0.49 ± 0.34
P3	CB:DCB	1:1	75 ± 3	0.57 ± 0.32	28 ± 2	-0.84 ± 0.28	0.19 ± 0.08
		1:3	71 ± 5	0.75 ± 0.18	29 ± 3	-1.04 ± 0.46	0.26 ± 0.09
Champion				**0.92**	**27**	**-1.66**	**0.41**
		1:3	116 ± 5	0.73 ± 0.23	28 ± 3	-0.61 ± 0.39	0.18 ± 0.02
P4	CB:DCB	1:1	71 ± 6	0.36 ± 0.23	27 ± 2	-0.32 ± 0.3	0.11 ± 0.04
		1:3	73 ± 4	0.63 ± 0.33	30 ± 4	-0.91 ± 0.61	0.16 ± 0.08
Champion				**0.86**	**27**	**-1.67**	**0.38**
		1:3	121 ± 9	0.62 ± 0.27	29 ± 3	-0.70 ± 0.10	0.15 ± 0.06
PCDTBT	CB:DCB	1:1	71 ± 6	0.65 ± 0.15	48 ± 9	-5.95 ± 1.92	3.38 ± 0.67
		1:3	73 ± 4	0.72 ± 0.28	52 ± 11	-6.45 ± 1.68	3.98 ± 0.96
Champion				**0.89**	**63**	**-7.48**	**4.38**

Table 4.3 - Device photovoltaic performance summary indicating the following: the solvent system used, weight ratio for polymer:$PC_{60}BM$, layer thickness as determined via DekTak, power conversion efficiency (PCE), fill factor (FF), short-circuit current (J_{sc}) and V_{oc}. The champion cell is indicated in bold for each polymer used in the active layer (bulk heterojunction). The data presented is taken from the average measured value with the error equal to the standard deviation (stdev) from 99 (P1), 99 (P2), 50 (P3), 50 (P4) and 28 (PCDTBT) individual pixels. [a] – The solvent system used for that batch of devices. [b] – Blend ratio for weight:weight (w:w) of polymer:PCBM. [c] – The champion cell was identified in a 1:3 batch of solar cells for all polymers with an active layer thickness around 71-75 nm, using a 1:1 solvent mixture of CB:DCB.

The 1:1 DCB:CB solvent system was chosen based on reported improvements in the efficiency of PBDTTT-C:PCBM solar cells through an improvement in surface morphology by a reduction in surface roughness thought to ameliorate carrier transport and reduce series resistance [40].

Table 4.3 shows a summary of device metrics determined as a result of a series of optimisation experiments. The best performing solvent system was found to be a 1:1 mixture of solvents CB and DCB with an active layer thickness between 71 and 75 nm. The best performing polymer:PCBM blend ratio for all polymers used was 1:3. For each measured quantity, the average value is stated with the error equal to the standard deviation. Champion devices are shown in bold for each experimental condition. A PCDTBT reference device was fabricated using a CB:DCB solvent system [67–69]. Here, the PCDTBT films achieved an average PCE of 4% (1:3 weight ratio) although the standard deviation is relatively high. This relatively lower PCE for PCDTBT:PCBM devices compared to previous literature values could be due to the $PC_{60}BM$ fullerene used in this experiment, which produces BH devices approximately 20% lower in efficiency than blends made with $PC_{70}BM$ [70].

A clear trend in device PCE can be seen for the new D-A polymers, with P1 producing more efficient devices, having an average PCE of 1.27% and a champion PCE of 1.77%. However, the standard deviation (relative to the mean) is fairly large for all the polymers used in this study, highlighting the complex processes and film quality variations involved in the fabrication routine. A similar trend is also seen for the fill factor (FF) and short-circuit current (J_{sc}) values, which are explained in more detail later. It is understood from literature that the V_{oc} measured from an OPV cell depends linearly on the energy difference between the HOMO level of the D-A polymer and the LUMO level of the electron acceptor [71,72]. This is an ideal picture, with other factors including active layer thickness, interface recombination and degree of phase-separation also being important. On the basis of LUMO-HOMO separation, one could expect the V_{oc} obtained from cells made using polymers P1 and P2 to have a lower V_{oc} than those based on P3 and P4. As is shown in **Table 4.3**, this is indeed the case, with P3 exhibiting the largest champion V_{oc} of 0.92 V at an average of 0.75 V across 50 pixels. The reference films made from

PCDTBT had an average V_{oc} of 0.72 V with a peak V_{oc} of 0.89 V. For the D-A polymers, the lowest average V_{oc} was achieved using polymer P2 (0.53 V). This result is consistent with data shown schematically in **Figure 4.11**, whereby the wider bandgap polymers (P3, P4) have lower-lying HOMO levels and thus have a larger HOMO (polymer) to LUMO (PCBM) energy separation.

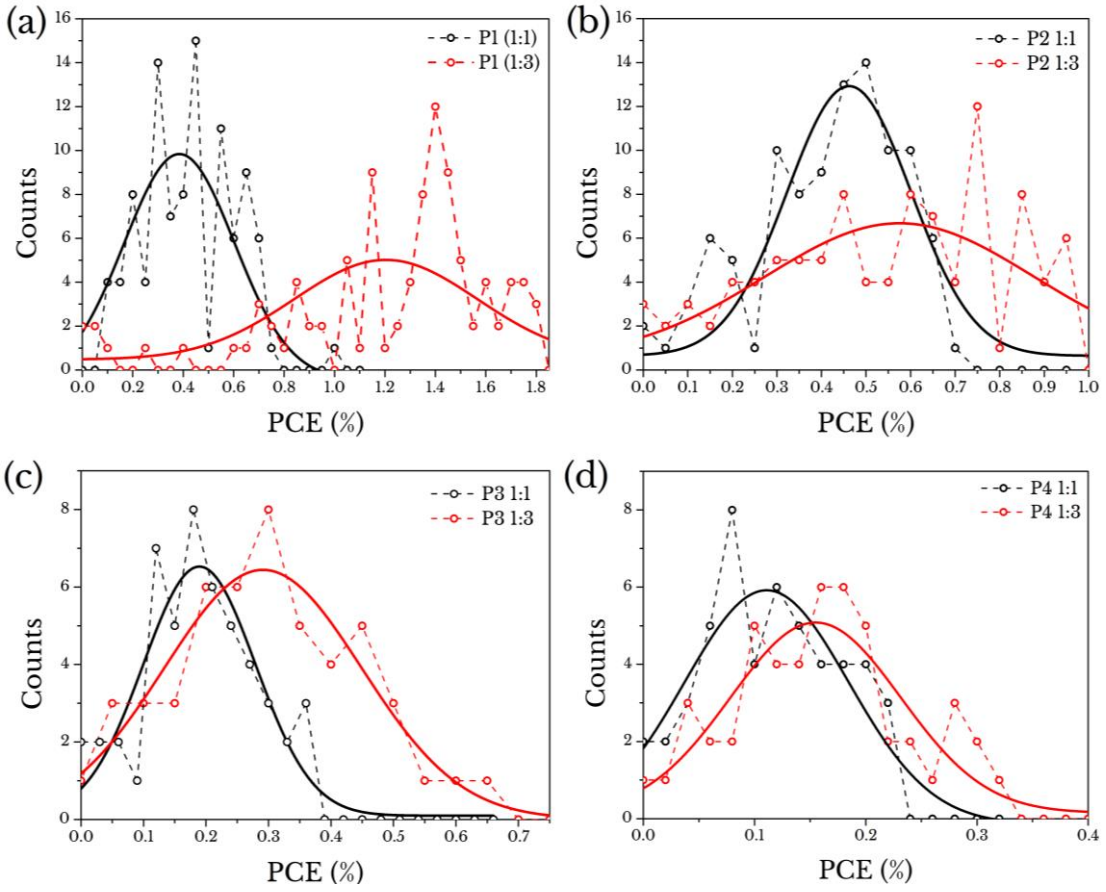

Figure 4.12 - Device PCE statistics for all novel D-A polymers without light-soaking (LS) at AM1.5 solar flux. (a) Raw device data from P1:PCBM ratios at 1:1 (black) and 1:3 (red). (b) Raw device data from P2:PCBM ratios at 1:1 (black) and 1:3 (red). (c) Raw device data from P3:PCBM ratios at 1:1 (black) and 1:3 (red). (d) Raw device data from P4:PCBM ratios at 1:1 (black) and 1:3 (red). P1 and P2 statistics are from 99 - 0.025 cm^2 pixels, P3 and P4 statistics are from 50 – 0.025 cm^2 pixels. The y-axis represents the number of pixels measured at a given PCE (%). The solid line represents a Gaussian fit.

The relatively poor PCE of blends based on P3 and P4 relative to P1 and P2 however results from low values of fill factor (FF) and J_{sc}, despite the clear improvements in V_{oc} obtained using wider bandgap polymers. The low Jsc is likely due to a combination of reduced optical density relative to the PCDTBT films as observed in **Figure 4.4**. Specifically, polymers P3 and P4 obtain champion J_{sc} values of -1.66 and -1.67 $mAcm^{-2}$, respectively. P3 performed better on average than P4, with an average J_{sc} value of -1.04 $mAcm^{-2}$ achieved compared to -0.91 $mAcm^{-2}$. Notably polymers P1 and P2 achieved a higher average J_{sc} value of -4.87 $mAcm^{-2}$ and -2.84 $mAcm^{-2}$ when used in a 1:3 (w:w) and 1:1 (CB:DCB) blend. The replacement of the donor unit from CDPT (P1 and P2) to DBS (P3 and P4) induced a hypsochromic shift on the overall absorption spectrum as shown in **Figure 4.4**; a result consistent with the reduced J_{sc} exhibited by P3 and P4, as these DBS-containing polymer blends have reduced absorption overlap with the AM1.5 spectrum.

Since the semiconducting properties of these polymers arise from the extended π-orbitals due to the unhybridised p_z orbital along the backbone, it is necessary to arrange polymer chains co-facially to increase the likelihood of π-orbital interactions [73]. The stacking of polymer chains in such a way causes the mobility of free carriers to be largely anisotropic. Significant efforts have been made to improve π-π stacking, which can ultimately be used to increase charge carrier mobility [74]. It is likely the charge transport properties of P3 and P4 are significantly worse than P1, P2 and PCDTBT, most probably due to insufficient intermolecular interactions and increased trap states within the material bandgap [75]. However, the results from the GIWAXS study indicated the π-π stacking distance in P1 (CPDT) and P3 (DBS) neat-polymer films appear relatively similar (4 Å), suggesting mobility issues could arise from defect states in the polymer. It is apparent that the FF is poor for the novel D-A polymers studied compared to the reference PCDTBT devices, a result that most likely results from reduced charge carrier mobilities that reduce the photocurrent and enhance non-geminate recombination.

Figure 4.12 shows data for all devices tested, from a series of 298 individual pixels (99 from P1 and P2, 50 from P3 and P4), where the number of pixels is plotted as a function

of the measured PCE. The solid lines in each figure represents a Gaussian distribution function. As is shown in **Table 4.3**, for all polymer:PCBM blends the PCE appears to increase as the PCBM concentration is increased from 1:1 to 1:3. This is clearly evident from the plots shown in **Figure 4.12**, in which it can be seen that mean PCE shifts towards higher values for devices having a 1:3 blend-ratio in all cases. The peak position of the Gaussian function is a good approximation to the statistical mean within each data set. A larger improvement in PCE was observed for polymers P1 and P2 over P3 and P4 as the blend ratio increased from 1:1 to 1:3. However, this is accompanied by an increase in statistical deviation from the mean value. A direct consequence of the overall improvement in PCE for all polymer:PCBM systems is an increase in the standard deviation; a trend also apparent in **Table 4.3**.

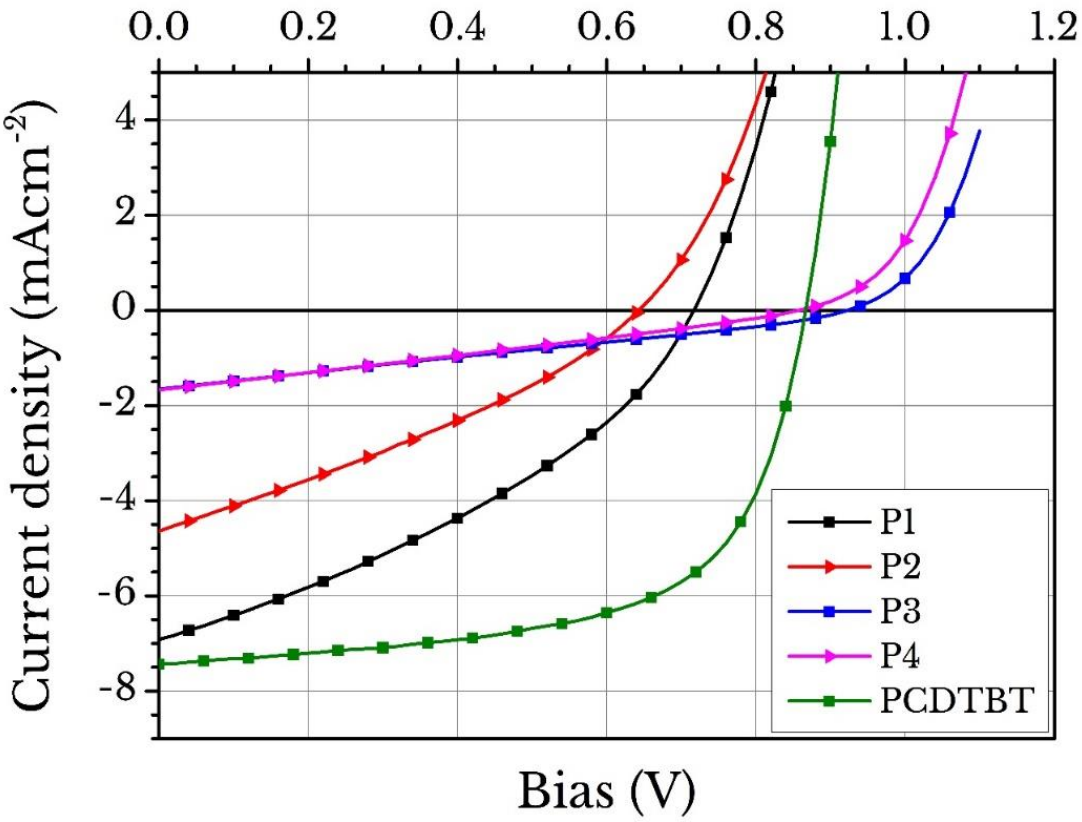

Figure 4.13 - Current-voltage (J-V) data for champion photovoltaic pixels made using a 1:3 blend ratio of P1:PCBM (black), P2:PCBM (red), P3:PCBM (blue), P4:PCBM (magenta) and PCDTBT:PCBM reference (green) under AM1.5 illumination. Each pixel has an area of 0.025 cm^2.

Figure 4.13 plots J-V sweeps of champion devices measured for all polymer:PCBM mixtures, with the individual pixel metrics displayed in bold in **Table 4.3**. The champion PCDTBT device (green) behaves similarly to previously reported devices made using a similar solvent system at 1:3 (w/w) with PCBM [17], highlighting that the fabrication routine is sufficient to produce literature-matching PCE values for PCDTBT. Efficient PV devices have a small series resistance (R_s) combined with a large shunt resistance (R_{sh}) component [40]. Here, the R_s values for each polymer:PCBM system were calculated from the J-V plots shown in **Figure 4.13** and found to be 34 Ω cm^2, 57 Ω cm^2, 235 Ω cm^2 and 305 Ω cm^2 for P1, P2, P3 and P4, respectively. The calculated series resistance for the champion PCDTBT pixel was determined as R_s = 4.1 Ω cm^2. The general trend of increasing series resistance from P1 to P4 is possibly related to the morphological structure of the post-annealed films [40]. As the same weight ratio was used in all high performing polymer:PCBM devices, a possible variation in percolation path length could also explain the sudden increase in R_s [76]. It is difficult to fully determine the origin of the series resistance as it can be caused by a number of processes including a combination of material junction resistances (ITO/PEDOT interface), charge carrier mobility and high resistivity materials used within the device stack [77,78].

The R_{sh} was measured to be ≈ 710 Ω cm^2 for the PCDTBT champion cell, whereas P1 and P2 had an R_{sh} of 209 Ω cm^2 and 200 Ω cm^2, respectively. The reduction of R_{sh} in polymer blends based on P1 and P2 relative to PCDTBT can be caused by several effects such as defects near the heterojunction allowing an alternative current pathway away from the load [79]. P3 and P4 champion cells had an R_{sh} value of 587 Ω cm^2 and 551 Ω cm^2, respectively, comparable to other shunt-resistances measured in similar BHJ solar cells with PCBM [80].

4.5. Conclusions

A series of new D-A polymers utilising a similar conjugated backbone to that of PCDTBT were studied for their potential use in photovoltaic applications. DFT calculations

suggest a promising delocalisation of the HOMO level overlapping well with the LUMO level of the acceptor moieties in D-A polymers that utilise the CDPT donor unit. Although no DFT was performed on the DBS-containing polymers P3 and P4, it is speculated that as the DBS moiety is a weaker donor unit (and thus a reduction in the delocalisation of the HOMO level), this would result in a widening of the electronic bandgap. Thin film absorption and PL analysis suggests that, in accordance with the DFT results, a delocalisation of the HOMO level causes a bathochromic shift of the ICT absorbance peak and PL emission for polymers P1 and P2 relative to P3 and P4. A larger Stokes shift present in polymers P3 and P4 relative to P1 and P2 is reminiscent of a greater reorganizational energy following excitation. AFM images suggest a small enlargement of domains when using a 1:3 (polymer:PCBM) weight ratio. GIWAXS analysis performed on polymer films of P1 and P3 indicated a similar π-π stacking distance of 4 Å which reduces as the films were heated beyond the glass-transition temperature. Further GIWAXS experiments made on polymer:PCBM (1:3) films suggested a disordered, amorphous phase present in the as-prepared films, with P2:PCBM indicating no structural change after high-temperature heating. Photovoltaic devices made from D-A polymers mixed in a 1:3 blend with PCBM spun-cast from a 1:1 (DCB:CB) solvent system produced the best devices, with champion pixels having a PCE of 1.77 %, 0.92 %, 0.41 % and 0.38 % for polymers P1, P2, P3 and P4, respectively. A combination of high series resistance and a low shunt resistance can be attributed to the reduction in performance relative to the reference PCDTBT device. It was speculated that poor mixing of polymer with fullerene when spinning and annealing the film may play an important role in reducing the efficiency of devices made from these polymers.

4.6. References

1. Yu, G., Gao, J., Hummelen, J. C., Wudl, F. & Heeger, A. J. Polymer Photovoltaic Cells: Enhanced Efficiencies via a Network of Internal Donor-Acceptor Heterojunctions. *Science.* **270,** 1789–1791 (1995).

2. Hoppe, H. & Sariciftci, N. S. Organic solar cells: An overview. *J. Mater. Res.* **19,** 1924–1945 (2004).

3. Saleh Ardestani, S., Ajeian, R., Nakhaee Badrabadi, M. & Tavakkoli, M. Improvement in stability of bilayer organic solar cells using an ultra-thin Au layer.

Sol. Energy Mater. Sol. Cells **111,** 107–111 (2013).

4. Tada, A., Geng, Y., Wei, Q., Hashimoto, K. & Tajima, K. Tailoring organic heterojunction interfaces in bilayer polymer photovoltaic devices. *Nat Mater* **10,** 450–455 (2011).

5. Tang, C. W. Two-layer organic photovoltaic cell. *Appl. Phys. Lett.* **48,** 183–185 (1986).

6. Groenendaal, L., Jonas, F., Freitag, D., Pielartzik, H. & Reynolds, J. Poly(3,4-ethylenedioxythiophene) and its derivatives: past, present, and future. *Adv. Mater.* **12,** 481–494 (2000).

7. Kirchmeyer, S. & Reuter, K. Scientific importance, properties and growing applications of poly(3,4-ethylenedioxythiophene). *J. Mater. Chem.* **15,** 2077 (2005).

8. Li, G. *et al.* High-efficiency solution processable polymer photovoltaic cells by self-organization of polymer blends. *Nat. Mater.* **4,** 864–868 (2005).

9. Irwin, M. D., Buchholz, D. B., Hains, A. W., Chang, R. P. H. & Marks, T. J. p-Type semiconducting nickel oxide as an efficiency-enhancing anode interfacial layer in polymer bulk-heterojunction solar cells. *Proc. Natl. Acad. Sci.* **105,** 2783–2787 (2008).

10. Fei, Z. *et al.* Influence of backbone fluorination in regioregular poly(3-alkyl-4-fluoro)thiophenes. *J. Am. Chem. Soc.* **137,** 6866–6879 (2015).

11. Facchetti, A. Polymer donor-polymer acceptor (all-polymer) solar cells. *Mater. Today* **16,** 123–132 (2013).

12. Kularatne, R. S., Magurudeniya, H. D., Sista, P., Biewer, M. C. & Stefan, M. C. Donor-acceptor semiconducting polymers for organic solar cells. *J. Polym. Sci. Part A Polym. Chem.* **51,** 743–768 (2013).

13. Wang, T. *et al.* Correlating Structure with Function in Thermally Annealed PCDTBT:PC70BM Photovoltaic Blends. *Adv. Funct. Mater.* **22,** 1399–1408 (2012).

14. Etzold, F. *et al.* Ultrafast Exciton Dissociation Followed by Nongeminate Charge Recombination in PCDTBT:PCBM Photovoltaic Blends. *J. Am. Chem. Soc.* **133,** 9469–9479 (2011).

15. Olieslaeger, L. D. *et al.* Solar Energy Materials & Solar Cells Tuning of PCDTBT: $PC_{71}BM$ blend nanoparticles for eco-friendly processing of polymer solar cells. *Sol. Energy Mater. Sol. Cells* **159,** 179–188 (2017).

16. Zhang, Y. *et al.* PCDTBT based solar cells: One year of operation under real-world conditions. *Sci. Rep.* **6,** 4–11 (2016).

17. Duan, C. *et al.* Toward green solvent processable photovoltaic materials for polymer solar cells: the role of highly polar pendant groups in charge carrier transport and photovoltaic behavior. 3022–3034 (2013).

18. Wang, D. H. *et al.* Transferable Graphene Oxide by Stamping Nanotechnology: Electron-Transport Layer for Efficient Bulk-Heterojunction Solar Cells. *Angew. Chemie Int. Ed.* **52,** 2874–2880 (2013).

19. Cheng, Y. *et al.* Carbazole-Based Ladder-Type Heptacylic Arene with Aliphatic Side Chains Leading to Enhanced Efficiency of Organic Photovoltaics. *Chem. Mater.* **23,** 2361–2369 (2011).

20. Tan, S. E. & Sarjadi, M. S. The recent development of carbazole-, benzothiadiazole-, and isoindigo-based copolymers for solar cells application: A review. *Polym. Sci. Ser. B* **59**, 479–496 (2017).

21. Dang, D. *et al.* Tuning the fused aromatic rings to enhance photovoltaic performance in wide band-gap polymer solar cells. *Polymer (Guildf).* **104**, 130–137 (2016).

22. Dominguez, R., Montcada, N. F., De La Cruz, P., Palomares, E. & Langa, F. Cyclopentadithiophene organic core in small molecule organic solar cells: Morphological control of carrier recombination. *Phys. Chem. Chem. Phys.* **19**, 3640–3648 (2017).

23. Müllen, K. & Pisula, W. Donor-acceptor polymers. *J. Am. Chem. Soc.* **137**, 9503–9505 (2015).

24. Hinkel, F. *et al.* Tuning packing and solubility of donor (D)-acceptor (A) polymers by cis - Trans isomerization within alkenyl side chains. *Chem. Mater.* **26**, 4844–4848 (2014).

25. Hanamura, H. & Nemoto, N. Synthesis and properties of cyclopentadithiophene-based poly(silarylenesiloxane) derivatives. *Polymer (Guildf).* **52**, 5282–5289 (2011).

26. Gao, Y. *et al.* Recent development on narrow bandgap conjugated polymers for polymer solar cells. *Polymers (Basel).* **9**, (2017).

27. Azoulay, J. D., Koretz, Z. A., Wong, B. M. & Bazan, G. C. Bridgehead imine substituted cyclopentadithiophene derivatives: An effective strategy for band gap control in donor-acceptor polymers. *Macromolecules* **46**, 1337–1342 (2013).

28. Coppo, P., Cupertino, D. C., Yeates, S. G. & Turner, M. L. Synthetic routes to solution-processable polycyclopentadithiophenes. *Macromolecules* **36**, 2705–2711 (2003).

29. Caffy, F. *et al.* Synthesis, optoelectronic properties and photovoltaic performances of wide band-gap copolymers based on dibenzosilole and quinoxaline units, rivals to P3HT. *Polym. Chem.* **7**, 4160–4175 (2016).

30. Beaupré, S., Boudreault, P. L. T. & Leclrec, M. Solar-energy production and energy-efficient lighting: Photovoltaic devices and white-light-emitting diodes using poly(2,7-fluorene), poly(2,7-carbazole), and poly(2,7-dibenzosilole) derivatives. *Adv. Mater.* **22**, (2010).

31. Boudreault, P.-L. T., Michaud, A. & Leclerc, M. A New Poly(2,7-Dibenzosilole) Derivative in Polymer Solar Cells. *Macromol. Rapid Commun.* **28**, 2176–2179 (2007).

32. Chan, K. L., McKiernan, M. J., Towns, C. R. & Holmes, A. B. Poly(2,7-dibenzosilole): A blue light emitting polymer. *J. Am. Chem. Soc.* **127**, 7662–7663 (2005).

33. Yao, B. *et al.* 2,1,3-Benzothiadiazole-5,6-dicarboxylic imide based low-bandgap polymers for solution processed photodiode application. *Org. Electron. physics, Mater. Appl.* **26**, 305–313 (2015).

34. Nielsen, C. B. *et al.* 2,1,3-benzothiadiazole-5,6-dicarboxylic imide - A versatile building block for additive- and annealing-free processing of organic solar cells with effi ciencies exceeding 8%. *Adv. Mater.* **27**, 948–953 (2015).

35. Yu, J. *et al.* 2,1,3-Benzothiadiazole-5,6-dicarboxylicimide-Based Polymer Semiconductors for Organic Thin-Film Transistors and Polymer Solar Cells. *ACS*

Appl. Mater. Interfaces **9**, 42167–42178 (2017).

36. Wu, Y. & Zhu, W. Organic sensitizers from D-π-A to D-A-π-A: Effect of the internal electron-withdrawing units on molecular absorption, energy levels and photovoltaic performances. *Chem. Soc. Rev.* **42**, 2039–2058 (2013).

37. Patil, H. *et al.* Donor-acceptor-donor modular small organic molecules based on the naphthalene diimide acceptor unit for solution-processable photovoltaic devices. *J. Electron. Mater.* **43**, 3243–3254 (2014).

38. Li, Y. *et al.* The effect of thieno[3,2-b]thiophene on the absorption, charge mobility and photovoltaic performance of diketopyrrolopyrrole-based low bandgap conjugated polymers. *J. Mater. Chem. C* **1**, 7526–7533 (2013).

39. Zhang, W. *et al.* Molecular engineering and sequential cosensitization for preventing the "trade-off" effect with photovoltaic enhancement. *Chem. Sci.* **8**, 2115–2124 (2017).

40. Chen, H. Y. *et al.* Morphologic improvement of the PBDTTT-C and PC71BM blend film with mixed solvent for high-performance inverted polymer solar cells. *Nanotechnology* **24**, (2013).

41. Murad, A. Development of New Conjugated Polymers for Organic Photovoltaics. *Thesis, The University of Sheffield* (2017).

42. Mumyatov, A. V., Prudnov, F. A., Inasaridze, L. N., Mukhacheva, O. A. & Troshin, P. A. High LUMO energy pyrrolidinofullerenes as promising electron-acceptor materials for organic solar cells. *J. Mater. Chem. C* **3**, 11612–11617 (2015).

43. Zhao, G. *et al.* Photovoltaic properties of poly(benzothiadiazole-thiophene-co-bithiophene) as donor in polymer solar cells. *Sol. Energy Mater. Sol. Cells* **95**, 704–711 (2011).

44. Leo, K. Elementary Processes in Organic Photovoltaics. **272**, *Springer International Publishing*, (2017).

45. Zhang, Z. G. & Wang, J. Structures and properties of conjugated Donor-Acceptor copolymers for solar cell applications. *J. Mater. Chem.* **22**, 4178–4187 (2012).

46. Gieseking, B. *et al.* Excitation dynamics in low band gap donor-acceptor copolymers and blends. *Adv. Energy Mater.* **2**, 1477–1482 (2012).

47. Brazovskii, S. & Kirova, N. Physical theory of excitons in conducting polymers. *Chem. Soc. Rev.* **39**, 2453–2465 (2010).

48. Vezie, M. S. *et al.* Exploring the origin of high optical absorption in conjugated polymers. *Nat. Mater.* **15**, 746–753 (2016).

49. Kästner, C., Vandewal, K., Egbe, D. A. M. & Hoppe, H. Revelation of Interfacial Energetics in Organic Multiheterojunctions. *Adv. Sci.* **4**, (2017).

50. Zhang, F. *et al.* Influence of $PC_{60}BM$ or $PC_{70}BM$ as electron acceptor on the performance of polymer solar cells. *Sol. Energy Mater. Sol. Cells* **97**, 71–77 (2012).

51. Kass, K. J., Forster, M. & Scherf, U. Incorporating an Alternating Donor–Acceptor Structure into a Ladder Polymer Backbone. *Angew. Chemie - Int. Ed.* **55**, 7816–7820 (2016).

52. Brédas, J. L., Beljonne, D., Coropceanu, V. & Cornil, J. Charge-transfer and energy-transfer processes in π-conjugated oligomers and polymers: A molecular

picture. *Chem. Rev.* **104**, 4971–5003 (2004).

53. Yang, L. *et al.* Naphthalene-fused BODIPY with large Stokes shift as saturated-red fluorescent dye for living cell imaging. *Dye. Pigment.* **122**, 1–5 (2015).

54. Baran, D. *et al.* Processable Multipurpose Conjugated Polymer for Electrochromic and Photovoltaic Applications. *Chem. Mater.* **22**, 2978–2987 (2010).

55. Pal, K., Sharma, V., Sahoo, D., Kapuria, N. & Koner, A. L. Large Stokes-shifted NIR-emission from nanospace-induced aggregation of perylenemonoimide-doped polymer nanoparticles: Imaging of folate receptor expression. *Chem. Commun.* **54**, 523–526 (2017).

56. Varma, P. C. R. & Namboothiry, M. A. G. Squaraine based solution processed inverted bulk heterojunction solar cells processed in air. *Phys. Chem. Chem. Phys.* **18**, 3438–3443 (2016).

57. Liu, Y. X., Summers, M. A., Scully, S. R. & McGehee, M. D. Resonance energy transfer from organic chromophores to fullerene molecules. *J. Appl. Phys.* **99**, (2006).

58. Lu, X. *et al.* Bilayer order in a polycarbazole-conjugated polymer. *Nat. Commun.* **3**, 795 (2012).

59. Blouin, N. *et al.* Toward a Rational Design of Poly(2,7-Carbazole) Derivatives for Solar Cells. *J. Am. Chem. Soc.* **130**, 732–742 (2008).

60. Kline, R. J. *et al.* Critical Role of Side-Chain Attachment Density on the Order and Device Performance of Polythiophenes. *Macromolecules* **40**, 7960–7965 (2007).

61. Beiley, Z. M. *et al.* Morphology-Dependent Trap Formation in High Performance Polymer Bulk Heterojunction Solar Cells. *Adv. Energy Mater.* **1**, 954–962 (2011).

62. MacHui, F., Rathgeber, S., Li, N., Ameri, T. & Brabec, C. J. Influence of a ternary donor material on the morphology of a P3HT:PCBM blend for organic photovoltaic devices. *J. Mater. Chem.* **22**, 15570–15577 (2012).

63. Rathgeber, S. *et al.* Correlation between polymer architecture, mesoscale structure and photovoltaic performance in side-chain-modified poly(p-arylene-ethynylene)-alt- poly(p-arylene-vinylene): PCBM bulk-heterojunction solar cells. *Polymer (Guildf).* **52**, 3819–3826 (2011).

64. Xiao, Z. *et al.* Effect of molecular weight on the properties and organic solar cell device performance of a donor-acceptor conjugated polymer. *Polym. Chem.* **6**, 2312–2318 (2015).

65. Yao, K., Chen, L., Chen, Y., Li, F. & Wang, P. Influence of water-soluble polythiophene as an interfacial layer on the P3HT/PCBM bulk heterojunction organic photovoltaics. *J. Mater. Chem.* **21**, 13780–13784 (2011).

66. Koyuncu, S. *et al.* Electrochromic and electroluminescent devices based on a novel branched quasi-dendric fluorene-carbazole-2,5-bis(2-thienyl)-1H-pyrrole system. *J. Mater. Chem.* **21**, 2684–2693 (2011).

67. Chen, Q. *et al.* Under the spotlight: The organic-inorganic hybrid halide perovskite for optoelectronic applications. *Nano Today* **10**, 355–396 (2015).

68. Nelson, J. Polymer:fullerene bulk heterojunction solar cells. *Mater. Today* **14**, 462–470 (2011).

69. Guo, B. *et al.* Improving efficiency of polymer solar cells via a treatment of methanol:water on the active layers. *J. Mater. Chem. A* 1–4 (2016).

70. Li, Z. *et al.* Toward Improved Lifetimes of Organic Solar Cells under Thermal Stress: Substrate-Dependent Morphological Stability of PCDTBT:PCBM Films and Devices. *Sci. Rep.* **5,** 1–9 (2015).

71. Jiang, Y. *et al.* Tuning optical and electronic properties of star-shaped conjugated molecules with enlarged π-delocalization for organic solar cell application. *J. Mater. Chem. A* **1,** 8270–8279 (2013).

72. Scharber, M. C. *et al.* Design rules for donors in bulk-heterojunction solar cells - Towards 10 % energy-conversion efficiency. *Adv. Mater.* **18,** 789–794 (2006).

73. Salleo, A. Charge transport in polymeric transistors. *Mater. Today* **10,** 38–45 (2007).

74. Bathula, C. *et al.* Concentration-Dependent Pyrene-Driven Self-Assembly in Benzo[1,2-b:4,5-b′]Dithiophene (BDT)-Thienothiophene (TT)-Pyrene Copolymers. *Macromolecules* **48,** 3509–3515 (2015).

75. Bajpai, M., Srivastava, R., Dhar, R. & Tiwari, R. S. Role of reduced pi-pi stacking in the charge transport in polyfluorene. *Mater. Sci. Eng. B Solid-State Mater. Adv. Technol.* **212,** 62–70 (2016).

76. Tong, S. W. *et al.* The use of thermal initiator to make organic bulk heterojunction solar cells with a good percolation path. *Appl. Phys. Lett.* **93,** 1–5 (2008).

77. Street, R. A., Song, K. W. & Cowan, S. Influence of series resistance on the photocurrent analysis of organic solar cells. *Org. Electron. physics, Mater. Appl.* **12,** 244–248 (2011).

78. Servaites, J. D., Yeganeh, S., Marks, T. J. & Ratner, M. A. Efficiency enhancement in organic photovoltaic cells: Consequences of optimizing series resistance. *Adv. Funct. Mater.* **20,** 97–104 (2010).

79. Dhass, A. D., Natarajan, E. & Ponnusamy, L. Influence of shunt resistance on the performance of solar photovoltaic cell. *Proc. - ICETEEEM 2012, Int. Conf. Emerg. Trends Electr. Eng. Energy Manag.* 382–386 (2012).

80. Usluer, Ö., Boudiba, S., Egbe, D. A. M., Hirsch, L. & Abbas, M. Control of carrier mobilities for performance enhancement of anthracene-based polymer solar cells. *RSC Adv.* **5,** 50668–50672 (2015).

Chapter 5

Solution engineering to improve the efficiency of perovskite solar cells

5.1 Introduction

Organic-inorganic halide perovskites are fascinating materials with great implications for optoelectronics. Their combination of high charge-carrier mobility, efficient light absorption and compatibility with low-temperature solution-based processes make them particularly suited to photovoltaic applications in perovskite solar cells (PSCs). Since the early work of Kojima et al. [1], recent research efforts have seen their power conversion efficiencies (PCEs) rise from 3.8% to 22.1% [2] in state-of-the art devices. Conventionally, PSC active layers are deposited from a precursor solution of which is most commonly composed of a blend of lead halides and methylammonium halides. After casting the precursor solution to create a wet thin-film, thermal annealing leads to the formation of a polycrystalline perovskite crystal film. Managing this process is key to producing high-efficiency PSCs, as their performance is very sensitive to active layer microstructure and crystal purity [3–5]. To address this issue, solution additives including water [6,7], hydrogen iodide (HI) [8–10], alkyl halides [11,12] and chloronaphthalene [13] (when added in the correct concentration), have all been shown to enhance PSC device efficiency by controlling the perovskite crystallisation kinetics. This can be done through the modulation of lead salt solubility and solvent drying rate [14–16]. Rather than the rapid perovskite crystal formation during film casting typical of single halide systems, mixed halide ink systems rely on extended thermal treatments to convert the precursor to the final perovskite form [17,18]. In such systems, the crystal formation

dynamics are distinctly different and thus require another set of processing conditions for the fabrication of efficient PSCs.

In this chapter, the well characterised MAI:$PbCl_2$ precursor ink formulation is used in the single-step deposition of $MAPbI_{3-x}Cl_x$ perovskite thin-films in planar PSC device architectures [19,20]. Two different techniques to deposit the MAI:$PbCl_2$ precursor are employed: spin-coating and spray-coating. While spin-coating has been the method of choice to fabricate PSCs, there is growing interest in the use of spray-coating [21–24], as it presents a ready means for possible manufacture scale-up [25]. Through careful optimisation of PSC fabrication conditions, the addition of acidic hydriodic acid (HI) to the perovskite precursor solution is shown to have a marked positive effect on device behaviour; an observation that applies to PSCs prepared both by spin-casting and spray-casting.

5.2 Hydriodic acid solution study using dynamic light scattering

Hydrogen iodide exists as gas at room temperature, which when dissolved in H_2O forms an hydriodic acid (HI) solution. For this study, a 57 wt. % solution of hydrogen iodide in H_2O was utilized. HI forms a pale yellow solution and is used primarily in industry as a reducing agent [26]. At 57 wt% in H_2O, HI has a density of 1.7 g/ml and a boiling point of 127°C, making it suitable for the processing temperatures used in this study. Previous work by Heo et al. demonstrated that adding HI at 9.1 vol% to a 1:1 MAI:PbI_2 precursor ink facilitates single-step deposition of a continuous $MAPbI_3$ film without pinholes or impurities, leading to standard-architecture devices having a remarkably high PCE (17.2% average) [9]. These authors attributed such effects to the enhanced solubility of $MAPbI_3$ that favours the growth of a continuous perovskite crystal during the film formation process. Furthermore, it was suggested that the HI facilitated a recovery of decomposed MAI, resulting in the formation of a pure perovskite crystal. In the following chapter, HI was incorporated into the perovskite precursor between 1 and 4

vol% before vortex mixing and solution heating, and its effects on PSC device efficiency is studied in detail.

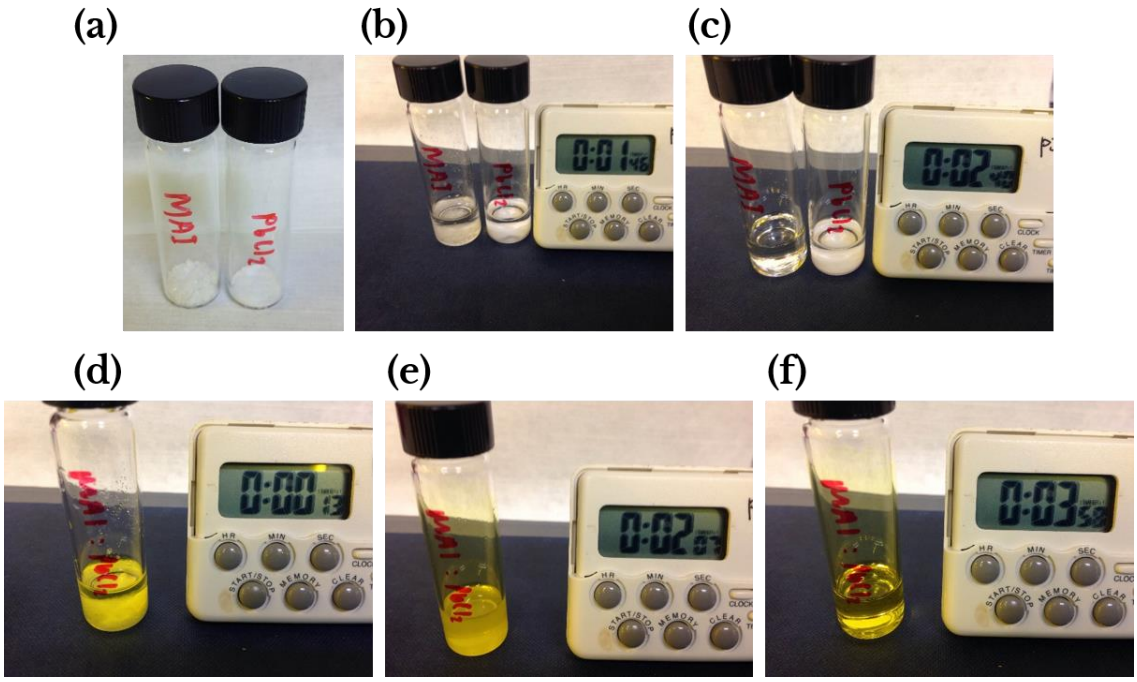

Figure 5.1 - Solution study of precursor materials mixed with N,N-dimethylformamide (DMF) with and without HI solution. Note that the vials shown here are clear for the purpose of visualisation. In the actual experiments amber vials were used to reduce any UV-degradation effects. A stop clock is included to record the timescale of the solution study. (a) An image of MAI and $PbCl_2$ powders in separate vials without solvent. (b) The same MAI and $PbCl_2$ vials after the addition of 1.5 ml of DMF. (c) After vortex mixing for 30 seconds. (d) 500mg/ml solution of 2.9:1 (MAI:$PbCl_2$) after adding DMF. (e) The same 500 mg/ml solution after vortex mixing for 30 seconds and (f) after addition of 1 vol% HI and a further 30 seconds vortex mixing of the 500 mg/ml solution.

The effect of HI in the context of solution engineering is presented in **Figure 5.1**. It can be seen in **Figure 5.1 (a)** to **(c)**, that by simply adding pure DMF to separate vials of MAI and $PbCl_2$ it is not possible to fully dissolve the lead-halide precursor, however the opposite is found for the organic MAI. After ink preparation, it is observed that the

perovskite precursor ink appears turbid, indicating the presence of unsolvated precursor materials. As shown in **Figure 5.1 (d)** to **(f)**, by adding small quantities of HI these suspended particles are effectively eliminated, leading to the formation of a clear solution. This observation is supported by the dramatic reduction in particulate size utilising the method of dynamic light scattering (DLS) after HI addition, as shown in **Figure 5.2**. This measurement confirms that on addition of HI, there is (i) a large reduction in solution turbidity, and (ii) a change in the average particle size. Without the presence of HI, the solution contains a significant population of micron-sized crystallites (1370 ± 480 nm). On addition of 1 vol% HI, these are apparently absent and replaced by a population of nanoparticles having a diameter of 1.7 ± 0.4 nm. Williams et al. [27] have also detected the presence of 40 nm diameter aggregates in this precursor ink formulation. Note that owing to difficulties associated with effectively separating the aggregates from their parent solutions, without significantly altering them, this investigation was limited to comparative studies of precursors in solution.

Mixing the precursors leads to a large increase in $PbCl_2$ solubility and gives the ink a yellow appearance implying the formation of a lead polyhalide-based soft coordination complex with corresponding red-shifted excitonic absorption [28]. This process alone does not appear to be sufficient to fully disrupt the cohesive forces within the $PbCl_2$ precursor, and some material remains undissolved in the ink without the presence of the HI additive. It is therefore clear that the HI additive has a marked effect on the $PbCl_2$ solubility. This can be evidenced in **Figure 5.1 (e)** to **(f)**, where addition of 1 vol% HI to a $PbCl_2$ solution just above its solubility limit in DMF (40 mg/ml), appears to solvate all the previously undissolved $PbCl_2$ solid. This solvation process is accompanied by a colour change of the solution from colourless to yellow, indicative of the presence of a mixed lead-halide coordination compound [29].

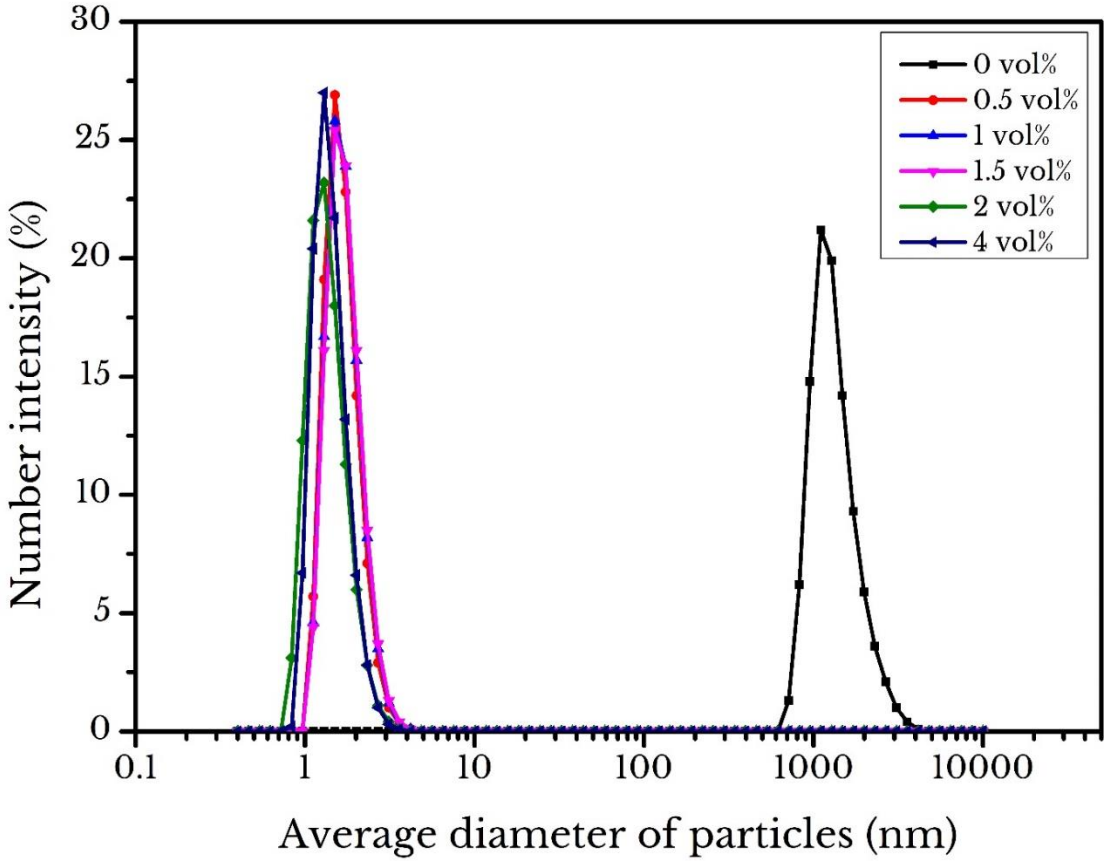

Figure 5.2 - Size distribution of chloride-based aggregates measured by dynamic light scattering from precursor solutions, which shows a decrease in particle size as the large aggregates that are initially present become dispersed and solvated as more HI is added.

5.3 Thin film characterisation

From **Figure 5.2**, it is clear the addition of hydriodic acid in to the perovskite precursor decreases the particulate size in solution. Before solar cell devices were fabricated, perovskite thin-film samples were prepared from precursor solutions from a range of hydriodic acid concentrations. These samples were used to study the crystallographic properties of the perovskite crystals before and after the addition of HI. The importance of optimising crystallinity in perovskite solar cells is well reported, leading to greater charge carrier mobilities and improved solar cell device performance [30,31].

5.3.1 Scanning electron and white light reflection microscopy

To explore the role of the HI precursor additive on modifying perovskite film-structure, scanning electron microscopy (SEM) was first used to explore $MAPbI_{3-x}Cl_x$/PEDOT:PSS films at high resolution, as shown in **Figure 5.3**. Here, spin-cast films from solutions without (**Figure 5.3 (a)**, **(c) and (e)**) and with a 1% HI additive (**Figure 5.3 (b)**, **(d)**, **(f)**) are measured at comparable thicknesses (see **Table 5.1**).

HI concentration (vol%)	Perovskite film thickness (nm)	
	Spin-coated	Spray-coated
0	397 ± 15	311 ± 70
1	394 ± 11	330 ± 60
2	433 ± 12	331 ± 60
3	418 ± 13	572 ± 80
4	503 ± 25	459 ± 25

Table 5.1 - Post annealed film thickness of $MAPbI_{3-x}Cl_x$ films spray-coated and spin-coated from precursor solutions containing different HI vol% onto ITO/PEDOT measured at five different locations by profilometry. Note the standard deviation in thickness is much higher for spray-coated samples.

In all SEM figures presented, the darkest areas correspond to gaps in the film that are most clearly identified in the back-scattered electron (BSE) images, as shown in **Figure 5.3 (a)** and **(b)**. From the latter, it is immediately clear that the film cast from the precursor containing the 1 vol% HI additive forms a more continuous layer and has a

significantly increased surface coverage, being 93.8% (without HI additive) and 99.7% with 1 vol% HI additive.

The secondary electron (SE) images (see **Figure 5.3 (c)** to **(f)**) reveal the individual grains wherein the average size of the crystallites in films cast from additive-free precursor inks are ≈ 40% smaller than films cast with the HI additive (**530 ± 20** and **390 ± 20** nm respectively). These findings are in agreement with morphological studies of such samples [14,32,33]. From the lower magnification SE images (see **Figure 5.3 (c)** and **(d)**) it is apparent that films cast from the precursor containing the HI additive show strong local morphology variations and contain two distinctly different morphologies: (1) rounded and (2) elongated crystallites. The latter is absent in the film cast from the precursor without the HI additive. This could be explained by an increase in the solubility of $PbCl_2$ when HI is added, where perovskite crystals are more likely to grow slowly and along the substrate surface producing larger crystal grains [34]. In the higher magnification images of both materials (**Figure 5.3 (e)** and **(f)**) it becomes clear that smaller grains are located on top of rather larger grains.

All of the above observations are consistent with a model proposed by Williams et al. [24], which explains the morphological variations in $MAPbI_{3-x}Cl_x$ films are a result of templated topotactic self-assembly in the presence of chloride. In this model, the larger rectangular structures in **Figure 5.3 (d)** and **(f)** are suggested to result from the rapid growth of $MAPbCl_3$, present only in films cast from fresh solutions containing $PbCl_2$, which is linked to subtle variations in chloride concentration due to aggregation in the solution [24]. It is worth noting that the absence of such rectangular features in films cast from solutions without the HI additive (**Figure 5.3 (c) and (e)**) can be related to the nature of $PbCl_2$ aggregates in the additive-free solutions. Thus, the addition of HI to the precursor solution has a strong influence on the perovskite crystallisation dynamics and subsequently the resultant morphology of the converted perovskite thin-film.

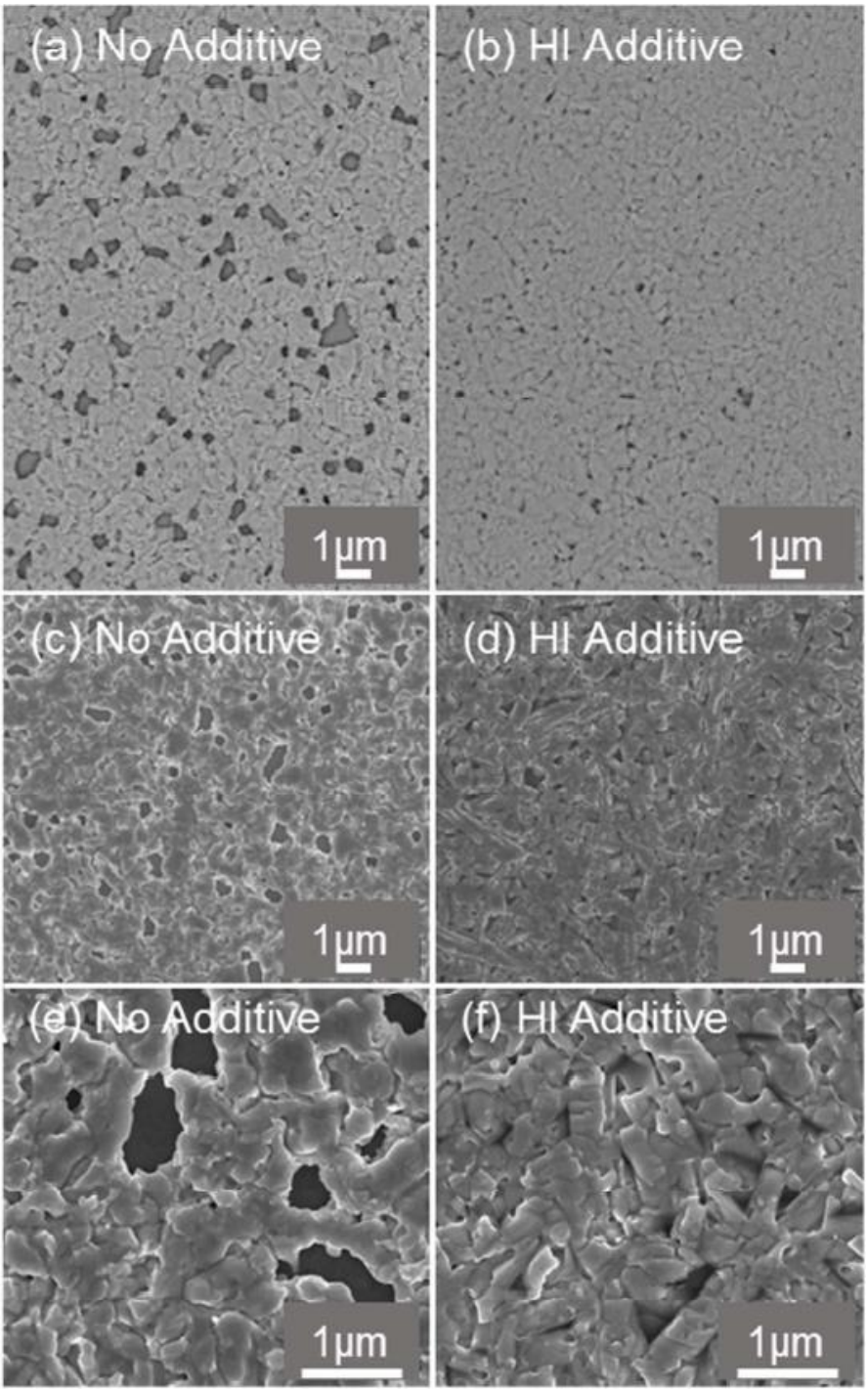

Figure 5.3 - SEM images of ITO/PEDOT:PSS/$MAPbI_{3-x}Cl_x$ thin-films spin-cast from additive free (parts (a), (c), (e)) and additive-containing at 1 vol% (parts (b), (d), (f)) precursor solutions imaged with different detectors and at different magnifications, respectively: (a) and (b) are backscattered electron (BSE) images, with (c) to (f) being secondary electron (SE) images. A 1 μm scale-bar is shown as the inset.

White light reflection microscopy was also used to characterise PEDOT:PSS/$MAPbI_{3-x}Cl_x$ thin-films (post anneal) that were cast using different initial concentrations of HI (see **Figure 5.4 (a) to (d)**). Here, it can be seen that films containing 0 vol % and 1 vol % of HI appear relatively compact, however as the HI concentration is increased, the film is increasingly characterised by large, disconnected crystallites having poor surface coverage. It will be apparent later that the addition of 1 vol% HI to the precursor solution enhances the performance of devices and emphasises the importance of this finding as a transferrable method for controlling perovskite crystallisation dynamics and promoting high PCE.

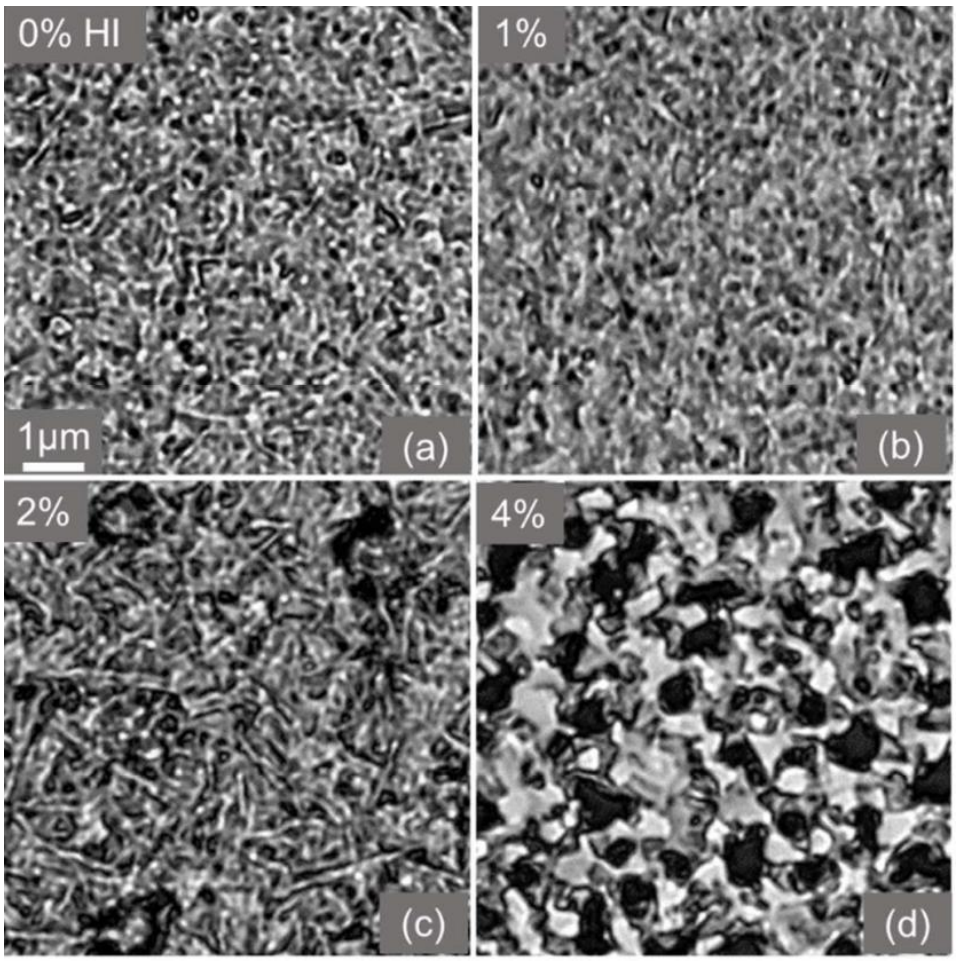

Figure 5.4 - White light microscope images taken in reflection mode showing the development of PEDOT:PSS/$MAPbI_{3-x}Cl_x$ thin-film microstructure upon increasing precursor ink HI vol% from 0 % (part (a)) up to 4 % (part (d)). A 1 µm scale bar is shown as the inset in part (a).

5.3.2 Absorption and photoluminescence

The optical absorption spectra of spin-cast perovskite films cast with and without the HI additive (1 vol%) deposited onto a glass substrate are shown in **Figure 5.5 (a)**. It is found that there is a clear increase in optical density (by 6 %) for 1 and 2 vol% across the entire spectrum resulting from the addition of HI to the precursor solution. Given that these films are of comparable thicknesses (except 4 vol%), this increase in absorption may be accounted for by an increase in surface coverage across the active layer; a fact that is supported by SEM images shown in **Figure 5.5 (a)** and **(b)**. However, since this disparity lies within the error of the profilometry measurement, it cannot be ruled out that a change in thickness between samples is responsible for the observed increase in optical density. Interestingly, the absorption onset is also red-shifted by 13 meV in the 1 vol% additive-containing films, as can be seen in **Figure 5.5 (a)**. This red-shift in absorption onset is accompanied by a similar red-shift in PL emission, as is also shown in **Figure 5.5 (b)**, which is believed to result from enhanced perovskite crystal growth [9]. Similar red-shift behaviour has been seen for perovskites with larger crystallites relative to a reference film [35]. An enhancement in crystallinity causes an overall increase in absorption across a wide spectral range producing a larger PL intensity. This is also due to a decrease in bandgap energy and longer carrier lifetimes in larger crystal domains, indicative of a reduction in biomolecular recombination and defect density. As discussed later, a reduction in lattice strain can also indicate a small change in the perovskite lattice parameters, aiding in the formation of larger crystallites and thus inducing a red-shift [36].

The inset to **Figure 5.5 (b)** presents SSPL spectra for perovskite films on quartz glass containing, 0, 1, 2 and 3 vol% HI in the precursor. It is clear the emission from the 1 and 2 vol% samples is enhanced relative to the reference (0 vol%) films most likely due to the improved crystallinity (see XRD analysis later). The PL emission peaks show a progressive red-shift with increasing HI concentration, with peaks at 761, 768, 774 and 781 nm for 0, 1, 2 and 3 vol% films, respectively. This appears to contradict the blue-shift observed in higher HI concentrations (3 and 4 vol%).

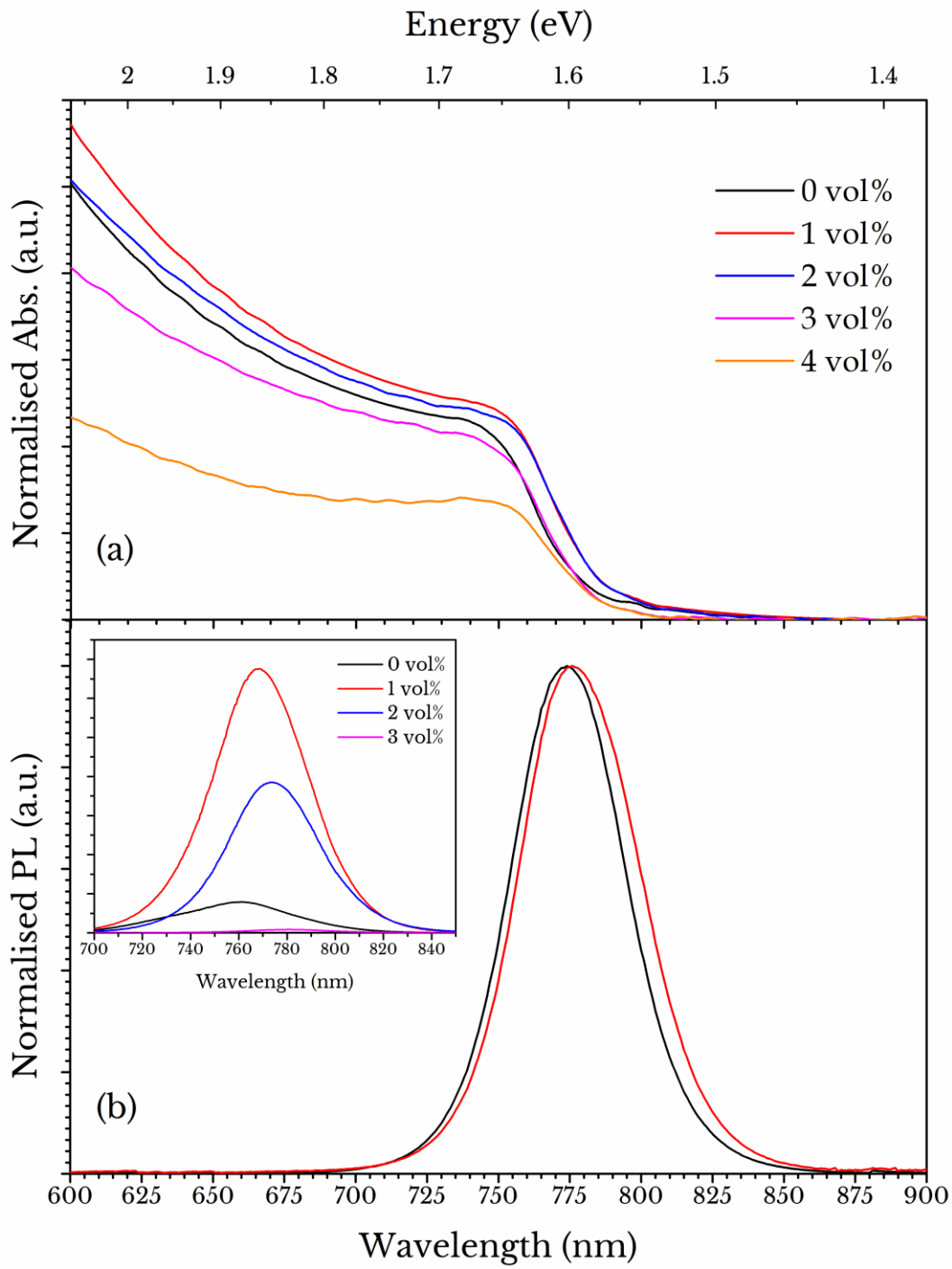

Figure 5.5 - Optical spectroscopy of spin-cast ITO/ $MAPbI_{3-x}Cl_x$ thin-films prepared from precursor solutions with (red line) a 1 vol% HI-additive and without (black line). Part (a) plots optical absorption spectra using a HI concentration between 0 and 4 vol%. Part (b) shows normalised steady-state PL spectra for 0 and 1 vol% HI concentration (black and red lines respectively). The inset in (b) shows steady-state PL spectra for varying HI concentration without a PEDOT:PSS layer.

One possible explanation for this red-shift behaviour is that higher concentrations of iodide in the precursor (in the form of acidic HI) could drive the perovskite formation dynamics in the drying film to produce more 'phase-pure' $MAPbI_3$ grains, instead of a mixed-halide system which incorporates chloride ions ($MAPbI_{3-x}Cl_x$). Introducing more electronegative halides into a pure-iodide perovskite precursor will blue-shift the peak emission from the sample [37,38]. Thus, it can be speculated that higher concentrations of iodine in the precursor reduces the chloride content in the resultant perovskite film.

To understand the free carrier and exciton kinetics of 0 vol% and 1 vol% HI-additive perovskite films on p-type PEDOT:PSS, time-resolved photoluminescence (TRPL) was performed at a range of fluencies at 290 K. For more information on the experimental setup used, please see **Section 3.8.2**. As shown in **Figure 5.6**, the PL decay characteristics show similar trends for both samples as a function of laser fluence, comparable to other fluence-dependant measurements performed on related perovskite materials [39,40]. The extracted fitting parameters from a bi-exponential fit [43,44] are shown in **Table 5.2**. Here, the fast decay component (τ_1) is attributed to non-radiative recombination pathways (charge extraction, traps and surface effects) [45] and the slow component (τ_2) is related to the radiative combination within the bulk of the perovskite [46,47].

The fast decay component (τ_1), associated with nonradiative charge recombination and charge transfer to the PEDOT:PSS layer, is largely unchanged with increasing fluence. However, it is worth noting that these perovskite films were prepared to replicate device conditions and as such the film thicknesses are in the order of 400 nm (see **Table 5.1**), with each sample being illuminated at the top perovskite surface (side away from the glass substrate). At an excitation wavelength of 405 nm, the expected penetration depth of $MAPbI_3$ is < 100 nm [48,49] and as such the true charge-extraction properties of these films is unclear. Previous bi-layer perovskite film studies have seen an increase in the τ_1 decay component when probing the interface side directly [50]. Future experiments studying the charge-extraction properties of solution additive perovskite films should take this effect in to consideration, with measurements being taken at the air/perovskite and PEDOT:PSS/perovskite interface.

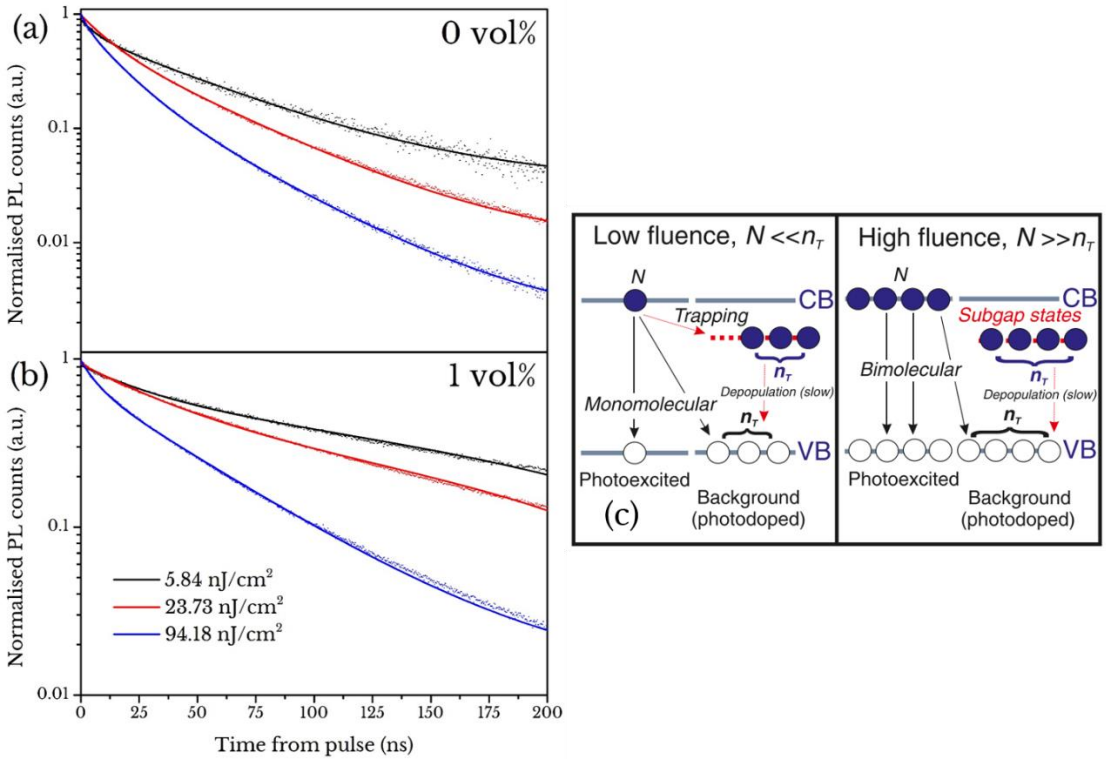

Figure 5.6 – Time-resolved photoluminescence (TRPL) spectra at 3 laser fluencies for (a) 0 vol % and (b) 1 vol% HI resultant films. (c) A schematic representation of the fluence-dependant recombination mechanism in perovskites. Image (c) was adapted from reference 41.

Across the range of laser fluencies, the HI additive (1 vol%) sample produced longer τ_2 lifetimes, indicative of a lower defect density (reduced levels of nonradiative recombination) and greater electron transport qualities in the bulk of the material [51]. This improved carrier lifetime in the bulk would also correlate with a longer charge diffusion length, which has been shown to significantly improve the performance of planar architecture perovskite solar cells [51,52]. At low fluence (5.8 nJ/cm^2), the inclusion of 1 vol% HI lengthens the radiative recombination lifetime from 52.8 ns to 101.2 ns, an increase of over 90%. Upon increasing the laser fluence, both samples displayed a reduced τ_2 lifetime. The decrease in PL lifetime as a function of laser fluence can be explained by a relationship between photoinduced electrons, trap states and the photodoped hole concentration. The term 'photodoped' here describes the large concentration of holes that exist due to filled electronic trap states in the steady-state [41].

HI conc.	Power density ($nJ.cm^{-2}$)	A_1 (%)	τ_1 (ns)	A_2 (%)	τ_2 (ns)	$\langle\tau\rangle$ (ns)
0 vol%	5.8	23.8	7.3	62.2	52.8	40.2
	23.7	38.3	11.2	58.9	42.1	29.9
	94.2	41.2	7.0	56.0	28.3	20.5
1 vol%	5.8	15.0	9.0	67.1	101.2	84.4
	23.7	27.6	7.6	68.5	49.1	37.2
	94.2	25.1	6.2	71.3	45.9	35.6

Table 5.2 – A summary of the extracted parameters from a bi-exponential fit of the TRPL traces. A_x and τ_x represent the amplitude and the decay lifetime of each exponential, respectively and $\langle\tau\rangle$ is the amplitude-weighted average lifetime.

Even at low laser fluencies, the concentration of photoinduced electrons is much lower than the total hole concentration, as the trap-assisted recombination lifetime for electrons is quite slow in the $MAPbI_3$ perovskite (microsecond timescale) [42]. Therefore, the level of photoexcitation at low fluence does not significantly change the hole concentration, which in turn will produce a near-monoexponential recombination mechanism. Moreover, by increasing the concentration of photoexcited electrons and holes to the point at which they becomes equal to the photodoped hole concentration, a bimolecular recombination mechanism is expected (**Figure 5.6 (c)**). As the free electron concentration decreases, the favoured pathway shifts to monomolecular recombination. This fluence-dependency trend has previously been observed in hybrid perovskites [53,54], attributed to fast second-order recombination with increasing charge carrier concentration.

After the observation of improved charge-carrier lifetimes in the HI-additive films, X-ray diffraction patterns were then taken from films cast from a range of HI-additive concentrations. The following section discusses results from such experiments, performed at the Department of Materials Science and Engineering, University of Sheffield.

5.3.3 X-ray diffraction

XRD patterns were recorded from films cast from precursor solutions both with and without a selection of HI additives onto a quartz glass surface, as shown in **Figure 5.7**. Peaks associated with the $MAPbI_3$ perovskite are located at 14.3 and 28.6 (tetragonal *I*4/*mcm* (β) phase) [57] corresponding to the (110) and (220) planes, respectively. The small reflection at 23.4° has been assigned to the (111) plane of the mixed halide $MAPbI_{3-x}Cl_x$ perovskite cubic *Pm3m* phase [58]. All of these peaks are more intense and shifted to smaller angles (larger d-spacing) in films cast using the HI additive. This result suggests that the perovskite lattice spacing increases from 6.29 to 6.32 Å in response to the addition of 1 vol% HI to the precursor ink; a result also consistent with red-shifted absorption and PL onsets, shown in **Figure 5.5**. A change in composition, possibly due to differences in chlorine concentration, may explain this effect in terms of lattice distortion [59].

In **Section 5.2** it was shown that by adding small quantities of HI, suspended particles were effectively eliminated leading to the formation of a clear solution containing particulates approximately one nanometre in size. This is supported by the peaks associated with increasing HI concentration beyond 1 vol%, where strong reflections are observed at 12.2° and 15.8°. These new peaks can be assigned to the (001) plane of PbI_2 [57,60] and the (100) plane of the $MAPbCl_3$ perovskite, respectively [61,62]. These reflections are not observed in the 0 vol% and 1 vol% samples. This further indicates that HI helps dissolve $PbCl_2$ particulates up to 1 vol%, as $MAPbCl_3$ and other chloride-based intermediates are not present in the final thin-films containing 0 and 1 vol% of HI additive. These extra I^- ions could assist in the removal of excess chloride in the form of CH_3NH_3Cl gas [59,63]. However, at concentrations greater than 2 vol% HI, the resultant film contains PbI_2 and $MAPbCl_3$ impurities which could be formed from the incomplete conversion of precursor materials into 3-dimensional (3D) $MAPbI_3$.

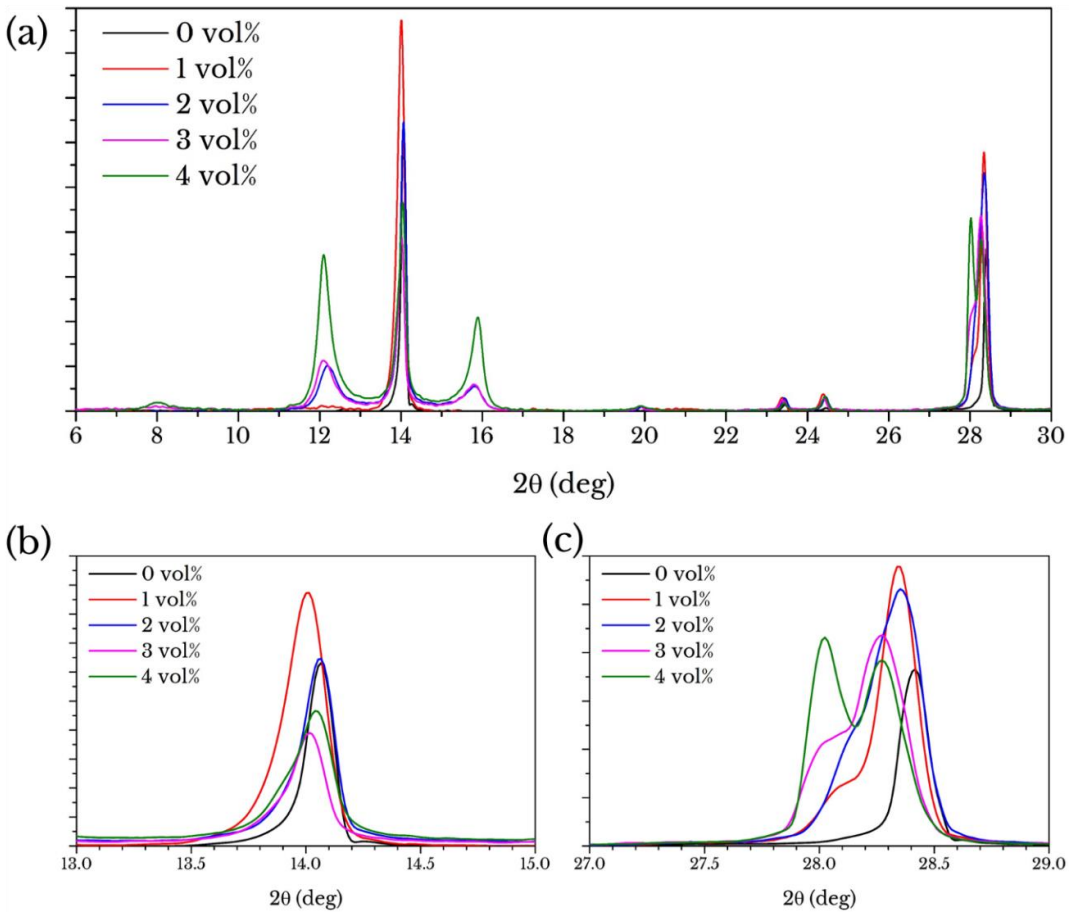

Figure 5.7 –X-ray diffractograms of representative quartz/$MAPbI_{3-x}Cl_x$ thin-films spin-casted from a precursor solution containing 0 vol% (black), 1 vol% (red). 2 vol% (blue), 3 vol% (magenta) and 4 vol% (green). (a) Indicates the full measured spectrum of the thin-film samples, (b) a close up of the (110)/(002) reflection and (c) a close-up version of the (220) and the emergence of the (004) plane. The XRD apparatus was first calibrated using a reference sample before running the above measurements.

Figure 5.7 (c) indicates the appearance of an additional peak at lower angles for higher HI concentrations as well as the (220) plane. The more intense peak for 0 – 3 vol% samples is assigned to the (220) plane, however, a shoulder appears around 28° for increasing HI concentrations. One possible explanation is that higher volumes of HI partially disrupt the growth of the $MAPbI_3$ resulting in perovskite crystal domains grown

with different orientations relative to the substrate. Previous reports suggest that the (00*l*) plane preferentially orientates parallel to the substrate for perovskite films cast from iodide-only precursors [66], from which the (004) plane is expected at 28°. Therefore, at higher HI concentrations, an increase in disordered crystal growth direction is observed through the appearance of the (004) plane. The introduction of crystal grains at different orientations would also present an increase in the number of grain boundaries. Therefore, films cast from relatively high HI concentrations (2 - 4 vol%) may have a greater potential for trap-assisted recombination and thus a reduction in short-circuit current.

5.4 Solar cell characterisation

A series of devices based on the inverted-structure ITO/PEDOT:PSS/ $MAPbI_{3-x}Cl_x$/LiF/Al were fabricated, where the active perovskite film was deposited from a MAI:$PbCl_2$ precursor solution in DMF with HI additive between 0 and 4 vol%. As two methods of deposition were used, namely spin and spray-coating, optimisation required several stages to create the best devices for study. First, a basic planar device architecture was developed and used in both deposition routines. The deposition of the PEDOT:PSS layer is described elsewhere in **Section 3.5** and was consistent throughout the following study. For the active layer, a solution made from a molar ratio of 2.9:1 (MAI:$PbCl_2$) was used containing DMF with varying amounts of HI solution. The precursor was held at a temperature of 70 °C before spin coating and the ITO/PEDOT:PSS films were held at 90°C or 70°C prior to perovskite deposition for spin and spray-cast techniques, respectively. The perovskite precursor solution was deposited at ambient temperature for spray-coating, with the substrates held at 70°C. Immediately after spin- or spray-coating, the ITO/PEDOT:PSS/$MAPbI_{3-x}Cl_x$ (wet) films were annealed at 90 °C for 90 minutes in air (30-32 RH%).

The perovskite films were coated via spin-coating with a $PC_{70}BM$ electron-extraction layer. Spin-cast films of $PC_{70}BM$ were deposited in a nitrogen-filled glove-box. $PC_{70}BM$

solutions for spin-casting were prepared at 50 mg ml^{-1} or 70 mg ml^{-1} in chlorobenzene, creating 150 and 200 nm thick films respectively. Prior to deposition, $PC_{70}BM$ solutions were heated to 70 °C for 1 hour, allowed to cool and then filtered through a 0.45 µm PTFE syringe filter. A cathode of LiF and aluminium was thermally evaporated at 2 nm at 0.1 Å s^{-1} and 100 nm at 1 Å s^{-1} respectively within a vacuum chamber held at *ca* 10^{-6} mbar. Devices were encapsulated using a UV-treated epoxy and encapsulation glass slide before testing. All pixel current-voltage (J-V) characteristic measurements underwent light-soaking (LS) to establish a stabilised power output. LS has been shown to improve device performance over several minutes due to the passivation of surface trap states at material interfaces [67,68].

Metric	Spin-cast		Spray-cast	
	0 vol%	**1 vol%**	**0 vol%**	**1 vol%**
PCE (%)	**6.7** (7.7) ± 0.9	**12.5** (13.8) ± 0.9	**6.1** (8.7) ± 1.5	**10.0** (11.4) ± 1.2
FF (%)	**58** (66) ± 8.8	**71** (77) ± 3.6	**65** (68) ± 2.2	**67** (70) ± 3.3
J_{sc} ($mAcm^{-2}$)	**14.1** (17.2) ± 1.3	**19.3** (22.6) ± 1.4	**12.8** (14.6) ± 1.3	**17.0** (17.4) ± 0.8
V_{oc} (V)	**0.82** (0.88) ± 0.07	**0.91** (0.97) ± 0.03	**0.73** (0.88) ± 0.10	**0.88** (0.93) ± 0.06

Table 5.3 - Performance metrics of PSC devices measured under 1 Sun simulated AM1.5G irradiation after 10 minutes light soaking (LS). LS is where a device is held under continuous illumination before a given measurement. Average values are expressed in bold. The spread in metrics is represented by the standard deviation.

Firstly, inverted perovskite devices were studied using the reference mixture (0 vol% HI) and a low concentration of HI additive at 1 vol% for spray and spin-coated devices. It is worth noting here that the active layer thicknesses between 0 and 1 vol% samples were very similar for both spray and spin coated layer, respectively. This implies that any device performance effects produced by the addition of HI should be associated with improved crystallinity or surface coverage and not simply a change in active layer thickness.

Without the addition of HI (0 vol%), devices had an average PCE of 6.1±1.5 % and 6.7±0.9 % for spray and spin coated active layers, respectively, after light soaking for 10 minutes. Champion PCEs for 0 vol% HI devices reached 8.7 % and 7.7 % for spray and spin coated devices, respectively. These values are lower than previous studies on spin-coated mixed iodide-chloride single cation inverted perovskite devices [69]. One possible reason for this reduced performance is incomplete solution mixing leaving undissolved material. Although the solution was left for an hour at 70 °C, particulates at micron size can still be detected as seen in **Figure 5.1**. However, after incorporating HI into the precursor at 1 vol%, a marked improvement in PCE is seen for both deposition routes. Average PCEs measured for spray-coated samples increases from 6.1±1.5 % (0 vol%) to 10.0±1.2 % (1 vol%); an overall improvement in PCE by 64% together with a small reduction in the deviation of pixel PCE from the mean. Enhancements in both V_{oc} and J_{sc} can be attributed to this significant change in device performance, discussed in more detail later. The same can be seen for devices with a spin-coated active layer, whereby the addition of 1 vol% HI improves the PCE from 6.7±0.9 % to 12.5±0.9 %; an improvement of 87 %.

Increasing the HI concentration above 1 vol% does not result in further PCE gains. At 2 vol%, the average PCE falls to around 10 % (3 %) for spin- (spray-) cast devices. However, this figure still exceeds that of the average reference 0 vol% devices created using the spin-cast route. At 2 vol% in spray-cast devices, the PCE decreases significantly whereby the average device performed worse than the reference devices as shown in **Figure 5.5 (b)** and **(d)**. It is likely doubling the HI concentration from the optimum alters the wet film drying dynamics such that the resultant perovskite film quality is reduced.

Although the average PCE improves slightly between 3 and 4 vol% (spin only), the standard deviation (represented by error bars in **Figure 5.8 (b)**) also increases. By 4 vol% in spray-coated devices, the average PCE had dropped below 1 %. It is likely the observed drop in PCE for larger HI concentrations is a result of introducing more grain boundaries in the annealed films as discussed earlier.

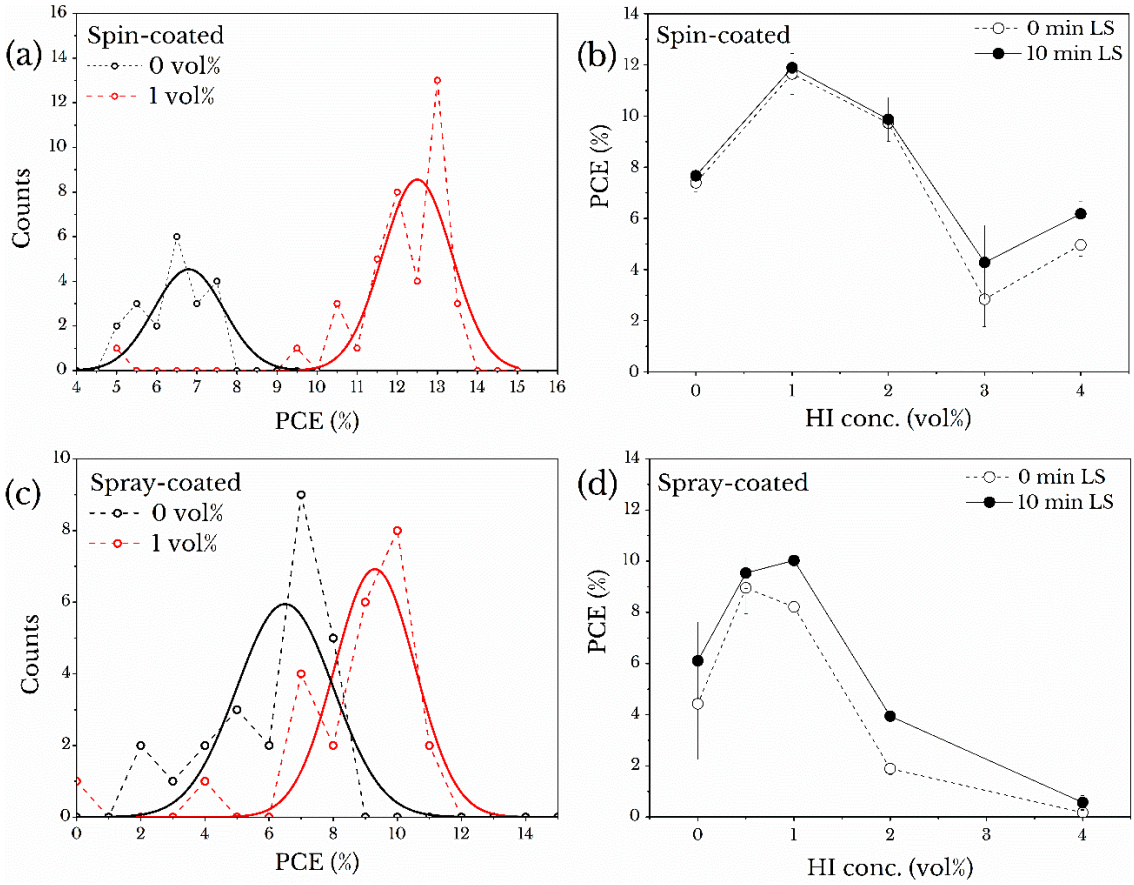

Figure 5.8 - Device PCE statistics from varying HI precursor concentration with and without light-soaking (LS) at AM1.5. (a) Raw device data from spin coated samples at 0 vol% and 1 vol% measured from 39 and 28 0.025 cm^2 pixels, respectively. The solid line represents a Gaussian fit. (b) HI additive tuning for spin-coated devices (c) Raw device data from spray-coated samples at 0 vol% and 1 vol% measured from 24 pixels in both cases. (d) HI additive tuning for spray-coated devices. The y-axis in (a) and (c) represent the number of pixels measured at a given PCE (%).

The average J_{sc} for spray cast reference devices was 12.8±1.3 $mAcm^{-2}$ and 14.1±1.3 $mAcm^{-2}$ for spin cast reference devices. The improved J_{sc} shown for spin coated samples could be explained by a discrepancy in final film surface coverage after annealing. Due to the mechanism in which films are coated via spray-coating deposition and droplet coalescence, surface coverage can be reduced when compared to films made via spin-coating as some droplets may not coalesce sufficiently leaving pin-holes. Another possible mechanism for the disparity between the two values could be that a rougher film is produced when spraying the perovskite films (**Table 5.1**), changing the reflective properties of the film and thus affecting J_{sc}. Upon the addition of HI, both deposition routes indicate an increase in J_{sc}. These values increase to 17.0±0.8 $mAcm^{-2}$ and 19.3±1.4 $mAcm^{-2}$ for spray and spin-coated devices respectively, indicating an overall improvement in film quality. This increase in film coverage is partially responsible for the observed increase in PSC photocurrent due to the enhanced optical absorption in these films, as presented in **Figure 5.3 (a) and (b)**. The TRPL results also indicate a longer τ_2 lifetime in films cast from 1 vol% HI precursor solutions, a result consistent with a reduction in non-radiative recombination pathways and increased J_{sc}.

The average V_{oc} for reference devices was measured at 0.73±0.10 V for spray coated and 0.82±0.07 V for spin-cast devices. After HI addition, these values increased to 0.88±0.06 V and 0.91±0.03 V, respectively. However, it is also likely that in devices processed without the HI additive, uncovered regions of PEDOT:PSS could form a Schottky junction with the overlying PCBM leading to an overall reduction in cell V_{oc} [70]. As both deposition routines show a similar trend in improved V_{oc}, it is possible that HI helps reduce recombination in the device and thus reducing the dark saturation current independent of the deposition route [71,72]. This is consistent with SEM images and absorption profiles (see **Figure 5.3** and **Figure 5.5**, respectively), showing both domain size increase and improved spectral absorbance after adding HI at 1 vol%. Comparing the FF achieved by both deposition techniques, it appears that the spray-coated reference devices have a higher FF than the spin-coated reference devices. This improved FF relative to spin-coated devices (65±2 vs 58±9 %) could be explained by the reduction in series resistance and other parasitic losses present in the active layer via spray-coating. The FF also improves for both deposition routes after HI addition, increasing from 65±2

and 58±9 % to 67±3 and 71±4 % for spray and spin cast, respectively. When spinning the solution there is a significant enhancement in the FF after adding HI by 22 %. It is not surprising that an improvement in FF is observed, as the FF depends strongly on the V_{oc} and J_{sc} due to the relationship discussed in **Section 2.3.**

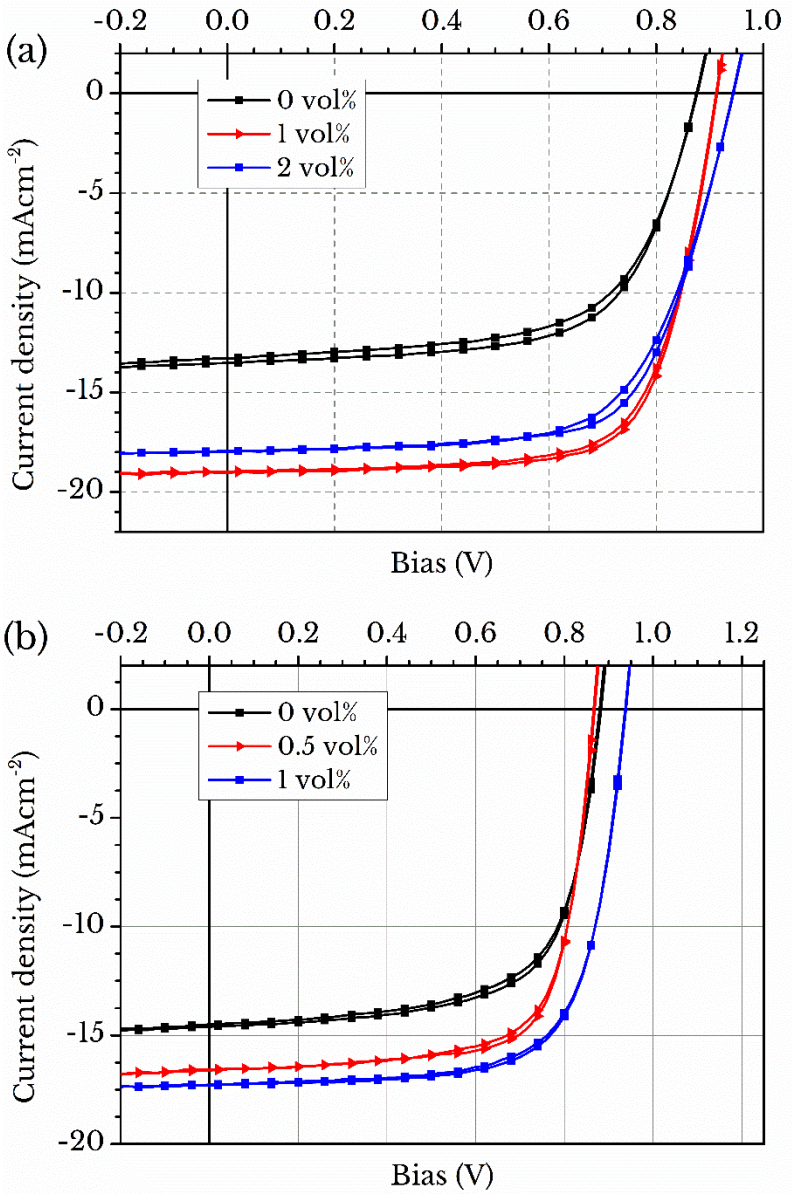

Figure 5.9 – Forward and reverse J-V sweeps shown for the champion pixels of (a) spin-coated at HI concentrations of 0 vol% (black line), 1 vol% (red line) and 2 vol% (blue line) and (b) spray-coated pixels at HI concentrations of 0 vol% (black line), 0.5 vol% (red line) and 1 vol% (blue line).

Finally, as indicated in **Figure 5.8 (b)** and **(d)**, higher concentrations of HI were used to fabricate devices using the spin- and spray-coating methods, with the J-V sweep for a champion 2 vol% device shown in **Figure 5.9 (a)**. The inclusion of 1 vol% was found to be the optimum for device performance, with 2 vol% still benefiting from improved device statistics over the reference spin-coated devices. The champion 2 vol% device produced a PCE of 11 %, a FF of 65 %, with V_{oc} and J_{sc} values measured at 0.98 V and 18 ma/cm^2, respectively. For completeness, 3 and 4 vol% spin-coated devices gave an average V_{oc} measurement of 0.81 and 0.35 V, respectively. The reduction in J_{sc} is likely due to a loss in bulk uniformity and surface coverage, coupled with the introduction of new perovskite domain growth directions as discussed in **Section 5.3.3**. It can be seen that spray-coating devices with an HI-additive above the optimum 1 vol% also performed worse than the reference control. This effect is likely caused by the differing deposition technique, which relies on small coalescing droplets forming a continuous film. Producing uniform films via spray-coating is a well-researched topic in photovoltaic research, and is likely the cause of the reduced photovoltaic performance for higher HI concentration precursors [73].

5.5 Conclusions

The effects of adding varying concentrations of acidic HI (57wt% hydrogen iodide in H_2O) into a perovskite precursor solution were explored. It was shown that after the inclusion of HI at small concentrations, such as 1 vol%, causes an improvement in PL intensity and absorbance strength. A reduction in bimolecular recombination could explain these improvements, as the HI facilitates the dissolution of $PbCl_2$, as shown with DLS. A 5% overall increase in absorbance across the visible spectrum was accompanied by better surface coverage imaged using SEM compared to films without the additive. Adding the HI to the precursor assists in a full conversion to a pure perovskite phase, as evidenced by enhanced reflections seen for the (110) plane of the $MAPbI_{3-x}Cl_x$ perovskite. Without the additive, reflections associated with PbI_2 and $MAPbCl_3$ based intermediates were detected, and reference films without HI did not fully convert to $MAPbI_{3-x}Cl_x$ after

annealing. Enhancement in the crystallinity of the 1 vol% additive films is observed through an improved XRD scattering signal off the characteristic (110) plane. This enhancement, along with a shift to lower angles, shows that the perovskite unit lattice expands slightly. Photovoltaic performance of devices incorporating perovskites from such precursors was studied by first varying the additive concentration via spin and spray-coating the active layer. For spin-coated active layer devices, an average PCE was shown to increase from 6.5 % to 12.5 % after 1 vol% HI addition. A small yet similar effect was also seen for spray-casted active layers, whereby the PCE improved from 6.1 % to 10.0 % after 1 vol% HI addition. Other additive concentrations of HI were also incorporated into precursor solutions at 0.5 vol% and 2 vol% for spray- and spin-coated layers, respectively. Although these other concentrations showed full dissolution of $PbCl_2$ in solution, photovoltaic performance was significantly reduced for both deposition routes as a function of increasing additive concentration.

5.6 References

1. Kojima, A., Teshima, K., Shirai, Y. & Miyasaka, T. Organometal Halide Perovskites as Visible-Light Sensitizers for Photovoltaic Cells. *J. Am. Chem. Soc.* **131,** 6050–6051 (2009).

2. Yang, W. S. *et al.* High-performance photovoltaic perovskite layers fabricated through intramolecular exchange. *Science.* **348,** 1234–1237 (2015).

3. Yang, Y. *et al.* Annealing Induced Re-crystallization in $CH_3NH_3PbI_{3-x}Cl_x$ for High Performance Perovskite Solar Cells. *Sci. Rep.* **7,** 46724 (2017).

4. Zhou, Q., Jin, Z., Li, H. & Wang, J. Enhancing performance and uniformity of $CH_3NH_3PbI_{3-x}Cl_x$ perovskite solar cells by air-heated-oven assisted annealing under various humidities. *Sci. Rep.* **6,** 21257 (2016).

5. Hsu, H.-L., Chen, C.-P., Chang, J.-Y., Yu, Y.-Y. & Shen, Y.-K. Two-Step Thermal Annealing Improves the Morphology of Spin-Coated Films for Highly Efficient Perovskite Hybrid Photovoltaics. *Nanoscale* **6,** Ahead of Print (2014).

6. Gong, X. *et al.* Controllable Perovskite Crystallization by Water Additive for High-Performance Solar Cells. *Adv. Funct. Mater.* **25,** 6671–6678 (2015).

7. Ling, L. *et al.* Precisely Controlled Hydration Water for Performance Improvement of Organic–Inorganic Perovskite Solar Cells. *Adv. Funct. Mater.* **26,** 5028–5034 (2016).

8. Heo, J. H., Song, D. H. & Im, S. H. Planar $CH_3NH_3PbBr_3$ Hybrid Solar Cells with

10.4% Power Conversion Efficiency, Fabricated by Controlled Crystallization in the Spin-Coating Process. *Adv. Mater.* **26,** 8179–8183 (2014).

9. Heo, J. H. *et al.* Planar $CH_3NH_3PbI_3$ perovskite solar cells with constant 17.2% average power conversion efficiency irrespective of the scan rate. *Adv. Mater.* **27,** 3424–3430 (2015).

10. Luo, P. *et al.* Solvent Engineering for Ambient-Air-Processed, Phase-Stable $CsPbI_3$ in Perovskite Solar Cells. *J. Phys. Chem. Lett.* **7,** 3603–3608 (2016).

11. Chueh, C. *et al.* The roles of alkyl halide additives in enhancing perovskite solar cell performance. *J. Mater. Chem. A* **3,** 9058–9062 (2015).

12. Liang, P. W. *et al.* Additive enhanced crystallization of solution-processed perovskite for highly efficient planar-heterojunction solar cells. *Adv. Mater.* **26,** 3748–3754 (2014).

13. Song, X., Wang, W., Sun, P., Ma, W. & Chen, Z. K. Additive to regulate the perovskite crystal film growth in planar heterojunction solar cells. *Appl. Phys. Lett.* **106,** (2015).

14. Barrows, A. T. *et al.* Monitoring the Formation of a $CH_3NH_3PbI_{3-x}Cl_x$ Perovskite during Thermal Annealing Using X-Ray Scattering. *Adv. Funct. Mater.* **26,** 4934–4942 (2016).

15. Dualeh, A. *et al.* Effect of Annealing Temperature on Film Morphology of Organic-Inorganic Hybrid Pervoskite Solid-State Solar Cells. *Adv. Funct. Mater.* **24,** 3250–3258 (2014).

16. Hamill, J. C., Schwartz, J. & Loo, Y.-L. Influence of Solvent Coordination on Hybrid Organic–Inorganic Perovskite Formation. *ACS Energy Lett.* 92–97 (2017).

17. You, J. *et al.* Moisture assisted perovskite film growth for high performance solar cells. *Appl. Phys. Lett.* **105,** 183902 (2014).

18. Eperon, G. E., Burlakov, V. M., Docampo, P., Goriely, A. & Snaith, H. J. Morphological Control for High Performance, Solution-Processed Planar Heterojunction Perovskite Solar Cells. *Adv. Funct. Mater.* **24,** 151–157 (2014).

19. Docampo, P., Ball, J. M., Darwich, M., Eperon, G. E. & Snaith, H. J. Efficient organometal trihalide perovskite planar-heterojunction solar cells on flexible polymer substrates. *Nat. Commun.* **4,** 2761 (2013).

20. Zhou, H. *et al.* Interface engineering of highly efficient perovskite solar cells. *Science.* **345,** 542–546 (2014).

21. Das, S. *et al.* High-Performance Flexible Perovskite Solar Cells by Using a Combination of Ultrasonic Spray-Coating and Low Thermal Budget Photonic Curing. *ACS Photonics* **2,** 680–686 (2015).

22. Tait, J. G. *et al.* Rapid composition screening for perovskite photovoltaics via concurrently pumped ultrasonic spray coating. *J. Mater. Chem. A* **4,** 3792–3797 (2016).

23. Barrows, A. *et al.* Efficient planar heterojunction mixed-halide perovskite solar cells deposited via spray-deposition. *Energy Environ. Sci.* **7,** 1–7 (2014).

24. Liang, Z. *et al.* A large grain size perovskite thin film with a dense structure for planar heterojunction solar cells via spray deposition under ambient conditions. *RSC Adv.* **5,** 60562–60569 (2015).

25. Krebs, F. C. Fabrication and processing of polymer solar cells: A review of printing and coating techniques. *Sol. Energy Mater. Sol. Cells* **93**, 394–412 (2009).

26. Jones, J. H. The Cativa(tm) Process for the Manufacture of Acetic Acid. *Platin. Met. Rev.* **44**, 94–105 (2000).

27. Williams, S. T. *et al.* Role of Chloride in the Morphological Evolution of Organo-Lead Halide Perovskite Thin Films. *ACS Nano* **8**, 10640–10654 (2014).

28. Yan, K. *et al.* Hybrid Halide Perovskite Solar Cell Precursors : The Colloidal Chemistry and Coordination Engineering behind Device Processing for High Efficiency. (2015).

29. Konstantakou, M., Perganti, D., Falaras, P. & Stergiopoulos, T. Anti-Solvent Crystallization Strategies for Highly Efficient Perovskite Solar Cells. *Crystals* **7**, 291 (2017).

30. Ahmadi, M., Wu, T. & Hu, B. A Review on Organic-Inorganic Halide Perovskite Photodetectors: Device Engineering and Fundamental Physics. *Adv. Mater.* **1605242**, 1605242 (2017).

31. Zhang, W. *et al.* Enhanced optoelectronic quality of perovskite thin films with hypophosphorous acid for planar heterojunction solar cells. *Nat. Commun.* **6**, 1–9 (2015).

32. Lilliu, S. *et al.* Grain rotation and lattice deformation during perovskite spray coating and annealing probed *in situ* by GI-WAXS. *CrystEngComm* **18**, 5448–5455 (2016).

33. Lilliu, S. *et al.* Mapping Morphological and Structural Properties of Lead Halide Perovskites by Scanning Nanofocus XRD. *Adv. Funct. Mater.* **26**, 8221–8230 (2016).

34. Fu, G. *et al.* Efficiency enhancement in planar $CH_3NH_3PbI_{3-x}Cl_x$ perovskite solar cells by processing with bidentate halogenated additives. *Sol. Energy Mater. Sol. Cells* **165**, 36–44 (2017).

35. Li, B. *et al.* Chlorobenzene vapor assistant annealing method for fabricating high quality perovskite films. *Org. Electron. physics, Mater. Appl.* **34**, 97–103 (2016).

36. Roldán-Carmona, C. *et al.* High efficiency methylammonium lead triiodide perovskite solar cells: the relevance of non-stoichiometric precursors. *Energy Environ. Sci.* **8**, 3550–3556 (2015).

37. Pathak, S. *et al.* Perovskite Crystals for Tunable White Light Emission. *Chem. Mater.* **27**, 8066–8075 (2015).

38. Kumawat, N. K., Gupta, D. & Kabra, D. Recent Advances in Metal Halide-Based Perovskite Light-Emitting Diodes. *Energy Technol.* **5**, 1734–1749 (2017).

39. Johnston, M. B. & Herz, L. M. Hybrid Perovskites for Photovoltaics: Charge-Carrier Recombination, Diffusion, and Radiative Efficiencies. *Acc. Chem. Res.* **49**, 146–154 (2016).

40. Sum, T. C., Chen, S., Xing, G., Liu, X. & Wu, B. Energetics and dynamics in organic-inorganic halide perovskite photovoltaics and light emitters. *Nanotechnology* **26**, (2015).

41. Stranks, S. D. *et al.* Recombination Kinetics in Organic-Inorganic Perovskites: Excitons, Free Charge, and Subgap States. *Phys. Rev. Appl.* **2**, 034007 (2014).

42. Leijtens, T. *et al.* Carrier trapping and recombination: The role of defect physics in enhancing the open circuit voltage of metal halide perovskite solar cells. *Energy Environ. Sci.* **9**, 3472–3481 (2016).

43. Tu, Y. *et al.* A gradient engineered hole-transporting material for monolithic series-type large-area perovskite solar cells. *J. Mater. Chem. A* **5**, 21161–21168 (2017).

44. Yang, Y. *et al.* Low-temperature solution-processed perovskite solar cells with high efficiency and flexibility. *ACS Nano* **8**, 1674–1680 (2014).

45. Saidaminov, M. I. *et al.* High-quality bulk hybrid perovskite single crystals within minutes by inverse temperature crystallization. *Nat. Commun.* **6**, 1–6 (2015).

46. Kong, L. *et al.* Simultaneous band-gap narrowing and carrier-lifetime prolongation of organic–inorganic trihalide perovskites. *Proc. Natl. Acad. Sci.* **113**, 8910–8915 (2016).

47. Li, Y. *et al.* High-efficiency robust perovskite solar cells on ultrathin flexible substrates. *Nat. Commun.* **7**, 1–10 (2016).

48. Li, Y. *et al.* Direct Observation of Long Electron-Hole Diffusion Distance in $CH_3NH_3PbI_3$ Perovskite Thin Film. *Sci. Rep.* **5**, 14485 (2015).

49. Marinova, N., Valero, S. & Delgado, J. L. Organic and perovskite solar cells: Working principles, materials and interfaces. *J. Colloid Interface Sci.* **488**, 373–389 (2017).

50. Grancini, G. *et al.* One-Year stable perovskite solar cells by 2D/3D interface engineering. *Nat. Commun.* **8**, 15684 (2017).

51. Chang, J. *et al.* Boosting the performance of planar heterojunction perovskite solar cell by controlling the precursor purity of perovskite materials. *J. Mater. Chem. A* **4**, 887–893 (2016).

52. Stranks, S. D. *et al.* Electron-hole diffusion lengths exceeding 1 micrometer in an organometal trihalide perovskite absorber. *Science.* **342**, 341–344 (2013).

53. Bi, Y. *et al.* Charge Carrier Lifetimes Exceeding 15 μs in Methylammonium Lead Iodide Single Crystals. *J. Phys. Chem. Lett.* **7**, 923–928 (2016).

54. Noel, N. K. *et al.* Enhanced Photoluminescence and Solar Cell Performance via Lewis Base Passivation of Organic–Inorganic Lead Halide Perovskites. *ACS Nano* **8**, 9815–9821 (2014).

55. Uratani, H. & Yamashita, K. Charge Carrier Trapping at Surface Defects of Perovskite Solar Cell Absorbers: A First-Principles Study. *J. Phys. Chem. Lett.* **8**, 742–746 (2017).

56. Han, C. *et al.* Unraveling surface and bulk trap states in lead halide perovskite solar cells using impedance spectroscopy. *J. Phys. D. Appl. Phys.* **51**, (2018).

57. Song, Z. *et al.* Impact of Processing Temperature and Composition on the Formation of Methylammonium Lead Iodide Perovskites. *Chem. Mater.* **27**, 4612–4619 (2015).

58. Luo, D. *et al.* Cubic structure of the mixed halide perovskite $CH_3NH_3PbI_{3-x}Cl_x$ via thermal annealing. *RSC Adv.* **5**, 85480–85485 (2015).

59. Yu, H. *et al.* The role of chlorine in the formation process of '$CH_3NH_3PbI_{3-x}Cl_x$' perovskite. *Adv. Funct. Mater.* **24**, 7102–7108 (2014).

60. Brenner, T. M. *et al.* Conversion of single crystalline PbI_2 to $CH_3NH_3PbI_3$: Structural relations and transformation dynamics. *Chem. Mater.* **28,** 6501–6510 (2016).

61. Park, B. *et al.* Enhanced Crystallinity in Organic–Inorganic Lead Halide Perovskites on Mesoporous TiO_2 via Disorder–Order Phase Transition. *Chem. Mater.* **26,** 4466–4471 (2014).

62. Maculan, G. *et al.* $CH_3NH_3PbCl_3$ Single Crystals: Inverse Temperature Crystallization and Visible-Blind UV-Photodetector. *J. Phys. Chem. Lett.* **6,** 3781–3786 (2015).

63. Xu, J. *et al.* The optimization of organic–inorganic perovskite films by annealing atmosphere for applications in transistors. *Phys. Status Solidi Appl. Mater. Sci.* **214,** (2017).

64. Stamplecoskie, K. G., Manser, J. S. & Kamat, P. V. Dual nature of the excited state in organic–inorganic lead halide perovskites. *Energy Environ. Sci.* **8,** 208–215 (2015).

65. Unger, E. L. *et al.* Chloride in Lead Chloride-Derived Organo-Metal Halides for Perovskite-Absorber Solar Cells. *Chem. Mater.* **26,** 7158–7165 (2014).

66. Bae, S., Park, J. S., Han, I. K., Shin, T. J. & Jo, W. H. $CH_3NH_3PbI_3$ crystal orientation and photovoltaic performance of planar heterojunction perovskite solar cells. *Sol. Energy Mater. Sol. Cells* **160,** 77–84 (2017).

67. Li, X. *et al.* The effect of external electric field on the performance of perovskite solar cells. *Org. Electron. physics, Mater. Appl.* **18,** 107–112 (2015).

68. Mei, A. *et al.* A hole-conductor–free, fully printable mesoscopic perovskite solar cell with high stability. *Sci.* **345,** 295–298 (2014).

69. Cao, C. *et al.* Iodine and Chlorine Element Evolution in $CH_3NH_3PbI_{3-x}Cl_x$ Thin Films for Highly Efficient Planar Heterojunction Perovskite Solar Cells. *Chem. Mater.* **28,** 2742–2749 (2016).

70. Wang, Q. *et al.* Large fill-factor bilayer iodine perovskite solar cells fabricated by a low-temperature solution-process. *Energy Environ. Sci.* **7,** 2359 (2014).

71. Juarez-Perez, E. J. *et al.* Role of the selective contacts in the performance of lead halide perovskite solar cells. *J. Phys. Chem. Lett.* **5,** 680–685 (2014).

72. Liu, D., Gangishetty, M. K. & Kelly, T. L. Effect of $CH_3NH_3PbI_3$ thickness on device efficiency in planar heterojunction perovskite solar cells. *J. Mater. Chem. A* **2,** 19873–19881 (2014).

73. Bishop, J. E., Routledge, T. J. & Lidzey, D. G. Advances in Spray-Cast Perovskite Solar Cells. *Journal of Physical Chemistry Letters* **9,** 1977–1984 (2018).

Chapter 6

Low-dimensional emissive states in non-stoichiometric methylammonium lead halide perovskites

6.1. Introduction

The ease by which hybrid organic-inorganic perovskites can be fabricated make them an attractive material for a variety of applications, including solar cells [1], light emitting diodes [2] and photodetectors [3]. However, certain perovskite materials are known to undergo degradation when exposed to combinations of moisture, ultraviolet light, oxygen and heat [4–7]. 2D and quasi-2D perovskite structures can be formed by partially or completely substituting the small amphiphile cation methylammonium (MA^+ = $CH_3NH_3^+$) with larger organic cations, such as butylammonium (BA = $CH_3(CH_2)_3NH_3^+$) and phenethylammonium (PEA = $C_8H_9NH_3^+$), into the perovskite precursor [8,9]. Introducing any hydrophobic cation into a system that exceeds Goldschmidt's tolerance factor (see **Section 2.5.1**) will result in a non-pure 3D crystal, as these ions are too large to become stable within an $APbX_3$ network [10,11]. The crystal structure of these low dimensional perovskites (LDPs) can be thought of as slicing a 3D-parent ABX_3 structure (such as $MAPbI_3$) along the crystallographic plane, where the large cations then form spacer layers breaking apart the 3D lattice along a *c*-axis [12].

Work by Mitzi *et.al* in 2001 then highlighted the various ways in which LDPs can form from a parent structure of ABX_3, and showed that two crystal planes could be

intercalated by long-chained amphiphilic cations along the (100) and (110) directions [13]. The spatial separation of PbI_4^{2-} octahedra along the (100) direction is shown in **Figure 6.1**. Stoumpos *et al.* controlled the spatial separation of $[PbI_6]^{4-}$ ions by adjusting precursor ratios of the spacer and small organic cations [14]. Here, the authors showed that a crystal structure based on a $MAPbI_3$ perovskite parent structure could be sliced along the (110) plane and terminated with BA cations, with the resulting compound described by $(BA)_2(MA)_{n-1}Pb_nI_{3n+1}$. Here, *n* defines the number of stacked octahedral layers separated by amphiphilic cations where $n \rightarrow \infty$ would produce a 3D bulk perovskite crystal. The class of perovskites that are described by the formula $(BA)_2(MA)_{n-1}Pb_nI_{3n+1}$ are called Ruddlesden-Popper perovskites (RPPs).

One way in which a parent 3D structure can be broken up into different n-sized octahedral layers by intercalated hydrophobic cations is shown in **Figure 6.1**. For n = 1 RPPs, only the larger cationic molecule '$R\text{-}NH_3^+$' is present in the mixture, and therefore a pure 2D structure is formed. When n = 2, the solution contains 2 moles of the hydrophobic cation $R\text{-}NH_3^+$ to 1 mole of molecule 'A', where for example 'A' is MA^+ [10]. For n > 2, this process is repeated by increasing the concentration of small molecule 'A', as shown in **Figure 6.1 (b)**. When the concentration of the cationic amphiphile ($R\text{-}NH_3^+$) in the solution is zero, the favoured crystal structure is the 3D ($n = \infty$) crystal, where only the smaller of the two cations (e.g. MA^+) can fit in between adjacent lead-halide octahedra (PbX_3^-) as a result of Goldschmidt's tolerance factor.

Pure 2D (n = 1) crystals have the widest electronic band gap [14]. This bandgap energy reduces as a function of increasing *n* in a quasi-2D structure; a process attributed to a reduction in quantum confinement [15,16]. The term quasi-2D describes a perovskite crystal structure that forms a structure where *n* is greater than 1 (pure 2D) but much less than ∞. 2D RPPs form natural quantum wells with cations acting as insulating barrier layers [9,17]. This permits stable excitons to form, having binding energies in the region of 200 meV [18,19]. These quasi-2D RPPs have improved moisture tolerance and stability when incorporated in a mixed quasi-2D/3D photovoltaic device [20]. Using this approach, pioneering work by Grancini *et al.* have incorporated 2D layers into 3D perovskite

materials to create solar cells that retain efficient performance after a year of operation [21–23]. It is also possible to form lower dimensional perovskite-like materials, such as 0D and 1D crystals, which have larger bandgaps compared to their 2D and 3D counterparts [14,24].

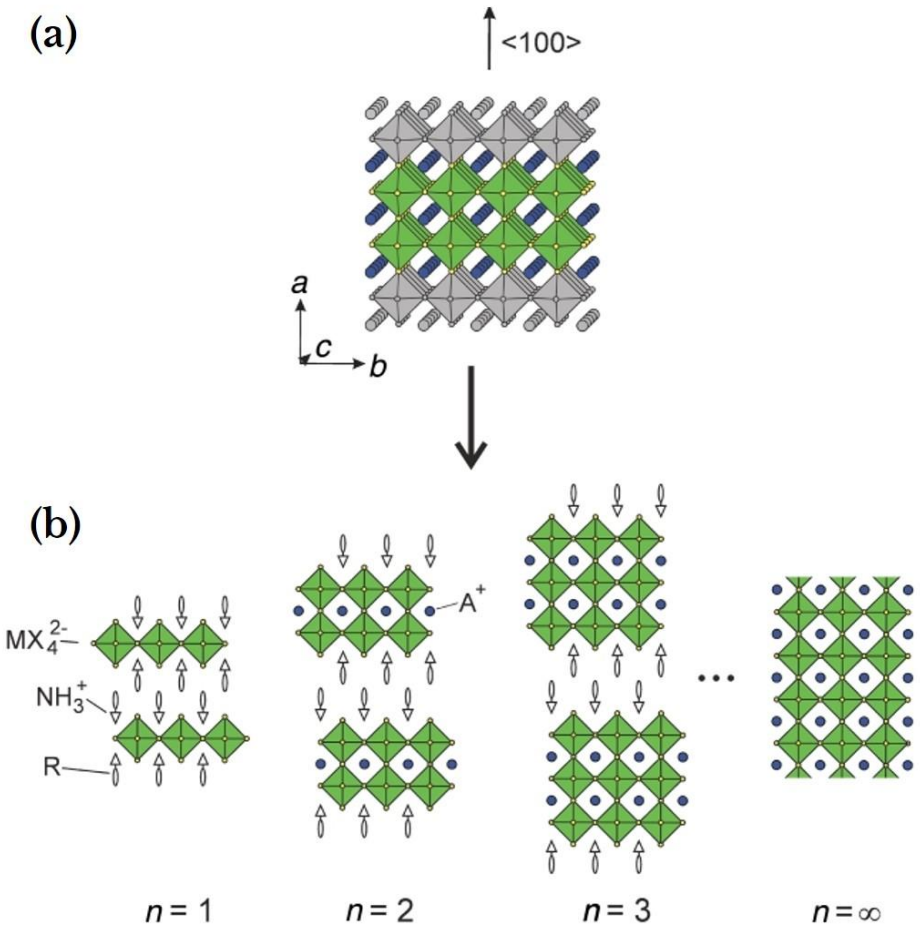

Figure 6.1 - (100) orientated crystal structures for n = 1 (2D), 2, 3 (quasi-2D) and ∞ (3D) perovskites made from a parent structure of ABX_3. Note the staggered lattice for $n < \infty$, which is present along both the a- and b-axis. For the system used in this chapter, $BX_4^{2-} = PbI_4^{2-}$, R = CH_3 and $A^+ = CH_3NH_3^+$. Image taken from reference 14.

Dion–Jacobson perovskites (DJPs) have similar 2D and quasi-2D phases that can be considered as being a (100) slice through a 3D perovskite crystal [25]. Again such DJPs have

the general formula $B(MA)_{n-1}Pb_nX_{3n+1}$, with MA being the smaller of the two cations. Such phases are formed where only one organic spacer cation (B) lies in the insulating region.

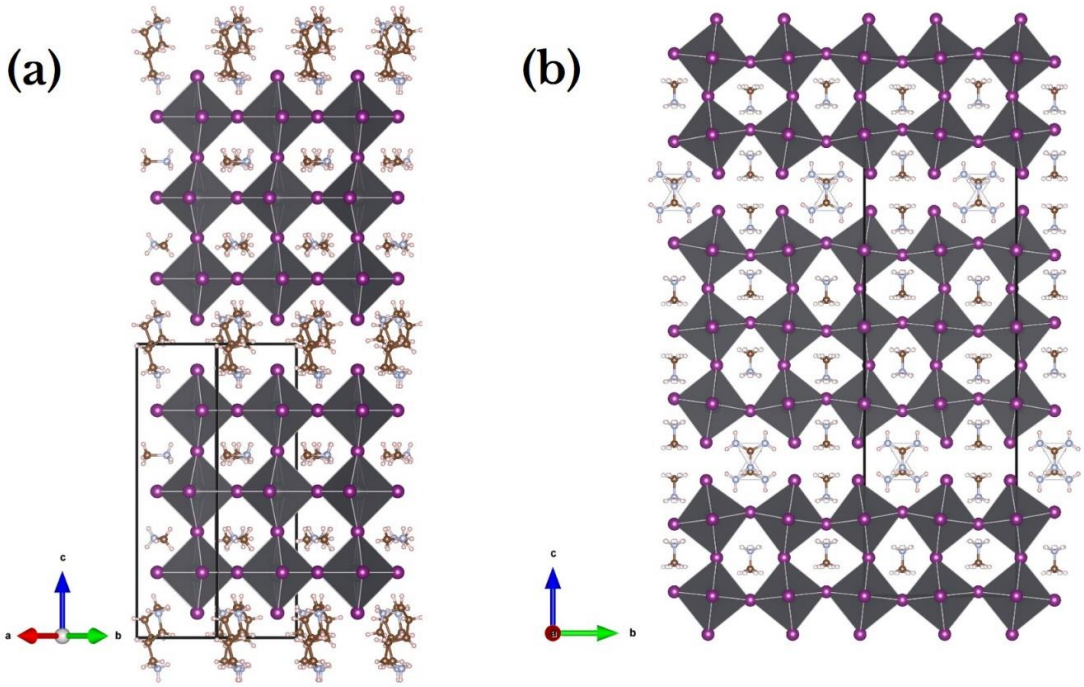

Figure 6.2 - Representative crystal structures for low-dimensional perovskites (LDPs) (a) hybrid Dion-Jacobson perovskite (DJP) with the large spacer cation as 3-(aminomethyl)piperidinium (3AMP) [25], and (b) alternating cation interlayer (ACI) perovskite shown with guanidinium ($C(NH_2)_3$, $GA)^+$ and MA^+ as the spacer cations. The above figures were taken from the CIF files provided in references 26 and 27 for (a) and (b), respectively. CIF files were then modelled using the VESTA crystallographic software [26].

A hybrid DJP structure is shown in **Figure 6.2 (a)**, having the formula $A'MA_{n-1}Pb_nI_{3n+1}$, in which A' (3-(aminomethyl)piperidinium) in this case is a large cation [25]. Interestingly, work by Soe *et al.* has shown that a mixture of cations in the interlayer also produces a low-dimensional perovskite, such as the n = 3 crystal structure shown in **Figure 6.2 (b)** [27]. These alternating cation interlayer (ACI) perovskites display a translation of (1/2,0) along the *ab*-plane for adjacent lead-iodide octrahedral layers, characteristic of a type II DJP [28]. This differs from RPPs which typically have a (1/2, 1/2) translation along the *ab*-

plane. DJPs generally have lower bandgaps for a given n-value than their RPP equivalent [25].

In the following chapter, the photophysics of mixed quasi-2D/3D perovskite films formed by adding an excess of MAI into a $MAPbI_{3-x}Cl_x$ (MAPIC) perovskite precursor blend is described. This study was based around previous work on non-stoichiometric perovskite films and its benefit towards solar cell performance and stability. During the initial experiments, it was found that excess-MAI films produced similar PL emission to other work on LDPs, which then lead to an investigation into the crystallographic properties of these films. Adding a small excess of PbI_2 into a stoichiometric mixture of MAI and PbI_2 has been shown to improve the device performance through a grain boundary passivation effect [29,30]. Similar experiments on the impact of 5 mol% excess of MAI in an otherwise stoichiometric precursor have revealed enhancements in the Jsc of solar cells [31]. A previous report by Song *et al.* indicated the formation of a variety of LDP structures and other phases in non-stoichiometric MAI:PbI_2 blends [32]. Small MAI excess in MAI:PbI_2 (1.05:1) has also been shown to benefit the performance of PV devices after exposure to moisture [33].

In a MAI:$PbCl_2$ 3:1 stoichiometric mixture, the MA molecule occupies the A-site within a ABX_3 3D perovskite crystal structure (tetragonal space group *I4/mcm* at room temperature) [34–36]. However, by using excess organic halide material (up to 1/3rd above a stoichiometric mixture), the MAI:$PbCl_2$ material system additionally forms a layered structure with MAI inducing the formation of sheets of lead-halide octahedra. The formation of low dimensional structures is unexpected, as the MA organic cation used here is relatively small compared to longer chain cations typically observed to form 2D RPPs [37]. To characterise such non-stoichiometric 2D/3D materials, a range of spectroscopic techniques are used including steady-state and time-resolved spectroscopy photoluminescence emission (SSPL and TRPL), along with photoluminescence excitation (PLE) and optical absorption. The structural properties of the materials are also studied by grazing incidence wide-angle X-ray-scattering (GIWAXS).

6.2. Thin film topography and X-ray diffraction analysis

A number of samples were prepared and are referred to on the basis of their corresponding dry-ingredient precursor molar ratio of MAI and $PbCl_2$. For example, the stoichiometric (MAI:$PbCl_2$), which produces a MAPIC perovskite film [38,39] is called a 3:1 perovskite. SEM images for films made from a molar ratio 2.5:1, 3:1 and 3.5:1 of MAI:$PbCl_2$ on a PEDOT:PSS/ITO substrate are shown in **Figure 6.3 (a), (b)** and **(c)**. Here, each film was made using a hot-cast technique, whereby the precursor solution was held at 70˚C with the substrate warmed to 90˚C before deposition [40]. It can be seen that the perovskite films formed are highly polycrystalline in nature. The 2.5:1 film shown in **Figure 6.3 (a)** has the lowest film coverage of all 3 samples. It is also clear that the 2.5:1 film exhibits the highest number of pin-holes as evidenced by the dark regions that are visible. One explanation for the reduced film coverage may be related to the non-stoichiometric nature of the precursor material. At a solution molar ratio of 2.5:1, there is an insufficient quantity of starting materials to produce the $MAPbI_{3-x}Cl_x$ crystal, which is likely to leave unreacted precursor within the film. Here, such a lead-excess film would be characterised by large defect regions resulting from a locally reduced MA^+ concentration, with the lead-halide octahedra being unable to crystallise into a 3-dimensional (3D) $MAPbI_{3-x}Cl_x$ lattice. Such excess lead compounds are instead likely to crystallise into PbI_2 containing domains [41,42].

The overall appearance of the 3:1 film shown in **Figure 6.3 (b)** is qualitatively similar to previous measurements on this system [43,44], with the film being characterised by features having a range of sizes up to around 1-2 µm. This film was considered to be a reference as it has been well studied throughout the perovskite literature [39,45,46]. It can be seen that relative to the 2.5:1 film shown in **Figure 6.3 (a)**, there is a noticeable improvement in surface coverage and crystallite growth in the 3:1 film. This suggests a more complete conversion to bulk $MAPbI_{3-x}Cl_x$ perovskite with fewer defect regions caused as a result of unreacted lead-halide materials.

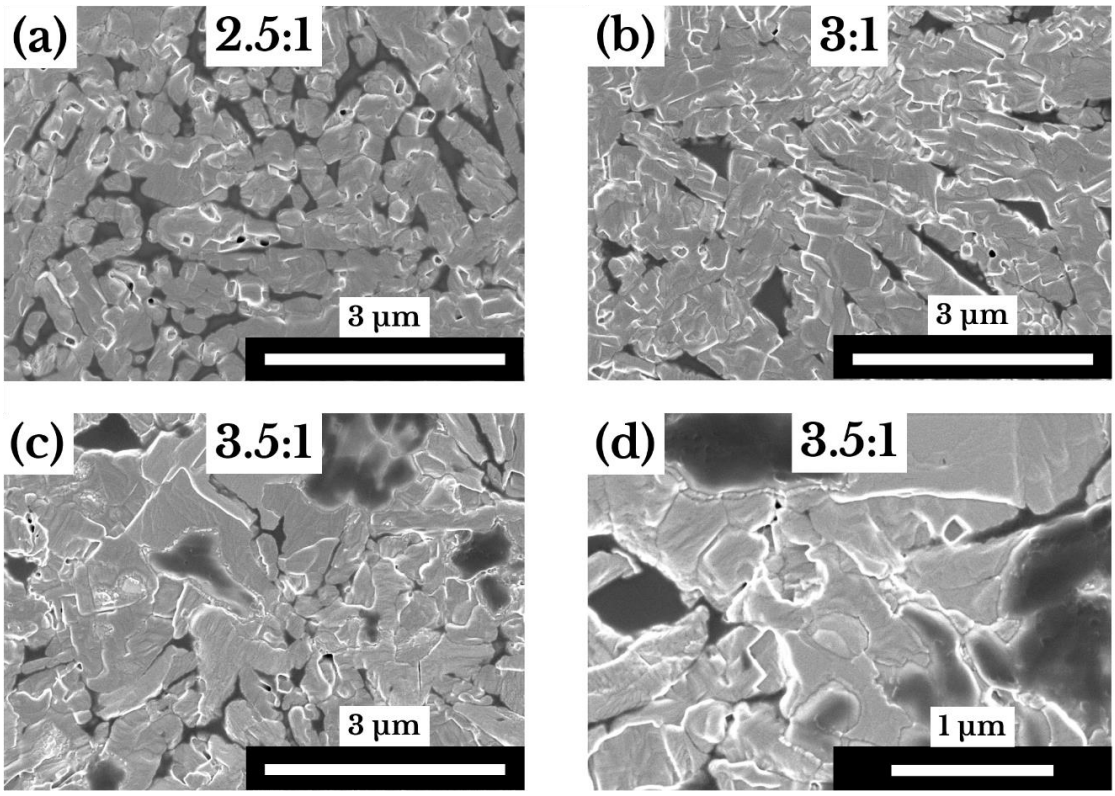

Figure 6.3 - Scanning electron microscope (SEM) images of (a) 2.5:1, (b) 3:1 and (c), (d) 3.5:1, using a secondary electron (SE) detector. The SEM images presented in parts (a), (b) and (c) are at a magnification of 40,000 x and part (d) is at a magnification of 80,000 x for sample 3.5:1 only. All samples were exposed to an electron beam energy of 1 kV. The white scale bar in (a), (b) and (c) represents a length of 3 µm and in (d) the scale bar represents a length of 1 µm.

It can be seen that further increasing the MA^+ concentration to 3.5:1 (17% stoichiometric excess of MAI) larger, seemingly flatter crystal zones at around 1 µm in length are created (see **Figure 6.3 (c)**). Such flatter crystal regions appear larger than in films cast from a lower MAI concentration. Large dark regions are also visible in this film, which in contrast to the dark regions observed in **Figure 6.3 (a)** and **(b)**, appear to result from reduced surface coverage, but are instead related to film structure. It is likely that these are regions containing a high fraction of organic material and thus have increased transparency to the imaging electrons. Areas that appear lighter in colour (such as the whiter grain boundaries in **Figure 6.3 (d)**) are also likely to contain a higher fraction of unreacted metal compounds, for example, PbI_2 or $PbCl_2$ [47]. Such regions are often found

around the circumference of the darker areas. This effect is apparent in the higher magnification image of the 3.5:1 film, shown in **Figure 6.3 (d)**.

$MAI:PbCl_2$	Typical sample thickness on quartz (nm)	Typical sample thickness on ITO/PEDOT:PSS (nm)
3:1 (air annealed)	310 ± 21	350 ± 10
3.5:1 (air annealed)	550 ± 73	615 ± 115
3.5:1 (GB annealed)	480 ± 32	460 ± 20

Table 6.1 - Typical sample thickness on different substrates for samples cast using warm (70°C) precursor inks onto hot (90°C) substrates. Samples were spun at 3000 rpm for 30 seconds and subsequently annealed at 90°C for 90 minutes. The annealing environment explored was air and a nitrogen filled glovebox (GB).

Atomic force microscope (AFM) images of 2.5:1, 3:1 and 3.5:1 films deposited on ITO/PEDOT:PSS (IP) substrates are shown in **Figure 6.4**. It can be seen that there is a clear trend in film roughness which increases with increasing MAI concentration, with the 3.5:1 film having a total height range of over 700 nm, whilst the 2.5:1 film has a thickness range of approximately 260 nm.

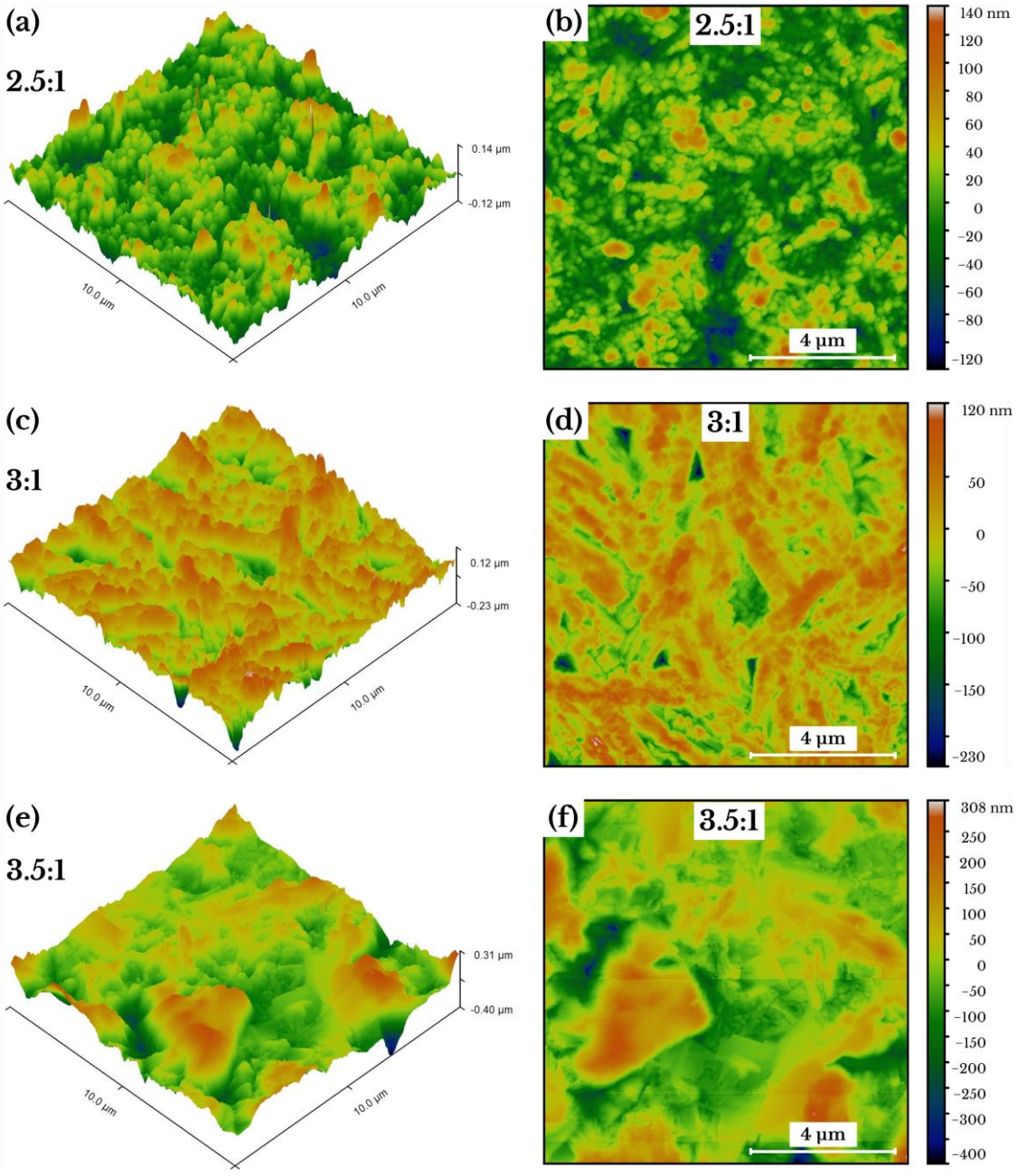

Figure 6.4 - Atomic force microscopy (AFM) images across a 10 x 10 µm² section of samples 2.5:1 (a) and (b), 3:1 (c) and (d) and 3.5:1 (e) and (f) hot-cast on to ITO/PEDOT:PSS substrates. Images (a), (c) and (e) on the left-hand column are 3-dimensional representations of the 2D images shown on the right-hand column in (b), (d) and (f). Methylammonium iodide (MAI) concentration increases down the column, *i.e.* (a) is 2.5:1 and (e) represents 3.5:1. Each sample was individually normalised to highlight particular surface features and the measurement was performed on different samples to those under SEM in **Figure 6.3**.

Comparing **Figure 6.4 (b)** and **(d)** (2.5:1 and 3:1), it is clear that the lead-excess 2.5:1 sample is characterised by small crystal domains. On increasing the MAI concentration to 3:1 domain size increases, as shown in **Figure 6.4 (c) and (d)**. This denotes a more efficient growth of perovskite crystals during the sample annealing stage. Within the 2.5:1 mixture (or any lead-excess perovskite solution), some MA^+ cations are able to sublime from the film during annealing by bonding with a Cl^- ion to form MACl gas, much like it would in a stoichiometric film [48–50]. If this is indeed the case, 3D crystal domain growth is expected to be supressed in lead-excess perovskite films. Due to limited concentration of MA^+ cations in a 2.5:1 film, unreacted lead-based compounds are expected to remain after annealing as some MA^+ will be lost in the sublimation of MACl gas. A further increase to a MAI-excess 3.5:1, shown in **Figure 6.4 (e) and (f)**, creates films having reduced uniformity, with relatively tall, flat domains dominating the scan area. These features match the large flat domains seen in the SEM images of sample 3.5:1.

SEM and AFM analysis techniques are excellent ways to characterise surface morphology. However, such techniques can only provide information relating to the surface of the sample. It is also useful to characterise semiconducting thin-films through a variety of crystallographic techniques to determine both crystal structures and purity. The following section describes the X-ray techniques and analysis used to determine the crystal structures within thin-film samples. GIWAXS was performed on a range of stoichiometries, with the following section describing stoichiometric (3:1) and 3.5:1 mixtures of MAI:$PbCl_2$. As described in **Section 3.8.5**, GIWAXS is a crystallographic analysis technique that is capable of probing the various crystal lattices and atomic distances within a thin-film sample. By using a large-area detector (≈ 300 cm^2), wide-angle scattering, which corresponds to the X-rays in- and out-of-plane relative to the sample surface, can be collected. Unless otherwise stated, the angle of incidence used for GIWAXS measurements was 0.3° with a corresponding penetration depth of ≈ 150 nm [51,52]. A typical sample to detector distance of ≈ 33 cm gave an equivalent Q-space range of 0.05 → 2.5 $Å^{-1}$ with incident X-rays of the wavelength $\lambda \approx 0.134$ nm.

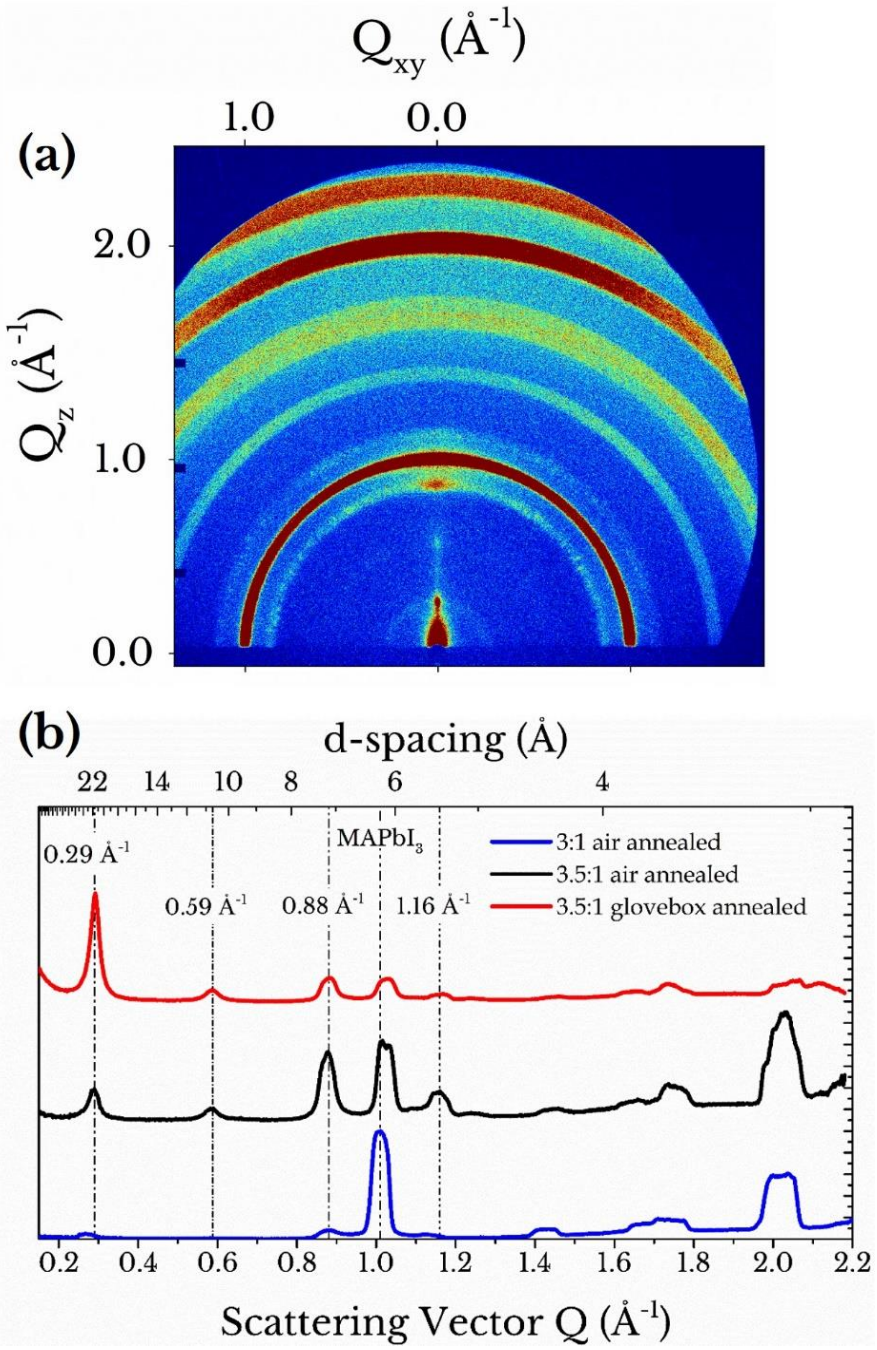

Figure 6.5 - (a) GIWAXS detector patterns for an air annealed sample spun from a 3:1 precursor and (b) radial integrations of scattering images shown for reference 3:1 in air (blue line), 3.5:1 annealed in air (black line) and 3.5:1 annealed under nitrogen (red). The dotted lines are a guide for the appropriate scattering features, including the well cited $MAPbI_3$ (002)/(110) as a reference.

Figure 6.5 (a) shows a typical 2D scattering pattern from a reference 3:1 film annealed in air on an IP substrate. **Figure 6.5 (b)** plots a radial integration from 3:1 (blue), 3.5:1 air anneal (black) and 3.5:1 glovebox anneal (red) films, respectively. In part (a), the characteristic (002)/(110) reflection at a scattering vector (Q) of ≈ 1.04 $Å^{-1}$ indicates the presence of a 3D $MAPbI_3$ or $MAPbI_{3-x}Cl_x$ perovskite phase [53–55]. In films also annealed under ambient air conditions but containing an excess of MAI (scattering pattern shown in **Figure 6.6 (a)** and radial line integration shown in **Figure 6.5 (b)** [black line]), a series of additional scattering features are detected at Q ≈ 0.29 $Å^{-1}$, 0.58 $Å^{-1}$, 0.88 $Å^{-1}$ and 1.16 $Å^{-1}$. The peak at Q ≈ 0.29 $Å^{-1}$ likely results from a self-organised structure within the film that has a repeating lattice spacing of 21 Å, based on the relationship $Q = 2\pi/d$, where Q is the scattering vector and *d* is the distance between repeating planes. This also suggests that the peak at 0.58 $Å^{-1}$ is a second order reflection for the same structure with peaks at 0.88 $Å^{-1}$ and 1.16 $Å^{-1}$, which would be indicative of third and fourth order reflections, respectively. As discussed below, such new scattering peaks are associated with low dimensional perovskites when forming in non-stoichiometric $MAI:PbCl_2$ films. Previous simulations of a MA_2PbI_4 (2D) perovskite indicate a unit cell geometry with a (100) d-spacing of 19.5 Å (Q ≈ 0.32 $Å^{-1}$), but this plane is not expected to strongly reflect for the *Pnm21* space group [56].

In the reference 3:1 film, small unexpected Q reflections can be seen at Q ≈ 0.27 $Å^{-1}$ and Q ≈ 0.88 $Å^{-1}$ (**Figure 6.5 (a)** and **(b)**). The origin of the reflection for Q ≈ 0.27 $Å^{-1}$ is unclear, however, there is a possibility that this feature could be caused by LDPs formed by an error in the weighing out of materials. Any excess of MAI over 3:1, such as 3.05:1, would increase the probability for LDP structures to form due to the higher concentration of MA^+ in the film after spin-casting [32]. This process would further allow the infiltration of MA^+ cations within lead-halide octahedral sheets, blocking the growth of a 3D bulk phase, giving rise to LDP peaks [32]. A reflection of Q ≈ 0.27 $Å^{-1}$ gives an approximate d-spacing of 23 Å.

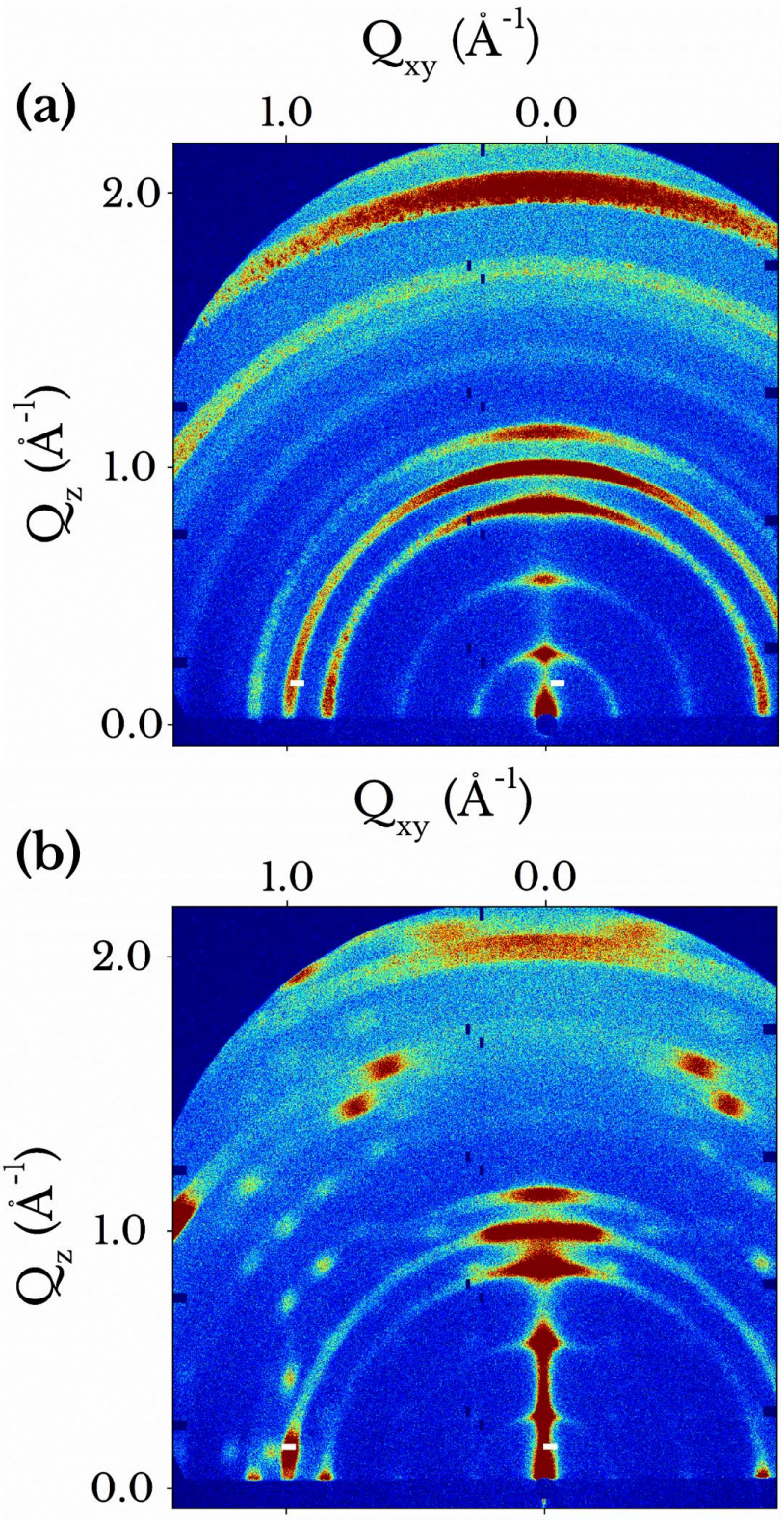

Figure 6.6 - GIWAXS detector patterns of films made from an excess MAI 3.5:1 precursor and annealed under (a) ambient conditions in air and (b) inside a nitrogen glovebox where the average H_2O and O_2 sensor readings were in the range of 0.1 – 0.9 ppm.

To explore the effect of atmosphere during thin-film annealing, a 3.5:1 film was thermally-annealed either in air or inside a nitrogen-filled glovebox. The GIWAXS detector image for 3.5:1 annealed under N_2 is shown in **Figure 6.6 (b)** with the radial integration profile in **Figure 6.5 (b)** (red line). Monohydrate and dihydrate perovskites have been formed in similar materials exposed to high humidity due to the hygroscopic nature of amine salts [57–60]. These amine salts form 1D and 0D structures respectively [58,61–64], with the (100) plane of monohydrate $MAPbI_3 \bullet H_2O$ expected at 0.61 $Å^{-1}$ [60], which is close to the experimentally observed peak at 0.58 $Å^{-1}$. It is worth noting that the (010) plane of the dihydrate perovskite $MA_4PbI_6 \bullet 2H_2O$ is expected at 0.55 $Å^{-1}$ [64]. This reflection coincides with the proposed (200) reflection that likely originates from an LDP phase. The annealing temperature used here (90°C) is expected to largely preclude the presence of significant hydrate phases in these films. 1D perovskite-like structures, such as $(MA)_2(DMF)PbI_5$, have been reported when an excess of MAI is used in the precursor solution [65], forming a DMF-complex with coordinating lead-iodide octahedra. However, the same study found that annealing at 70°C was sufficient to remove all DMF from their films.

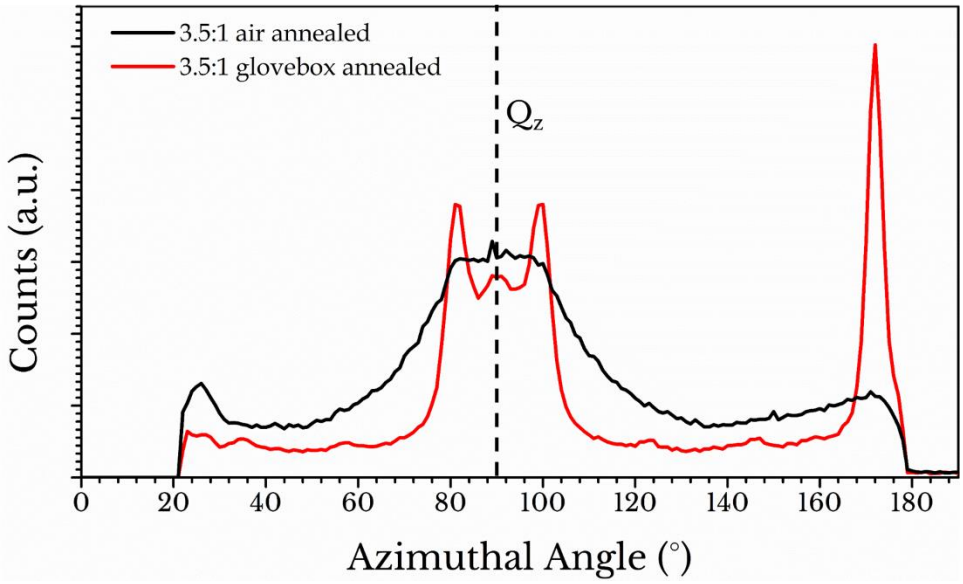

Figure 6.7 - Azimuthal integrations around Q = 1.04 $Å^{-1}$ for 3.5:1 annealed in air (black) and in the glovebox (red) with the Q_z axis (perpendicular to the beam path) marked in a dashed line.

The 3.5:1 films annealed under a nitrogen atmosphere are characterised by the same reflections as seen in the air-annealed sample, which confirms that hydrated phases are not present in either case. The solutions for 3.5:1 annealed under nitrogen were never exposed to air, and the dry powders being mixed with DMF inside the glovebox. Notably, the reflection at 0.29 $Å^{-1}$ appears significantly more intense in the glovebox annealed sample (**Figure 6.5 (b)**). It can be seen that crystalline planes in the 3.5:1 perovskite film annealed in air (**Figure 6.6 (a)**) have some partial orientation, however, there appears to be preferential alignment in the same film annealed under nitrogen, where there is a strong modulation in the azimuthal reflection intensity. Other studies on RPPs have observed similar orientation effects in films containing the larger cations BA and PEA that were hot-cast [8,66,67]. The glovebox-annealed film clearly has an increased state of order in the out-of-plane direction (Q_z), with some larger Q peaks oriented in plane (Q_{xy}). This is shown in **Figure 6.7**, where an azimuthal integration of the $Q \approx 1.04$ $Å^{-1}$ scattering feature (expected reflection for the (110) plane of the $MAPbI_{3-x}Cl_x$ perovskite) shows orientation and partial splitting of the primary reflection. These observations suggest a more phase-pure and preferentially oriented system in the glove-box annealed samples.

Returning to **Figure 6.6 (a)**, the origin of some of the additional peaks observed in the non-stoichiometric samples will now be considered. It is possible that the 1.16 $Å^{-1}$ reflection observed in the 3.5:1 film may coincide with that of the (100) plane of $MAPbCl_3$ [68], expected at $Q \approx 1.10$ $Å^{-1}$. To investigate this, energy-dispersive X-ray spectroscopy (EDX) was performed on 2.5:1. 3:1 and 3.5:1 samples annealed in air, with the results summarised in **Table 6.2**. A small amount of chloride can be seen in the 2.5:1 sample, an observation that indicates that insufficient iodide was present in the precursor to displace chloride, allowing the sublimation of MACl. No chloride trace was detected for both the stoichiometric 3:1 and the excess MAI 3.5:1 samples; suggesting complete sublimation of methylammonium chloride (MACl) during film formation. The 1.16 $Å^{-1}$ reflection is thus attributed to the presence of LDPs.

Precursor molar ratio [MAI:$PbCl_2$]	Element	Formula	Mass (%)	Atom (%)
2.5:1	**C**	41.2	89.2	0.2
	Cl	0.3	0.2	0.2
	I	40.0	8.3	2.2
	Pb	18.5	2.3	1.1
3:1	**C**	4.1	37.7	0.0
	Cl	0.0	0.0	0.0
	I	74.3	53.3	0.3
	Pb	20.7	9.1	0.1
3.5:1	**C**	6.4	44.0	0.0
	Cl	0.0	0.0	0.0
	I	74.6	48.4	0.4
	Pb	19.0	7.6	0.2

Table 6.2 - Energy-dispersive X-ray spectroscopy (EDX) analysis summary for thin-film samples made from 2.5:1, 3:1 and 3.5:1 solutions annealed in air. Each value expressed in the table above is an average from 5 different regions on the sample.

To understand the origin of the additional peaks seen in the non-stoichiometric films, a careful search of relevant literature on LDPs was performed. Here, a report by Soe *et al.* described the synthesis of a family of DJP/RPP-like materials, which they term alternating cation in the interlayer space (ACI) perovskites [27]. Using mixtures of guanidinium ($C(NH_2)_3^+$ or GA^+) and MA^+ it was shown that a material family $GA(MA)_nPb_nI_{3n+1}$ was formed. Comparing simulated powder XRD patterns [26] from their crystallographic information files for the n = 3 variant with the radially integrated GIWAXS for a 3.5:1 GB annealed sample data, a strong correlation in reflected peak positions is observed (see **Figure 6.8 (a)**). From the simulated data, a reflection corresponding to the (002) plane of the $GA(MA)_3Pb_3I_{10}$ ACI-perovskite is found to locate at $Q \approx 0.29$ Å^{-1} (d-spacing ≈ 22 Å^{-1}). Additional features corresponding to (004) and (006) planes are found at $Q \approx 0.57$ and 0.86 Å^{-1}, followed by stronger reflections from the (101)

and (020) planes at Q ≈ 0.99 and 1.01 $Å^{-1}$ (d-spacing ≈ 6.30 and 6.20 $Å^{-1}$), respectively. This suggests that the thin-films fabricated consist of a crystal structure similar in nature to the DJ/RPP hybrid class of perovskites with MA^+ cations located in the spacer layer, forming a multiple quantum well structure. The lattice parameters for the study by Soe *et* al. on $GA(MA)_3Pb_3I_{10}$ single crystals were determined as approximately a = 6.35 Å, b = 12.44 Å, c = 43.97 Å and a volume of 3473.85 $Å^3$ in an orthorhombic centrosymmetric *Imma* space group [27]. Structurally, the ACI perovskite exhibits a type II DJP structure [28] with a lateral offset between adjacent octahedral layers in the *a*-plane but not in the *b*-plane (semi-eclipsed configuration), as opposed to an RPP perovskite which would be offset in both *a* and *b* (staggered configuration).

If the formation of a $MA_4Pb_3I_{10}$ structure is possible in the 3.5:1 films, MA^+ would fully replace the GA^+ cation in the spacer layer, rather than the mixed GA/MA ACI structure. To confirm the presence of an n = 3 $MA_4Pb_3I_{10}$ perovskite, simulations by means of density functional theory (DFT) using the VV (Vydrov - Van Voorhis) van der Waals-corrected functional (using CP2K software) were performed at 0K, containing MA^+ only (replacing GA^+) from the coordinates provided by the CIF file in the Soe *et al.* study. The simulated powder-XRD results of the $MA_4Pb_3I_{10}$ crystal are displayed in **Figure 6.8 (b)**, together with the GIWAXS radial integration from a 3.5:1 glovebox-annealed sample.
The n = 3 $(MA)_4Pb_3I_{10}$ perovskite adopts a triclinic *P1* space group with unit cell parameters of *a* = 6.47 Å, *b* = 12.56 Å and *c* = 23.23 Å and a unit cell volume of 1804.51 $Å^3$. It is worth noting that the nearest Pb-Pb distance across the interlayer increases when MA^+ replaces GA^+ (9.8 Å to 10.1 Å) as shown in **Figure 6.9 (b)**.

From the simulated powder-XRD diffraction pattern shown in **Figure 6.8 (b)**, there appears to be some similarities between the simulated and experimental diffraction patters. The peak observed in the experimental data (red line) at Q ≈ 0.29 $Å^{-1}$ (d-spacing ≈ 22 $Å^{-1}$) corresponds to the (001) plane of the $(MA)_4Pb_3I_{10}$ crystal. Moreover, the second and third order reflections for this plane (the (002) and (003) planes) are expected at Q ≈ 0.57 $Å^{-1}$ and Q ≈ 0.85 $Å^{-1}$, respectively. A small shift (0.2 Å in d-space) to smaller angles is observed in the experimental data relative to the calculated structure, again for the

peaks around Q ≈ 0.58 Å^{-1} and Q ≈ 0.89 Å^{-1}. The calculated structure was performed on a 0K system, whereas the experimental data was taken from a sample held at 290 K. Another consideration to make is that the error value between expected reflection (black line) and measured value (red line) for the (001) peak is likely to be enhanced by the (003) reflection. Therefore, larger errors between theoretical and experimental are expected for higher-order reflections of the same plane assuming a non-perfect match in reflection values.

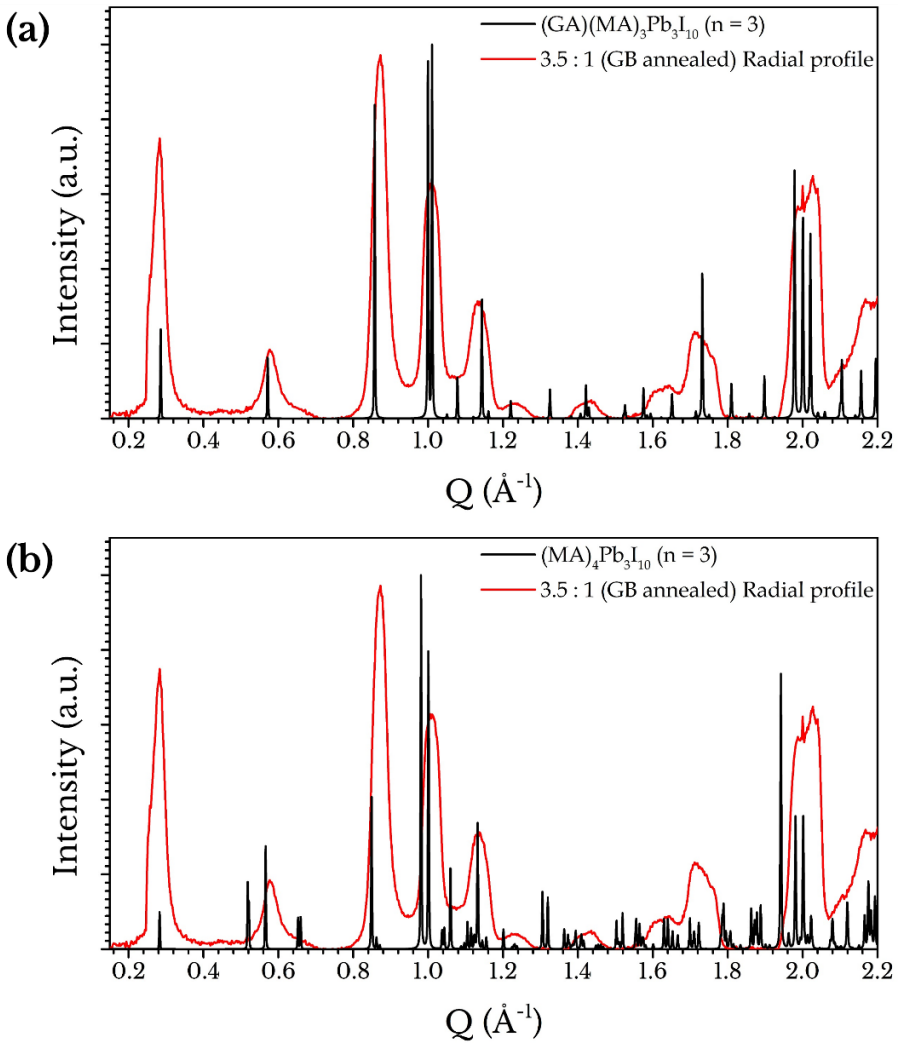

Figure 6.8 - (a) Radially integrated GIWAXS pattern from a 3.5:1 GB annealed sample (red line) plotted together with a powder-XRD simulation using the CIF file for an n=3 ACI perovskite (black lines) provided in reference [27]. (b) Radially integrated GIWAXS pattern from a 3.5:1 GB annealed sample (red line) plotted together with a powder-XRD simulation of a $MA_4Pb_3I_{10}$ crystal (black line).

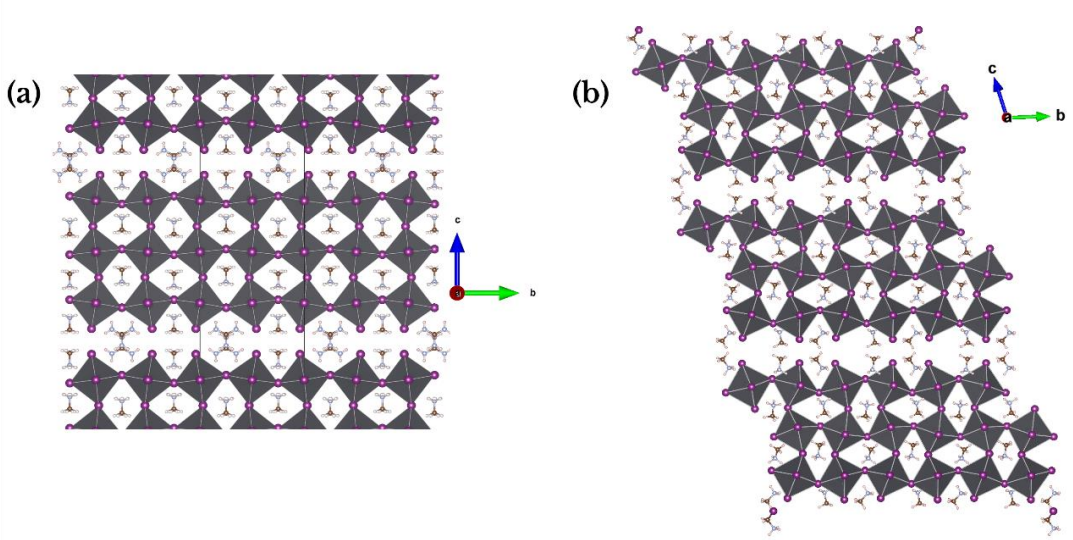

Figure 6.9 - Crystal representations of the (a) $GA(MA)_3Pb_3I_{10}$ and (b) $(MA)_4Pb_3I_{10}$ perovskites. Both crystal models indicate a 1/2 translation along the *b*-axis. The axis label underneath parts (b) and (c) represent the vectors along the a-axis (red), b-axis (green) and c-axis (blue).

The contraction in the unit cell coupled with an increased interlayer distance possibly leads to reduced phase stability compared to the mixed cation ACI perovskite, consistent with an observation of a metastable phase described below.

Experimentally, a transition between the 2D layered structure and the bulk 3D perovskite can be observed through the exposure of the non-stoichiometric films to moisture. During exposure, LDP containing films rapidly lose their dark-red colour when exposed to high humidity (> 40 RH %) air and convert to a dark-brown perovskite (see **Figure 6.10**). GIWAXS images of a 33% MAI excess (4:1) film annealed in ambient (air) conditions before and after high humidity exposure are shown in **Figure 6.10**, along with radial integrations for a large X-ray angle of incidence. The angle of incidence between the sample and incident X-rays was increased from 0.3° to 1°, which progressively probes a greater depth of the sample. Firstly, it is apparent that texturing (in-plane/out-of-plane) does not substantially change as a result of moisture exposure.

Before exposure, LDP peaks can be seen at Q ≈ 0.29 Å^{-1}, 0.58 Å^{-1}, 0.87 Å^{-1} and 1.14 Å^{-1} for angles of incidence up to 0.52°, similar to those seen in 3.5:1. However, when the angle is increased to 1°, additional scattering features corresponding to values at Q ≈ 0.69 Å^{-1} and 0.71 Å^{-1} (9.1 Å and 8.9 Å, respectively) which can be seen more clearly in **Figure 6.10 (c)**.

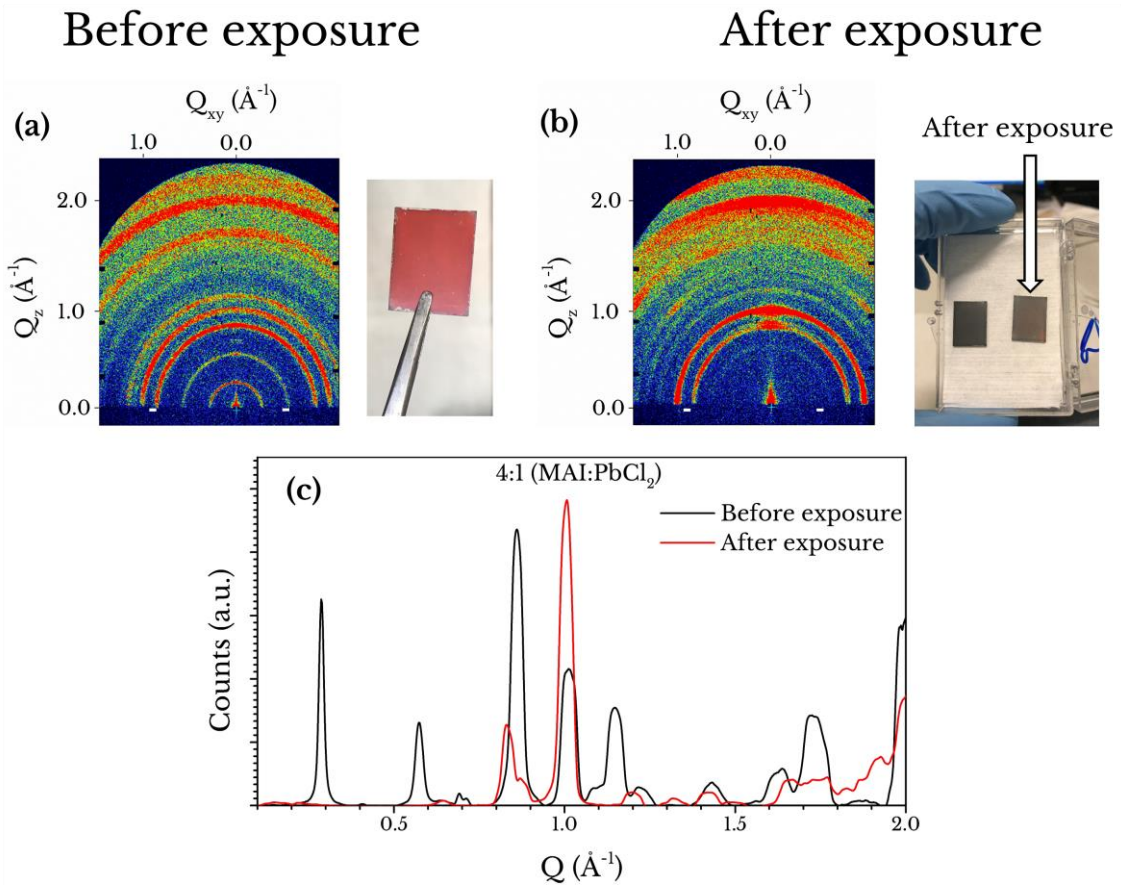

Figure 6.10 - GIWAXS detector images and radial integrations across Q-space for a 4:1 post-annealed film before and after moisture exposure (> 40 RH %). (a) Indicates a detector image before exposure and a photograph of the 4:1 film. (b) Presents a detector image after exposure to moisture with a photograph of the converted film (right, shown with an arrow) next to a 3:1 reference film (left). (c) Radial integrated profiles for a 4:1 film before (black line) and after (red line) moisture exposure at a grazing incidence of 1°. Note the detector images presented in parts (a) and (b) were taken at a grazing incidence of 0.3°.

These reflections (0.69 $Å^{-1}$ and 0.71 $Å^{-1}$) closely match those seen in excess MAI fabrication routes with a reported value of Q ≈ 0.70 $Å^{-1}$ and have been assigned to crystallised MAI in the film [69,70]. Due to the high concentration of MAI for a 4:1 precursor sample, it is expected that excess MAI will crystallise before reacting to form LDPs or a bulk 3D perovskite phase. It is found that exposing the 4:1 sample to moisture produces a dark film, reminiscent of a bulk 3D perovskite phase (as shown in **Figure 6.10 (b)**). This reaction appears to be humidity dependant, with lower humidity values (< 30 RH%) taking longer to convert the film. However, in high MAI excess films (e.g. 4:1), this reaction happens on a much faster timescale. For example, samples made from a 3.5:1 film appeared to be stable under ambient conditions at a relative humidity of ≈ 30%. Furthermore, increasing the MAI excess from ≈ 17% to 33% (3.5:1 to 4:1) lowers the stability of the films when exposed to moisture, a result likely caused by excess crystallised MAI contained within the film. MAI molecules are known to be highly soluble in water, with exposure to humidity likely to produce mobile ions within the film [71–73]. There is clearly a complex crystallisation process during the annealing stage for films containing an off-stoichiometric excess of MAI. This effect suggests the presence of moisture allows the excess MA to escape, allowing the LDP to collapse to a more energetically favourable 3D perovskite structure [74,75].

6.3. Optical absorption and temperature-dependant steady-state photoluminescence

To investigate the co-existence of the LDPs and 3D $MAPbI_{3-x}Cl_x$ phases, steady-state photoluminescence (SSPL) and optical absorption were recorded as a function of temperature.

Figure 6.11 (a) plots the normalised absorption (red line) and PL emission from a stoichiometric 3:1 perovskite film at 290 K (black line) and 12 K (dashed line). It can be seen that the film absorption (at 290K) is relatively featureless and is characterised by a band-edge at 758 nm. The PL emission from this film is dominated by a peak centred at

763 nm, which is expected from the charge carrier recombination within $MAPbI_{3-x}Cl_x$ [53]. A second, less intense peak is detected at 740 nm, which has previously been ascribed to the presence of $MAPbI_3$ nanocrystals [76]. The dominant peak at 763 nm red shifts to 772 nm at 12 K, which is similar to a previous measurement made on a $MAPbI_{3-x}Cl_x$ perovskite film on glass [77]. Emission from such nanocrystals become weaker as the temperature is reduced, with the low energy-region of the spectrum becoming dominated by an emission-peak centred at 770 nm. corresponding the tetragonal phase of the perovskite [53,78].

In **Figure 6.11 (b)** and **(c)**, the normalised absorption and PL emission spectra is plotted for a 3.5:1 air-annealed perovskite film at 290 K and 11 K, respectively. In contrast to the 3:1 film, a more complex absorption spectrum at 290 K is characterised by a broad unresolved band centred on 550 nm, together with a weak band edge at 760 nm. As the temperature is reduced, both the absorption and emission evolve into the spectra shown in **Figure 6.11 (c)**, indicative of a complex energy landscape seen in mixed quasi-2D/3D perovskites [12]. It can be seen that as the temperature is reduced, the absorption band between 500 and 590 nm splits into peaks at 500, 515, 542, 562 and 582 nm, with the lower energy band-edge blue-shifting slightly to 750 nm. The overall appearance of the absorption profile shown in **Figure 6.11 (c)** resembles that of a quasi-2D perovskite thin-films based on larger cation spacers than MA^+ [79–81].

Through an analysis of the complete temperature-dependent absorption spectral-series, the broad absorption peaks observed at 547 and 567 nm undergo a blue-shift of 5 nm as the temperature is reduced from 290 K to 12 K. Similar features have been observed in quasi-2D perovskite films at room temperature [66,82,83] and have been ascribed to excitonic absorption and emission by n-dimensional perovskite crystals, including RPPs and ACIs [14,37,62,84]. Consequently, absorption peaks at shorter wavelengths were assigned to perovskite structures having reduced dimensionality. The PL is similarly structured in the 3.5:1 sample, with strong emission peaks observed at 546, 566, 586, 606, 641 and 803 nm at 12 K, with a weaker emission peak observed at 512 nm (see **Figure 6.11 (c)** inset). Note that the inset spectrum was recorded using the PL mapping system – *vide infra*.

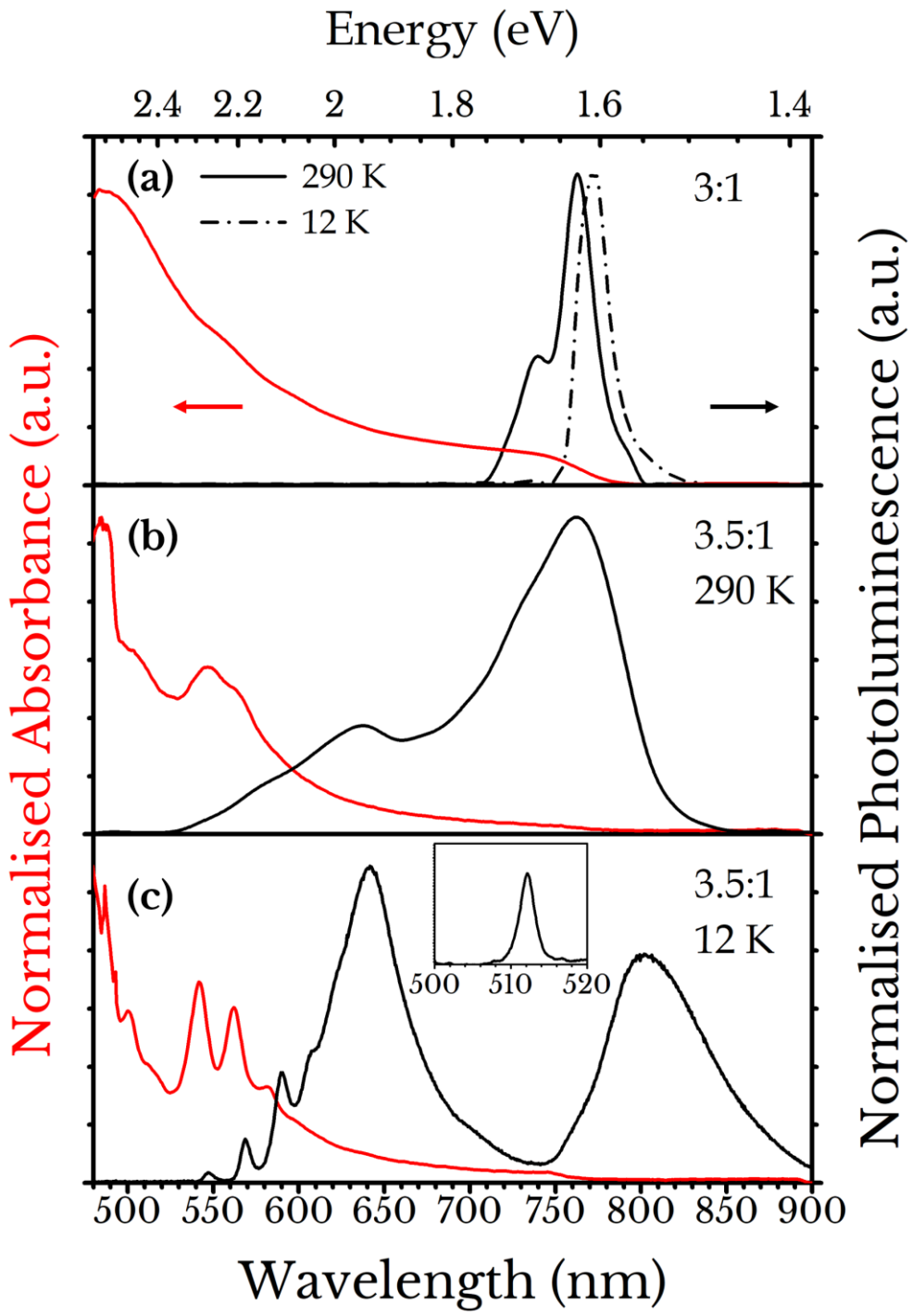

Figure 6.11 - (a) Steady-state photoluminescence (SSPL) at 290 K (black), 12 K (dashed black) and absorption at 290 K (red) of a 3:1 perovskite film. (b,c) Typical SSPL (black) and absorption (red) of 3.5:1 at (b) 290 K and (c) 12 K. All samples here were prepared on clean quartz. The inset in part (c) was taken from the laser-mapping setup described in Section 6.6 and features a small peak centred on 512 nm. The laser fluence used in this figure was approximately 47 nJ/cm² at an excitation wavelength of 405 nm.

There seems to be an almost one-to-one correspondence between peaks observed in the emission spectrum at 512, 546, 566 and 586 nm than to the peaks observed in absorption at 505, 542, 562 and 582 nm. This observation suggests a series of independent and localised excitonic states.

A full temperature series of PL emission for the 3.5:1 perovskite is plotted in **Figure 6.12** on two different substrates; quartz and ITO/PEDOT:PSS (IP). When the 3.5:1 solution is cast on to quartz as seen in **Figure 6.12 (a)**, the broad band-edge PL emission at 763 nm at 290 K (presumably from the 3D bulk perovskite phase) undergoes a small red-shift of 24 nm to 787 nm as the film is cooled to 160 K. This peak then blue shifts to 776 nm at 85 K, a temperature below the tetragonal to orthorhombic transition [85] and then broadens considerably as the film is cooled to 12 K. This broadening at a low temperature can be attributed to a distribution of sub band-gap states [86]. A different behaviour is observed in **Figure 6.12 (b)**, for a 3.5:1 perovskite solution cast on to an IP substrate. At room temperature (290 K) low-energy emission can be seen at ≈ 762 nm, which is likely due to the fully-crystallised 3D $MAPbI_{3-x}Cl_x$ phase; a result consistent with the same film cast onto a quartz substrate at this temperature. However, the emission peak observed from the quartz cast film is much broader and is located at similar wavelengths (700 - 785 nm).

A second, slightly less intense peak is observed at 734 nm at room temperature on the IP-cast film. This is likely part of the broad emission band seen from the quartz-cast film at 290 K. The origin of this higher-energy peak is uncertain, although lowering the dimensionality of bulk 3D perovskites to nanorods to 20 nm-sized dots induces a progressive blue-shift in PL emission [15,76,87]. This blue-shift behaviour is due to a charge confinement effect, which raises the overall energy of the system as the confinement energy, E, is inversely proportional to the square of the particle radius [88]. Thus, the second phase present within the 3.5:1 film cast on IP, which produces PL emission around 734 nm, is likely caused by small regions of 3D perovskite, which are unable to crystallise into larger, more bulk-like 3D crystals. Similar blue-shifted PL emission has been observed in $PEA_2(CH_3NH_3)_{n-1}Pb_nI_{3n+1}$ perovskites when the lead-iodide sheet layers ($\langle n \rangle$) are reduced from bulk 3D ($\langle n \rangle = \infty$) to $\langle n \rangle \leq 10$ [89].

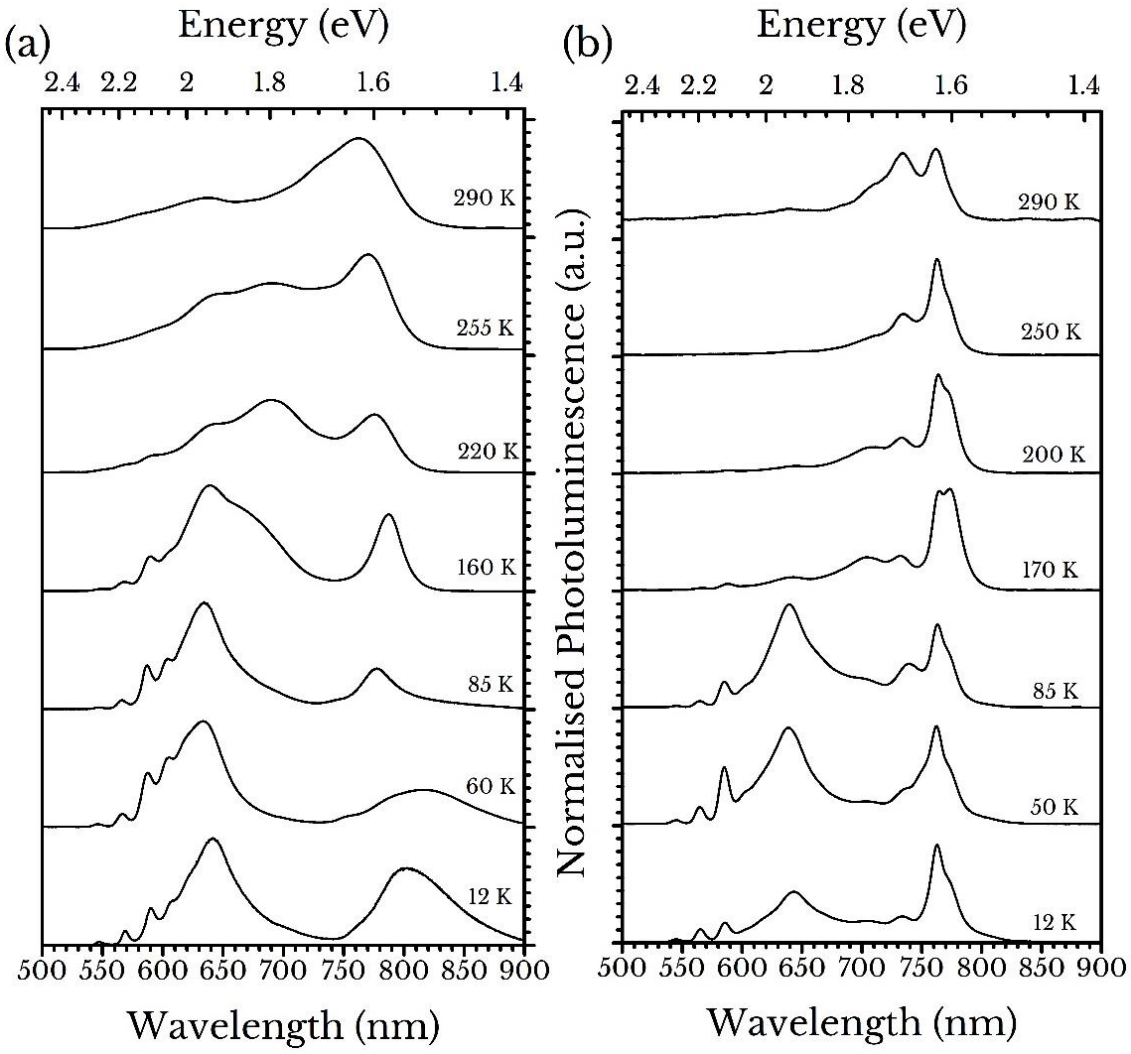

Figure 6.12 - Temperature-dependant normalised steady-state photoluminescence (SSPL) from a 3.5:1 perovskite film spin-casted on to (a) quartz and (b) ITO/PEDOT:PSS (IP). The samples used in both (a) and (b) were fabricated using the hot-cast technique (70°C ink, 90°C substrate) and subsequently annealed in air for 90 minutes. Note the slight difference in sample temperature for each substrate. Each sample was under low pressure (≈10^{-5} mBar) and excited at 405 nm with a laser fluence of 47 nJ/cm².

Interestingly, as the sample is cooled, the emission from this phase appears to remain relatively stationary and fluctuates by less than 2 nm between 290 K and 12 K, contrary to the similar emission observed from the sample coated directly on to quartz.

The following section will consider the origin and behaviour of emission peaks observed around 500 nm to 700 nm. Here, films cast with both types of substrate have a complex emission spectrum that emerges as the samples are cooled below ≈ 200 K.

As each spectra is individually normalised, it can be seen that the emission from the higher-energy peaks dominate the spectrum of the quartz-cast film (**Figure 6.12 (a)**), whereas emission from the film cast on an IP substrate is dominated by bulk-3D phases until the film is cooled below 100 K. The strong temperature dependence of PL emission intensity demonstrates the existence of a thermally activated process that results in the dissociation of excitons localised on LDPs. A strong PL peak is observed at 641 nm that is broader than the narrower excitonic peaks observed at higher-energies. Currently the origin of this feature is not clear, but the result may occur from charge transfer states that exist at the interface between the LDP and 3D material. This speculation is based on the peak being relatively supressed in the glovebox-annealed 3.5:1 film which has relatively enhanced phase-purity. Low-temperature photoluminescence of 3.5:1 (GB and air annealed) and 4:1 (air annealed) excess MAI perovskite films is shown in **Figure 6.13**. Emission spectra of encapsulated films are shown deposited on IP substrates and annealed in air (red + blue lines) or in the glovebox (black). The glovebox annealed sample has reduced emission at around 640 nm and more defined emissive peaks are detected at 605 and 625 nm.

It has been previously speculated that MAI (or its ionic constituents) becomes more mobile in the presence of water vapour [71]. This increase in MAI mobility could perhaps help to facilitate full 3D perovskite conversion, whereas under nitrogen it is favourable to first crystallise the LDP phases, consuming the surrounding MA^+ cations as they are less mobile under nitrogen. The reduced movement of MA^+ cations in a sample annealed under nitrogen could induce regions of higher MA^+ concentration, likely leading to the formation of LDP states. From the normalised PL shown between 3.5:1 air and GB annealed samples (red and black lines, respectively), the air annealed sample shows broad PL centred around 630 nm, with the GB annealed sample having reduced emission between 650 – 750 nm. 3D emission associated with the lower-energy emission (> 740 nm) is much more intense in the air annealed sample, which could be a

consequence of increased mobility for the MAI molecule in the presence of moisture. The GIWAXS images of air and GB annealed samples with a 3.5:1 stoichiometry shows that a more phase-pure sample is created when annealed under nitrogen. This implies the formation of LDP phases is preferred over larger-sized quasi-2D or perhaps 3D perovskite crystals. Enhanced emission at 605 nm and 625 nm for the GB annealed 3.5:1 sample may be further proof of the preferred crystallisation of lower-dimensional crystals over lower-bandgap, 3D perovskite phases when the presence of moisture is removed.

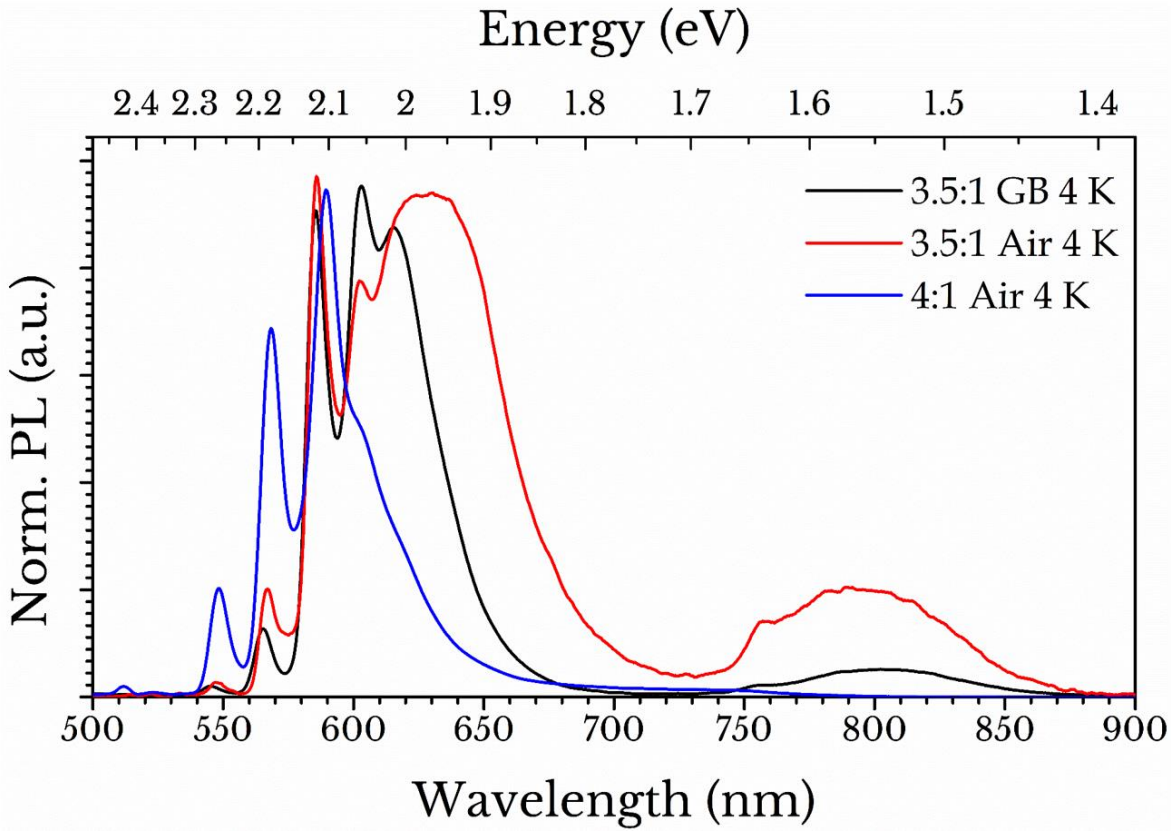

Figure 6.13 - Normalised SSPL at 4K for thin samples of 3.5:1 glovebox (GB) anneal (black line), 3.5:1 air anneal (red line) and 4:1 air anneal (blue line). Each sample was under low pressure (≈ 10^{-5} mBar) and excited at 405 nm with a laser fluence of 47 nJ/cm².

For the 4:1 (blue line in **Figure 6.13**) sample, 3D emission is barely detectable with only weak emission around 700 – 750 nm. There is also a small red-shift observed for the

LDP emission peaks. The reduction in PL intensity of features occurring at lower-energy indicates that a higher MAI concentration somewhat suppresses the formation of the bulk perovskite phases. If 3D regions were indeed present in the 4:1 sample, some emission might be expected from the 3D regions as a result of an energy transfer process. However, the suppression of features at lower-energy may arise from a competition between 3D perovskite growth and LDP formation. Although the formation energy for LDPs is higher than that for 3D perovskites [90–92], **Figure 6.13** seems to suggest changing the stoichiometry from 3.5:1 to 4:1 supresses any emission from the 3D perovskite crystals. As the MAI concentration is increased, the film tends towards a 2D/quasi-2D formation due to the excess MA^+ cations supressing the formation of a 3D perovskite crystal.

At present, it is difficult to provide a quantitative description of the low-dimensional states that have been observed. However, previous reports indicate that certain n = 1 RPPs; namely $(PMA)_2PbI_4$ (PMA = $C_8H_9NH_3$) and $(PEA)_2PbI_4$, exhibit PL emission over the wavelength-range 520 to 530 nm [84]. Significant red-shifts in PL intensity (optical band-gap) have been observed as a function of increasing number (<n>) of octrahedral layers in RRPs; an effect that is accompanied by reduced exciton-binding energy [16]. Therefore, the films may contain some fraction of quasi-2D lead-halide octahedra layers, separated by MA insulator layers and so emission is expected from states to occur at a similar wavelength to that of quasi-2D states in $(PMA)_2PbI_4$ and $(PEA)_2PbI_4$.

6.4. Temperature-dependant photoluminescence excitation spectroscopy

To understand the origins of the various states and possible energy-transfer routes within the film, 2D temperature-dependant photoluminescence excitation (PLE) was performed. Typical PLE spectra are plotted in **Figure 6.14 (a)** and **(b)** for a non-stoichiometric 3.5:1 sample recorded at a temperature of 295 and 77 K, respectively. Here

the scatter from the excitation laser appears as a diagonal band across the image (note that the emission spectra are only plotted for wavelengths > 450 nm due to the limited operational range of the spectrometer grating used to detect emission). It can be seen that at all temperatures the excitation of the sample up to approximately 550 nm results in strong band-edge perovskite emission around 750 nm.

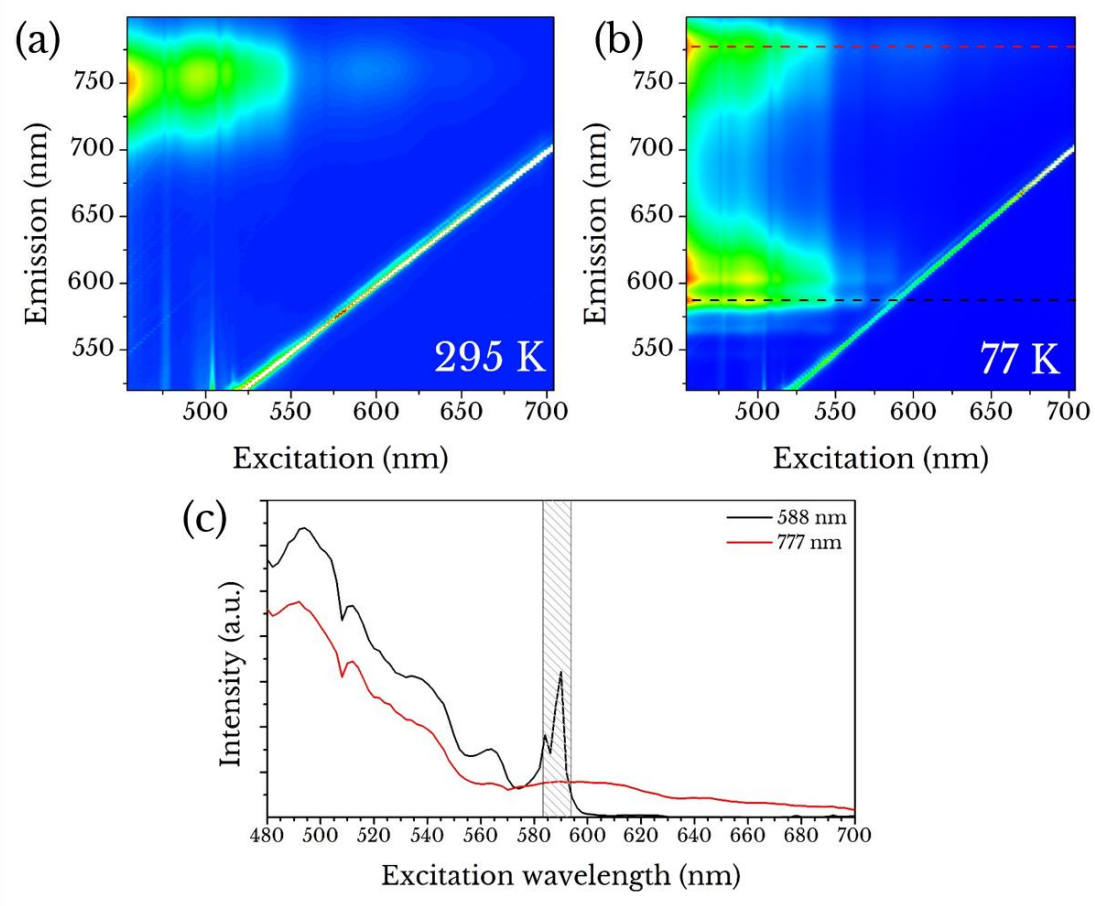

Figure 6.14 - Photoluminescence excitation (PLE) contour plots shown for a 3.5:1 sample glovebox annealed sample on quartz at (a) 295 K and (b) 77 K. (c) Horizontal slices of the plot in (b) at given emission wavelengths 588 nm (black) and 777 nm (red). The shaded section indicates scattered signal from the excitation source around 588 nm.

However, at 77 K, excitation at wavelengths up to 550 nm also results in additional emission from the LDPs over the wavelength-range 575 - 650 nm. In **Figure 6.14 (c)**, a horizontal cross-section is plotted through **Figure 6.14 (b)** (location shown using a dotted line), at wavelengths of 588 nm and 777 nm, corresponding to a PLE spectrum of one of the excitonic emission peaks and emission around the perovskite band-edge, respectively.

Interestingly, the PLE spectrum of the excitonic emission at 588 nm indicates weak excitation resonances at 542 and 562 nm, signifying some excitonic energy transfer (most likely by dipole-dipole coupling) between the different LDP states. This has been observed previously in RPP systems with excitonic energy transfer from a wider bandgap, lower n-dimensional regions to a narrower bandgap, high n-dimensional and 3D regions [89]. However, in this system such resonance features appear relatively suppressed in the PLE of the bulk emission, with the PLE spectrum at 777 nm being comparatively featureless. This observation indicates that direct energy transfer between the LDP states and the co-existing bulk perovskite phase is a relatively inefficient process.

6.5. Time-resolved photoluminescence spectroscopy

To further understand the photophysics of such LDP states, time-resolved luminescence (TRPL) as a function of wavelength was measured at a temperature of 12 K and 185 K. Here, the emission from the various features is described using a stretched exponential function approach [93,94]. The inclusion of a stretched decay, where the decay rate itself is dependent on time modifies **Equation 2.16** such that:

$$\frac{dN}{dt} = -C\frac{N}{t^{\gamma}} \tag{6.1}$$

where γ is a characteristic constant. Amending the decay rate and assuming the rate constant is a sum over only radiative and non-radiative process yields:

$$\frac{I(t)}{I(0)} = A_1 e^{-\left(\frac{t}{\tau_1}\right)^{\beta_1}} + A_2 e^{-\left(\frac{t}{\tau_2}\right)^{\beta_2}} \quad (6.2)$$

where I(t) is the photoluminescence intensity at time 't', A and B are amplitude constants, t is the time, τ_1 and τ_2 are the characteristic lifetimes and β_1 and β_2 are the stretching factors where $\beta = (1-\gamma)$ [93]. The emission wavelength of mixed-phase perovskites was first monochromated to resolve the lifetime of each peak feature shown in **Figure 6.11 (c)**. Measuring the intensity of the emission and fitting the resulting decay curves to **Equation 6.2** yielded two decay lifetimes.

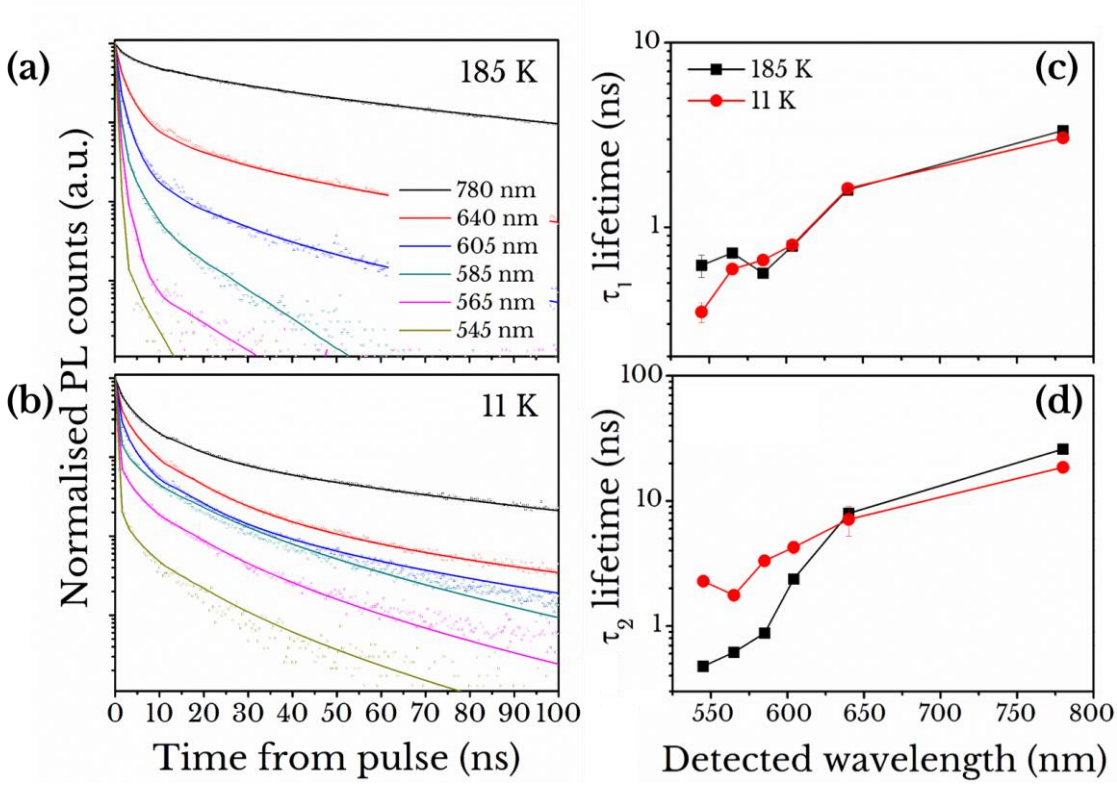

Figure 6.15 - Time resolved photoluminescence spectroscopy for 3.5:1 film air annealed on quartz at (a) 185 K and (b) 12 K shown with fitting (solid lines). The coloured lines represent isolated wavelengths of 780 nm (black), 640 nm (red), 605 nm (blue), 585 nm (cyan), 565 nm (magenta) and 545 nm (gold). (c) First (τ_1) and (d) second (τ_2) time constant parameters of double stretched exponential fits to the decay transients for the emissive peaks plotted against their emission wavelength. The sample was exposed to a laser fluence of 3.8 nJ/cm^2.

It has been suggested that in certain perovskites, the decay dynamics of I(t) is comprised of both a slow and a fast component. Here, the fast decay component (τ_1) is due to non-radiative recombination in the film, likely from surface effects and trap sites [95]. In contrast, the slower decay (τ_2) is due to bulk properties, revealing the bimolecular radiative-recombination lifetime of carriers within the bulk of the material [96]. **Figure 6.15 (a)** and **(b)** plot the (normalised) PL decay lifetime corresponding to the emissive peaks observed at 546, 566, 586, 646 and 770 nm. To quantify the transient behaviour, these were then fitted to double stretched exponentials of the form shown in **Equation 6.2**. The PL decay lifetime in relation to the fast and slow PL decay transients extracted from the fits are displayed in **Figure 6.15 (c)** and **(d)**.

It can be clearly seen that decay lifetimes increase as a function of detection wavelength; an observation consistent with an increase in PL intensity from the LDP states as a function of increasing wavelength. The increase in decay lifetime of LDP emission at longer wavelengths is consistent with a reduced radiative rate as a result of reduced electron-hole confinement [97,98]. Notably, a clear effect of temperature on the τ_2 (slow transient) emission lifetime of the LDP states (detection wavelengths <610 nm) increases as the temperature is reduced. PLE measurements indicate that direct energy transfer between the LDPs and bulk perovskite is a relatively inefficient process, and thus the excitons on isolated LDPs are able to undergo dissociation at temperatures >200 K by either the electron or hole undergoing thermally assisted tunnelling into the surrounding bulk perovskite.

6.6. Photoluminescence mapping

The observation of energy transfer between LDP states and charge-carrier tunnelling from LDP states into the bulk perovskite suggests that such phases must be relatively mixed. To understand the length-scales of this mixing, PL mapping performed at 4K has been used to characterise the distribution of emission from the various emissive states from a 3.5:1 film.

This is shown in **Figure 6.16 (a), (b), (c)** and **(d)**, where the integrated-distribution of luminescence is plotted centred around 510, 546, 566 (LDP emission) and 760 nm (bulk perovskite), respectively. The emission spectrum was integrated around the centre wavelengths with limits λ ± 5 nm. Significantly, the distribution of emission from the LDPs and the bulk perovskite are remarkably similar. Any discrepancies in emission distribution from the different states most likely result from changes in self-absorption, which would be attributed to thickness fluctuations in the film.

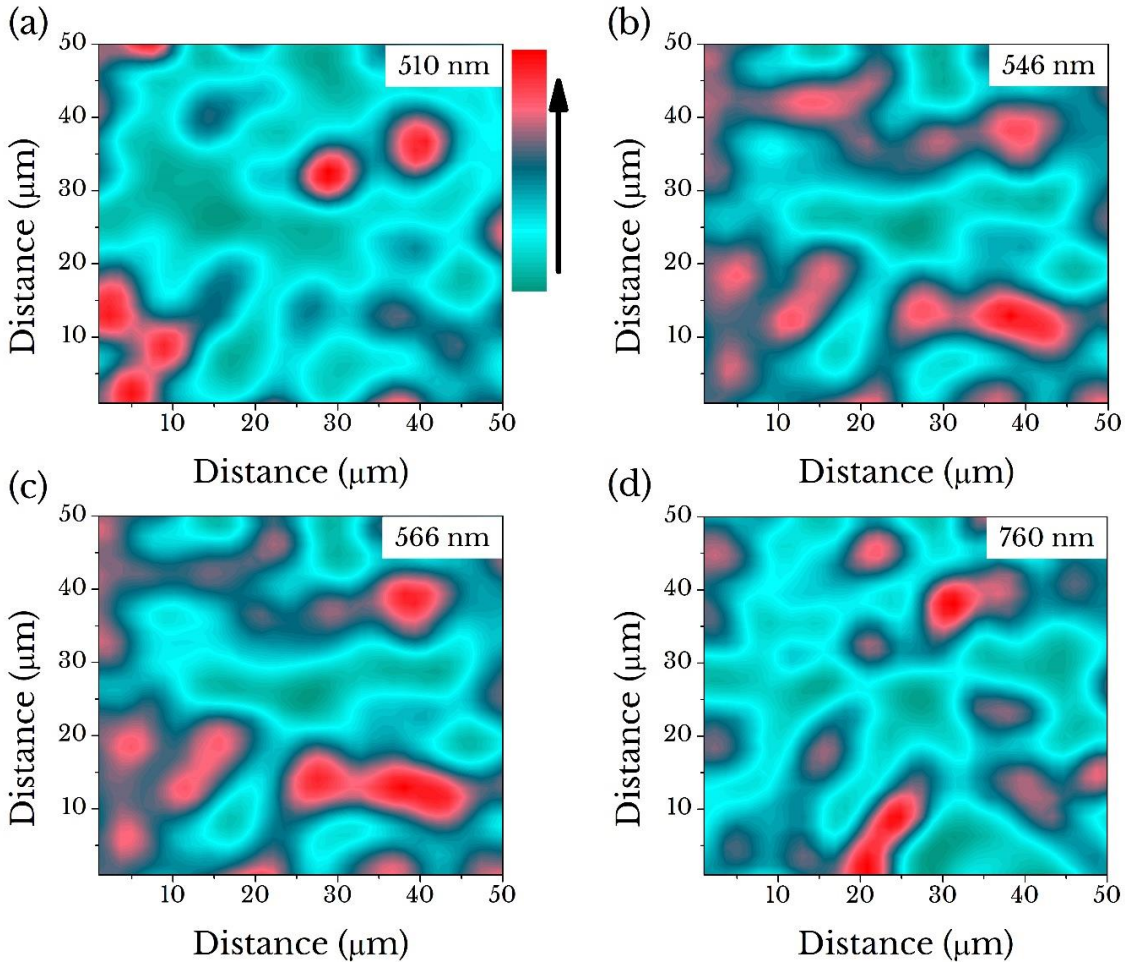

Figure 6.16 - Contour plots of the PL emission from LDP and bulk perovskite states integrated around (a) 510 nm, (b) 546 nm, (c) 566 nm and (d) 760 nm. The z-axis here is the integrated total PL intensity under the spectrum with limits ± 5 nm around the centre wavelength. Each plot has individual z-axis limits between its maximum and minimum value and are therefore not normalised to one another. The sample above was fabricated on to quartz glass only and regions of very low intensity are without any material.

The similarity between the different images suggests that LDP and bulk perovskite are mixed at a length-scale that is finer than the spatial resolution of our PL mapping setup (around 1.3 μm); a result consistent with facile energy and charge transfer between the different states. **Figure 6.16** also suggests that processed films cast from a 3.5:1 solution on to quartz glass are rather discontinuous. Regions of little to no material present a significant reduction in PL intensity indicated by a light-blue/green colour. As shown in the AFM images in **Figure 6.4**, these same 3.5:1 solutions cast on to an IP substrate also produce regions of reduced material and therefore result in a non-ideal surface coverage; albeit an improvement in coverage can be seen compared to the quartz substrate samples.

In the following section, 3.5:1 [MAI:PbCl2] solutions are cast into thin-films for use as the absorber layer in an inverted-architecture solar cell device.

6.7. Photovoltaic performance

The apparent complexity of these thin-films suggests they may have interesting optoelectronic properties. Mixed-phase perovskite films, similar to the ones studied in this chapter, have been studied using a $PEA_2(CH_3NH_3)_{n-1}Pb_nI_{3n+1}$ blend to form energy-funnels for light-emitting diodes [89]. In this study, Yuan *et al.* reported on lower <n> value (octahedral thickness) layers funnelling energy to a lower bandgap material across a complex energy landscape, whereby the fluorescence is produced from a lower energy-gap phase. Photovoltaic devices using an n=4 RPP 2D $(BA)_2(MA)_3Pb_4I_{13}$ perovskite have shown an excellent short-circuit currents (J_{sc}), over 1 V open-circuit voltages (V_{oc}) and a power conversion efficiency (PCE) over 12% [9].

In the following section, inverted architecture devices were fabricated using the 3.5:1 solution, which was hot-cast and annealed under a nitrogen atmosphere. The active layer was coated on to an ITO/PEDOT:PSS substrate using the same deposition routine as used to prepare thin-film samples discussed previously. Once annealed for 90

minutes at 90 °C, some devices were removed from the glovebox and exposed to high humidity (> 40% RH) for 30 seconds which was shown in **Figure 6.10** to collapse the LDP structures, forming a mostly 3D perovskite material. The moisture-treated (MT) films were then returned to the glovebox and annealed for a further 5 minutes at 90°C to remove any excess moisture in the film. Once cooled, both sets of perovskite films were then coated with PCBM to effectively planarise the rough mixed-phase perovskite surface and complete the p-i-n junction. The ITO / PEDOT:PSS / Perovskite / PCBM films were then annealed at 60°C for 5 minutes to remove any excess solvent.

Sample	Voc (V)	Jsc ($mAcm^{-2}$)	FF (%)	PCE (%)	Rs (Ωcm^2)	Rsh (Ωcm^2)
3.5:1 - Forward	0.98	-1.72	38.0	0.64	112	1413
3.5:1 - Reverse	1.03	-1.60	50.4	0.83	68	1558
3.5:1 - Forward (MT)	0.95	-1.94	33.9	0.62	223	1125
3.5:1 - Reverse (MT)	1.02	-1.81	50.9	0.94	115	3413

Table 6.3 – A summary of the measured device metrics for 3.5:1 devices with and without moisture treatment (MT) under AM1.5 for forward and reverse bias. The R_s and R_{sh} values have been estimated using the gradient of the J-V curve close to the V_{oc} and J_{sc} values, respectively.

Following this annealing step, sequential thermal evaporation of lithium fluoride (LiF) and aluminium (Al) top contacts completed the devices. The approximate layer thickness for each step is as follows: ITO / PEDOT:PSS (30 nm) / Perovskite (450 nm) / PCBM (80 nm) / LiF (4 nm) / Al (100 nm). The device metrics determined under AM1.5 solar irradiation is shown under forward and reverse bias in **Table 6.3**. It is clear from **Table 6.3** that such excess organic 3.5:1 devices produce a high V_{oc} that is close to 1 V in both forward and reverse bias conditions. The large V_{oc} in mixed-phase perovskites is

likely due to the wider bandgaps of the LDP absorbers within the film [8,20,99], which absorb strongly at ≈ 2.2 eV relative to the 3D perovskite band-edge at ≈ 1.6 eV. The increase in V_{oc} shown for both cells under reverse bias is likely the product of passivated defect sites, lowering the probability of charge recombination at the interface [100,101]. The low J_{sc} values measured for both cells can be explained by a combination of poor surface coverage and a large number of charge recombination sites [102]. From the PL mapping images shown in **Figure 6.16**, there appear to be large gaps (≈ 10 μm) between photo-active grains. Photo-generated charge carriers near to these grain boundaries are likely to recombine before successfully migrating through the film to the external circuit, resulting in a loss of measured photocurrent. It has been previously reported that a reduction of charge recombination at interfaces leads to an increase of the fill factor (FF) [103,104].

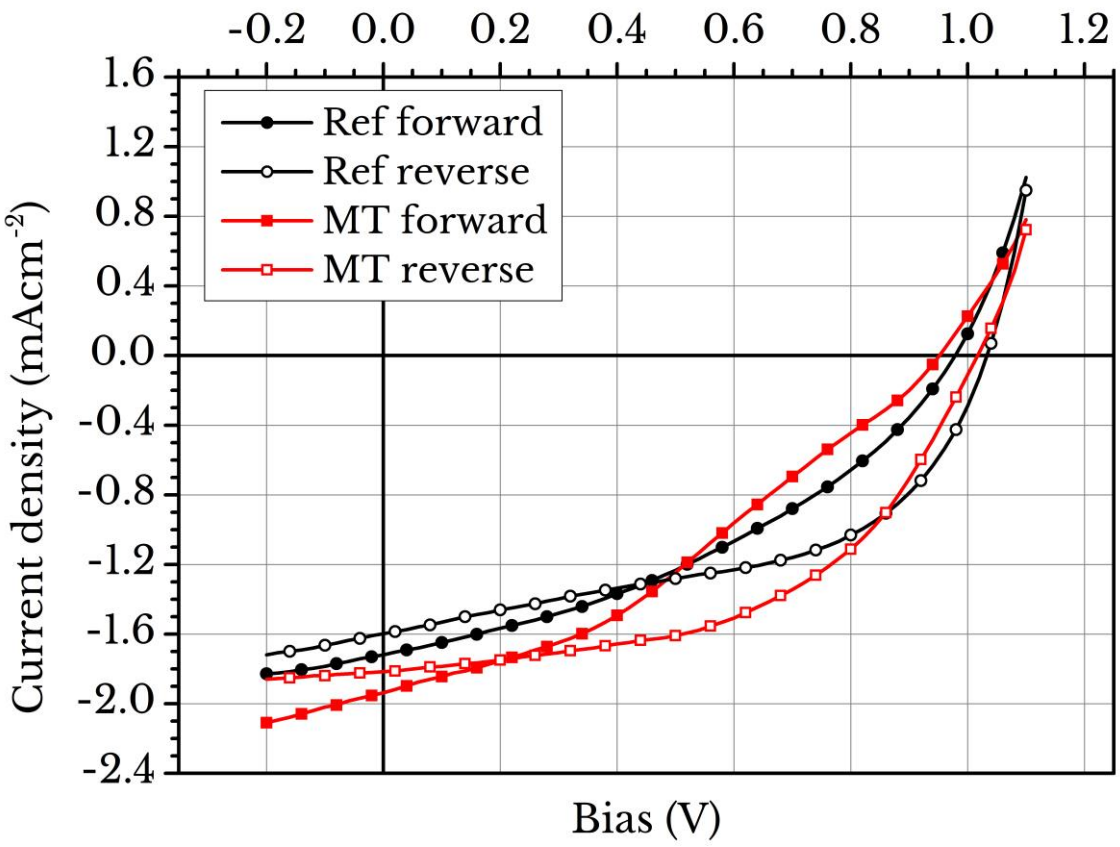

Figure 6.17 – Forward and reverse bias J-V plots of inverted 3.5:1 devices without (black) and with (red) moisture treatment (MT).

During J-V measurements (shown in **Figure 6.17**), devices were swept under forward bias from -0.2 V to 1.1 V and immediately returned to -0.2 V under reverse bias at a rate of 0.2 Vs^{-1}, consistent with other studies on inverted perovskite solar cells [105–107]. What is clear from **Table 6.3** is an improvement in both series resistance (R_s) and shunt resistance (R_{sh}) under reverse bias conditions. One possible explanation for this behaviour is the idea of charge-trap filling during the forward bias sweep, caused by the movement of mobile charges guided by the applied bias [108]. It is highly likely these excess-MAI (3.5:1) films contain a large number of defects which could be in the form of mobile halide interstitials (anions) or iodide vacancies (cations). Previous first-principle simulations have suggested under excess-iodine conditions, surplus iodine atoms will act as trap sites for charge carriers at grain boundaries [109]. As is apparent from the topographical analysis, the large number of grains suggests the excess iodide from the solution is concentrated towards the boundaries after annealing, acting as charge trapping sites for mobile cations [110]. When the device is then swept under reverse bias, an improvement in both R_s and R_{sh} is likely linked to a reduction in trap states in the bulk and at the grain surfaces. Other hysteresis mechanisms in perovskites have been ascribed to the capacitive effect [111] and intrinsic ferroelectric domains [112].

6.8. Conclusions

In summary, the structure and photophysics of mixed-halide perovskites containing a non-stoichiometric (3.5:1) excess of methylammonium (MA) has been explored. Using optical and electron microscopy, the thin-films created using a hot-cast technique are highly polycrystalline. Grazing incidence X-ray scattering reveals the presence of new scattering features at Q = 0.29, 0.58, 0.89 and 1.16 $Å^{-1}$, which co-exist with the bulk (3D) perovskite phase as shown in the emission spectra. On comparing the radially integrated scattering patterns of a 3.5:1 film to the simulated scattering patterns from work published by Soe *et al.*, as well as the simulated structure of an n = 3 $(MA)_4Pb_3I_{10}$ perovskite, a distinct correlation in reflected planes can be seen indicative of a type II DJP. It is speculated that the reflections produced from crystal planes in a 3.5:1 film are

of a similar nature to those shown from the ACI perovskite, although no conclusive evidence can be drawn from this work. It was found that the simulated n = 3 $(MA)_4Pb_3I_{10}$ perovskite adopts a triclinic *P1* space group with unit cell parameters of a = 6.47 Å, b = 12.56 Å and c = 23.23 Å and a unit cell volume of 1804.51 $Å^3$.

When such films are annealed in a glove-box under low-moisture conditions, the crystalline phase-purity improves, with a highly oriented film being formed. Optical spectroscopy performed on films as a function of temperature reveals the presence of excitonic-like features in both emission and absorption at temperatures <200 K; an observation consistent with the presence of a series of different low-dimensional states. Using photoluminescence excitation spectroscopy and time-resolved emission, the excitonic states are shown to have reduced lifetime at elevated temperature; however, this reduced lifetime most likely results from exciton dissociation caused by thermally assisted tunnelling of charge-carriers into regions of bulk (3D) perovskite. Photoluminescence mapping of the emission from the bulk perovskite and the low-dimensional emitters performed with a spatial resolution of ≈ 1.3 µm indicates strong co-localisation of states; a result consistent with facile energy and charge transfer. The measurements indicate a significant degree in energetic inhomogeneity in a perovskite film in which the organic cation is in excess. The local electronic properties of non-stoichiometric films are at present unknown, however, such films cannot be used to fabricate efficient photovoltaic devices. It is therefore likely that such structures and the interface between LDP and the 3D perovskite are associated with a range of charge-trap states that are related to a series of recombination pathways. This structural inhomogeneity may well be common in a range of related perovskite systems, and indeed may well be present at lower levels in films prepared much closer to their stoichiometric-ratio. The relatively poor surface coverage and associated defect density is likely the cause of a reduced photovoltaic performance of the devices, however, the excellent open-circuit voltage can be linked to the lower-dimensional phases present in these films.

6.9. References

1. Green, M. A., Ho-Baillie, A. & Snaith, H. J. The emergence of perovskite solar cells. *Nat. Photonics* **8,** 506–514 (2014).

2. Li, G., Price, M. & Deschler, F. Research Update: Challenges for high-efficiency hybrid lead-halide perovskite LEDs and the path towards electrically pumped lasing. *APL Mater.* **4,** (2016).

3. Ahmadi, M., Wu, T. & Hu, B. A Review on Organic-Inorganic Halide Perovskite Photodetectors: Device Engineering and Fundamental Physics. *Adv. Mater.* **29,** 1605242 (2017).

4. Bracher, C., Freestone, B. G., Mohamad, D. K., Smith, J. A. & Lidzey, D. G. Degradation of inverted architecture $CH_3NH_3PbI_{3-x}Cl_x$ perovskite solar cells due to trapped moisture. *Energy Sci. Eng.* **6,** 35–46 (2018).

5. Luo, S. & Daoud, W. a. Recent progress in organic–inorganic halide perovskite solar cells: mechanisms and material design. *J. Mater. Chem. A* **3,** 8992–9010 (2015).

6. Aristidou, N. *et al.* Fast oxygen diffusion and iodide defects mediate oxygen-induced degradation of perovskite solar cells. *Nat. Commun.* **8,** 15218 (2017).

7. Conings, B. *et al.* Intrinsic Thermal Instability of Methylammonium Lead Trihalide Perovskite. *Adv. Energy Mater.* **5,** 1500477 (2015).

8. Smith, I. C., Hoke, E. T., Solis-Ibarra, D., McGehee, M. D. & Karunadasa, H. I. A Layered Hybrid Perovskite Solar-Cell Absorber with Enhanced Moisture Stability. *Angew. Chemie Int. Ed.* **53,** 11232–11235 (2014).

9. Tsai, H. *et al.* High-efficiency two-dimensional Ruddlesden–Popper perovskite solar cells. *Nature* **536,** 312–316 (2016).

10. Milot, R. L. *et al.* Charge-Carrier Dynamics in 2D Hybrid Metal–Halide Perovskites. *Nano Lett.* **16,** 7001–7007 (2016).

11. Filip, M. R. & Giustino, F. Steric engineering of metal-halide perovskites with tunable optical band gaps. *Nat. Commun.* **5,** 1–19 (2014).

12. Vassilakopoulou, A., Papadatos, D., Zakouras, I. & Koutselas, I. Mixtures of quasi-two and three dimensional hybrid organic-inorganic semiconducting perovskites for single layer LED. *J. Alloys Compd.* **692,** 589–598 (2017).

13. Mitzi, D. B. Templating and structural engineering in organic–inorganic perovskites. *J. Chem. Soc. Dalt. Trans.* 1–12 (2001).

14. Stoumpos, C. C. *et al.* Ruddlesden–Popper Hybrid Lead Iodide Perovskite 2D Homologous Semiconductors. *Chem. Mater.* **28,** 2852–2867 (2016).

15. Sichert, J. A. *et al.* Quantum Size Effect in Organometal Halide Perovskite Nanoplatelets. *Nano Lett.* **15,** 6521–6527 (2015).

16. Wang, Q. *et al.* Quantum confinement effect and exciton binding energy of layered perovskite nanoplatelets. *AIP Adv.* **8,** 025108 (2018).

17. Kataoka, T. *et al.* Magneto-optical study on the excitonic spectrum of $(C_6H_{13}NH_3)_2PbI_4$. *Phys. B Condens. Matter* **184,** 132–136 (1993).

18. Tanaka, K. *et al.* Image charge effect on two-dimensional excitons in an inorganic-organic quantum-well crystal. *Phys. Rev. B - Condens. Matter Mater. Phys.* **71**, 1–6 (2005).

19. Papagiannouli, I., Maratou, E., Koutselas, I. & Couris, S. Synthesis and characterization of the nonlinear optical properties of novel hybrid organic-inorganic semiconductor lead iodide quantum wells and dots. *J. Phys. Chem. C* **118**, 2766–2775 (2014).

20. Chen, Y. *et al.* 2D Ruddlesden–Popper Perovskites for Optoelectronics. *Adv. Mater.* **30**, 1–15 (2018).

21. Grancini, G. *et al.* One-Year stable perovskite solar cells by 2D/3D interface engineering. *Nat. Commun.* **8**, 15684 (2017).

22. Mei, A. *et al.* A hole-conductor–free, fully printable mesoscopic perovskite solar cell with high stability. *Sci.* **345**, 295–298 (2014).

23. Wang, Z. *et al.* Efficient ambient-air-stable solar cells with 2D-3D heterostructured butylammonium-caesium-formamidinium lead halide perovskites. *Nat. Energy* **2**, 1–10 (2017).

24. Kamminga, M. E. *et al.* Confinement Effects in Low-Dimensional Lead Iodide Perovskite Hybrids. *Chem. Mater.* **28**, 4554–4562 (2016).

25. Mao, L. *et al.* Hybrid Dion–Jacobson 2D Lead Iodide Perovskites. *J. Am. Chem. Soc.* **140**, 3775–3783 (2018).

26. Momma, K. & Izumi, F. VESTA 3 for three-dimensional visualization of crystal, volumetric and morphology data. *J. Appl. Crystallogr.* **44**, 1272–1276 (2011).

27. Soe, C. M. M. *et al.* New Type of 2D Perovskites with Alternating Cations in the Interlayer Space, $(C(NH_2)_3)(CH_3NH_3)_nPb_nI_{3n+1}$: Structure, Properties, and Photovoltaic Performance. *J. Am. Chem. Soc.* **139**, 16297–16309 (2017).

28. Tilley, R. J. D. *Perovskites: Structure–Property Relationships*. *MRS Bulletin* **42**, (John Wiley & Sons, Ltd, 2016).

29. Chen, Q. *et al.* Controllable Self-Induced Passivation of Hybrid Lead Iodide Perovskites toward High Performance Solar Cells. *Nano Lett.* **14**, 4158–4163 (2014).

30. Bi, D. *et al.* Efficient luminescent solar cells based on tailored mixed-cation perovskites. *Sci. Adv.* **2**, e1501170 (2016).

31. Park, N.-G. Nonstoichiometric Adduct Approach for High-Efficiency Perovskite Solar Cells. *Inorg. Chem.* **56**, 3–10 (2017).

32. Song, Z. *et al.* Impact of Processing Temperature and Composition on the Formation of Methylammonium Lead Iodide Perovskites. *Chem. Mater.* **27**, 4612–4619 (2015).

33. Petrus, M. L. *et al.* The Influence of Water Vapor on the Stability and Processing of Hybrid Perovskite Solar Cells Made from Non-Stoichiometric Precursor Mixtures. *ChemSusChem* **9**, 2699–2707 (2016).

34. Ong, K. P., Goh, T. W., Xu, Q. & Huan, A. Structural Evolution in Methylammonium Lead Iodide $CH_3NH_3PbI_3$. *J. Phys. Chem. A* **119**, 11033–11038 (2015).

35. Fang, H. H. *et al.* Photophysics of organic-inorganic hybrid lead iodide perovskite

single crystals. *Adv. Funct. Mater.* **25,** 2378–2385 (2015).

36. Sewvandi, G. A., Kodera, K., Ma, H., Nakanishi, S. & Feng, Q. Antiferroelectric Nature of $CH_3NH_3PbI_{3-x}Cl_x$ Perovskite and Its Implication for Charge Separation in Perovskite Solar Cells. *Sci. Rep.* **6**, 30680 (2016).

37. Saidaminov, M. I., Mohammed, O. F. & Bakr, O. M. Low-Dimensional-Networked Metal Halide Perovskites: The Next Big Thing. *ACS Energy Lett.* **2,** 889–896 (2017).

38. Noel, N. K. *et al.* Unveiling the Influence of pH on the Crystallization of Hybrid Perovskites, Delivering Low Voltage Loss Photovoltaics. *Joule* **1,** 328–343 (2017).

39. Heo, J. H. & Im, S. H. Highly reproducible, efficient hysteresis-less $CH_3NH_3PbI_{3-x}Cl_x$ planar hybrid solar cells without requiring heat-treatment. *Nanoscale* **8,** 2554–2560 (2016).

40. Mohamad, D. K. *et al.* Optimized organometal halide perovskite solar cell fabrication through control of nanoparticle crystal patterning. *J. Mater. Chem. C* **5,** 2352–2359 (2017).

41. Klein, J. R., Flender, O., Scholz, M., Oum, K. & Lenzer, T. Charge carrier dynamics of methylammonium lead iodide: from PbI_2 -rich to low-dimensional broadly emitting perovskites. *Phys. Chem. Chem. Phys.* **18,** 10800–10808 (2016).

42. Kim, T. G., Seo, S. W., Kwon, H., Hahn, J. & Kim, J. W. Influence of halide precursor type and its composition on the electronic properties of vacuum deposited perovskite films. *Phys. Chem. Chem. Phys.* **17,** 24342–24348 (2015).

43. Huang, Y. C. *et al.* Insight into Evolution, Processing and Performance of Multi-length-scale Structures in Planar Heterojunction Perovskite Solar Cells. *Sci. Rep.* **5,** 1–11 (2015).

44. Cronin, H. M., Jayawardena, K. D. G. I., Stoeva, Z., Shkunov, M. & Silva, S. R. P. Effects of ambient humidity on the optimum annealing time of mixed-halide Perovskite solar cells. *Nanotechnology* **28,** (2017).

45. Fu, G. *et al.* Efficiency enhancement in planar $CH_3NH_3PbI_{3-x}Cl_x$ perovskite solar cells by processing with bidentate halogenated additives. *Sol. Energy Mater. Sol. Cells* **165,** 36–44 (2017).

46. Yang, Y. *et al.* Annealing induced re-crystallization in $CH_3NH_3PbI_{3-x}Cl_x$ for high performance perovskite solar cells. *Sci. Rep.* **7,** 1–9 (2017).

47. Wang, J.-F. *et al.* Surface engineering of perovskite films for efficient solar cells. *Sci. Rep.* **7,** 14478 (2017).

48. Williams, S. T. *et al.* Role of Chloride in the Morphological Evolution of Organo-Lead Halide Perovskite Thin Films. *ACS Nano* **8,** 10640–10654 (2014).

49. Unger, E. L. *et al.* Chloride in Lead Chloride-Derived Organo-Metal Halides for Perovskite-Absorber Solar Cells. *Chem. Mater.* **26,** 7158–7165 (2014).

50. Berhe, T. A. *et al.* Organometal halide perovskite solar cells: degradation and stability. *Energy Environ. Sci.* **9,** 323–356 (2016).

51. Alsari, M. *et al.* In situ simultaneous photovoltaic and structural evolution of perovskite solar cells during film formation. *Energy Environ. Sci.* **11,** 383–393 (2018).

52. Lilliu, S. *et al.* Grain rotation and lattice deformation during perovskite spray

coating and annealing probed *in situ* by GI-WAXS. *CrystEngComm* **18**, 5448–5455 (2016).

53. Yang, Y. *et al.* Annealing Induced Re-crystallization in $CH_3NH_3PbI_{3-x}Cl_x$ for High Performance Perovskite Solar Cells. *Sci. Rep.* **7**, 46724 (2017).

54. Barrows, A. T. *et al.* Monitoring the Formation of a $CH_3NH_3PbI_{3-x}Cl_x$ Perovskite during Thermal Annealing Using X-Ray Scattering. *Adv. Funct. Mater.* **26**, 4934–4942 (2016).

55. Lilliu, S. *et al.* Mapping Morphological and Structural Properties of Lead Halide Perovskites by Scanning Nanofocus XRD. *Adv. Funct. Mater.* **26**, 8221–8230 (2016).

56. Tang, G., Yang, C., Stroppa, A., Fang, D. & Hong, J. Revealing the role of thiocyanate anion in layered hybrid halide perovskite $(CH_3NH_3)_2Pb(SCN)_2I_2$. *J. Chem. Phys.* **146**, 224702 (2017).

57. Noh, J. H., Im, S. H., Heo, J. H., Mandal, T. N. & Seok, S. Il. Chemical Management for Colorful, Efficient, and Stable Inorganic–Organic Hybrid Nanostructured Solar Cells. *Nano Lett.* **13**, 1764–1769 (2013).

58. Manser, J. S., Saidaminov, M. I., Christians, J. A., Bakr, O. M. & Kamat, P. V. Making and Breaking of Lead Halide Perovskites. *Acc. Chem. Res.* **49**, 330–338 (2016).

59. Patel, J. B., Milot, R. L., Wright, A. D., Herz, L. M. & Johnston, M. B. Formation Dynamics of $CH_3NH_3PbI_3$ Perovskite Following Two-Step Layer Deposition. *J. Phys. Chem. Lett.* **7**, 96–102 (2016).

60. Leguy, A. M. A. *et al.* Reversible Hydration of $CH_3NH_3PbI_3$ in Films, Single Crystals, and Solar Cells. *Chem. Mater.* **27**, 3397–3407 (2015).

61. Papavassiliou, G. C. Three- and low-dimensional inorganic semiconductors. *Prog. Solid State Chem.* **25**, 125–270 (1997).

62. Ishihara, T. Optical properties of PbI-based perovskite structures. *J. Lumin.* **60–61**, 269–274 (1994).

63. Imler, G. H. *et al.* Solid state transformation of the crystalline monohydrate $(CH_3NH_3)PbI_3(H_2O)$ to the $(CH_3NH_3)PbI_3$ perovskite. *Chem. Commun.* **51**, 11290–11292 (2015).

64. Vincent, B. R. *et al.* Alkylammonium lead halides. Part 1. Isolated PbI_6^{4-} ions in $(CH_3NH_3)_4PbI_6 \cdot 2H_2O$. *Can. J. Chem.* **65**, 1042–1046 (1987).

65. Petrov, A. A. *et al.* Crystal Structure of DMF-Intermediate Phases Uncovers the Link between $CH_3NH_3PbI_3$ Morphology and Precursor Stoichiometry. *J. Phys. Chem. C* **121**, 20739–20743 (2017).

66. Milot, R. L. *et al.* Charge-Carrier Dynamics in 2D Hybrid Metal–Halide Perovskites. *Nano Lett.* **16**, 7001–7007 (2016).

67. Cao, D. H., Stoumpos, C. C., Farha, O. K., Hupp, J. T. & Kanatzidis, M. G. 2D Homologous Perovskites as Light-Absorbing Materials for Solar Cell Applications. *J. Am. Chem. Soc.* **137**, 7843–7850 (2015).

68. Park, B. *et al.* Enhanced Crystallinity in Organic–Inorganic Lead Halide Perovskites on Mesoporous TiO 2 via Disorder–Order Phase Transition. *Chem. Mater.* **26**, 4466–4471 (2014).

69. Raga, S. R. & Qi, Y. The Effect of Impurities on the Impedance Spectroscopy

Response of $CH_3NH_3PbI_3$ Perovskite Solar Cells. *J. Phys. Chem. C* **120**, 28519–28526 (2016).

70. Patel, J. B., Milot, R. L., Wright, A. D., Herz, L. M. & Johnston, M. B. Formation Dynamics of $CH_3NH_3PbI_3$ Perovskite Following Two-Step Layer Deposition. *J. Phys. Chem. Lett.* **7**, acs.jpclett.5b02495 (2015).

71. Huang, J., Tan, S., Lund, P. & Zhou, H. Impact of H2O on organic-inorganic hybrid perovskite solar cells. *Energy Environ. Sci.* **10**, 2284–2311 (2017).

72. Xu, Y. *et al.* The Effect of Humidity upon the Crystallization Process of Two-Step Spin-Coated Organic-Inorganic Perovskites. *ChemPhysChem* **17**, 112–118 (2016).

73. Gangishetty, M. K., Scott, R. W. J. & Kelly, T. L. Effect of relative humidity on crystal growth, device performance and hysteresis in planar heterojunction perovskite solar cells. *Nanoscale* **8**, 6300–6307 (2016).

74. Xing, J. *et al.* Color-stable highly luminescent sky-blue perovskite light-emitting diodes. *Nat. Commun.* **9**, 3541 (2018).

75. Quan, L. N. *et al.* Ligand-Stabilized Reduced-Dimensionality Perovskites. *J. Am. Chem. Soc.* **138**, 2649–2655 (2016).

76. Zhu, F. *et al.* Shape evolution and single particle luminescence of organometal halide perovskite nanocrystals. *ACS Nano* **9**, 2948–2959 (2015).

77. Tombe, S. *et al.* Optical and electronic properties of mixed halide (X = I, Cl, Br) methylammonium lead perovskite solar cells. *J. Mater. Chem. C* **5**, 1714–1723 (2017).

78. D'Innocenzo, V. *et al.* Excitons versus free charges in organo-lead tri-halide perovskites. *Nat. Commun.* **5**, 3586 (2014).

79. Shang, Q. *et al.* Unveiling Structurally Engineered Carrier Dynamics in Hybrid Quasi-Two-Dimensional Perovskite Thin Films toward Controllable Emission. *J. Phys. Chem. Lett.* **8**, 4431–4438 (2017).

80. Mercier, N., Poiroux, S., Riou, A. & Batail, P. Unique Hydrogen Bonding Correlating with a Reduced Band Gap and Phase Transition in the Hybrid Perovskites $(HO(CH_2)_2NH_3)_2PbX_4$ (X = I, Br). *Inorg. Chem.* **43**, 8361–8366 (2004).

81. Papadatos, D., Vassilakopoulou, A. & Koutselas, I. Energy transfer yellow light emitting diodes based on blends of quasi-2D perovskites. *J. Lumin.* **188**, 567–576 (2017).

82. Blancon, J.-C. *et al.* Extremely efficient internal exciton dissociation through edge states in layered 2D perovskites. *Science.* **355**, 1288–1292 (2017).

83. Mitzi, D. B., Medeiros, D. R. & Malenfant, P. R. L. Intercalated organic-inorganic perovskites stabilized by fluoroaryl-aryl interactions. *Inorg. Chem.* **41**, 2134–2145 (2002).

84. Du, K. Z. *et al.* Two-Dimensional Lead(II) Halide-Based Hybrid Perovskites Templated by Acene Alkylamines: Crystal Structures, Optical Properties, and Piezoelectricity. *Inorg. Chem.* **56**, 9291–9302 (2017).

85. Wu, K. *et al.* Temperature-dependent excitonic photoluminescence of hybrid organometal halide perovskite films. *Phys. Chem. Chem. Phys.* **16**, 22476–22481 (2014).

86. Meggiolaro, D. *et al.* Iodine chemistry determines the defect tolerance of lead-

halide perovskites. *Energy Environ. Sci.* **11**, 702–713 (2018).

87. Merdasa, A. *et al.* Super-resolution luminescence microspectroscopy reveals the mechanism of photoinduced degradation in $CH_3NH_3PbI_3$ perovskite nanocrystals. *J. Phys. Chem. C* **120**, 10711–10719 (2016).

88. Protesescu, L. *et al.* Nanocrystals of Cesium Lead Halide Perovskites ($CsPbX_3$, X = Cl, Br, and I): Novel Optoelectronic Materials Showing Bright Emission with Wide Color Gamut. *Nano Lett.* **15**, 3692–3696 (2015).

89. Yuan, M. *et al.* Perovskite energy funnels for efficient light-emitting diodes. *Nat. Nanotechnol.* **11**, 872–877 (2016).

90. Qian, J., Guo, Q., Liu, L., Xu, B. & Tian, W. A theoretical study of hybrid lead iodide perovskite homologous semiconductors with 0D, 1D, 2D and 3D structures. *J. Mater. Chem. A* **5**, 16786–16795 (2017).

91. Quan, L. N. *et al.* Quasi-2D perovskites for efficient solar cells and LEDs. *SPIE Newsroom* 8–10 (2016).

92. Xing, J. *et al.* Color-stable highly luminescent sky-blue perovskite light-emitting diodes. *Nat. Commun.* **9**, 3541 (2018).

93. Lee, K. C. B. *et al.* Application of the Stretched Exponential Function to Fluorescence Lifetime Imaging. *Biophys. J.* **81**, 1265–1274 (2001).

94. Phillips, J. C. Stretched exponential relaxation in molecular and electronic glasses. *Reports Prog. Phys.* **59**, 1133–1207 (1996).

95. Saidaminov, M. I. *et al.* High-quality bulk hybrid perovskite single crystals within minutes by inverse temperature crystallization. *Nat. Commun.* **6**, 1–6 (2015).

96. Shi, D. *et al.* Low trap-state density and long carrier diffusion in organolead trihalide perovskite single crystals. *Science.* **347**, 519–522 (2015).

97. Hong, X., Ishihara, T. & Nurmikko, A. V. Dielectric confinement effect on excitons in PbI4-based layered semiconductors. *Phys. Rev. B* **45**, 6961–6964 (1992).

98. Tabuchi, Y., Asai, K., Rikukawa, M., Sanui, K. & Ishigure, K. Preparation and characterization of natural lower dimensional layered perovskite-type compounds. *J. Phys. Chem. Solids* **61**, 837–845 (2000).

99. Eperon, G. E. *et al.* Perovskite-perovskite tandem photovoltaics with optimized band gaps. *Science.* **354**, 861–865 (2016).

100. Bi, C. *et al.* Understanding the formation and evolution of interdiffusion grown organolead halide perovskite thin films by thermal annealing. *J. Mater. Chem. A* **2**, 18508–18514 (2014).

101. Zhao, T., Chueh, C.-C., Chen, Q., Rajagopal, A. & Jen, A. K. Y. Defect Passivation of Organic–Inorganic Hybrid Perovskites by Diammonium Iodide toward High-Performance Photovoltaic Devices. *ACS Energy Lett.* **1**, 757–763 (2016).

102. Wetzelaer, G. J. A. H. *et al.* Trap-Assisted Non-Radiative Recombination in Organic-Inorganic Perovskite Solar Cells. *Adv. Mater.* **27**, 1837–1841 (2015).

103. Dagar, J., Castro-Hermosa, S., Lucarelli, G., Cacialli, F. & Brown, T. M. Highly efficient perovskite solar cells for light harvesting under indoor illumination via solution processed SnO_2/MgO composite electron transport layers. *Nano Energy* **49**, 290–299 (2018).

104. Bartesaghi, D. *et al.* Competition between recombination and extraction of free charges determines the fill factor of organic solar cells. *Nat. Commun.* **6,** 7083 (2015).

105. Cao, C. *et al.* Iodine and Chlorine Element Evolution in $CH_3NH_3PbI_{3-x}Cl_x$ Thin Films for Highly Efficient Planar Heterojunction Perovskite Solar Cells. *Chem. Mater.* **28,** 2742–2749 (2016).

106. Momblona, C. *et al.* Efficient vacuum deposited p-i-n and n-i-p perovskite solar cells employing doped charge transport layers. *Energy Environ. Sci.* **9,** 3456–3463 (2016).

107. Yan, K. *et al.* Hybrid Halide Perovskite Solar Cell Precursors: Colloidal Chemistry and Coordination Engineering behind Device Processing for High Efficiency. *J. Am. Chem. Soc.* **137,** 4460–4468 (2015).

108. Meloni, S. *et al.* Ionic polarization-induced current-voltage hysteresis in $CH_3NH_3PbX_3$ perovskite solar cells. *Nat. Commun.* **7,** (2016).

109. Uratani, H. & Yamashita, K. Charge Carrier Trapping at Surface Defects of Perovskite Solar Cell Absorbers: A First-Principles Study. *J. Phys. Chem. Lett.* **8,** 742–746 (2017).

110. Do Kim, H. & Ohkita, H. Charge traps in lead-halide perovskites with different grain sizes. *Jpn. J. Appl. Phys.* **57,** 08RE03 (2018).

111. Chen, B. *et al.* Impact of Capacitive Effect and Ion Migration on the Hysteretic Behavior of Perovskite Solar Cells. *J. Phys. Chem. Lett.* **6,** 4693–4700 (2015).

112. Röhm, H., Leonhard, T., Hoffmann, M. J. & Colsmann, A. Ferroelectric domains in methylammonium lead iodide perovskite thin-films. *Energy Environ. Sci.* **10,** 950–955 (2017).

Chapter 7

Conclusions and further work

The use of solution-processed materials has seen a rapid progression in the field of photovoltaics (PV) and opens up the potential for large-scale, roll-to-roll applications. To challenge pre-existing technologies such as Silicon-based PV, new materials are being synthesised and implemented in a cost-effective, low-temperature fabrication protocol. In the last few decades, interest in organic-photovoltaics (OPVs) has explored the potential for solution-processible PV devices through the synthesis of new copolymer donor materials, with devices efficiencies upwards of 14% demonstrated. Organic-inorganic hybrid perovskites have also been shown to have power conversion efficiencies (PCEs) in excess of 20%, challenging the current leading PV technologies. The ease by which organic and hybrid perovskites can be processed make them an attractive method to generate renewable solar energy. However, gains in device efficiency can still be expected through engineering the nanoscale composition and structure of the active semiconductor layer.

In this thesis, the crystallographic and photophysical nature of new solution-processible semiconducting systems have been studied for use in photovoltaic applications. This includes solution-additive engineering of a perovskite precursor and its impact on spray-coated PV devices. In order to optimise these photovoltaic materials, each chapter consists of an investigation into the structure and optoelectronic properties of thin-film samples, which were then used in photovoltaic devices.

In **Chapter 4**, a series of new D-A polymers utilising a similar conjugated backbone to that of PCDTBT were studied for their potential use in photovoltaic applications. Copolymers P1 and P2 were synthesised with a cyclopentadithiophene (CPDT) electron-donating unit, whilst P3 and P4 were synthesised with a dibenzosilole (DBS) donor unit.

Thin film absorption and PL analysis suggests that, in accordance with DFT calculations, a bathochromic shift of the intramolecular charge transfer (ICT) absorbance peak and photoluminescence (PL) emission for polymers P1 and P2 relative to P3 and P4 occurs as a result of a delocalisation of the HOMO level. The emission produced from polymer:PCBM blends indicated a significant quenching for the CPDT-containing polymers, which is linked to efficient charge carrier transfer across the donor:acceptor interface. In contrast, DBS-based polymers P3 and P4 showed poor quenching abilities possibly caused by insufficient mixing of the polymer molecules with PCBM. Glancing-incidence wide-angle X-ray scattering (GIWAXS) performed on polymer films of P1 (CPDT) and P3 (DBS) indicated a similar π-π stacking distance to that of PCDTBT (4 Å). The best PV devices were fabricated from the CPDT-containing polymer P1 in a 1:3 ratio with PCBM, producing a champion PCE of 1.77 %. Polymers P2, P3 and P4 were fabricated in an identical device architecture to P1, producing champion PCEs of 0.92 %, 0.41 % and 0.38 %, respectively. A combination of a high series resistance and a low shunt resistance can be attributed to the reduction in performance relative to the reference PCDTBT devices. It is speculated that poor mixing of polymer with fullerene in the as-cast films significantly reduces the J_{sc} in related devices, a result confirmed by the PL quenching capabilities of the blends.

The effects of adding varying concentrations of acidic hydriodic acid (HI) into a 3:1 molar ratio of methylammonium iodide (MAI):lead chloride ($PbCl_2$) perovskite precursor solution was explored in **Chapter 5**. Dynamic light scattering (DLS) confirms the presence of HI reduces the density of particulates (thought to be $PbCl_2$ aggregates) in solution from 1μm to just over 1 nm. At a concentration of 1 vol%, HI increases the crystallinity of the perovskite thin films, causes a red-shift of the absorption edge and increases the PL emission intensity of the perovskite film compared to films cast without such an additive.. It was then shown that the addition of 1 vol% of HI improved the relative efficiency of spin- and spay-cast PV devices by 90 % and 60 %, respectively. Champion devices measured under AM1.5 solar irradiance achieved PCEs of 13.8 % and 11.4 % for spin- and spray-cast deposition techniques, respectively. Higher concentrations of HI additive were incorporated into precursor solutions that also showed full dissolution of $PbCl_2$ in solution, however, photovoltaic performance was

significantly reduced for both deposition routes. It is speculated that a reduced surface coverage coupled with a poor interface between perovskite and fullerene could cause such a drop in efficiency.

In **Chapter 6**, non-stoichiometric perovskite precursors were studied for their potential use in PV devices. Upon adding a 17% molar excess of MAI to an otherwise stoichiometric perovskite precursor blend (3:1 to 3.5:1 [MAI:$PbCl_2$]), additional scattering features are observed for films measured using grazing incidence X-ray scattering (GIWAXS). Fitting the radial profiles of these scattering patterns revealed a similarity between measured GIWAXS data and a simulated quasi-2D type II Dion-Jacobson perovskite (DJP). The results of theoretical calculations suggest the presence of an n = 3 DJP $(MA)_4Pb_3I_{10}$ perovskite, which adopts a triclinic *P1* space group with unit cell parameters of a = 6.47 Å, b = 12.56 Å and c = 23.23 Å and a unit cell volume of 1804.51 $Å^3$. However, this calculation assumed a temperature of 0 K, and as such the experimental GIWAXS is likely to be imaging this same material in a different space group at 290 K. Measuring the PL emission from these non-stoichiometric films revealed a complex PL emission spectrum below 200 K. Transient spectroscopy (TRPL) revealed PL lifetimes decreased as a function of increasing temperature, with expected LDP emission having a lifetime of less than one nanosecond. Low-temperature PL mapping of non-stoichiometric films also showed a close packing of emitting states between 510 – 780 nm, consistent with a cascade-like energy-transfer process from large- to smaller-bandgap perovskite phases. The relatively low-performing photovoltaic devices is likely a product of a large defect density and poor surface coverage, although the high open-circuit voltage can be attributed to lower-dimensional perovskite absorbers in the film.

7.1. Further work

An extension to the work undertaken in **Chapter 4** would be to investigate the phase separation of the polymer:fullerene matrix. It was found that when blended with PCBM,

the quenching of PL was incomplete. A thorough investigation into the causes of such PL quenching effects may help increasing the overall efficiency of these devices. Unfortunately due to material quantity limitations, a wider range of weight ratios with PCBM (i.e. 1:1, 1:3) was not explored. A clear extension to this work would also be to investigate the X-ray diffraction patterns of a full range of polymer:PCBM blends, which may help to explain the mixing capabilities of these donor-acceptor copolymers. Combining X-ray diffraction data with the PL quenching efficiency of a range of donor polymer:PCBM blends should allow a better picture of film structure to be developed.

Work performed in **Chapter 5** could be developed by exploring the effect of the HI-additive effect in 'standard architecture' devices. In this thesis, devices were fabricated in an inverted architecture, however, perovskite devices have also been shown to perform well in standard device architectures. A full temperature-dependant SSPL and TRPL study could also be performed as a function of increasing HI concentration to probe the charge carrier dynamics in post-annealed films. From the TRPL data in **Chapter 5**, it appears as though 1 vol% HI in the precursor provides a longer carrier diffusion length relative to films made from a 0 vol% solution. Further work could probe this parameter space, with a temperature and HI concentration series performed to fully understand the charge-carrier dynamics in films cast from small or large amounts of the HI additive. In addition, other alkyl halides such as 1,4-dichlorobutane (1,4-DClB) and 1,8-diiodooctane (1,8-DIO) have been shown to improve the crystallinity of perovskite thin-films [1,2]. However, these studies have not explored the temperature-dependant charge-carrier dynamics under steady-state and time-resolved conditions.

The new quasi-2D perovskite described in **Chapter 6** is the first material reported that comprises of MA^+ cations in the insulating interlayer between lead-halide octahedral slabs. Further work based on this framework could explore the potential use of larger organic-halides as the cation species in the precursor, such as formamadinium (FA^+) or ethylammonium (EA^+) iodide, in a simple 2-component precursor. Alternatively, a GIWAXS study on the temperature-dependant behaviour of the $(MA)_4Pb_3I_{10}$-containing films could explore possible phase-transitions that may occur between 4 K and 290 K. This would complement the temperature-dependent spectroscopy work performed in

Chapter 6. These mixed-phase 2D/3D perovskite thin-films are of growing interest as they have previously shown interesting charge-transfer characteristics, as well as prolonged device stability when incorporating hydrophobic cations in the precursor [3–5].

7.2. References

1. Chueh, C. *et al.* The roles of alkyl halide additives in enhancing perovskite solar cell performance. *J. Mater. Chem. A* **3,** 9058–9062 (2015).
2. Chen, Y., He, M., Peng, J., Sun, Y. & Liang, Z. Structure and growth control of organic–inorganic halide perovskites for optoelectronics: From polycrystalline films to single crystals. *Adv. Sci.* **3,** (2015).
3. Grancini, G. *et al.* One-Year stable perovskite solar cells by 2D/3D interface engineering. *Nat. Commun.* **8,** 15684 (2017).
4. Ma, C. *et al.* 2D/3D perovskite hybrids as moisture-tolerant and efficient light absorbers for solar cells. *Nanoscale* **338,** 643–647 (2016).
5. Li, M. H. *et al.* Highly Efficient 2D/3D Hybrid Perovskite Solar Cells via Low-Pressure Vapor-Assisted Solution Process. *Adv. Mater.* **30,** 1–13 (2018).